Stony Brook University

Synthesis and Characterization of Carbon Nanotube-Metal Chalcogenide/Oxide Heterostructures for Energy-related Applications

A Dissertation Presented

by

Lei Wang

to

The Graduate School

in Partial Fulfillment of the

Requirements

for the Degree of

Doctor of Philosophy

in

Chemistry

Stony Brook University

August 2016

Stony Brook University

The Graduate School

Lei Wang

We, the dissertation committee for the above candidate for the

Doctor of Philosophy degree, hereby recommend

acceptance of this dissertation.

Dr. Stanislaus S. Wong – Dissertation Advisor
Professor, Department of Chemistry

Dr. John B. Parise - Chairperson of Defense
Distinguished Professor, Department of Geosciences

Dr. Amy C. Marschilok - Third Member of Academic Committee
Research Professor, Department of Chemistry

Dr. Hong Gan – Outside Member
Chemist, Sustainable Energy Technologies Department
Brookhaven National Laboratory

This dissertation is accepted by the Graduate School

Nancy Goroff

Interim Dean of the Graduate School

Abstract of the Dissertation

Synthesis and Characterization of Carbon Nanotube-Metal Chalcogenide/Oxide Heterostructures for Energy-related Applications

by

Lei Wang

Doctor of Philosophy

in

Chemistry

Stony Brook University

2016

With the increasing strain on existing fossil fuel resources and the serious concerns associated with the environmental impacts on CO_2 release through the burning of fossil fuels, clean energy innovation is needed to "get us on the right path" to energy sustainability. Achieving this objective will necessitate a rational design, development, and deployment of schemes to create novel sources of 'carbon-free' power using materials with specific and desired functions or properties. In this dissertation, we have attempted to develop two different categories of carbon nanotube (CNT)-based nanoscale heterostructures, namely (a) CNT- CdSe quantum dot (QD) heterostructures and (b) CNT-$Li_4Ti_5O_{12}$ (LTO) heterostructures, and to study their intriguing properties for applications associated with photovoltaics and lithium-ion batteries (LIBs). In terms of the potential of CNT-CdSe QD heterostructures for photovoltaic devices, we have put forth a unique compilation of complementary data from experiment and theory, including results from transmission electron microscopy (TEM), near-edge X-ray absorption fine structure (NEXAFS) spectroscopy, Raman spectroscopy, electrical transport measurements, and theoretical modeling studies, in order to probe charge transfer behavior within nanoscale composites composed of double-walled carbon nanotubes (DWNT) coupled with CdSe QDs.

These heterostructures were probed as a function of QD size, the nature of the distinctive bridging ligand molecules used, as well as their unique attachment modalities. With respect to CNT-LTO heterostructures for LIB applications, a novel flower-like nanostructured LTO motif was synthesized by a facile, low-cost, and large-scale hydrothermal process involving re-useable and recyclable precursors followed by a short, relatively low-temperature calcination step in air. Furthermore, 3D “flower-like” LTO - multiwalled carbon nanotube (MWNT) composites were generated via different preparative approaches, including (i) physical sonication, (ii) an in situ direct deposition approach, as well as (iii) a covalent chemical attachment protocol. To the best of our knowledge, we are the first to correlate the actual preparative strategy, i.e. the particular chemical treatment process used to generate these composite materials, of a novel hierarchical nanoscale motif, relevant for battery applications, with its resulting physically significant electrochemical performance.

This dissertation is dedicated to my family, friends, and all of those who have supported me during my period of study.

Table of Contents

List of Figures

List of Tables

List of Abbreviations

0D	zero-dimensional
1D	one-dimensional
2D	two-dimensional
AET	2-aminoethanethiol
ATP	4-aminothiophenol
BET	Brunauer-Emmett-Teller
CB	conduction band
CdSe	cadmium selenide
CdS	cadmium sulfide
CNTs	carbon nanotubes
CVD	chemical vapor deposition
DCC	dicyclohexylcarbodiimide
DMF	dimethylformamide
DMSO	dimethylsulfoxide
DSSCs	dye-sensitized solar cells
DFT	density functional theory
DWNTs	double-walled carbon nanotubes
EDC	N-(3-dimethylaminopropyl)-N'-ethylcarbodiimide
EIS	electrochemical impedance spectroscopy
FESEM	field emission scanning electron microscopy
FTIR	Fourier transform infrared spectroscopy
HDA	hexadecylamine
HOMO	highest occupied molecular orbital
HRTEM	high resolution transmission electron microscopy

ITO	indium tin oxide
JCPDS	Joint Committee on Powder Diffraction Standards
LIBs	lithium-ion batteries
LTO	lithium titanate
LUMO	lowest unoccupied molecular orbital
MTH	4-mercaptophenol
MWNTs	multi-walled carbon nanotubes
NEXAFS	near-edge X-ray absorption fine structure
P3HT	poly (3-hexylthiophene)
PEDOT: PSS	poly(3,4-ethylenedioxythiophene)-poly(styrenesulfonate)
PL	photoluminescence
PPD	p-phenylenediamine
PV	photovoltaic
SAED	selected area electron diffraction
SE	secondary electrons
SEM	scanning electron microscopy
TBP	tributylphosphine
TEM	transmission electron microscopy
TGA	thermogravimetric analysis
TOPO	tri-n-octylphosphine oxide
XRD	X-ray diffraction
UV-Vis	ultraviolet-visible
V_{OC}	open-circuit voltage
VB	valence band

Acknowledgments

First, I would like to thank my advisor Dr. Stanislaus Wong, for providing me with the valuable opportunities to participate in various research projects and collaborate with many outstanding scientists. His guidance, expertise, and support over the past five years have greatly enhanced my Ph.D. career. I would also like to extend my sincerest thanks to my academic committee including my committee chair, Dr. John Parise and my third member, Dr. Amy Marschilok, for their challenging questions and insightful suggestions on my research projects. I am also grateful to Dr. Hong Gan for his time and consideration to serve as the outside member on my academic committee.

I also would like to acknowledge my fellow group members, Dr. Megan Scofield, Dr. Crystal Lewis, Dr. Haiqing Liu, Coray McBean, Shiyu Yue, Luyao Li, Dominic Moronta, Yuchen Zhou, Shihui Zou, Gerard Mattei, and Chao Qin for their support and help during my research career, in addition to a previous group member, Dr. Jinkyu Han for his guidance in the initial stages of my research career. Additionally, I would like to thank Dr. James Quinn and Susan Van Horn, and Dr. Vyacheslav Volkov for their assistance and expertise in electron microscopy; Yiman Zhang, Dr. Esther Takeuchi, Dr. Kenneth Takeuchi, and Dr. Amy Marschilok for the acquisition and interpretation of the electrochemical data for the work conducted on $Li_4Ti_5O_{12}$; Yuqi Zhu, Ruiping Zhou, and Dr. Joerg Appenzeller for the collection and interpretation of electrical transport results; Bryan Sundahl, Scott Thornton, and Dr. Robert Harrison for their theoretical modeling results on carbon nanotubes and quantum dots; Zhuo-Qun Li, Fang Hu, Dr. Molly Gentleman, and Dr. Gordon Taylor for their assistance in Raman data collection, as well as Dr. Cherno Jaye and Dr. Daniel Fischer for helping with the NEXAFS data acquisition. Furthermore, I would like to acknowledge the faculty and staff from the Chemistry Department at Stony Brook University and the Condensed Matter Physics and Materials Science Department as well as the Center for Functional Nanomaterials at Brookhaven National Laboratory.

Finally, I would like to thank my friends and family for all of their support throughout my Ph.D. career. I am extremely grateful to my parents for their unconditional love and support and for believing in me.

List of Publications

1. **Wang, L.**; Han, J.; Sundahl, B.; Thornton, S.; Zhu, Y.; Zhou, R.; Jaye, C.; Liu, H.; Li, Z.-Q.; Taylor, G. T.; Fischer, D. A.; Appenzeller, J.; Harrison, J. R. and Wong, S. S., **"Ligand-induced dependence of charge transfer in nanotube–quantum dot heterostructures",** *Nanoscale*, **2016,** *in press*.
2. Scofield, M. E.; Zhou, Y.; **Wang, L.**; Vukmirovic, M.; Adzic, R. R. and Wong, S. S., **"Correlating the Chemical Composition of Various Pt-based Alloyed Ultrathin Nanowires with Catalytic Activity for the Hydrogen Oxidation Reaction under Alkaline Conditions",** *ACS Catal.*, **2016**, *6*, 3895–3908.
3. Lewis, C. S.; Liu, H.; Han, J.; **Wang, L.**; Yue, S.; Brennan N. A. and Wong, S. S., **"Probing charge transfer in a novel class of luminescent perovskite-based heterostructures composed of quantum dots bound to RE-activated $CaTiO_3$ phosphors"**, *Nanoscale*, **2016,** *8,* 2129-2142.
4. Scofield, M. E.; Koenigsmann, C.; Semple, D. B.;, Tao, J.; Tong, X.; **Wang, L.**; Lewis, C. S.; Vukmirovic, M.; Zhu, Y.; Adzic, R. R. and Wong, S. S., **"Correlating the Chemical Composition and Size of Various Metal Oxide Substrates with the Catalytic Activity and Stability of As-Deposited Pt Nanoparticles for the Methanol Oxidation Reaction",** *Catal. Sci. Technol.*, **2016**, *6*, 2435.
5. **Wang, L.**; Han, J.; Zhu, Y.; Zhou, R.; Jaye, C.; Liu, H.; Li, Z.-Q.; Taylor, G. T.; Fischer, D. A.; Appenzeller, J. and Wong, S. S., **"Probing the Dependence of Electron Transfer on Size and Coverage in Carbon Nanotube–Quantum Dot Heterostructures",** *J. Phys. Chem. C*, **2015**, *119*, 26327–26338.
6. **Wang, L**.; Zhang, Y.; Scofield, M. E.; Yue, S.; McBean, C.; Marschilok, A. C.; Takeuchi, K. J.; Takeuchi, E. S. and Wong, S. S., **"Enhanced Performance of Novel 'flower-like' $Li_4Ti_5O_{12}$ Motifs as Anode Materials for High-rate Li-ion Batteries"**, *ChemSusChem*, **2015**, ***8,*** 3304-3313.
7. Patete, J. M. ; Scofield, M. E.; Koenigsmann, C.; Volkov, V.; Zhang, Y.; Marschilok, A. C.; Wang, X.; Bai, J.; Han, J.; **Wang, L**.; Wang, F.; Zhu, Y.; Graetz, J. A. ; and Wong, S. S., **"Ambient Synthesis, Characterization, and Electrochemical Activity of $LiFePO_4$ Nanomaterials derived from Iron Phosphate Intermediates",** *Nano Research*, **2015**, ***8,*** 2573-2594.
8. Han, J.; McBean, C.; **Wang, L**.; Jaye,C.; Liu, H.; Fischer, D. A. and Wong, S. S., **"Synthesis of Compositionally-Defined Single-Crystalline Eu^{3+}-Activated Molybdate-Tungstate Solid Solution Composite Nanowires and Observation of Charge Transfer in a Novel Class of 1D $CaMoO_4$-$CaWO_4$: Eu^{3+}–0D CdS/CdSe QD Nanoscale Heterostructures"**, *J. Phys. Chem. C*, **2015**, ***119,*** 3826-3842.
9. Scofield, M. E.; Koenigsmann, C.; **Wang, L**.; Liu, H. and Wong, S. S., **"Tailoring the Composition of Ultrathin, Ternary Alloy PtRuFe Nanowires for the Methanol**

Oxidation Reaction and Formic Acid Oxidation Reaction", *Energy Environ. Sci.*, **2015**, ***8,*** 350-363.

10. Han, J.; McBean, C.; **Wang, L.**; Hoy, J. Jaye,C.; Liu, H.; Li, Z.; Sfeir, M. Y. ; Fischer, D. A.; Taylor, G.T. ; Misewich, J. A. and Wong, S. S., **"Probing structure-induced optical behavior in a new class of self-activated luminescent 0D/1D $CaWO_4$ metal oxide – CdSe nanocrystal composite heterostructures",** *Chem. Mater.*, **2015**, ***27,*** 778-792.

11. Wang, L.; Han, J.; Hoy, J.; Hu, F.; Liu, H.; Gentleman, M. M. ; Sfeir, M. Y. ; Misewich, J. A. and Wong, S. S., **"Probing differential optical and coverage behavior in nanotube–nanocrystal heterostructures synthesized by covalent versus non-covalent approaches",** invited contribution, 'Organometallic and Coordination Derivatives of Nanocarbons' special issue, *Dalton Trans.*, **2014**, *43*, 7480 – 7490.

12. Han, J.; **Wang, L.** and Wong, S. S., **"Observation of photoinduced charge transfer in novel luminescent CdSe quantum dot – $CePO_4$: Tb metal oxide nanowire composite heterostructures",** *J. Phys. Chem. C,* **2014**, *118,* 5671-5682

13. Han, J.; **Wang, L.** and Wong, S. S., **"Morphology and dopant-dependent optical characteristics of novel composite 1D and 3D based heterostructures of CdSe nanocrystals and $LaPO_4$: Re (Re = Eu, Ce, Tb) metal oxide nanowires",** *RSC Adv.*, **2014**, ***4,*** 34963-34980.

14. Lewis, C. S.; **Wang, L.**; Liu, H.; Han, J. and Wong, S. S., **"Synthesis, Characterization, and Formation Mechanism of Crystalline Cu and Ni Metallic Nanowires under Ambient, Seedless, Surfactantless Conditions",** *Cryst. Growth Des.*, **2014**, ***14,*** 3825-3838.

15. Wang, **L.**; Liu, H.; Konik, R. M.; Misewich, J. A. and Wong, S. S., **"Carbon Nanotube-based Heterostructures for Solar Energy Applications",** invited contribution, *Chem. Soc. Rev.*, **2013**, ***42,*** 8134-8156.

16. Zhang, Z.; **Wang, L.**; Kou, S. X.; Lee, Y. I.; Hao, J. C. and Liu, H. G., **"One-step synthesis and assembly of one-dimensional parallel chains of CdS nanoparticles at the air–water interface templated by 10,12-pentacosadiynoic acid supermolecules"** *J. Colloid Interface Sci.*, **2012,** *375*, 118-1

Chapter 1. Carbon Nanotube-Metal Chalcogenide/Oxide Heterostructures: Promising Structural Paradigms for Photovoltaics and Li-ion Batteries

1.1. Global Energy Crisis and the Applications of Nanostructures in Energy Conversion

Over the years, with the rapid increase in global population and accompanying economic growth and consumption, there has been an increasing strain upon existing fossil fuel resources, which has led to a corresponding hike in oil and gas prices.[1,2] Moreover, the environmental impacts, associated with energy production utilizing fossil fuels, have given rise to serious concerns. The increasing atmospheric concentrations of carbon dioxide (CO_2) through the burning of fossil fuels have a profound impact on global climate change, which has become a focal point of significant socio-political attention.[3] The need to control CO_2 levels has led to extensive research into developing attractive, alternative energy systems that do not rely on traditional fossil fuels as a source of primary energy. The International Energy Agency's report, entitled 'Energy Technology Perspectives 2015: Mobilizing Innovation to Accelerate Climate Action,' notes that clean energy innovation is needed to "get us on the right path" to energy sustainability. Therefore, achieving this objective will necessitate a rational design, development, and deployment of schemes to create novel sources of 'carbon-free' power using "materials with specific and desired functions or properties, predicted from first principles".

The most obvious choice of an alternative energy resource is sunlight, which can be used for heating, lighting, as well as electricity generation. For example, when properly concentrated in usable form, sunlight can be used to provide steam in order to run turbines.[4] In fact, when the sun is directly overhead with a clear sky, radiation impinging upon a horizontal surface can reach ~1,000 W m^{-2}. Significantly, in the United States, for example, the total amount of solar energy

striking the surface of the continental 48 states is ~$4.67 \bullet 10^4$ quads per year (wherein a quad, derived from 'quadrillion', is $1.05 \cdot 10^{18}$J or $2.9 \cdot 10^{11}$ kWh), a value which is well in excess of the 98.6 quads that the nation consumes annually, on average.[4] It has been estimated that by the year 2050, a minimum of 20 terawatts of carbon-free energy (*i.e.*, 1.5 times the total amount of all forms of energy, consumed today globally), in the form of electricity and fuels, will be needed in order to meet the increasing demands of both an economically and sustainably viable world.[5]

One way to convert sunlight directly into electrical energy is through the mediation of photovoltaic cells. Currently about 0.08 quads of energy are produced each year in the United States from solar thermal energy and solar photovoltaic device sources, which are able to convert sunlight directly into electrical energy.[4] According to Tomokazu et al.[6], there are three major processes associated with converting sunlight into electrical power: (i) absorption of solar photons using a photoactive layer to form locally confined excitons, (ii) migration of the excitons to the donor–acceptor interface and subsequent dissociation to form free electrons and holes, and (iii) transfer and separation of the charges towards respective electrodes so as to eventually yield a photocurrent in an external circuit. Generally, there are three generations of photovoltaic devices of interest: (i) the first generation consisting of single-crystalline silicon-based photovoltaic devices, which are commercially available for installation, can deliver power with a 15% efficiency, but suffers from the high cost of manufacturing and installation, and (ii) the second generation is composed of cheaper $CuInGaSe_2$ (CIGS) polycrystalline semiconductor thin films, which can address cost considerations but unfortunately, possess poor overall efficiency.

At this time, extensive active research work has been focused on fabricating so-called third generation devices, which are expected to deliver high efficiency at an acceptable economic cost by utilizing semiconducting entities, such as quantum dots, as fundamental building blocks.[1] In effect,

the efficiency of solar photon conversion possesses an intrinsic limit that complicates matters. That is, sunlight consists of photons possessing a wide range of energies from 0.5 to 3.5 eV, though only ~1/3 of the total energy can be utilized in current solar cell configurations. Indeed, photons possessing a lower energy than the optical bandgap are frequently not absorbed, while for photons maintaining a higher energy than the bandgap, the excess kinetic energy of the photogenerated electrons and holes created above the bandgap (termed 'hot' carriers) is often lost as heat through processes such as electron-phonon scattering. This unavoidable reality results in an upper bound to the thermodynamic efficiency of single-bandgap cells.

Indeed, Shockley and Queisser (SQ) predicted a limiting power efficiency of 30% under simulated black body radiation conditions, which has been re-calculated as 33% under AM 1.5 solar irradiance,[7-9] and this limit applies to both photovoltaic and solar fuel devices. Through the utilization of third-generation devices, energy losses associated with the cooling of hot carriers can be potentially reduced. At the same time, these devices render the absorption of sub-bandgap photons possible. That is, through multi-exciton generation involving the production of two or more excitons from hot excitons created by the absorption of high-energy photons, third-generation devices can be created to realistically increase the measured conversion efficiency by as much as a factor of 4/3.[5]

Although photovoltaics can convert sunlight into electricity, they are constrained by the diffuse nature of the solar flux, which can vary considerably depending upon parameters that cannot be necessarily controlled including incident solar radiation, weather conditions, and temperature. Hence, there are basic issues associated with collecting, converting, and storing solar energy into a usable and practical form, especially to account for situations where either there is less demand or when solar radiation is not available, *i.e.* at night. As a major device for electric energy storage,

lithium-ion batteries (LIBs) have attracted worldwide attention, because they play an important role in our daily lives as the dominant power sources for portable electronics such as cell phones and laptops and possess great potential to completely power electric vehicles and the like in order to find use in large-scale electrical grids. Lithium ion batteries (LIBs) have achieved commercial success in the field of portable electronic devices, due to their outstanding properties, such as high energy density, light weight, long lifespan, and ambient temperature operation.[10-12]

Generally, an integrated LIB system includes three indispensable parts, namely a negative electrode (anode), an aqueous/non-aqueous electrolyte and a positive electrode (cathode).[13] The predominant active electrode materials usually consist of a lithiated metal oxide for the cathode and a graphitic carbon as the anode. The active materials are combined with a binder (e.g. polyvinylidene fluoride – PVDF) and conductive additives (e.g. carbon black, graphite, etc.) before subsequently being deposited onto the metal foil current collectors. A polymer separator with a microporous polypropylene/polyethylene laminate is necessary to be placed between the electrodes in order to render them electrically insulated while allowing for lithium ion diffusion. A LIB operates by movement of lithium ions from the cathode to the anode upon charging and the reversible process occurs during discharging, as illustrated by the schematic in Figure 1.1.

The lithiated $LiCoO_2$ serves as the cathode, and graphitic carbon is the anode. Both materials possess layered structures with interstitial spaces receptive to lithium ion intercalation. The active material is able to store the lithium due to the simultaneous electron transport from the current collector in order to reduce the lithium ion at the active material ‘‘host’’ site. The intercalation process is facilitated by the formation of a necessary solid-electrolyte interface (SEI) on the surface of each electrode which can passivate the electrode surface from further solvent reduction and act as a selective layer to allow only lithium ions to diffuse. The lithium ions are present in an electrolyte

comprising a lithium salt, most often $LiPF_6$, solvated by a mixed solution of alkyl carbonates (*i.e.* ethylene carbonate (EC), dimethyl carbonate (DMC), etc.).[14] With the growing demand for applications in energy storage stations and modern electric vehicles, the development of LIBs possessing a desirable mixture of positive attributes, such as high energy and power densities, superior durability, long cycling performance, as well as favorable environmental sustainability remains a highly sought-after objective.[15, 16]

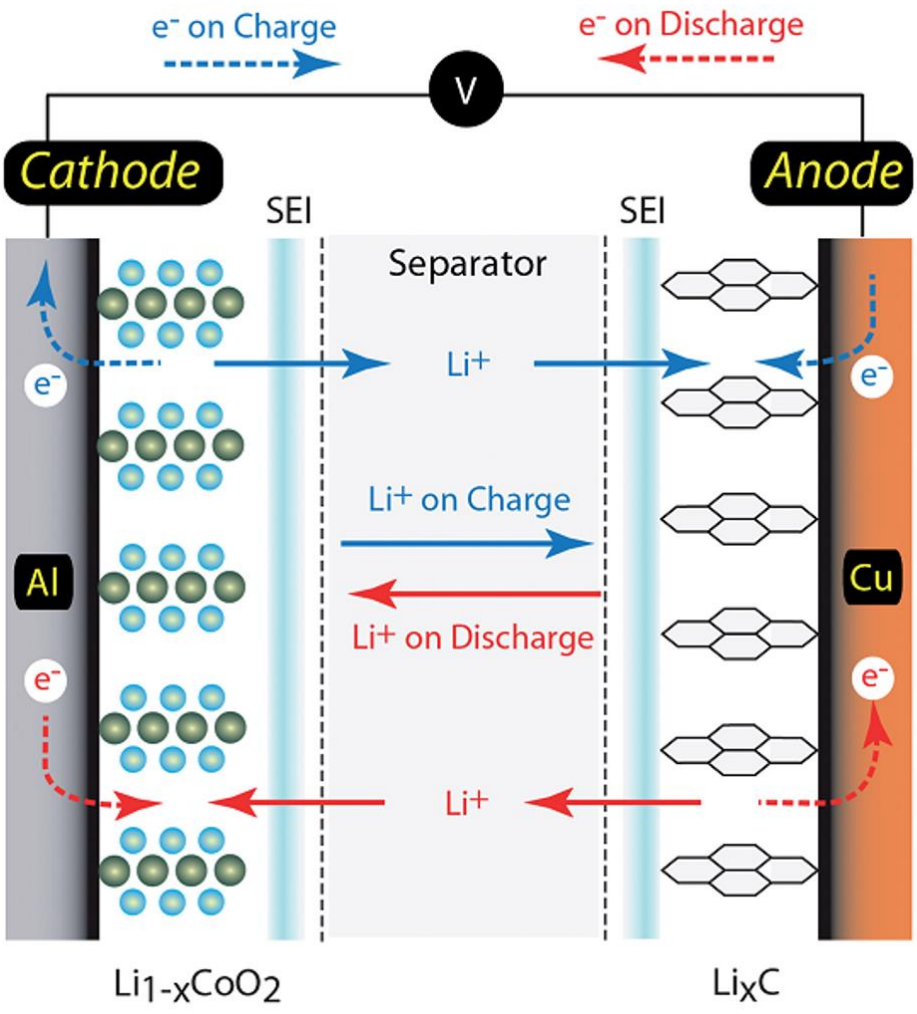

Figure 1.1 Schematic illustrating the mechanism of operation for a lithium ion battery including the movement of ions between electrodes (solid lines) and the electron transport through the complete electrical circuit (dashed lines) during charge (blue) and discharge (red) states. (Adapted in part from Ref. 14).

In recent years, nanomaterials have emerged as the new building blocks, applicable in the development of both photovoltaic devices and LIBs. According to the National Nanotechnology Initiative (NNI), a "nanomaterial" refers to a material possessing at least 1 dimension at the nanoscale, namely 1- 100 nm. The prefix "nano" stems from the Greek word "nanos", which means 'dwarf' and is assigned by the international system of units (SI) as referring to 1×10^{-9} of the base unit.[17] Compared with their bulk counterparts, nanoscale materials, with their large surface areas and possible quantum confinement effects, exhibit distinctive optical, catalytic, electronic, and thermal properties. The intriguing properties of nanomaterials can be tailored by varying their shapes, which allows one to differentiate among various types of nanostructures through their dimensionality. The shapes of nanomaterials are categorized by their dimensionality. For example, (i) nanospheres and nanocubes, for example, denote zero-dimensional (0D) nanomaterials, since all of their dimensions are confined at the nanoscale, (ii) anisotropic nanowires, nanorods, or nanotubes are one-dimensional (1D) nanomaterials with one dimension of the nanostructure outside the nanometer range, (iii) nanosheets and nanoplates are considered as two dimensional (2D) nanomaterials, with only 1 dimension limited and the other two outside the nanometric size range, whereas (iv) nano-flowers are three-dimensional (3D) nanomaterials, representing materials outside the nanosize range in all dimensions but which are composed of the individual blocks at the nanometer scale.

In the interim, a lot of research interest has shifted from single-component nanomaterials towards the synthesis and design of more complex, multi-component nanostructures. In effect, nanoscale heterostructures, consisting of two or more chemically distinctive components, provide for a unique path to merge the favorable properties of individual nanoscale components into an integrated whole, whose specific properties are different from and potentially better than the sum of their separate parts. Such intriguing structural motifs demonstrated great potential for revolutionizing

nanomaterials' research. Hence, through a judicious choice of complementary nanoscale moieties, the synthetic potential herein is the ability to produce truly astonishing nanostructures with distinctive and unforeseeable properties and functionalities. The effective, reliable and facile fabrication of high-quality nanoscale heterostructures as well as the fundamental understanding of their desirable electronic and optical properties are essential for promoting significant breakthroughs in the development of renewable clean energy.

In this dissertation, we have reported on facile and reliable synthetic routes to generate two different categories of nanoscale heterostructures, namely (i) 0D-1D heterostructures, consisting of 0D quantum dots (QDs) attached onto 1D carbon nanotubes (CNTs), and (ii) 3D-1D heterostructures, composed of 3D metal oxides coupled with 1D CNTs, respectively. Furthermore, we have probed their intriguing opto-electronic and electrochemical properties associated with applications associated with photovoltaics and LIB devices, separately. Specifically, in terms of 0D-1D heterostructures, we have correlated the charge transfer properties of CNT-QD heterostructures with their connective attachment strategies (Chapter 3), the average size of the QDs used (Chapter 4), as well as the identity of the bridging ligand molecules (Chapter 5), respectively, which not only sheds light on the possibility of chemically tuning for efficient charge transfer of the CNT-QD heterostructures via the manipulation of the properties individual constituent components as well as the attachment methodologies but also provides for valuable guidance towards the construction of high-efficiency solar devices.

With respect to 3D-1D heterostructures, we have discussed the rational design of a novel 3D flower-like $Li_4Ti_5O_{12}$ (LTO) structure (Chapter 6) and further investigated the effect of the attachment modality upon the resulting 3D- 1D LTO-CNT heterostructures upon the performance of the resulting LIB anode materials (Chapter 7). As a means of providing relevant background and

context, the synthetic methods employed to generate the various 0D, 1D, and 3D nanomaterials as well as the compilation of both experimental and theoretical characterization techniques utilized within this thesis will be discussed in detail in Chapter 2.

In light of the properties of the individual building components as well as the current applications of the resulting heterostructures in the field of photovoltaics and LIBs, the following sections provide for a concise introduction into the nature of CNTs, QDs, and metal oxides, as well as their corresponding heterostructures, with the aim of targeting specific applications in photovoltaics and LIBs. Specifically, we first provide a concise introduction into 1D CNTs in Section 1.2, including their synthesis and functionalization/purification procedures as well as their potential applications in photovoltaic and LIB devices. In Section 1.3, we summarize the synthesis of QDs as well as the subsequent ligand-exchange process with an emphasis on elaborating upon their potential applicability in photovoltaics.

Subsequently, the common intriguing electrochemical properties of 3D metal oxides relevant for their application in LIBs and structural details regarding the model $Li_4Ti_5O_{12}$ motif are outlined in Section 1.5. In the context of the resulting heterostructures, synthetic methods associated with CNT-QD nanostructures with potential applicability in photovoltaics are highlighted in Section 1.4. The 3D metal oxide-CNT heterostructures denote a promising structural paradigm for the development of high rate LIBs, and are presented in Section 1.6, with an emphasis on discussing the attachment modalities of CNTs onto the surfaces of metal oxides. In this Chapter, we present, in Section 1.7, the objectives of the current work, which includes the purpose of this thesis, the goal of which is to generate, characterize, and analyze the various nanoscale carbon nanotube-based heterostructures. Being able to tailor the structure and

properties of these novel composites can lead to considerable enhancements in both their activity and durability for applications in photovoltaics and LIBs.

1.2. One-dimensional (1D) carbon nanotubes (CNTs)

Carbon nanotubes (CNTs) denote allotropes of carbons with a cylindrical nanostructure. These motifs have been widely studied, since their discovery in 1991 by Ijima.[18] Due to their unique electronic and chemical properties, they are considered as attractive candidates for a number of diverse photochemical and electronic applications, ranging from photovoltaic devices to field effect transistors. The CNTs are composed of a long, hollow structure with the walls formed by one-atom-thick sheets of carbon, called graphene. These sheets are rolled at specific and discrete angles, θ, known as chiral angles, which in combination with the nanotube radius, dictate the electronic properties of the CNTs.

The walls of the CNTs can be often described, except for their length, by an intrinsic geometric chiral vector, $\mathbf{C}_h$, which is defined by the equation $\mathbf{C}_h = n\mathbf{a}_1 + m\mathbf{a}_2$, wherein the integers (*n, m*) represent the number of steps along the zig-zag carbon bonds and $\mathbf{a}_1$ and $\mathbf{a}_2$ represent the graphene lattice basis vectors in real space (Figure 1.2a).[19] The chiral vector makes an angle, i.e. the chiral angle, with the $\mathbf{a}_1$ direction. This angle determines the amount of "twist" in the nanotube, and two limiting cases exist, where the chiral angle is at 0° and 30°. These are known as zig-zag (0°) and armchair (30°), respectively, based upon the geometry of the carbon bonds around the circumference of the nanotube (Figure 1.2b, c). All other conformations in which the C–C bonds lie at angles $0° < \theta < 30°$ are known as chiral tubes (Figure 1.2d). The *n, m* integers completely describe nanotube chirality, and determine the electronic band structure of the CNTs. Thus, it is the chirality that yields the most impact upon the electronic properties of carbon nanotubes. In particular, a slight change in the chiral angle gives rise to nanotubes that are either

metallic conductors or consist of either low bandgap or high bandgap semiconductors. Depending upon the numbers of graphene walls, CNTs can be categorized as single-walled nanotubes (SWNTs) with average diameters of 0.4-2 nm and multi-walled nanotubes (MWNTs) with average overall diameters of 2-100 nm, depending on the number of concentric carbon layers.[20] CNTs with small diameters tend to align themselves into "bundles" held together by van der Waals forces, more specifically, pi-stacking.

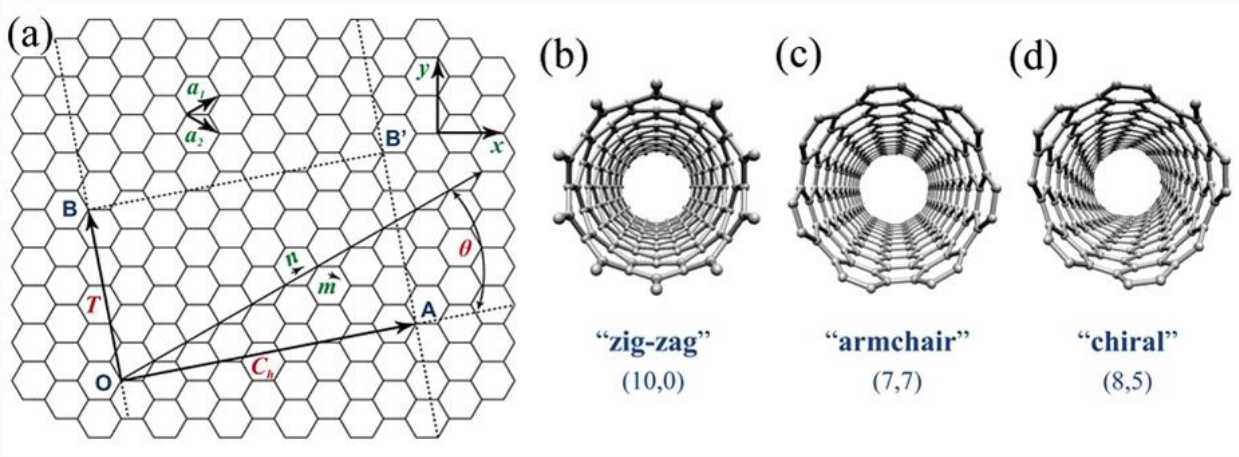

Figure 1.2 a) Unrolled graphene sheet showing the geometry of the (6, 3) nanotube ($\mathbf{C}_h$ and **T**: chiral translational vectors, respectively). b–d) Examples of the three classes of nanotube sidewall; zig-zag, armchair, and chiral. (Adapted in part from Ref. 19)

1.2.1. Synthesis method of CNTs

Various techniques have been developed to generate CNTs, including arc discharge, laser ablation, and chemical vapor deposition (CVD) protocols. The arc-discharge method was first used to prepare carbon nanotubes in 1991 by Ijima while attempting to synthesize C_{60}. Such a technique required a high voltage and current to be applied between two closely spaced (1-2 mm), highly pure graphite electrodes in an inert atmosphere.[18] The type of carbon nanotube produced can be tailored to be single-, double- or multi-walled through careful tuning of the catalyst composition, atmosphere, current/voltage conditions, and carbon feedstock. The laser

ablation method was reported for the first time by Smalley and his group to grow high quality nanotubes. A carbon target is placed in a tube-furnace, heated to 1200°C, and ablated by the application of intense laser pulses. A flow of inert gas is used to carry the as-grown CNTs from the chamber to the copper collector.[21] Multi-walled nanotubes can be generated through the use of pure carbon, while the addition of a catalyst, including elements, such as iron, yttrium, sulphur, nickel, and molybdenum, can lead to the formation of a single-walled CNTs.[22] In catalytic chemical vapor deposition (CCVD) growth, which is the most widely used method for the production of carbon nanotubes,[23] a volatile gaseous carbon source (typically CH_4, CO, or C_2H_2) is decomposed at high temperature (approximately 700°C) in a process gas (such as NH_3, N_2, or H_2) atmosphere over metallic nanoparticle substrates, commonly Ni, Co, and Fe.[24] The decomposed carbon atoms diffuse into the metal nanoparticles, and, upon saturation, precipitate at the surface and thereby initiate nanotube growth directly from the nanoparticle.

1.2.2. Chemical functionalization of CNTs

Pristine CNTs contain a number of impurities, such as metal catalyst particles, amorphous carbon, and other carbonaceous species, and are difficult to be dispersed in either aqueous media or organic solvents. Moreover, strong van der Waals interactions between pristine nanotubes result in their bundling and aggregation. These inherent challenges represent a huge gap between the theoretical potential and practical utilization of using pristine nanotubes in applications. To mitigate for the aforementioned problems, chemical functionalization of CNTs represents the most effective means for manipulating and processing nanotubes.

Prior research has demonstrated that CNTs can be reliably modified by a number of chemical treatments. Examples of typical methods include either acid-based wet-chemical oxidation,[25, 26] esterification,[27] carbodiimide activation,[25, 28] fluorination,[29, 30] or hydrophobic

adsorption of aromatic derivatives.[31, 32] To summarize, these functionalization strategies generally fall into two major categories, namely, non-covalent and covalent functionalization, respectively, according to the nature of the interaction between the CNTs and the surface functional moieties. With respect to non-covalent functionalization, CNTs are usually wrapped by either conducting polymers or other organic molecules containing conjugated carbon systems through π-π stacking interactions, thereby obtaining the desired solubility or biological functionality for various applications without introducing defects.[33]

Covalent functionalization usually breaks the intrinsic C=C sp^2 structure and is suggested as a means for disrupting the electronic structure of CNTs. However, it provides for a robust and effective methodology with a high degree of flexibility in introducing a variety of chemical moieties onto the surfaces of CNTs. In this thesis, our as-prepared heterostructures have incorporated oxidized, oxygenated CNTs, generated by the treatment of CNTs with strong acids so as to form pendant carboxylic acid functionalities (as well as keto, aldehyde, and alcoholic groups) on the nanotube surface. Such a treatment can not only remove the metal catalyst and amorphous carbon impurities within the CNTs but also introduce functional carboxylic acid moieties, which can facilitate the subsequent covalent attachment of other components onto the external CNT surfaces.

1.2.3. Application of CNTs in photovoltaic devices and LIBs

With respect to photovoltaic applications, CNTs possess unique electrical and opto-electronic properties, a high surface area, and a wide electrochemical stability window, all of which render CNTs as promising components of energy conversion devices.[34-36] For example, when subjected to appropriate bandgap excitation, semiconducting CNTs can undergo measurable charge separation. It is worth noting that when the diameter of the CNTs approaches 1 nm, excitons with huge binding

energies tend to be generated due to quantum confinement effects, which are a result of their anisotropic one-dimensional (1D) structures. Transient absorption and emission measurements have been used to probe a variety of exciton annihilation and charge separation processes in these systems.[1, 37] Moreover, nanotubes are capable of transporting charge ballistically over relatively large distances at room temperature.[38-40]

Hence, by 'merging' CNTs with other nanostructures, unique heterostructures with intriguing, favorable, and potentially unexpected opto-electronic properties can be generated. For example, charge carriers are susceptible to recombination loss at the boundaries of semiconducting particles. Chemically attaching CNTs to these systems represents a convenient and practical strategy of not only capturing photogenerated charges but also efficiently transporting them to the electrode surface.[1] Specifically, extensive research has focused on the development of CNT-based organic solar cells, *e.g.* carbon nanotube-conducting polymer systems, such as (a) polyaniline (PANI) nanocomposites to replace transparent conductive oxide (TCO) layers within dye-sensitized solar cell (DSSCs),[41] as well as (b) SWNT/pyrene^{+}/ZnP^{8} and single-walled carbon nanotube (SWNT)-sodium poly(styrene-4-sulfonate) (PSS^{n-})/ZnP^{8+} composites to substitute for semi-transparent indium tin oxide (ITO) in photovoltaic cells.[42] CNT-based heterostructures as components of inorganic semiconductor-based solar cells have also been reported. These include not only CNT-silicon heterojunction solar cell architectures, demonstrating power conversion efficiencies of up to ~14%,[43] but also CNT-metal oxide hybrid composites, possessing nearly double the photoconversion efficiency, as compared with that of the pure metal oxide-based systems, especially when SWNTs are used as the underlying support for the deposition of the TiO_2 nanoparticles.[44] In this particular thesis, we have placed a special emphasis upon CNT-quantum dot (QD) heterostructures, which have potential applicability in QD-sensitized solar cells (QDSCs).

With respect to LIBs, CNTs have been recognized as potential candidate materials, due to their outstanding set of electrochemical and mechanical properties. Generally, there are two common ways of utilizing CNTs in LIBs, namely the incorporation of CNTs either as i) conductive additives or as ii) active lithium ion storage materials or physical supports for ultra-high capacity anode materials in free-standing electrodes. The advantages of using of CNTs as conducting additives for either the anode or cathode are several fold. First, as compared with other carbon-based additives like carbon black, acetylene black, or carbon fibers, CNTs possess outstanding electrical conductivity, exceeding 5×10^5 S m^{-1} at room temperature.[45] Second, the high aspect ratios of CNTs allow for lower weight doping levels to be achieved in order to achieve a comparable percolation threshold (i.e. the concentration in a composite that sustains either long range connectivity or contiguous pathways for electrons to move),[14] demonstrating more than an order of magnitude reduction in additive mass as compared with other conventional carbon counterparts. Third, the π-orbital overlap between metallic CNTs enables the ballistic transport of electrons with mean free paths on the order of microns along the length of the CNTs,[46] which leads to the opportunity for enhanced C-rate performance, particularly in conjunction with the poor transport inherent to cathode materials. Lastly, CNTs also possess remarkable mechanical strength and excellent thermal conductivity,[47, 48] which prevent cracking during battery operation and promote effective heat dissipation within a composite, thereby potentially enhancing the safety of these materials over composite electrodes incorporating inferior carbon additives.

Another intriguing application of CNTs in LIBs is the concept of using a free-standing CNT "paper" as an electrode, which can serve in the capacity of both an active material and a current collector. Figure 1.3a provides for a representative image of a free-standing SWNT paper electrode, generated through vacuum filtration along with a detailed SEM image and a photograph highlighting

a twisted electrode depicted in Figure 1.3b and c, respectively.[14] The most important advantage of using a free-standing electrode is that the usable capacity can be increased by removing the inactive copper foil. In addition, CNTs are better active materials as compared with the conventional graphite electrodes. The lithium ion capacity in CNTs results from the effective diffusion of lithium ions into stable sites located on the nanotube surface and/or inside individual nanotubes through either endcap or sidewall openings. In addition, lithium ion intercalation can occur between the MWNT layers (entering through lattice defects or open nanotube ends) or the interstitial sites of close-packed SWNT bundles. In addition to Li_xC capacity, there are calculations which propose a curvature-induced lithium condensation inside the core of the nanotubes. Overall, the theoretical calculations suggest that reversible capacities exceeding a LiC_2 stoichiometry (>1116 mAh g^{-1}) are attainable for SWNTs, denoting a dramatic improvement over use of conventional graphite (~300 mAh g^{-1}).[49-51]

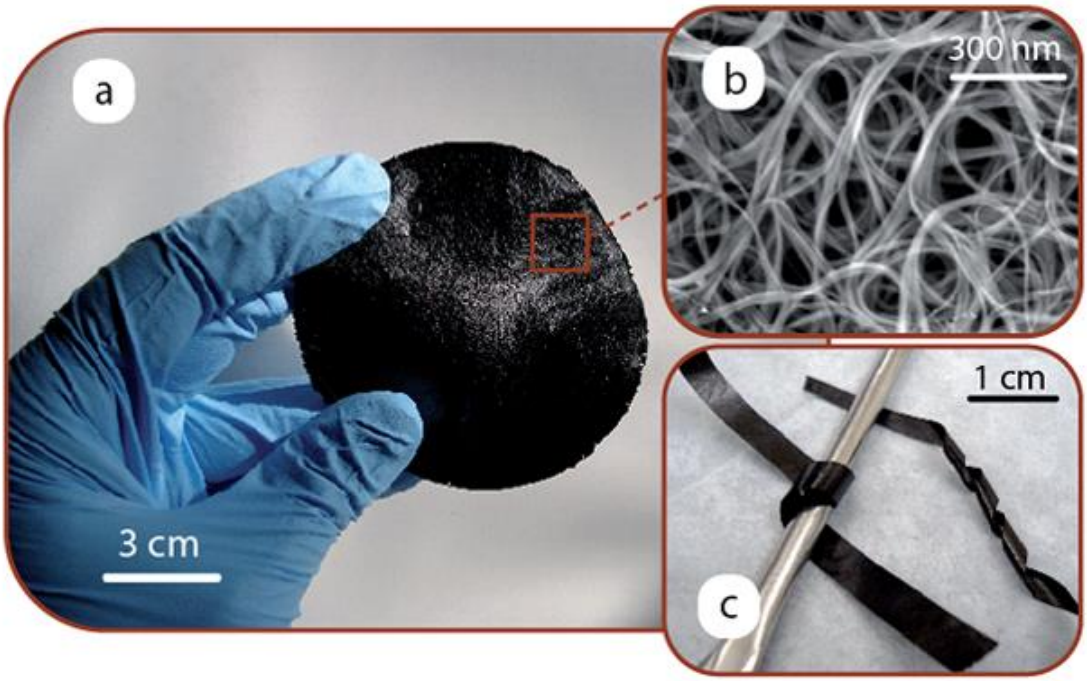

Figure 1.3 (a) Photograph of a free-standing SWNT paper prepared using vacuum filtration. (b) SEM image of high purity SWNTs. (c) Image of SWNT paper strips which are bent around a curved surface and twisted without any unintended or irreversible deformation to illustrate their flexible mechanical properties. (Adapted in part from Ref. 14)

1.3. Zero-dimensional (0D) quantum dots (QDs)

Chalcogenide quantum dots (QDs) are nanometer-scale colloidal semiconductor nanocrystals, typically composed of groups II to VI or III to V elements, and are defined as particles with physical dimensions smaller than the exciton Bohr radius.[52] These were initially discovered at the beginning of the 1980s by Alexei Ekimov in a glass matrix and by Louis E. Brus in colloidal solutions.[53] QDs have been intensively studied, because of their quantum confinement effects and size-dependent optical properties with band-edge absorption and emission wavelengths that are tunable across the visible range (400-700 nm). Usually, the larger the size of the quantum dot, the smaller the band gap (Figure 1.4A). This interesting trend can be deduced both from ultraviolet-visible (UV-Vis) spectroscopy and photoluminescence (PL) spectroscopy (Figure 1.4B and C) data.

As the reaction time is prolonged, the size of QD grows larger, indicative of a narrower band gap. This can cause a red shift in the peak positions in both the UV-Vis and PL spectra.[54] An ensemble of quantum dots of different sizes can in principle be designed to match and overlap the overall absorption spectrum with the entire solar spectrum. Moreover, an intriguing recent discovery suggests the possibility of multiple exciton generation (MEG) in quantum dots, which are thought to be able to effectively convert a photon into more than one electron-hole pair, thereby allowing for more efficient use of solar energy and a potential for quantum efficiencies greater than 100%.[55-57] Such size and shape-dependent optical and electronic properties of CdSe QDs make it meaningful for chemists to exploit their role in the rational development of nanoscale assemblies for solar cells.[58, 59]

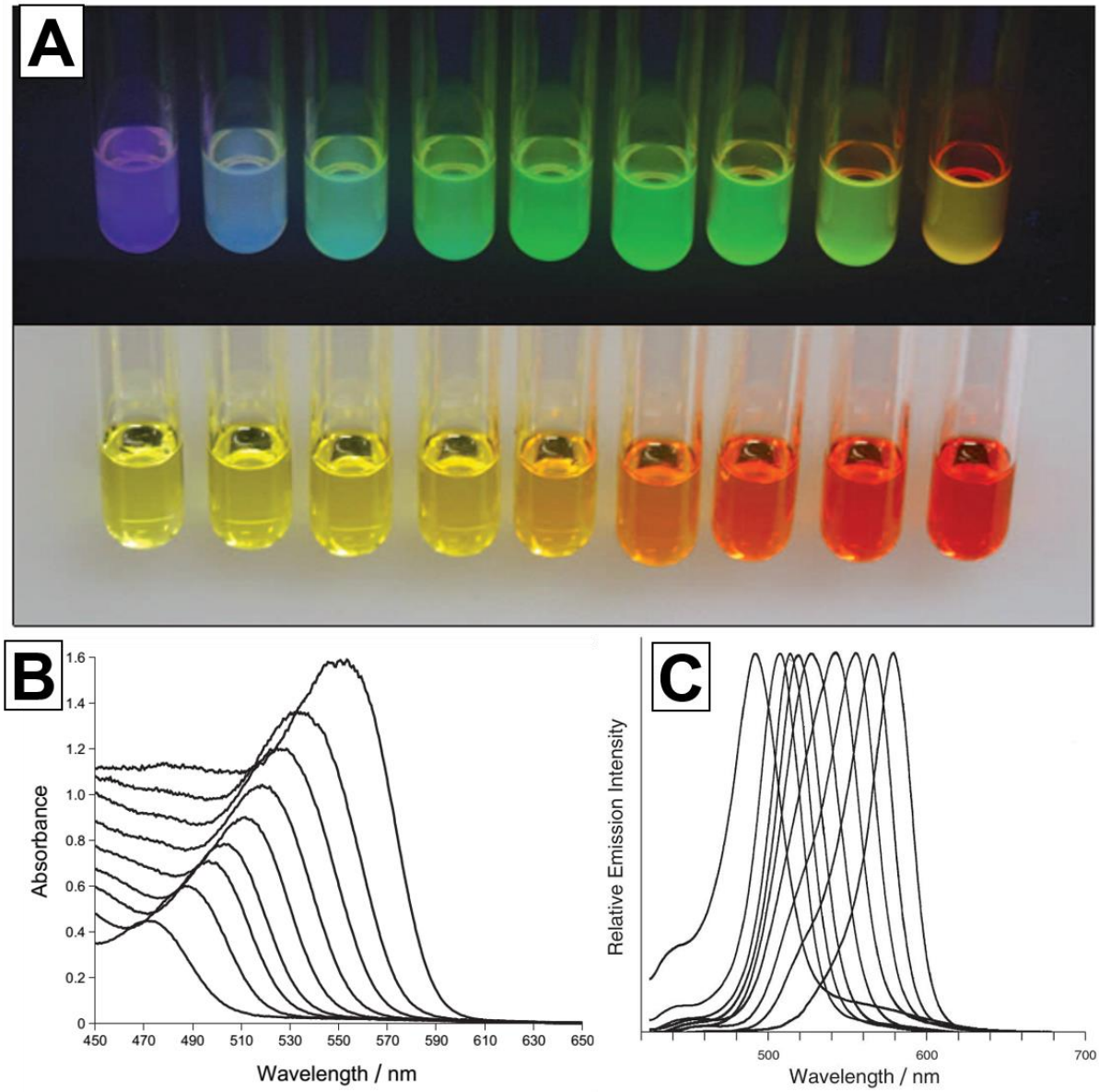

Figure 1.4 (A) Colloidal suspensions of CdSe quantum dots of increasing size from left (approximately 1.8 nm in diameter) to right (approximately 4.0 nm in diameter). Bottom: Samples viewed in ambient light vary in color from green–yellow to orange–red. Top: The same samples viewed under long-wave ultraviolet illumination vary in color from blue to yellow. (B) Visible absorption spectra of CdSe QD samples, from left to right, corresponding to reaction times of 20 s to 2 min. (C) Fluorescence emission spectra of identical samples using 400-nm excitation. (Adapted in part from Ref. 54)

1.3.1. Synthesis of QDs

Usually, the QD formation in solution entails both nucleation and growth processes. That is, the burst of nucleation is followed by a supersaturation of monomers. The growth of nuclei is then accompanied by consumption of the additional monomers present in the system. QDs with different shapes and size distributions can be synthesized by tuning parameters such as but not limited to the monomer concentration, the identity of capping agents, as well as the reaction times. The QD growth is governed by both thermodynamics and kinetics. Specifically, nanocrystals with low aspect ratios can be obtained in the slow growth limit under thermodynamic control, while the nanocrystals with highly anisotropic shapes require a kinetic growth regime.[60, 61]

The Alivisatos group proposed that at a relatively low monomer concentration, nearly round nanospheres are formed with a relatively large size distribution. Under that regime, a size "defocusing" or "Ostwald ripening" is observed due to the depletion of smaller particles and the concomitant continuous growth of larger particles. When the monomer concentration increases, nanocrystals with low aspect ratio are still observed with a narrower size distribution. This size "focusing" process is due to the faster growth rate of smaller particles as opposed to larger particles, which finally results in a monodisperse nanocrystal ensemble. Usually, the growth rate of a facet depends exponentially upon the surface energy, thereby resulting in the faster growth of higher-energy facets as opposed to their lower-energy counterparts. Hence, when the monomer concentration continues to increase, kinetics will begin to control nanocrystal growth, thereby resulting in the production of nanocrystals with highly anisotropic shapes.[62]

Generally, two methods have been commonly adopted to synthesize QDs, *i.e.* the solvothermal method using organometallic reagents and the hydrothermal method using aqueous

precursors. The synthesis of quantum dots via the solvothermal method is based upon a three-component system, including precursors, organic surfactants, and solvents. A solvothermal reaction could provide for elevated temperatures and pressures, thereby generating unique synthesis conditions for nanocrystal growth. The solvothermal method usually starts from the mixing of two individual precursors at a lower temperature, and then involves temperature increases to the desired growth temperature within a sealed argon-filled three-neck flask for QD production. Such an approach has been well-developed by Peng's group,[63] wherein metal oxides (e.g. cadmium oxide, CdO) are employed as cadmium precursors in order to substitute for the more conventional toxic precursor reagents (*e.g.* dimethyl cadmium, $Cd(CH_3)_2$).

In a typical experiment, aliquots of solution, containing chalcogenide precursors stabilized by organic capping agents, are rapidly injected into the cationic precursor solution containing surfactants (e.g. trioctylphosphine oxide, tri-*n*-butylphosphine, oleylamine, hexadecylamine, and oleic acid) at a temperature of between 200 – 330°C in order to induce nucleation, followed by a growth stage at a relatively low temperature. The presence of these molecular capping agents stabilizes QDs within a colloidal dispersion and allows for reproducible and precise control over QD size, and by extension, the corresponding tuning of the QD bandgap.[63, 64] The cleavage of the phosphorus-chalcogenide double bond (TOP = E, wherein E = Se, Te, S) is activated by the nucleophilic attack of either phosphonate or oleate on a (TOP=E)-Cd complex, thereby generating the initial Cd-E bond.[65] The QDs synthesized in organic solvents tend to be water-insoluble and usually need to be transferred to the aqueous phase for further applications.[66]

The second route is to directly synthesize QDs in aqueous solution, which is especially attractive for biological application, due to their compatibility with water. Thiols and thioalkyl

acids including thioglycolic acid (TGA) and 3-mercaptopropionic acid (MPA) are popular capping agents used for aqueous-synthesized quantum dots.[67, 68] The as-prepared quantum dots generated in aqueous medium usually have relatively low quantum yield and possess a large size distribution as compared with analogues generated using an organic approach. Most of these protocols require additional post-synthesis treatments, such as size-selective precipitation, selective photochemical etching, and surface modification, in order to further improve upon the size distribution and quality of QDs.

In a typical synthesis of CdTe QDs under aqueous conditions, $NaBH_4$ was used to react with tellurium in deionized (DI) water to form NaHTe as the Te-containing precursor, whereas $CdCl_2$ and the thiol ligand, N-acetyl-l-cysteine (NAC; as the surfactant), were dissolved in DI water to form the Cd-containing precursor. The pH value of the Cd precursor was adjusted to 9.5 by the stepwise addition of NaOH at 4°C. The NaHTe solution was then added into the aforementioned Cd precursor solution at 0°C with rigorous stirring, and the mixture was subsequently loaded into a Teflon-lined stainless steel autoclave. CdTe quantum dots were formed by heating the autoclave at 200°C for ~1 h.[69] Control over the pH value is more essential for dictating the progression of aqueous-based reactions as opposed to their organic-based analogues, and necessitates careful monitoring in order to achieve the desired results.

A real and practical application in the energy field requires the synthesis of QDs, possessing high quantum yields, good stability, and relatively narrow particle monodispersity, all of which have been proven to be easier to achieve using the organometallic synthetic route. Hence, in this thesis, the CdSe QDs will be prepared by following the well-established method, previously proposed by the Peng group, to be discussed in Chapter 2.[61]

1.3.2. Surface modification of QDs

The unwieldy, bulky, and often non-conjugated ligands on the surfaces of as-prepared QDs can effectively hamper charge transport and flow, which are inherently critical parameters to optimize for improving upon photovoltaic cell efficiency. Moreover, due to the insulating properties of these ligands, they often act as a potential barrier to the charge transport capability between adjacent nanoparticles and nanostructures.[70, 71] Hence, not surprisingly, a lot of research has focused on understanding the nature of surface ligand exchange reactions, wherein long alkyl chains are replaced by relatively short ligands with efficient hole and electron scavenging properties so as to mitigate for obstacles preventing effective charge transfer and transport.

Properly chosen electroactive ligand molecules can replace native insulating long-chain ligands through the so-called 'ligand exchange' processes, in order to chemically modify and coat the external surfaces of these QDs with more conductive entities.[72] In this light, to tailor QDs for desirable photovoltaic behavior, a wide variety of ligands has been studied as candidates for potential capping agents of these nanoparticles, including bidentate aliphatic and aromatic thiols,[73] primary amines,[74] carboxylic acids,[75] and halide ions.[76] The judicious choice of ligands and the chemical modification of the outer surfaces of QDs through ligand exchange reactions are crucial for a number of reasons.

First, ligands can help to passivate surface defects, which play an important role in the surface-related emission and corresponding photostability of QDs. *Second*, on a relevant device level, the electronic properties of coupled colloidal QD solids can be precisely tuned through modification of the QD surface chemistry *via* ligand exchange, and such an approach designates a complementary strategy to control the QD bandgap through predictable variation of nanocrystal size.[77] Specifically, Liu *et al.* reported that the PL intensity of CdSe quantum dots is

affected by the ligand involved with a decreasing order of TOPO > α-toluenethiol > thiophenol > *p*-hydroxythiophenol. Aromatic rings and their associated π electron clouds within the ligands apparently acted as effective quenchers of CdSe emission and scavengers of photogenerated holes.[78] Moreover, in the corresponding photovoltaic devices tested, thiophenol-capped QDs exhibited a 10-fold increase in the short circuit current density as compared with TOPO-capped CdSe. *Third*, specific short bidentate ligands, such as ethanedithiol, not only reduce the interdot separation, thereby facilitating exciton dissociation and subsequent carrier transport towards the collecting contacts,[76, 79] but also serve as a molecular ligand bridge with which to connect QDs with other charge-transporting components, such as double-walled carbon nanotubes, studied in that particular work, through either covalent or non-covalent attachment strategies.[80]

A more systematic approach to controlling PL QY through ligand chemistry would be to match the energy level band alignment of the ligands themselves with that of the QDs to which they are attached. For instance, in order to incur efficient PL quenching of QDs due to photo-induced charge transfer, the highest occupied molecular orbital (HOMO) of ligands needs to be situated above the valence band (VB) of QDs. As an example, the HOMO of 2-aminoethanethiol (AET) lies at a considerably higher energy level as compared with the VB of CdSe QDs, but is situated at a lower energy as compared with the VB of CdTe QDs, thereby resulting in PL enhancement for CdTe QDs and PL quenching for CdSe QDs, when TOPO molecules in as-prepared QDs are replaced with AET through a ligand exchange reaction.

Therefore, by deliberatively altering the identity of the ligands, one can vary the ligand length, the nature of the chemical binding groups, and the associated dipole moments, thereby leading to a shift in the positions of the QD valence band maximum and conduction band

minimum. In doing so, efficient charge transfer can be potentially tuned for, which is crucial to the development of QD-based photovoltaics.

1.3.3. Application of QDs in photovoltaic devices

In recent years, the size-dependent properties of QDs have rendered them as promising replacements for conventional organic dyes as light sensitizers in dye-sensitized solar cell (DSSCs). Semiconducting quantum dots (QDs) have been considered as candidate materials for the next generation of photovoltaic devices as a result of their unique attributes including (a) size-dependent opto-electronic properties, (b) a potential to maximize the production of hot photogenerated carriers through a multi-exciton generation effect, which would increase photoconversion efficiency, (c) a remarkable photostability, including resistance to photoinduced quenching, as well as (d) high extinction coefficients.[81]

In fact, quantum dot solar cells (QDSCs) represent a very exciting third-generation solar cell architecture. Specifically, the unusual morphology-dependent opto-electronic properties of QDs provide for an unconventional means of potentially exceeding the traditional Shockley-Queisser limit of 32% for Si-based solar cells,[82] because by contrast with dyes, multiple charge carriers can be potentially generated by QDs upon absorption of one photon.[55] Moreover, in early studies, it was shown that charge separation can be enhanced by coupling two different types of semiconductors as long as their bandgaps satisfy certain criteria.[83-85] Hence, the essence of using QDs instead of traditional dyes lies in the mechanism, wherein electrons can be injected from semiconductors, such as CdSe, directly into wider bandgap materials, such as TiO_2, thereby resulting in charge rectification.[86] Finding a means of efficiently capturing these photo-induced electrons at the interface has been a particular challenge.

1.4. Application of CNT-QD heterostructures in photoconversion

While QDs possess a great potential as components in photovoltaic cells, a number of obstacles cannot be neglected and need to be overcome for practical applications. For example, in a typical photochemical solar cell, the photoinduced charge carriers (*e.g.* electrons and holes) are susceptible to recombination loss at the boundaries of semiconducting particles before they become separated and end up being transported to electrodes, which is a crucial step in generating the photocurrent. Hence, in order to enhance the power conversion efficiency of QD-based solar cell, a decrease in the amount of recombination of charge carrier species is essential. Specifically, there has been an intense level of interest in generating QD-based nanotube architectures, incorporating either carbon nanotubes (CNTs)[87] or metal oxide nanotubes such as TiO_2[88] and ZnO[89], as a means of improving upon photo-induced charge transport at the nanoscale by both maximizing charge separation and minimizing charge recombination.

It has been reported that CNTs can act as good electron acceptors in their photoexcited state, wherein charge and energy transfer between conjugate species and CNTs may occur. A popular concept has been to utilize CNT networks as supports in order to anchor light-harvesting semiconducting particles, namely CdSe QDs in this thesis, thereby providing for a convenient means of capturing photo-generated charges and transporting them back to the electrode surface. Previous studies have focused on using and chemically attaching either CdS[90] or CdSe[91-93] QDs directly onto SWNT templates (*e.g.* Figure 1.5) in order to optimize the practical efficiency of generating photocurrent in these systems under visible light illumination. Transient absorption experiments have confirmed the quick deactivation of excited CdS species on the SWNT surface, as the transient bleaching activity recovers in about 200 ps.[94]

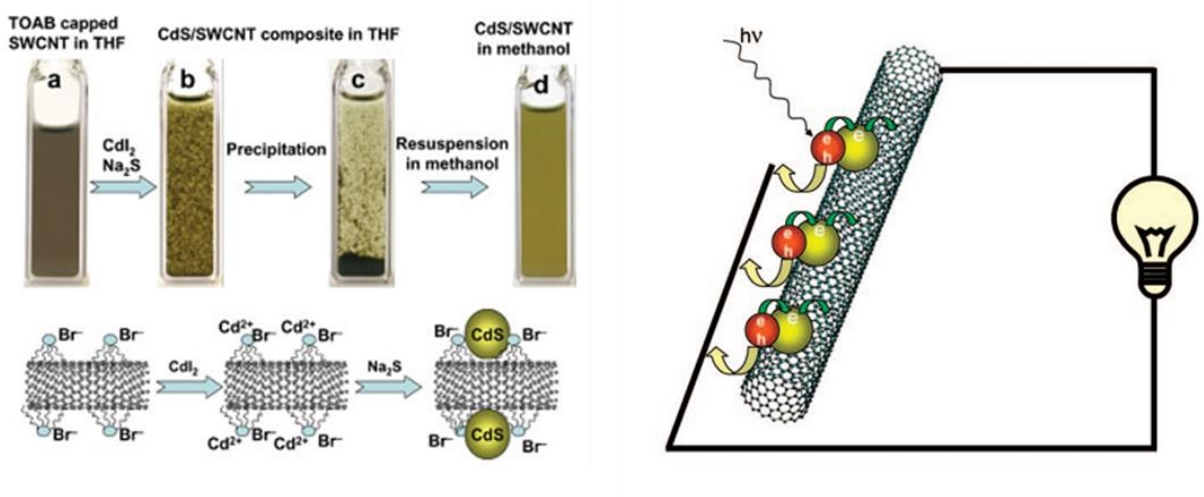

Figure 1.5 Left: Synthetic steps involved in the preparation of the SWNT–CdS composite: a) SWNT suspension in THF, following the addition of CdI_2 solution, b) dropwise addition of Na_2S, c) completion of the reaction, as the SWNT–CdS composite settles down in THF, and d) re-suspension of SWNT–CdS in methanol. (Reprinted from ref. 90). **Right:** Photocurrent generation using SWNT-CdSe composite materials (Reprinted from ref. 93).

To date, enormous efforts have been expended for the fabrication of nanoscale heterostructures, comprised of QDs deposited onto CNTs for improving solar device performance. Generally, CNT– QD heterostructures have been fabricated via either in situ growth, covalent, or non-covalent approaches. The in situ deposition of QDs onto the 1D CNTs can be realized by either chemical bath deposition or successive ionic layer adsorption and reaction (SILAR) protocols.[95] However, the in situ growth and immobilization of QDs on the CNT scaffold surface usually encounters the difficulty of precise control over the morphology and size of the as-deposited QDs. Normally, to obtain QD-CNT composites with a narrow size distribution and a uniform morphology, a covalent attachment method is often employed. Surface oxygenated moieties are required for the covalent bond formation between CNTs and QDs, and these oxygen-rich species are often generated by the treatment of CNTs with strong acids, so as to form carboxylic acid functionalities (as well as keto, aldehyde, and alcoholic groups) on the external nanotube surface. Such a chemical treatment necessarily also however increases the possibility of localized defects, thereby disrupting the π-

bonding symmetry of the sp^2-hybridized orbitals and potentially resulting in unwanted alterations in not only conductivity but also other desirable electrical and mechanical properties.

To mitigate for this issue, Olek et al. reported on a polymer wrapping technique that has been used to non-covalently attach QDs onto the surfaces of MWNTs without introducing defects;[96] this mild functionalization method represents a promising means of preserving the high conductivity of CNTs in the subsequent QDSCs. Moreover, a hybrid architecture in which polymers, CNTs, and QDs are collectively utilized and combined into one discrete functional configuration has drawn significant attention, recently. Specifically, a P3HT: PbS QD / MWNT nanohybrid-based solar cell[97] has been reported to efficiently harvest the "often-lost" but important near-IR photons from the solar spectrum. It has been proposed that this effect can be attributed to the involvement of the NIR harvesting capability of PbS QDs coupled with the enhanced separation and transport of photo-excited charge carriers along the MWNT and polymer networks towards the electrodes themselves.

Although the non-covalent strategy can reduce the possibility of breaking the desired C=C sp^2 symmetry, the resulting composites often suffer from the poor structure stability, due to the relative weak electrostatic interactions and/or π-π stacking. The lack of long-term stability, high sensitivity to changes in pH and ionic strength, and difficulty in terms of control over QD stoichiometry and loading limit the practical application of heterostructures, specifically prepared using this method.[98]

1.5. Three-dimensional (3D) metal oxides

Metal oxide nanostructures are promising electrode materials for lithium ion batteries (LIBs) and supercapacitors, because of their high specific capacity, which is typically 2-3 times higher than that of the traditional graphite electrodes.[99] In particular, transition metal oxides are of great interest because of their capability of storing lithium by the conversion mechanism, in which the active material is fully reduced by lithium to the metal form. In addition, some metal

oxides such as iron and manganese oxides are abundant in nature and therefore low-cost. The size and morphology of metal oxide nanostructures can also be easily tuned, which makes it possible to systematically investigate possible structure-electrochemical property relationships and correlations.[100] However, several unfortunate issues have limited the practical application of various metal oxides. First, the wide bandgaps of some of the most extensively studied oxides (such as MnO_2, Co_3O_4, and NiO) often lead to poor electrical conductivity, which can thereby result in legitimate safety concerns, due to the generation of a large amount of heat during the charge/discharge cycles. Second, metal oxides generally suffer from poor ion transport kinetics.[101] Lastly, some metal oxides inevitably are limited by pronounced volume expansion and contraction during cycling, thereby resulting in pulverization of the electrode film.[102]

To mitigate for such problems, extensive research efforts have been expended in downsizing oxides into nanoscale motifs, which can facilitate ions to enter the internal region of the electrode matrix by providing for sufficient ion transport. Among the various nanoscale metal oxides, the 3D nanostructures hold many inherent and critical advantages for energy storage over electrodes comprised of either 0D nanoparticles or 1D nanowires of electroactive materials: i) High surface area: the hierarchical structural design increases the relative surface area of the electrode material, which is extremely important for LIBs, owing to an improvement in the accessibility for lithium ions and the electrochemical kinetics between the metal oxide materials and electrolytes. ii) Tunable free volume of the 3D architecture accommodates for the expansion of the metal oxides upon lithium insertion. iii) Shortened lithium diffusion distance: The nanostructured nature of the electrodes implies a shortened transport length for Li-ion diffusion either through the lattice (in the case of intercalation materials) or through the regions of lithium oxide (in the case of either conversion or alloying reactions).[103]

The model metal oxide system studied in this thesis is $Li_4Ti_5O_{12}$ (LTO) with a cubic space group Fd-3m, illustrated in Figure 1.6,[104] known as the 'zero-strain' material. In LTO, all of the tetrahedral 8a sites are occupied by lithium, and the octahedral 16d sites are shared by lithium and titanium with an atomic ratio of 1: 5 within the cubic oxygen array. LTO can be denoted as $[Li_3]_{8a}[Ti_5Li]_{16d}[O_{12}]_{32e}$. During the lithiation process, three lithium atoms at the 8a sites move to the empty 16c sites, and the new lithium atoms will also take up the 16c sites, converting the initial spinel structure to a rock salt structure $Li_7Ti_5O_{12}$ ($[Li_6]_{16c}[Ti_5Li]_{16d}[O_{12}]_{32e}$). The occupation of these sites by lithium ions does not change the structure of LTO, thereby resulting in an intriguing 'zero-strain' property. Moreover, it has been proven that more than three lithium ions can be inserted per formula, as the 8a, 8b, and 48f sites can be occupied after the 16c sites are fully occupied. Thus, $Li_4Ti_5O_{12}$ can be further denoted as $Li_9Ti_5O_{12}$, corresponding to the capacity below 1.0 V.[105]

LTO has also been extensively studied as an excellent alternative anode material, due to several intrinsic advantages, including (i) its outstanding structural stability, due to its 'zero-volume' change during electrochemical cycling; (ii) its high and stable potential plateau value (i.e. 1.55 V *versus* Li/Li^+), which circumvents solid electrolyte interphase (SEI) formation and avoids the possibility for a battery short circuit issue, triggered by the formation of lithium dendrite deposition on the surface of the electrode; as well as (iii) its fast electrode kinetics, enhanced by possible 3-dimensional Li^+-ion diffusion pathways within the spinel structure.[16, 106] However, the inherently sluggish lithium ion diffusion coefficient of bulk $Li_4Ti_5O_{12}$ (i.e. 10^{-9} to 10^{-13} cm^2/s)[107, 108] coupled with its low intrinsic electronic conductivity (i.e. 10^{-13} S/cm)[109,110] greatly limit its overall rate capability. In this dissertation, we will focus on mitigating these

problems through i) generating novel hierarchical flower-shape LTO motifs and ii) attaching CNTs as conductive additives onto as-prepared LTO structures.

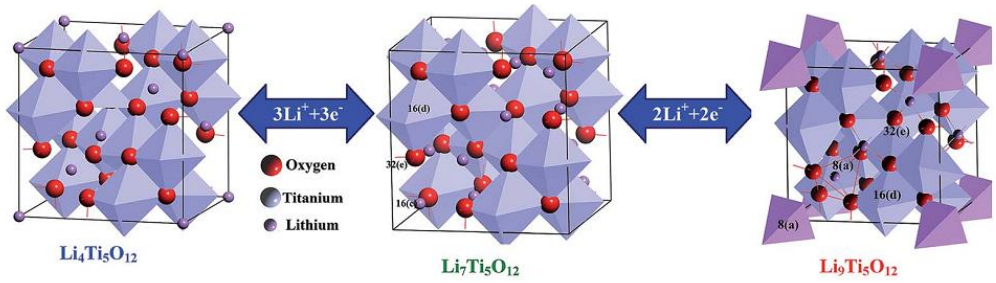

Figure 1.6 Structure of $Li_4Ti_5O_{12}$, $Li_7Ti_5O_{12}$, and $Li_9Ti_5O_{12}$ (Reprinted from Ref. 104).

1.6. Application of CNT-metal oxide heterostructures in Li-ion batteries

As discussed in Section 1.2.3, in order to enhance the electron conductivity of either the semiconducting or insulating metal oxide electrode materials, CNTs are often incorporated, due to their superior electron conductivity and structural stability. Two rational strategies have been mainly utilized to form the CNT-metal oxide hybrids. First, CNTs are often coated on the oxide surface, which is mostly realized by soaking the oxides into a dispersion of CNTs, either at room temperature or under hydrothermal/solvothermal conditions. Another hybrid structure consists of coaxial carbon core-oxide shell nanostructures. Several important advantages are associated with this hybrid configuration, including (i) good electron conduction due to the presence of a carbon core, (ii) a homogeneous electrochemical accessibility and a high ionic conductivity by avoiding binders and other additives that could give rise to additional detrimental grain boundaries, and more interestingly, (iii) a dual energy-storage mechanism.[111]

Currently, substantial research has successfully highlighted the plausibility of incorporating CNTs within the context of 0D, 1D, and 2D LTO-based anode materials using either physical mixing or *in situ* deposition methods.[112-117] For example, Fang *et al.* prepared

LTO/CNT-based composites by embedding submicron LTO particles within a network of conductive multi-walled carbon nanotubes (MWNTs); the resulting composite exhibited excellent rate and cycling performance, i.e. a value of 163 mAh g^{-1} at 2 C after 1000 cycles.[118] In addition, Ni *et al.* reported on the use of CNTs to which LTO nanoparticles had been immobilized by means of liquid phase deposition as a composite anode material for high rate LIBs; these materials delivered 112 mAh g^{-1} at a 20 C discharge rate.[119] Additional examples abound. Shen *et al.* were able to grow LTO sheathes with a measured thickness of ~25 nm on the exterior of a MWNT core, and noted that these structures exhibited significantly higher rate capabilities of 158.9, 147.8, 136.3, and 123.6 mAh g^{-1} at rates of 1, 5, 10, and 20 C, and an even better capacity retention potential, as compared with their uncoated analogues.[120] Zhang *et al.* recently developed LTO nanosheet/CNT composites, which demonstrated 145 mAh g^{-1} and 118 mAh g^{-1} at discharge rates of 11C and 23 C, respectively.[117]

1.7. Objectives of Current Work

In terms of the application of CNT-QD heterostructures in photovoltaic devices, although CNT-CdSe QD nanocomposites have been widely investigated in the recent literature with the goal of enhancing the photovoltaic efficiency, there is still a lack of systematical study in CNT-QD systems with a focus on probing and correlating the effect of varying attachment strategies (Chapter 3), QD sizes (Chapter 4), and linker molecules (Chapter 5), with the resulting charge transfer properties of as-prepared nanocomposites.

This dissertation demonstrates the first attempt to put forth a unique compilation of complementary data from experiment and theory, including results from transmission electron microscopy (TEM), near-edge X-ray absorption fine structure (NEXAFS) spectroscopy, Raman spectroscopy, electrical transport measurements, and theoretical modeling studies, in order to probe charge transfer behaviors within 2 nanoscale entities, i.e. DWNT and CdSe QDs with

different sizes, in the context of a heterostructure, joined together by various chemical ligand bridging molecules as well as various attachment modalities. Experimentally, while NEXAFS, Raman, and electrical transport measurements have been separately applied as tools to investigate charge transfer in various types of carbon nanotube-based heterostructures for years. However, to the best of our knowledge, this is the first time in which all of these unique experimental protocols have been applied within the context of DWNT-linker-QD heterostructures in order to study the nature of interfacial charge transfer.

Theoretical modeling has been utilized to i) probe the intrinsic properties of individual linker, i.e. the linker lengths and energy levels, and ii) calculate the NEXAFS spectra in order to understand the contributions of constituent groups of carbons to the total spectra and further correlate the intensity variations in the NEXAFS spectra with the actual charge transfer process. In effect, we have engaged in deliberative and systematic efforts to employ a complementary suite of all of experimental and theoretical methodologies to address the issue of charge transfer in nanotube-QD model systems with the objective of understanding the effect of varying QD size, coverage density, ligand composition, and attachment strategy, which can potentially lead to very practical improvements in terms of both photovoltaic efficiency and cost-effectiveness.

With respect to CNT-LTO heterostructures for LIB application, a novel flower-like nanostructured LTO motif was synthesized by a facile, low-cost, and large-scale hydrothermal process involving unique, re-useable, and recyclable precursors followed by a short, relatively low-temperature calcination in air. The material (i) delivered capacity of 141, 137, 123, and 60 mAh g^{-1} under high discharge rates of 10 C, 20 C, 50 C, and 100 C at cycles of 55, 60, 65, and 70, respectively; (ii) maintained a capacity retention value of ~97% from cycle 10 – 100; ~99% from cycle 20 – 100 at discharge rate of 0.2 C; and an impressive ~87% using a more rigorous

discharge rate of 20 C from cycles 101-300, respectively; and (iii) at the highest discharge rate of 100 C, the 'flower-like' LTO provided for ~3X the discharge capacity of the spherical commercial material (Chapter 6).

Furthermore, 3D "flower-like" LTO-multiwalled carbon nanotube (MWNT) composites were generated via different preparative approaches, including (i) physical sonication, (ii) an in situ direct deposition approach, as well as (iii) a covalent chemical attachment protocol. Such composites possessed a number of structural advantages that can assist in improving the measured anode performance. First, the thin constituent nanosheets within the flower-like LTO micron-scale spheres can provide for a reduced lithium ion diffusion distance. Second, the numerous roughened surfaces of the thin petal-like nanosheets, associated with a high surface area, represent potentially favorable active sites for the interaction of the electrolyte with LTO. Third, the incorporation of the MWNT network not only efficiently provides for viable electrical pathways to the LTO flower-like structure from the current collector but also increases the mechanical stability of the underlying electrode through the interweaving of the electrode components. To the best of our knowledge, we are the first to correlate the actual preparative strategy, i.e. the particular chemical treatment process used to generate these composite materials, of a novel hierarchical nanoscale motif, relevant for battery applications, with its resulting physically significant electrochemical performance. (Chapter 7).

The following sections provide a concise outline of each chapter.

1.7.1. Synthetic methods for CNT-based heterostructures as well as experimental and theoretical characterization techniques of the structural, opto-electronic, and electrochemical properties of the as-prepared composites (Chapter 2)

In this chapter, we will provide a core set of experimental methods, which have been employed to purify and functionalize CNTs, synthesize and initiate a ligand-exchange for CdSe QDs, generate LTO, as well as fabricate CNT-QD and CNT-LTO heterostructures. In order to examine the structure of our as-prepared nanostructures as a function of composition, crystallinity, size, structure, and morphology, we discuss data collected using powder X-ray diffraction (XRD), Fourier transform infrared spectroscopy (FT-IR), and electron microscopy techniques including scanning electron microscopy (SEM), and transmission electron microscopy (TEM). In addition, we describe results from the methods used for evaluating opto-electronic properties including near-edge X-ray absorption fine structure (NEXAFS) spectroscopy, Raman spectroscopy, electrical transport measurements, UV-visible (UV-visible), and photoluminescence spectroscopies.

Additionally, self-consistent density functional theory (DFT) calculations using the PBE-0 functional[121, 122] within the 6-31G*[123] basis set will be discussed, with the focus on modeling the differentially functionalized CNT-QD systems and obtaining theoretical X-ray absorption spectra (XAS), according to Fermi's Golden Rule. Furthermore, for work on LIBs, electrode preparation, and electrochemical characterization methods (*e.g.* charge/discharge profiles and electrochemical impedance spectroscopy (EIS) measurements) will be described.

1.7.2. Probing differential optical and coverage behavior in nanotube–nanocrystal heterostructures synthesized by covalent versus non-covalent approaches (Chapter 3)

Double-walled carbon nanotube (DWNT) - CdSe QD heterostructures with the individual nanoscale building blocks linked together by 4-aminothiophenol (4-ATP) have been successfully synthesized using two different and complementary routes, i.e. covalent attachment and π-π stacking. Specifically, using a number of characterization methods, we have probed the effects of these differential synthetic coupling approaches on the resulting CdSe quantum dot (QD) coverage onto the underlying nanotube template as well as the degree of charge transfer between the CdSe QDs and the DWNTs. In general, we noted that heterostructures generated by non-covalent π-π stacking interactions evinced not only higher QD coverage density but also possibly more efficient charge transfer behavior as compared with their counterparts, produced using covalent linker-mediated protocols.

1.7.3. Probing the Dependence of Electron Transfer on Size and Coverage in Carbon Nanotube–Quantum Dot Heterostructures (Chapter 4)

As a model system for understanding charge transfer in novel architectural designs for solar cells, double-walled carbon nanotube (DWNT) – CdSe quantum dot (QD) (QDs with average diameters of 2.3 nm, 3.0 nm, and 4.1 nm, respectively) heterostructures have been fabricated. The individual nanoscale building blocks were successfully attached and combined using a hole-trapping thiol linker molecule, i.e. 4-mercaptophenol (MTH), through a facile, non-covalent π-π stacking attachment strategy.

Transmission electron microscopy (TEM) confirmed the attachment of QDs onto the external surfaces of the DWNTs. We herein demonstrate a meaningful and unique combination of near-edge X-ray absorption fine structure (NEXAFS) and Raman spectroscopies, bolstered by

complementary electrical transport measurements in order to elucidate the synergistic interactions between CdSe QDs and DWNTs, which are facilitated by the bridging MTH molecule that can scavenge photo-induced holes and potentially mediate electron redistribution between the conduction bands in CdSe QDs and the C 2*p*-derived states of the DWNTs. Specifically, we correlated evidence of charge transfer as manifested by *(i)* changes in the NEXAFS intensities of the π^* resonance in the C *K*-edge and Cd M_3-edge spectra, *(ii)* a perceptible outer tube G-band down-shift in frequency in the Raman spectra, as well as *(iii)* alterations in the threshold characteristics present in transport data, which varied as a function of the nature of CdSe QD deposition onto the underlying DWNT surface. In particular, the separate effects of *(i)* varying QD sizes and *(ii)* QD coverage densities on the electron transfer were independently studied.

1.7.4. Ligand-induced Dependence of Charge Transfer in Nanotube-Quantum Dot Heterostructures (Chapter 5)

As a model system to probe ligand-dependent charge transfer in complex composite heterostructures, we fabricated double-walled carbon nanotube (DWNT) – CdSe quantum dot (QD) composites. Whereas the average diameter of the QDs probed was kept fixed at ~4.1 nm and the nanotubes analyzed were similarly oxidatively processed, by contrast, the ligands used to mediate the covalent attachment between the QDs and DWNTs were systematically varied to include *p*-phenylenediamine (PPD), 2-aminoethanethiol (AET), and 4-aminothiophenol (ATP). Herein, we have put forth a unique compilation of complementary data from experiment and theory, including results from transmission electron microscopy (TEM), near-edge X-ray absorption fine structure (NEXAFS) spectroscopy, Raman spectroscopy, electrical transport measurements, and theoretical modeling studies, in order to fundamentally assess the nature of

the charge transfer between CdSe QDs and DWNTs, as a function of the structure of various, intervening bridging ligand molecules.

Specifically, we correlated evidence of charge transfer as manifested by changes and shifts associated with NEXAFS intensities, Raman peak positions, and threshold voltages both *before* and *after* CdSe QD deposition onto the underlying DWNT surface. Importantly, for the first time ever in these types of nanoscale composite systems, we have sought to use theoretical modeling to justify and account for our experimental results. Our overall data suggest that (i) QD coverage density on the DWNTs varies, based upon the different ligand pendant groups used and that (ii) the presence of a π-conjugated carbon framework within the ligands themselves and the electron affinity of the pendant groups collectively play important roles in the resulting charge transfer from QDs to the underlying CNTs.

1.7.5. Enhanced Performance of "Flower-like" $Li_4Ti_5O_{12}$ Motifs as Anode Materials for High-rate Li-ion Batteries (Chapter 6)

Flower-like motifs of $Li_4Ti_5O_{12}$ have been synthesized by using a facile and large-scale hydrothermal process involving unique precursors followed by a short, relatively low-temperature calcination in air. Specifically, the resulting flower-like $Li_4Ti_5O_{12}$ microspheres consisting of thin nanosheet constituents can provide for an enhanced surface area and a reduced lithium ion diffusion distance. The high surface areas of the exposed roughened, thin petal-like component nanosheets are beneficial for the interaction of the electrolyte with $Li_4Ti_5O_{12}$, thereby ultimately providing for improved high-rate performances and favorable charge/discharge dynamics. Electrochemical studies of the as-prepared nanostructured $Li_4Ti_5O_{12}$ clearly reveal their promising potential as an enhanced anode material for lithium ion batteries, thereby presenting both excellent rate capabilities (delivering 148, 141, 137, 123, and 60 mAh g^{-1} under

discharge rates of 0.2 C, 10 C, 20 C, 50 C, and 100 C, at cycles of 50, 55, 60, 65, and 70, respectively) and stable cycling performance (exhibiting a capacity retention of ~97% from cycles 10 – 100, under a discharge rate of 0.2 C, and an impressive capacity retention of ~87% using a more rigorous discharge rate of 20 C from cycles 101-300).

1.7.6 Understanding the Effect of Preparative Approaches in the Formation of "Flower-like" $Li_4Ti_5O_{12}$ - Multiwalled Carbon Nanotube Composite Motifs with Performance as High-rate Anode Materials for Li-ion Battery Applications (Chapter 7)

We have correlated nanoscale attachment modality with electrochemical performance, herein. Specifically, various loading ratios of multi-walled carbon nanotubes (MWNTs) have been successfully anchored onto the surfaces of a unique "flower-like" $Li_4Ti_5O_{12}$ (LTO) micro-scale sphere motif, for the first time, using a number of different and distinctive preparative approaches, including *(i)* a sonication method, *(ii)* an *in situ* direct-deposition approach, as well as *(iii)* a covalent attachment protocol. In terms of structural characterization, the composite generated by *physical sonication* retained the intrinsic hierarchical "flower-like" morphology and exhibited a similar crystallinity as compared with that of pure LTO. By comparison, the composite prepared by an *in situ direct deposition* approach yielded not only a fragmented LTO structure, likely due to the possible interfering presence of the MWNTs themselves during the relevant hydrothermal reaction, but also a larger crystallite size, owing to the higher annealing temperature associated with its preparation. Finally, the composite created via *covalent attachment* was covered with an amorphous linker, which probably led to a decreased contact area between the LTO and the MWNTs and hence, a lower crystallinity in the resulting composite. Electrode tests suggested that the composite generated by sonication out-performed the other two analogous heterostructures, due to a smaller charge transfer resistance. In

particular, the LTO-MWNT 10 wt% composite, produced by physical sonication, exhibited a reproducibly *high rate capability* as well as a reliably solid *cycling stability*, delivering 148 mA h g^{-1} at 20 C with a 96% capacity retention from cycles 25-95. Such data denote the highest measured performance measured to date for LTO-carbon nanotube-based composite materials.

1.8. References

1. Kamat, P. V. Meeting the clean energy demand: Nanostructure architectures for solar energy conversion. *J. Phys. Chem. C* **2007**, *111*, 2834-2860.
2. Hou, Y.; Cheng, Y. W.; Hobson, T.; Liu, J. Design and Synthesis of Hierarchical MnO2 Nanospheres/Carbon Nanotubes/Conducting Polymer Ternary Composite for High Performance Electrochemical Electrodes. *Nano Lett.* **2010**, *10*, 2727-2733.
3. Mann, M. E.; Bradley, R. S.; Hughes, M. K. Global-scale temperature patterns and climate forcing over the past six centuries. *Nature* **1998**, *392*, 779-787.
4. Dresselhaus, M. S.; Thomas, I. L. Alternative energy technologies. *Nature* **2001**, *414*, 332-337.
5. Nozik, A. J.; Miller, J. Introduction to Solar Photon Conversion. *Chem. Rev.* **2010**, *110*, 6443-6445.
6. Umeyama, T.; Imahori, H. Carbon nanotube-modified electrodes for solar energy conversion. *Energy Environ Sci.* **2008**, *1*, 120-133.
7. Lunt, R. R.; Osedach, T. P.; Brown, P. R.; Rowehl, J. A.; Bulovic, V. Practical Roadmap and Limits to Nanostructured Photovoltaics. *Adv. Mater.* **2011**, *23*, 5712-5727.
8. Hanna, M. C.; Nozik, A. J. Solar conversion efficiency of photovoltaic and photoelectrolysis cells with carrier multiplication absorbers. *J. Appl. Phys.* **2006**, *100*.
9. Green, M. A.; Emery, K.; Hishikawa, Y.; Warta, W.; Dunlop, E. D. Solar cell efficiency tables (Version 38). *Progress in Photovoltaics* **2011**, *19*, 565-572.
10. Wu, F. X.; Li, X. H.; Wang, Z. X.; Guo, H. J. Petal-like $Li_4Ti_5O_{12}$-TiO_2 nanosheets as high-performance anode materials for Li-ion batteries. *Nanoscale* **2013**, *5*, 6936-6943.
11. Zhang, Z. H.; Li, G. C.; Peng, H. R.; Chen, K. Z. Hierarchical hollow microspheres assembled from N-doped carbon coated $Li_4Ti_5O_{12}$ nanosheets with enhanced lithium storage properties. *J. Mater. Chem. A* **2013**, *1*, 15429-15434.
12. Tang, Y. F.; Yang, L.; Fang, S. H.; Qiu, Z. $Li_4Ti_5O_{12}$ hollow microspheres assembled by nanosheets as an anode material for high-rate lithium ion batteries. *Electrochim. Acta* **2009**, *54*, 6244-6249.
13. Chen, P. C.; Shen, G.; Shi, Y.; Chen, H.; Zhou, C. Preparation and characterization of flexible asymmetric supercapacitors based on transition-metal-oxide nanowire/single-walled carbon nanotube hybrid thin-film electrodes. *ACS Nano* **2010**, *4*, 4403-4411.
14. Landi, B. J.; Ganter, M. J.; Cress, C. D.; DiLeo, R. A.; Raffaelle, R. P. Carbon nanotubes for lithium ion batteries. *Energy Environ. Sci.* **2009**, *2*, 638-654.

15. Kong, D.; Ren, W.; Luo, Y.; Yang, Y.; Cheng, C. Scalable synthesis of graphene-wrapped $Li_4Ti_5O_{12}$ dandelion-like microspheres for lithium-ion batteries with excellent rate capability and long-cycle life. *J. Mater. Chem. A* **2014**, *2*, 20221-20230.
16. Zhu, G. N.; Wang, Y. G.; Xia, Y. Y. Ti-based compounds as anode materials for Li-ion batteries. *Energy Environ. Sci.* **2012**, *5*, 6652-6667.
17. Tiwari, J. N.; Tiwari, R. N.; Kim, K. S. Zero-dimensional, one-dimensional, two-dimensional and three-dimensional nanostructured materials for advanced electrochemical energy devices. *Progress in Materials Science* **2012**, *57*, 724-803.
18. Iijima, S. Helical Microtubules of Graphitic Carbon. *Nature* **1991**, *354*, 56-58.
19. Moore, K. E.; Tune, D. D.; Flavel, B. S. Double-Walled Carbon Nanotube Processing. *Adv. Mater.* **2015**, *27*, 3105-3137.
20. Lin, Y.; Taylor, S.; Li, H. P.; Fernando, K. A. S.; Qu, L. W.; Wang, W.; Gu, L. R.; Zhou, B.; Sun, Y. P. Advances toward bioapplications of carbon nanotubes. *J. Mater. Chem.* **2004**, *14*, 527-541.
21. Guo, T.; Nikolaev, P.; Thess, A.; Colbert, D. T.; Smalley, R. E. Catalytic Growth of Single-Walled Nanotubes by Laser Vaporization. *Chem. Phys. Lett.* **1995**, *243*, 49-54.
22. Journet, C.; Maser, W. K.; Bernier, P.; Loiseau, A.; delaChapelle, M. L.; Lefrant, S.; Deniard, P.; Lee, R.; Fischer, J. E. Large-scale production of single-walled carbon nanotubes by the electric-arc technique. *Nature* **1997**, *388*, 756-758.
23. Kumar, M.; Ando, Y. Chemical Vapor Deposition of Carbon Nanotubes: A Review on Growth Mechanism and Mass Production. *J. Nanosci. Nanotechnol.* **2010**, *10*, 3739-3758.
24. Inami, N.; Mohamed, M. A.; Shikoh, E.; Fujiwara, A. Synthesis-condition dependence of carbon nanotube growth by alcohol catalytic chemical vapor deposition method. *Science and Technology of Adv. Mater.* **2007**, *8*, 292-295.
25. Liu, J.; Rinzler, A. G.; Dai, H. J.; Hafner, J. H.; Bradley, R. K.; Boul, P. J.; Lu, A.; Iverson, T.; Shelimov, K.; Huffman, C. B.; Rodriguez-Macias, F.; Shon, Y. S.; Lee, T. R.; Colbert, D. T.; Smalley, R. E. Fullerene pipes. *Science* **1998**, *280*, 1253-1256.
26. Hiura, H.; Ebbesen, T. W.; Tanigaki, K. Opening and Purification of Carbon Nanotubes in High Yields. *Adv. Mater.* **1995**, *7*, 275-276.
27. Fu, K. F.; Huang, W. J.; Lin, Y.; Riddle, L. A.; Carroll, D. L.; Sun, Y. P. Defunctionalization of functionalized carbon nanotubes. *Nano Lett.* **2001**, *1*, 439-441.
28. Diao, P.; Liu, Z. F.; Wu, B.; Nan, X. L.; Zhang, J.; Wei, Z. Chemically assembled single-wall carbon nanotubes and their electrochemistry. *ChemPhysChem* **2002**, *3*, 898-901.
29. Khabashesku, V. N.; Billups, W. E.; Margrave, J. L. Fluorination of single-wall carbon nanotubes and subsequent derivatization reactions. *Acc. Chem. Res.* **2002**, *35*, 1087-1095.
30. Mickelson, E. T.; Huffman, C. B.; Rinzler, A. G.; Smalley, R. E.; Hauge, R. H.; Margrave, J. L. Fluorination of single-wall carbon nanotubes. *Chem. Phys. Lett.* **1998**, *296*, 188-194.
31. Rahman, G. M. A.; Guldi, D. M.; Campidelli, S.; Prato, M. Electronically interacting single wall carbon nanotube-porphyrin nanohybrids. *J. Mater. Chem.* **2006**, *16*, 62-65.
32. Ehli, C.; Rahman, G. M. A.; Jux, N.; Balbinot, D.; Guldi, D. M.; Paolucci, F.; Marcaccio, M.; Paolucci, D.; Melle-Franco, M.; Zerbetto, F.; Campidelli, S.; Prato, M. Interactions in single wall carbon nanotubes/pyrene/porphyrin nanohybrids. *J. Am. Chem. Soc.* **2006**, *128*, 11222-11231.
33. Olek, M.; Busgen, T.; Hilgendorff, M.; Giersig, M. Quantum dot modified multiwall carbon nanotubes. *J. Phys. Chem. B* **2006**, *110*, 12901-12904.

34. Hammel, E.; Tang, X.; Trampert, M.; Schmitt, T.; Mauthner, K.; Eder, A.; Potschke, P. Carbon nanofibers for composite applications. *Carbon* **2004**, *42*, 1153-1158.
35. Wang, J.; Deo, R. P.; Poulin, P.; Mangey, M. Carbon nanotube fiber microelectrodes. *J. Am. Chem. Soc.* **2003**, *125*, 14706-14707.
36. Rajesh, B.; Thampi, K. R.; Bonard, J. M.; Mathieu, H. J.; Xanthopoulos, N.; Viswanathan, B. Conducting polymeric nanotubules as high performance methanol oxidation catalyst support. *Chem. Commun.***2003**, 2022-2023.
37. Wang, F.; Dukovic, G.; Brus, L. E.; Heinz, T. F. The optical resonances in carbon nanotubes arise from excitons. *Science* **2005**, *308*, 838-841.
38. Berger, C.; Yi, Y.; Wang, Z. L.; de Heer, W. A. Multiwalled carbon nanotubes are ballistic conductors at room temperature. *Appl. Phys. A* **2002**, *A74*, 363-365.
39. Wind, S. J.; Appenzeller, J.; Avouris, P. Lateral scaling in carbon-nanotube field-effect transistors. *Phys. Rev. Lett.* **2003**, *91*, 058301/058301-058301/058304.
40. Javey, A.; Jing, G.; Qian, W.; Lundstrom, M.; Dai, H. Ballistic carbon nanotube field-effect transistors. *Nature* **2003**, *424*, 654-657.
41. Brennan, L. J.; Byrne, M. T.; Bari, M.; Gun'ko, Y. K. Carbon Nanomaterials for Dye-Sensitized Solar Cell Applications: A Bright Future. *Adv. Energy. Mater.* **2011**, *1*, 472-485.
42. Campidelli, S.; Klumpp, C.; Bianco, A.; Guldi, D. M.; Prato, M. Functionalization of CNT: Synthesis and applications in photovoltaics and biology. *J. Phys. Org. Chem.* **2006**, *19*, 531-539.
43. Tune, D. D.; Flavel, B. S.; Krupke, R.; Shapter, J. G. Carbon Nanotube-Silicon Solar Cells. *Adv. Energy. Mater.* **2012**, *2*, 1043-1055.
44. Zhang, W. D.; Xu, B.; Jiang, L. C. Functional hybrid materials based on carbon nanotubes and metal oxides. *J. Mater. Chem.* **2010**, *20*, 6383-6391.
45. Zhang, Z. H.; Peng, J. C.; Zhang, H. Low-temperature resistance of individual single-walled carbon nanotubes: A theoretical estimation. *Appl. Phys. Lett.* **2001**, *79*, 3515-3517.
46. Dai, H. J. Carbon nanotubes: opportunities and challenges. *Surf. Sci.* **2002**, *500*, 218-241.
47. Berber, S.; Kwon, Y. K.; Tomanek, D. Unusually high thermal conductivity of carbon nanotubes. *Phys. Rev. Lett.* **2000**, *84*, 4613-4616.
48. Zhang, X. F.; Sreekumar, T. V.; Liu, T.; Kumar, S. Properties and structure of nitric acid oxidized single wall carbon nanotube films. *J. Phys. Chem. B* **2004**, *108*, 16435-16440.
49. Zhao, M. W.; Xia, Y. Y.; Liu, X. D.; Tan, Z. Y.; Huang, B. D.; Li, F.; Ji, Y. J.; Song, C. Curvature-induced condensation of lithium confined inside single-walled carbon nanotubes: First-principles calculations. *Phys. Lett. A* **2005**, *340*, 434-439.
50. Zhao, M. W.; Xia, Y. Y.; Mei, L. M. Diffusion and condensation of lithium atoms in single-walled carbon nanotubes. *Phys. Rev. B* **2005**, *71*.
51. Zhao, J.; Buldum, A.; Han, J.; Lu, J. P. First-principles study of Li-intercalated carbon nanotube ropes. *Phys. Rev. Lett.* **2000**, *85*, 1706-1709.
52. Valizadeh, A.; Mikaeili, H.; Samiei, M.; Farkhani, S. M.; Zarghami, N.; Kouhi, M.; Akbarzadeh, A.; Davaran, S. Quantum dots: synthesis, bioapplications, and toxicity. *Nanoscale Research Letters* **2012**, *7*.
53. Rossetti, R.; Nakahara, S.; Brus, L. E. Quantum Size Effects in the Redox Potentials, Resonance Raman-Spectra, and Electronic-Spectra of Cds Crystallites in Aqueous-Solution. *J. Chem. Phys.* **1983**, *79*, 1086-1088.
54. Boatman, E. M.; Lisensky, G. C.; Nordell, K. J. A safer, easier, faster synthesis for CdSe quantum dot nanocrystals. *J. Chem. Educ.* **2005**, *82*, 1697-1699.

55. Schaller, R. D.; Klimov, V. I. High efficiency carrier multiplication in PbSe nanocrystals: Implications for solar energy conversion. *Phys. Rev. Lett.* **2004**, *92*.
56. Ellingson, R. J.; Beard, M. C.; Johnson, J. C.; Yu, P. R.; Micic, O. I.; Nozik, A. J.; Shabaev, A.; Efros, A. L. Highly efficient multiple exciton generation in colloidal PbSe and PbS quantum dots. *Nano Lett.* **2005**, *5*, 865-871.
57. Beard, M. C.; Knutsen, K. P.; Yu, P. R.; Luther, J. M.; Song, Q.; Metzger, W. K.; Ellingson, R. J.; Nozik, A. J. Multiple exciton generation in colloidal silicon nanocrystals. *Nano Lett.* **2007**, *7*, 2506-2512.
58. Weller, H. Quantized Semiconductor Particles - a Novel State of Matter for Materials Science. *Adv. Mater.* **1993**, *5*, 88-95.
59. Alivisatos, A. P. Perspectives on the physical chemistry of semiconductor nanocrystals. *J. Phys. Chem.* **1996**, *100*, 13226-13239.
60. Hu, M. Z.; Zhu, T. Semiconductor Nanocrystal Quantum Dot Synthesis Approaches Towards Large-Scale Industrial Production for Energy Applications. *Nanoscale Research Letters* **2015**, *10*.
61. Peng, Z. A.; Peng, X. G. Nearly monodisperse and shape-controlled CdSe nanocrystals via alternative routes: Nucleation and growth. *J. Am. Chem. Soc.* **2002**, *124*, 3343-3353.
62. Yin, Y.; Alivisatos, A. P. Colloidal nanocrystal synthesis and the organic-inorganic interface. *Nature* **2005**, *437*, 664-670.
63. Peng, Z. A.; Peng, X. G. Formation of high-quality CdTe, CdSe, and CdS nanocrystals using CdO as precursor. *J. Am. Chem. Soc.* **2001**, *123*, 183-184.
64. Yu, W. W.; Peng, X. Formation of high-quality CdS and other II-VI semiconductor nanocrystals in noncoordinating solvents: tunable reactivity of monomers. *Angew. Chem. Int. Ed.* **2002**, *41*, 2368-2371.
65. Owen, J. S.; Chan, E. M.; Liu, H. T.; Alivisatos, A. P. Precursor Conversion Kinetics and the Nucleation of Cadmium Selenide Nanocrystals. *J. Am. Chem. Soc.* **2010**, *132*, 18206-18213.
66. Reiss, P.; Bleuse, J.; Pron, A. Highly luminescent CdSe/ZnSe core/shell nanocrystals of low size dispersion. *Nano Lett.* **2002**, *2*, 781-784.
67. Kalasad, M. N.; Rabinal, A. K.; Mulimani, B. G. Ambient Synthesis and Characterization of High-Quality CdSe Quantum Dots by an Aqueous Route. *Langmuir* **2009**, *25*, 12729-12735.
68. Zhou, L.; Gao, C.; Hu, X. Z.; Xu, W. J. One-Pot Large-Scale Synthesis of Robust Ultrafine Silica-Hybridized CdTe Quantum Dots. *ACS Appl. Mater. Interfaces* **2010**, *2*, 1211-1219.
69. Zhang, H.; Wang, L. P.; Xiong, H. M.; Hu, L. H.; Yang, B.; Li, W. Hydrothermal synthesis for high-quality CdTe nanocrystals. *Adv. Mater.* **2003**, *15*, 1712.
70. Virgili, T.; López, I. S.; Vercelli, B.; Angella, G.; Zotti, G.; Cabanillas-Gonzalez, J.; Granados, D.; Luer, L.; Wannemacher, R.; Tassone, F. Spectroscopic Signature of Trap States in Assembled CdSe Nanocrystal Hybrid Films. *J. Phys. Chem. C* **2012**, *116*, 16259-16263.
71. Querner, C.; Reiss, P.; Sadki, S.; Zagorska, M.; Pron, A. Size and ligand effects on the electrochemical and spectroelectrochemical responses of CdSe nanocrystals. *Phys. Chem. Chem. Phys.* **2005**, *7*, 3204-3209.
72. Newton, J. C.; Ramasamy, K.; Mandal, M.; Joshi, G. K.; Kumbhar, A.; Sardar, R. Low-Temperature Synthesis of Magic-Sized CdSe Nanoclusters: Influence of Ligands on Nanocluster Growth and Photophysical Properties. *J. Phys. Chem. C* **2012**, *116*, 4380-4389.

73. Klem, E. J. D.; MacNeil, D. D.; Cyr, P. W.; Levina, L.; Sargent, E. H. Efficient solution-processed infrared photovoltaic cells: Planarized all-inorganic bulk heterojunction devices via inter-quantum-dot bridging during growth from solution. *Appl. Phys. Lett.* **2007**, *90*, 183113.
74. Talapin, D. V.; Murray, C. B. PbSe nanocrystal solids for n- and p-channel thin film field-effect transistors. *Science* **2005**, *310*, 86-89.
75. Pattantyus-Abraham, A. G.; Kramer, I. J.; Barkhouse, A. R.; Wang, X.; Konstantatos, G.; Debnath, R.; Levina, L.; Raabe, I.; Nazeeruddin, M. K.; Gratzel, M.; Sargent, E. H. Depleted-heterojunction colloidal quantum dot solar cells. *ACS Nano* **2010**, *4*, 3374-3380.
76. Tang, J.; Kemp, K. W.; Hoogland, S.; Jeong, K. S.; Liu, H.; Levina, L.; Furukawa, M.; Wang, X.; Debnath, R.; Cha, D.; Chou, K. W.; Fischer, A.; Amassian, A.; Asbury, J. B.; Sargent, E. H. Colloidal-quantum-dot photovoltaics using atomic-ligand passivation. *Nat. Mater.* **2011**, *10*, 765-771.
77. Brown, P. R.; Kim, D.; Lunt, R. R.; Zhao, N.; Bawendi, M. G.; Grossman, J. C.; Bulovic, V. Energy level modification in lead sulfide quantum dot thin films through ligand exchange. *ACS Nano* **2014**, *8*, 5863-5872.
78. Liu, I. S.; Lo, H. H.; Chien, C. T.; Lin, Y. Y.; Chen, C. W.; Chen, Y. F.; Su, W. F.; Liou, S. C. Enhancing photoluminescence quenching and photoelectric properties of CdSe quantum dots with hole accepting ligands. *J. Mater. Chem.* **2008**, *18*, 675-682.
79. Mora-Sero, I.; Bertoluzzi, L.; Gonzalez-Pedro, V.; Gimenez, S.; Fabregat-Santiago, F.; Kemp, K. W.; Sargent, E. H.; Bisquert, J. Selective contacts drive charge extraction in quantum dot solids via asymmetry in carrier transfer kinetics *Nat. Commun.* **2013**, *4*, 3272.
80. Peng, X. H.; Wong, S. S. Controlling Nanocrystal Density and Location on Carbon Nanotube Templates. *Chem. Mater.* **2009**, *21*, 682-694.
81. Carey, G. H.; Abdelhady, A. L.; Ning, Z.; Thon, S. M.; Bakr, O. M.; Sargent, E. H. Colloidal Quantum Dot Solar Cells. *Chem. Rev.* **2015**, *115*, 12732–12763.
82. Shockley, W.; Queisser, H. J. Detailed Balance Limit of Efficiency of p-n junction Solar Cells. *J. Appl. Phys.* **1961**, *32*, 510-&.
83. Gerischer, H.; Lubke, M. A Particle-Size Effect in the Sensitization of Tio2 Electrodes by a Cds Deposit. *J. Electroanal. Chem.* **1986**, *204*, 225-227.
84. Vogel, R.; Pohl, K.; Weller, H. Sensitization of Highly Porous, Polycrystalline Tio2 Electrodes by Quantum Sized Cds. *Chem. Phys. Lett.* **1990**, *174*, 241-246.
85. Kohtani, S.; Kudo, A.; Sakata, T. Spectral Sensitization of a Tio2 Semiconductor Electrode by Cds Microcrystals and Its Photoelectrochemical Properties. *Chem. Phys. Lett.* **1993**, *206*, 166-170.
86. Liu, D.; Kamat, P. V. Electrochemical Rectification in Cdse+Tio2 Coupled Semiconductor-Films. *J. Electroanal. Chem.* **1993**, *347*, 451-456.
87. Azoz, S.; Jiang, J.; Keskar, G.; McEnally, C.; Alkas, A.; Ren, F.; Marinkovic, N.; Haller, G. L.; Ismail-Beigi, S.; Pfefferle, L. D. Mechanism for strong binding of CdSe quantum dots to multiwall carbon nanotubes for solar energy harvesting. *Nanoscale* **2013**, *5*, 6893-6900.
88. Kao, L. C.; Liou, S. Y. H.; Dong, C. L.; Yeh, P. H.; Chen, C. L. Tandem Structure of QD Cosensitized TiO2 Nanorod Arrays for Solar Light Driven Hydrogen Generation. *ACS. Sustain. Chem. Eng.* **2016**, *4*, 210-218.
89. Wang, L. D.; Zhao, D. X.; Su, Z. S.; Shen, D. Z. Hybrid polymer/ZnO solar cells sensitized by PbS quantum dots. *Nanoscale Research Letters* **2012**, *7*, 1-6.

90. Robel, I.; Bunker, B. A.; Kamat, P. V. Single-walled carbon nanotube-CdS nanocomposites as light-harvesting assemblies: Photoinduced charge-transfer interactions. *Adv. Mater.* **2005**, *17*, 2458.
91. Banerjee, S.; Wong, S. S. Formation of CdSe nanocrystals onto oxidized, ozonized single-walled carbon nanotube surfaces. *Chem. Commun.***2004**, 1866-1867.
92. Haremza, J. M.; Hahn, M. A.; Krauss, T. D.; Chen, S.; Calcines, J. Attachment of Single CdSe Nanocrystals to Individual Single-Walled Carbon Nanotubes. *Nano Lett.* **2002**, *2*, 1253-1258.
93. Kamat, P. V. Quantum Dot Solar Cells. Semiconductor Nanocrystals as Light Harvesters. *J. Phys. Chem. C* **2008**, *112*, 18737-18753.
94. Vietmeyer, F.; Seger, B.; Kamat, P. V. Anchoring ZnO Particles on Functionalized Single Wall Carbon Nanotubes. Excited State Interactions and Charge Collection. *Adv. Mater.* **2007**, *19*, 2935-2940.
95. Tian, J. J.; Shen, T.; Liu, X. G.; Fei, C. B.; Lv, L. L.; Cao, G. Z. Enhanced Performance of PbS-quantum-dot-sensitized Solar Cells via Optimizing Precursor Solution and Electrolytes. *Sci. Rep.* **2016**, *6*.
96. Olek, M.; Büsgen, T.; Hilgendorff, M.; Giersig, M. Quantum Dot Modified Multiwall Carbon Nanotubes. *J. Phys. Chem. B* **2006**, *110*, 12901-12904.
97. Wang, D.; Baral, J. K.; Zhao, H.; Gonfa, B. A.; Truong, V.-V.; El Khakani, M. A.; Izquierdo, R.; Ma, D. Controlled Fabrication of PbS Quantum-Dot/Carbon-Nanotube Nanoarchitecture and its Significant Contribution to Near-Infrared Photon-to-Current Conversion. *Adv. Funct. Mater.* **2011**, *21*, 4010-4018.
98. Schulz-Drost, C.; Sgobba, V.; Gerhards, C.; Leubner, S.; Calderon, R. M. K.; Ruland, A.; Guldi, D. M. Innovative Inorganic-Organic Nanohybrid Materials: Coupling Quantum Dots to Carbon Nanotubes. *Angew. Chem. Int. Ed.* **2010**, *49*, 6425-6429.
99. Ji, L. W.; Lin, Z.; Alcoutlabi, M.; Zhang, X. W. Recent developments in nanostructured anode materials for rechargeable lithium-ion batteries. *Energy Environ. Sci.* **2011**, *4*, 2682-2699.
100. Wang, B.; Chen, J. S.; Wu, H. B.; Wang, Z.; Lou, X. W. Quasiemulsion-templated formation of alpha-Fe2O3 hollow spheres with enhanced lithium storage properties. *J. Am. Chem. Soc.* **2011**, *133*, 17146-17148.
101. Liu, H.; Du, X. W.; Xing, X. R.; Wang, G. X.; Qiao, S. Z. Highly ordered mesoporous Cr2O3 materials with enhanced performance for gas sensors and lithium ion batteries. *Chem. Commun.***2012**, *48*, 865-867.
102. Li, H.; Wang, Z. X.; Chen, L. Q.; Huang, X. J. Research on Adv. Mater. for Li-ion Batteries. *Adv. Mater.* **2009**, *21*, 4593-4607.
103. Ellis, B. L.; Knauth, P.; Djenizian, T. Three-Dimensional Self-Supported Metal Oxides for Advanced Energy Storage. *Adv. Mater.* **2014**, *26*, 3368-3397.
104. Yi, T.-F.; Liu, H.; Zhu, Y.-R.; Jiang, L.-J.; Xie, Y.; Zhu, R.-S. Improving the high rate performance of Li4Ti5O12 through divalent zinc substitution. *J. Power Sources* **2012**, *215*, 258-265.
105. Chen, Z.; Belharouak, I.; Sun, Y. K.; Amine, K. Titanium-Based Anode Materials for Safe Lithium-Ion Batteries. *Adv. Funct. Mater.* **2013**, *23*, 959-969.
106. Choi, J.-H.; Ryu, W.-H.; Park, K.; Jo, J.-D.; Jo, S.-M.; Lim, D.-S.; Kim, I.-D. Multi-layer electrode with nano-Li4Ti5O12 aggregates sandwiched between carbon nanotube and graphene networks for high power Li-ion batteries. *Sci. Rep.* **2014**, *4*.

107. K. M. Colbow, J. R. D., R. R. Haering. Structure and electrochemistry of the spinel oxides LiTi2O4 and Li4/3Ti5/3O4. *J. Power Sources* **1989**, *26*, 397-402.
108. Norio Takami, K. H., Hiroki Inagaki. Lithium Diffusion in Li4/3Ti5/3O4 Particles during Insertion and Extraction. *J. Electrochem. Soc.* **2011**, *158*, A725-A730.
109. T. Brousse, P. F., R. Marchand, D. M. Schleich, O. Bohnke, K. West. All oxide solid-state lithium-ion cells. *J. Power Sources* **1997**, *1997*, 412-415.
110. C.Y. Ouyang, Z. Y. Z., M.S. Lei. Ab initio studies of structural and electronic properties of Li4Ti5O12 spinel. *Electrochem. Commun.* **2007**, *2007*, 1107-1112.
111. Jiang, J.; Li, Y.; Liu, J.; Huang, X.; Yuan, C.; Lou, X. W. Recent advances in metal oxide-based electrode architecture design for electrochemical energy storage. *Adv. Mater.* **2012**, *24*, 5166-5180.
112. Huang, J. J.; Jiang, Z. Y. The preparation and characterization of $Li_4Ti_5O_{12}$/carbon nano-tubes for lithium ion battery. *Electrochim. Acta* **2008**, *53*, 7756-7759.
113. Jhan, Y. R.; Duh, J. G. Synthesis of entanglement structure in nanosized $Li_4Ti_5O_{12}$/multi-walled carbon nanotubes composite anode material for Li-ion batteries by ball-milling-assisted solid-state reaction. *J. Power Sources* **2012**, *198*, 294-297.
114. Jia, X. L.; Kan, Y. F.; Zhu, X.; Ning, G. Q.; Lu, Y. F.; Wei, F. Building flexible $Li_4Ti_5O_{12}$/CNT lithium-ion battery anodes with superior rate performance and ultralong cycling stability. *Nano Energy* **2014**, *10*, 344-352.
115. Kim, H. K.; Roh, K. C.; Kang, K.; Kim, K. B. Synthesis of nano-$Li_4Ti_5O_{12}$ decorated on non-oxidized carbon nanotubes with enhanced rate capability for lithium-ion batteries. *RSC Adv.* **2013**, *3*, 14267-14272.
116. Shu, J.; Hou, L.; Ma, R.; Shui, M.; Shao, L. Y.; Wang, D. J.; Ren, Y. L.; Zheng, W. D. In situ fabrication of $Li_4Ti_5O_{12}$@CNT composites and their superior lithium storage properties. *RSC Adv.* **2012**, *2*, 10306-10309.
117. Zhang, P.; Chen, M.; Shen, X.; Wu, Q.; Zhang, X.; Huan, L.; Diao, G. Preparation of $Li_4Ti_5O_{12}$ nanosheets/carbon nanotubes composites and application of anode materials for lithium-ion batteries. *Electrochim. Acta* **2016**, *204*, 92-99.
118. Fang, W.; Zuo, P. J.; Ma, Y. L.; Cheng, X. Q.; Liao, L. X.; Yin, G. P. Facile preparation of $Li_4Ti_5O_{12}$/AB/MWCNTs composite with high-rate performance for lithium ion battery. *Electrochim. Acta* **2013**, *94*, 294-299.
119. Ni, H. F.; Fan, L. Z. Nano-$Li_4Ti_5O_{12}$ anchored on carbon nanotubes by liquid phase deposition as anode material for high rate lithium-ion batteries. *J. Power Sources* **2012**, *214*, 195-199.
120. Shen, L. F.; Yuan, C. Z.; Luo, H. J.; Zhang, X. G.; Xu, K.; Zhang, F. In situ growth of $Li_4Ti_5O_{12}$ on multi-walled carbon nanotubes: novel coaxial nanocables for high rate lithium ion batteries. *J. Mater. Chem.* **2011**, *21*, 761-767.
121. Ernzerhof, M.; Scuseria, G. E. Assessment of the Perdew-Burke-Ernzerhof exchange-correlation functional. *J. Chem. Phys.* **1999**, *110*, 5029-5036.
122. Adamo, C.; Barone, V. Toward reliable density functional methods without adjustable parameters: The PBE0 model. *J. Chem. Phys.* **1999**, *110*, 6158-6170.
123. Rassolov, V. A.; Pople, J. A.; Ratner, M. A.; Windus, T. L. 6-31G* basis set for atoms K through Zn. *J. Chem. Phys.* **1998**, *109*, 1223-1229.

Chapter 2. Synthetic methods for CNT-based heterostructures as well as experimental and theoretical characterization techniques associated with the structural, opto-electronic, and electrochemical properties of as-prepared composites

2.1. Synthesis methods used in this thesis

2.1.1. Purification and surface functionalization of CNTs

DWNTs. Specifically, 50 mg of pristine DWNTs (Helix Material Solutions) (Figure 2.1A) were dispersed in 8 M HNO_3 by sonication and then heated to 95°C for 20 h so as to remove metal catalysts and carbonaceous impurities, including SWNTs and amorphous carbon. The resulting purified and oxidized DWNTs (Figure 2.1B) were filtered through a 200 nm polycarbonate membrane (Millipore), thoroughly washed with excess water, and dried at 80°C for 18 h.

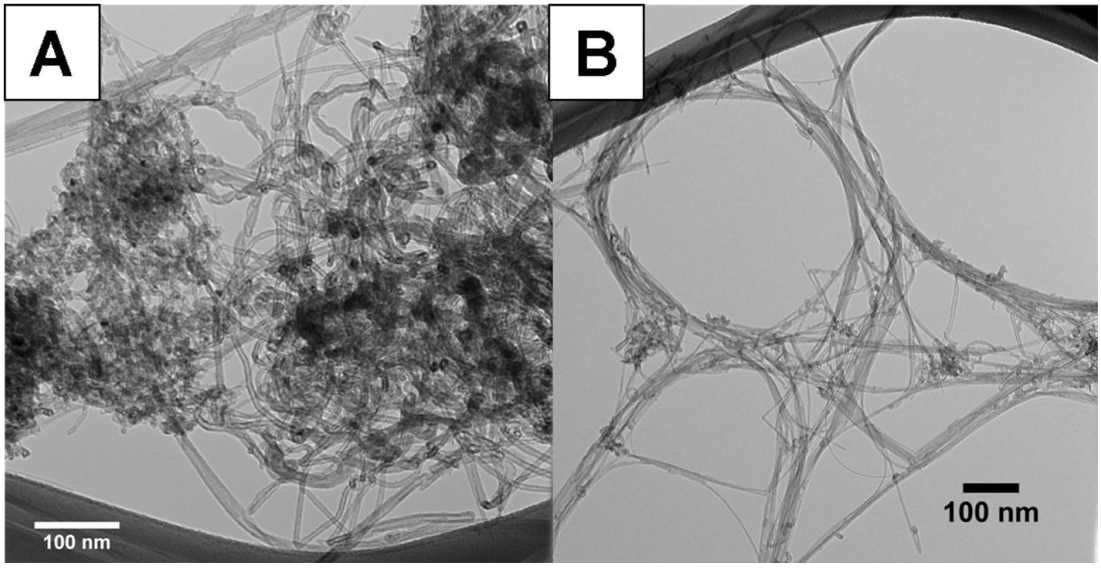

Figure 2.1 TEM images of (A) pristine and (B) purified DWNTs. (Reprinted with permission from *Dalton Trans.*, **2014**, *43*, 7480 – 7490. Copyright 2014 Royal Society of Chemistry.)

MWNTs. Pristine MWNTs (SES Research) (Figure 2.2A) were initially dispersed in concentrated HNO_3 by sonication and further refluxing at 120°C for 4 h in order to *(a)* remove any remnant metal catalysts and carbonaceous impurities, as well as to *(b)* generate functional,

oxygenated carboxylic acid moieties onto the nanotube surfaces. The resulting purified and oxidized MWNTs (Figure 2.2B), possessing a diameter range of 10 to 30 nm, were filtered through a 200 nm polycarbonate membrane (Millipore), thoroughly washed with excess water, and dried at 80°C for 18 h.

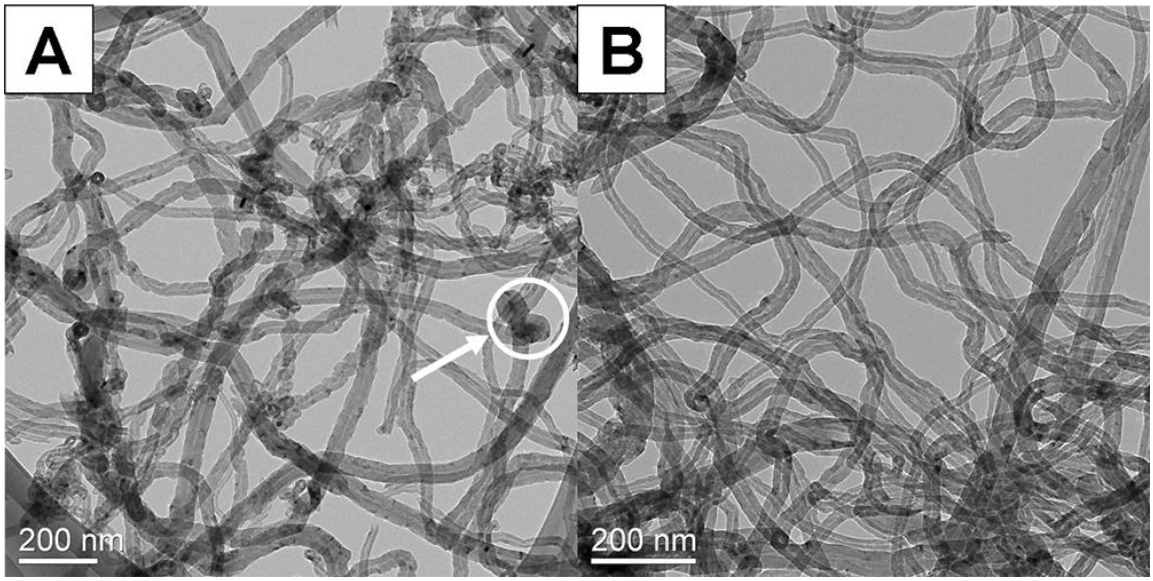

Figure 2.2 TEM images associated with (A) pristine MWNTs and (B) functionalized MWNTs after an HNO_3 treatment. The region containing amorphous carbonaceous impurities is indicated by the white circle.

2.1.2. Synthesis and ligand-exchange of CdSe

In order to synthesize CdSe quantum dots, we started off with a number of molecular precursors including hexadecylamine (HDA) (90%), selenium powder (100 mesh, 99.5%), 1, 3-dicyclohexyl-carbodiimide (DCC) (99%), *p*-phenylenediamine (PPD) (99%), 4-mercaptophenol (MTH) (97%), and 4-aminothiophenol (4-ATP) (97%), all of which were procured from Aldrich. In addition, we also purchased tri-*n*-octylphosphine oxide (TOPO) (99%), stearic acid (97%), cadmium oxide (CdO) (99%), tri-*n*-butylphosphine (TBP) (95%), and 2-aminoethanethiol hydrochloride (98%) (AET) from Acros Organics.

Synthesis of CdSe with various sizes. CdSe QDs with various sizes have been prepared, according to a well-known protocol, developed by the Peng group.[1] Briefly, 0.2 mmol of cadmium oxide (CdO) and 0.8 mmol of stearic acid were added to a three-necked round bottom flask, then de-gassed, and ultimately heated at 150°C under an Ar atmosphere. Once the contents were dissolved, 3.88 g each of trioctylphosphine oxide (TOPO) and hexadecylamine (HDA) were added to the flask and heated to 320°C under an Ar atmosphere. Separately, a precursor selenium (Se) solution was prepared in an air-sensitive glovebox environment wherein the Se was dissolved in tributylphosphine (TBP) and dioctylamine (DOA). Once the solution mixture had attained 320°C within the flask, the Se precursor was injected therein, and QD growth was allowed to proceed for different time intervals in order to obtain the desired QD size at 270°C. Depending on the targeted QD sizes, different sources of TOPO were chosen with minor modifications of the reaction algorithm. For example, to create QDs possessing average particle diameters of 2.3 nm and 3.0 nm, TOPO from Alfa Aesar was used, with corresponding reaction times of 15 s and 20 min, respectively. As for the synthesis of QDs with average diameters of 4.1 nm, TOPO from Acros Organics was utilized with reaction times of ~100 s (Figure 2.3). After growth was achieved, the mixture was later cooled to room temperature, then washed with either methanol (MeOH) or acetone, and ultimately stored in hexane.

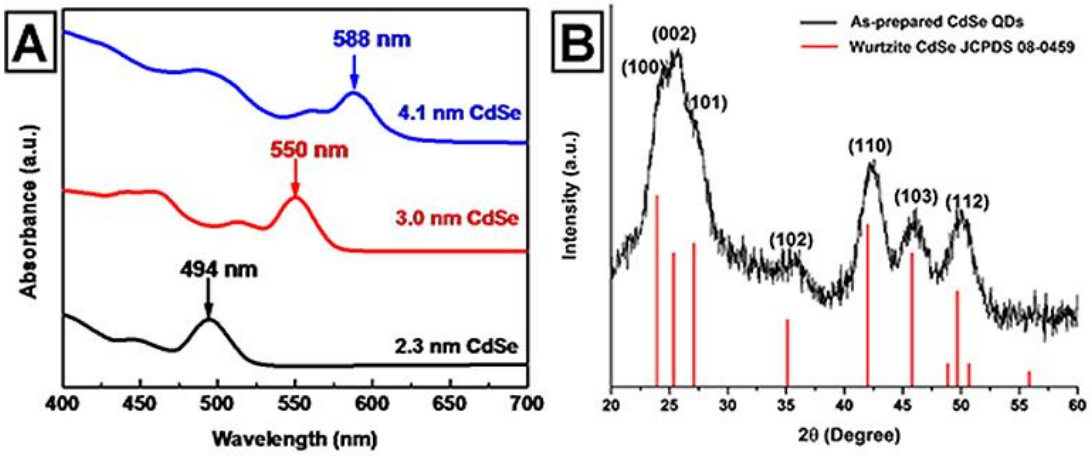

Figure 2.3 (A) UV-visible spectra of as-prepared CdSe QDs possessing average diameters of 2.3, 3.0, and 4.1 nm, respectively. (B) XRD patterns of as-prepared CdSe QDs (measuring 3.0 nm in diameter). The corresponding literature database standard (JCPDS #08-0459) is shown immediately below and is highlighted in red. (Reprinted with permission from *J. Phys. Chem. C*, **2015**, *119*, 26327–26338. Copyright 2015 American Chemical Society.)

Ligand-exchange process of CdSe QDs with targeting ligands. The ligand exchange process was carried out on our as-prepared CdSe QDs in order to substitute the native TOPO and HDA capping agents with a targeted series of specific ligand moieties of interest. In a typical experiment, 0.1 mmol of each ligand was dissolved in 2 mL methanol and added drop-wise to a suspension of as-prepared, TOPO/HDA-capped CdSe QDs (0.04 mmol) in 4 mL of hexane ([ligands]/[QDs] = 25). Under dark conditions, individual methanolic mixtures of thiol-based AET, ATP and MTH ligands were stirred for 30 min; the analogous methanolic solution of PPD was heated at 40°C and stirred for 6 h under argon atmosphere, until the CdSe QDs could be subsequently precipitated, upon completion of the ligand exchange process. As-generated ligand-exchanged QDs were then collected by centrifugation and subsequently washed with methanol and ethanol at 9000 rpm for 5 min for three successive times. As-generated MTH-capped QDs were then collected by centrifugation and subsequently washed with a methanol and chloroform

mixture (with a volume ratio of 1: 8) at 9000 rpm for 5 min for three successive times. The resulting processed QDs were ultimately re-dispersed in dimethyl sulfoxide (DMSO) for additional characterization.

2.1.3. Synthesis of DWNT-ligand-CdSe QD heterostructures

Non-covalent attachment/ π-π stacking strategy. In a typical run (Scheme 2.1),[2] 1 mg of pDWNT was dispersed in 10 mL DMSO by sonication followed by the addition of 2 mL of ATP-CdSe/MTH-CdSe QDs (0.004 mmol) in DMSO in a drop-wise manner. The resulting mixture was further sonicated for 10 min. Upon completion of the reaction, the solution was filtered using 200 nm polycarbonate membranes (Millipore), extensively washed with distilled water and ethanol in order to remove the excess free-standing CdSe QDs, and ultimately stored at 4°C, prior to further measurements.

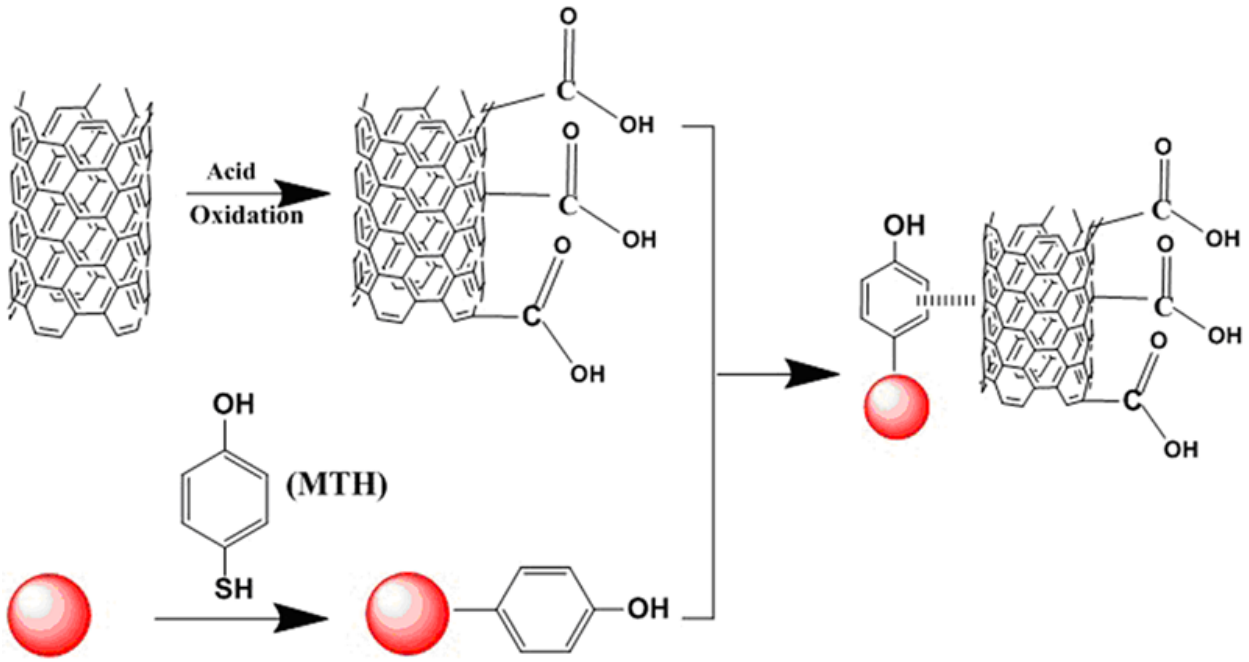

Scheme 2.1. Synthetic route associated with the non-covalent attachment of MTH-functionalized CdSe QDs onto underlying DWNT frameworks. (Reprinted with permission from *J. Phys. Chem. C*, **2015**, *119*, 26327–26338. Copyright 2015 American Chemical Society.)

Covalent attachment strategy. In a representative run (Scheme 2.2),[3] 1 mg of pDWNTs were dispersed in 10 mL DMSO by sonication followed by the addition of 35 mg DCC in dimethylformamide (DMF) solution, a biochemically inspired protocol allowing for the activation of the surface carboxylic acid groups on the exterior of the pDWNTs and thereby facilitating the subsequent and effective immobilization of larger amounts of QDs anchored onto the DWNT surface in as little as 4 h of overall reaction time. We note that we added 1-hydroxybenzotriazole (HOBT) to DCC in a molar ratio of 1: 1 in order to minimize the formation of an unwanted side product, e.g. diisopropylurea (DIU). A solution of 2 mL PPD/AET/ATP-capped CdSe QDs (0.004 mmol) in DMSO was subsequently introduced to the resulting solution and stirred in the dark for 4 h. Upon reaction completion, the solution was filtered using 200 nm polycarbonate membranes (Millipore), extensively washed with distilled water and ethanol in order to remove excess free-standing CdSe QDs, and ultimately stored at 4°C, prior to further analysis.

Scheme 2.2 highlights a plausible reaction scheme associated with the synthesis of our DWNT–QD heterostructures, using a covalent attachment strategy. It is also worth mentioning that the creation of an amide bond (indicated in black) may not necessarily be the only bonding interaction that results in the attachment of QDs onto underlying DWNTs. Specifically, some QDs may additionally interact with the presence of oxygenated defects localized on the outer DWNT surface through the plausible mediation of a Cd–O–C linkage (highlighted as red dotted lines), due to the relatively favorable affinity for metal–oxygen bond formation.

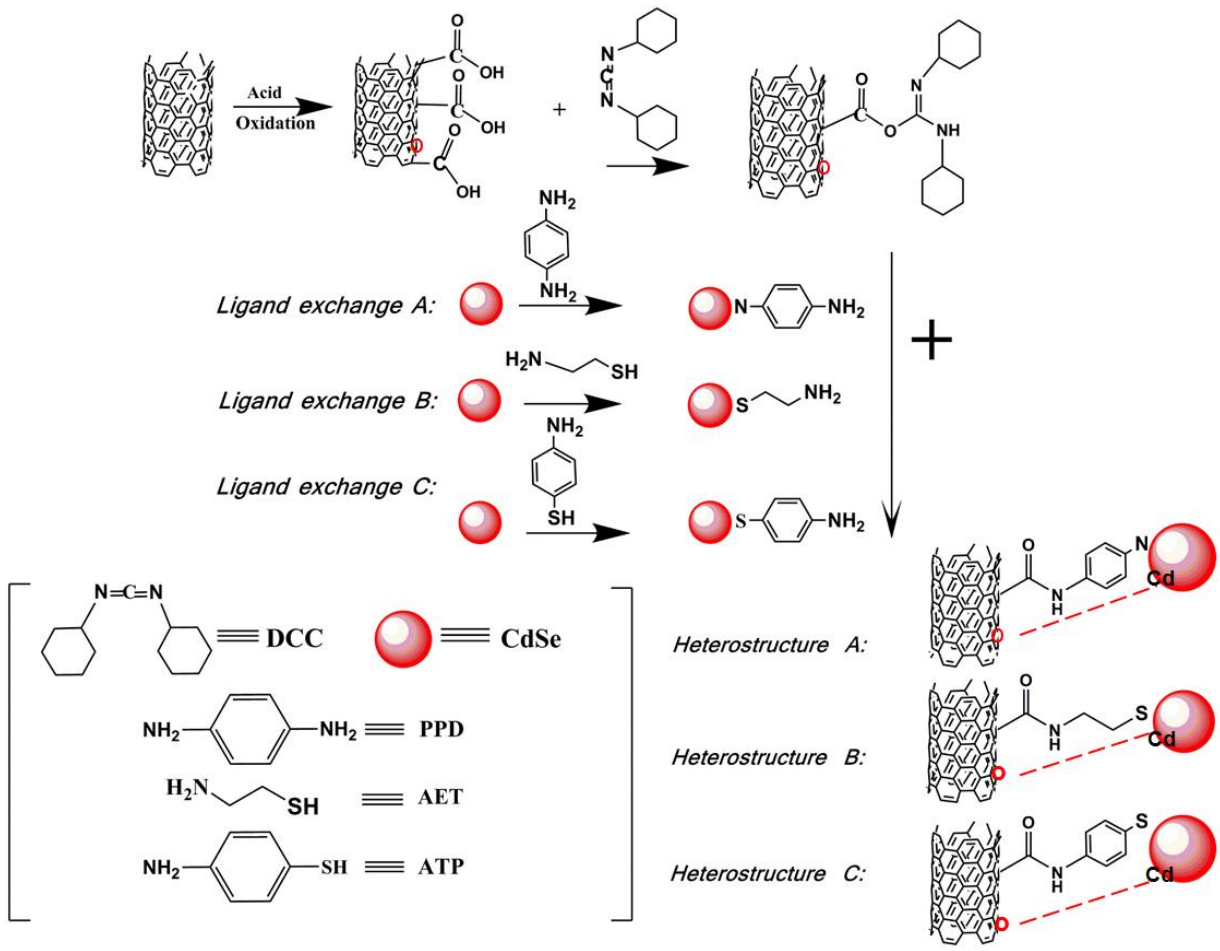

Scheme 2.2. Synthetic route associated with the covalent attachment of DWNTs with CdSe QDs functionalized with PPD, AET, and PPD ligands, respectively (Reprinted with permission from *Nanoscale,* **2016**, DOI**:** 10.1039/C6NR03091B. Copyright 2016 Royal Society of Chemistry.)

2.1.4. Synthesis of "flower-like" $Li_4Ti_5O_{12}$ microspheres

The synthesis strategy we have chosen herein to generate the flower-like $Li_4Ti_5O_{12}$ (LTO) is a hydrothermal reaction. The term *hydrothermal* was first used by the British geologist, Sir Roderick Murchison, to describe the action of water at elevated temperatures and pressures in bringing about changes in the earth's crust, thereby leading to the formation of various rocks and minerals. A deeper understanding of this concept has led to the development of the hydrothermal technique. In 1845, Schafthaul was first to take advantage of this mineral formation process in nature to obtain quartz crystals upon transformation of freshly precipitated silicic acid in Papin's

digester.[4] Hydrothermal reactions can be defined as any heterogeneous reactions in the presence of aqueous solvents or mineralizers under high pressure and temperature conditions, performed in an apparatus consisting of a steel pressure vessel called an autoclave, to dissolve and recrystallize materials that are relatively insoluble under ordinary conditions. The hydrothermal method possesses several intriguing advantages over other synthesis strategies, such as high product purity and homogeneity, the capability of generating metastable compounds with unique physicochemical properties, narrow particle size distributions, as well as fast reaction times.[4]

In a typical synthesis of flower-like LTO, the relevant precursors, i.e. flower like Li-Ti-O hydrate micron-scale spheres, were fabricated using a straightforward hydrothermal reaction. Specifically, we cut the Ti foil (STREM chemicals, 99.7%) into 40 pieces, measuring 1 cm x 1 cm squares, and placed pieces of this Ti foil into the bottom of the Teflon liner of an 120 mL autoclave. In particular, 86.1 mL of 0.5 M LiOH and 7.83 mL of 30% (w/w) H_2O_2 aqueous solution were then added to the solution, followed by strong stirring at room temperature for 15 min. Afterwards, the as-prepared solution mixture was transferred into a stainless steel autoclave, which was subsequently heated at 130°C for 4 h. After cooling down to room temperature, the suspension and associated white precipitate, which had formed, were separated by vacuum filtration, washed with aliquots of deionized water and ethanol for several times, and then ultimately oven dried at 80°C. The final products were annealed at 500°C in air for 3 h in a muffle furnace in order to obtain flower-like $Li_4Ti_5O_{12}$ micron-scale spheres.

2.1.5. Synthesis of 'flower-like' $Li_4Ti_5O_{12}$ micron-scale sphere - MWNT composites.

To demonstrate the inherent flexibility of our preparative methodology and to further study the correlation between synthetic strategies, *i.e.* the chemistry of heterostructure formation, and electrode performance, composites were generated by three complementary strategies,

namely by means of (1) a physical mixing of pre-formed structures by sonication; (2) a direct *in situ* deposition of MWNTs onto the underlying LTO micron-scale spheres within the context of a hydrothermal reaction environment; and (3) the covalent attachment of the two constituent components through the mediation of linker molecules.

Sonication method. The acid-functionalized MWNTs were well dispersed in dimethyl sulfoxide (DMSO) by ultrasonication for 1 h in order to obtain a clear black solution. As-prepared LTO micron-scale spheres were sonicated in water for 30 min before being added into the MWNT solution in a drop-wise manner. The solution mixture was further ultra-sonicated for another 1 h. The final product was collected by filtration, washed with deionized water, and dried at 80°C in order to obtain the resulting LTO-MWNT composites.

***In situ* direct deposition approach.** The functionalized MWNTs were added to the autoclave together with the precursors of lithium titanate, namely H_2O_2, LiOH, and Ti foil, using the same reaction parameters, as previously described. The resulting grey product was further annealed at 600°C for 3 h under an N_2 atmosphere in a tube furnace in order to preserve the underlying structural integrity of MWNTs.

Covalent attachment protocol. The relevant reaction procedures are depicted in Scheme 1. As-prepared LTO micron-scale spheres were initially functionalized with (3-aminopropyl) triethoxysilane (APTES) linker molecules by dispersing them in anhydrous organic DMSO solvent, in order to inhibit the formation of undesirable polysilsesquioxane that normally is generated through the hydrolytic condensation of organosilanes in either water or ethanol–water media.[5-7] The coated LTO sample was subsequently reacted at 85°C for 18 h under a N_2 atmosphere, followed by thermal curing at 120°C for 24 h in order to generate amine-terminated LTO. The resulting NH_2-terminated LTO product was collected by centrifugation and further

washed with DMSO for three times to remove any remaining, free-standing APTES molecules.

The acid-functionalized MWNTs were dispersed in a H_2O: DMSO mixture (v: v = 1: 2) by sonication followed by the addition of 1-ethyl-3-(3-dimethylaminopropyl) carbodiimide (EDC) and N-hydroxysuccinimide (NHS) in order to activate pendant carboxylic acid groups. The APTES-derivatized LTO were dispersed in water and mixed in with the MWNT solution in a 2-morpholino-ethanesulfonic acid (MES) buffer solution. The resulting mixture was reacted under vigorous stirring for 24 h. The final product was ultimately filtered, washed with excess deionized water, and finally dried at 80°C to obtain LTO-MWNT composites.

2.2. Brief introduction to common experimental and theoretical characterization techniques

2.2.1. Powder X-ray Diffraction

X-ray powder diffraction (XRD) is utilized to probe the crystallinity, crystalline structure, and chemical composition of as-synthesized nanostructures. Diffraction occurs when light is scattered by a periodic array with long-range order, producing constructive interference at specific angles. The atoms in a crystal are arranged in a periodic array and therefore can diffract light. Electromagnetic waves with wavelengths of the order of 10^{-10} m are called X-rays. The electric field of such waves interacts with the charges of all electrons of an atom, which then emit an almost spherical wave with the same wavelength as the incident radiation. The incidence of a primary X-ray beam onto a sample volume would produce scattering in all directions without the presence of diffraction effect. Diffraction redistributes intensity from the whole scattering sphere into distinctive directions. Figure 2.3 illustrates one way of describing these directions. It entails the notion of scattering lattice planes and interference between the wavelets

scattered by neighboring lattice planes.[8] The so-called Bragg reflection occurs when the path of the wavelet scattered from the lower of the two planes is longer by an integer number of wavelengths λ than that of the wavelet scattered from the upper plane. A reflection will thus occur when

$$n\lambda = 2d \sin\theta. \qquad \text{[Equation 2.1]}$$

Equation 2.1 above is the so-called Bragg equation, where λ is the wavelength of the radiation, 'n' is an integer number, θ is the angle between the lattice planes and the incident beam, and 'd' is the distance between the lattice planes for which the peak occurs. The scattering of X-rays from atoms produces a diffraction pattern, which contains information about the atomic arrangement within the crystal. Amorphous materials like glass do not have a periodic array with long-range order, so they do not produce a diffraction pattern. Information regarding the crystalline structure was determined by comparing the experimental diffraction patterns with standard patterns obtained from the Joint Committee on Powder Diffraction Patterns (JCPDS).

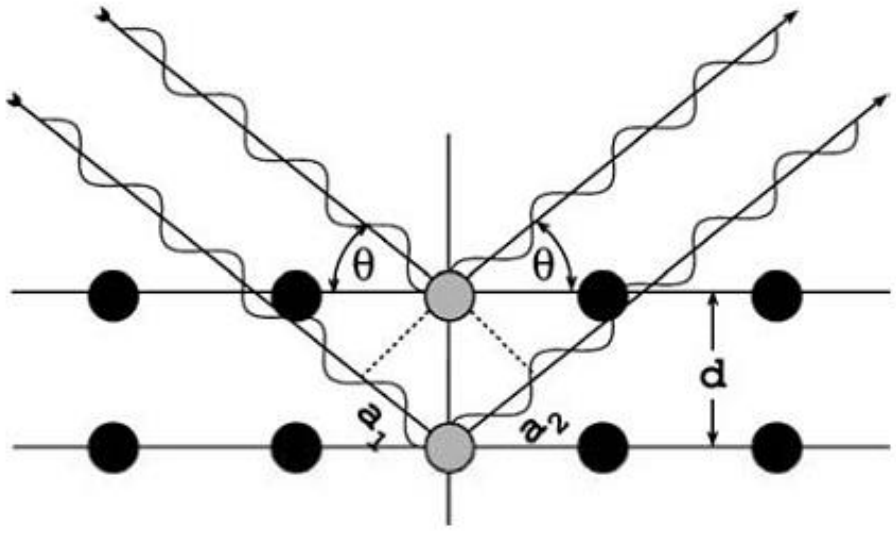

Figure 2.3. Geometric representation of Bragg's law: Constructive interference occures when the delay between waves scattered from adjacent lattice planes given by a_1+a_2 is an integer

multiple of the wavelength λ (reprinted from Ref. 8).

2.2.2. Electron Microscopy

In addition to XRD, two electron microscopy techniques, i.e. transmission electron microscopy (TEM) and scanning electron microscopy (SEM), have been widely used in this thesis in order to enable direct examination of the morphology, size, homogeneity, crystallinity, chemical composition, and surface structure of our as-prepared nanoscale heterostructures as well as of their individual building blocks. Transmission electron microscopy (TEM), which was developed by Max Knoll and Ernest Ruska in 1931,[9] is a microscopy technique that functions similarly to a light microscope, except that a beam of electrons instead of light is transmitted through an ultra-thin specimen, interacting with the specimen as it passes through it. An image is formed from the interaction of the electrons transmitted through the specimen, which is then magnified and focused onto a fluorescence screen containing a layer of photographic film.

There are four main components to a TEM: an electron optical column, a vacuum system, the necessary electronics (lens supplies for focusing and deflecting the beam and the high voltage generator for the electron source), and control software (Figure 2.4A).[10] Inside the electron microscope, the electron source is collimated into a parallel beam by the condenser lens; this passes through the sample and is then focused as an enlarged image onto a fluorescent screen, which emits light when struck by electrons, or, more frequently in modern instruments, an electronic imaging device such as a CCD (charge-coupled device) camera. The whole trajectory from source to screen is under vacuum, and the specimen has to be very thin to allow the electrons to travel through it. Not all specimens can be made thin enough for the TEM. Alternatively, if we want to look at the surface of the specimen, rather than a projection through it, a scanning electron microscope is a more appropriate technique.

It is not completely clear who first proposed the principle of scanning the surface of a specimen with a finely focused electron beam in order to produce an image. The first published description appeared in 1935 in a paper by the German physicist Max Knoll. Although another German physicist, Manfred von Ardenne, performed some experiments with what could be called a scanning electron microscope (SEM) in 1937, it was not until 1942 that three Americans, namely Zworykin, Hillier, and Snijder, first described a true SEM with a resolving power of 50 nm.[10] Modern SEMs can have resolving power better than 1 nm. An SEM, similar to TEM, consists of an electron optical column, a vacuum system, electronics, and software. The column is considerably shorter, because the only lenses needed are those above the specimen and these are specifically used to focus the electrons into a fine spot on the specimen surface.

Generally, a SEM microscope operates by generating an electron beam at the specimen surface with a spot size of less than 10 nm in diameter. The specimen that is impacted by the accelerated electrons emits signal in the form of electromagnetic radiation. Selected portions of this radiation, usually known as secondary (SE) and/or backscattered electrons (BSE), are collected by a detector, and the resulting signal is amplified and displayed on a computer monitor. In the most common or standard detection mode, i.e. secondary electron imaging (SEI), the secondary electrons are emitted from very close to the specimen surface. Back-scattered electrons (BSE) represent beam electrons that are reflected from the sample by elastic scattering, which emerge from deeper locations within the specimen and as such, yield a poorer image quality than that of the SE images. There are no lenses below the specimen. The specimen chamber, on the other hand, is larger, because the SEM technique does not impose any restriction on specimen size other than that set by the size of the specimen chamber (Figure 2.4B). The most important differences between TEM and SEM are as follows:

i) Rather than the broad static beam used in TEM, the SEM beam is focused to a fine point and scanned line by line over the sample surface in a rectangular raster pattern.

ii) The accelerating voltages, i.e. typically 50 to 30,000 volts, are much lower than in TEM, because it is not necessary to penetrate the specimen; and

iii) The specimen is not required to be thin, greatly simplifying specimen preparation.

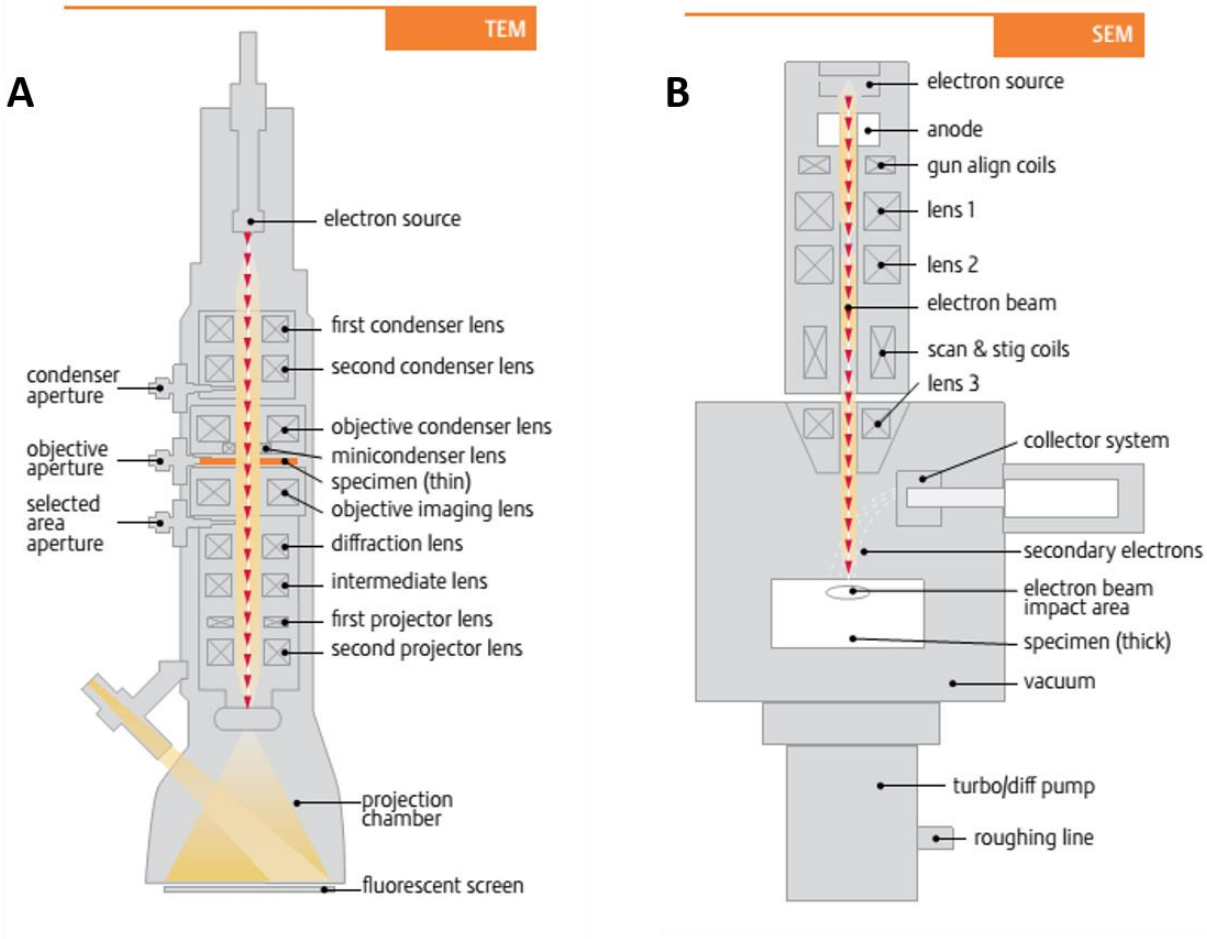

Figure 2.4. Comparison between TEM and SEM microscopes (adapted in part from ref. 10).

2.2.3. Thermo-gravimetric Analysis (TGA)

TGA is a thermal analysis technique, which monitors the mass change of the materials as a function of the increasing temperature and time within a controlled atmosphere. A TGA consists of a sample pan that is supported by a precision balance. That pan resides in a furnace,

and is either heated or cooled during the experiment. The mass of the sample is monitored during the experiment. A sample purge gas controls the sample environment. This gas may be inert or a reactive gas that flows over the sample and exits through an exhaust. The TGA instrument can quantify the loss of water, the loss of solvent, the loss of plasticizer, decarboxylation, pyrolysis, oxidation, decomposition, weight % filler, the amount of metallic catalytic residue remaining on carbon nanotubes, and weight % ash.[11]

2.2.4. BET (Brunauer–Emmett–Teller) surface area measurement

Brunauer, Emmett, and Teller (BET) denotes the most common method used to provide precise specific surface area evaluation of materials by nitrogen multilayer adsorption, measured as a function of relative pressure using a fully automated analyser, which was first proposed by these three scientists in 1938.[12] BET theory is basically an extension of the Langmuir theory, which describes monolayer molecular adsorption, onwards to multilayer adsorption with the following hypotheses: i) gas molecules physically adsorb onto a solid in infinite layers; ii) there is no interaction between each adsorption layer; and iii) the Langmuir theory can be applied to each layer.[13] The true surface area, including surface irregularities and pore interiors, is determined at the atomic level by the adsorption of either an unreactive or inert gas. In BET surface area analysis, nitrogen is usually used, because of its availability in high purity and its strong interaction with most solids. The amount of the adsorbates measured is a function not only of the total amount of exposed surface but also i) temperature, (ii) gas pressure, and (iii) the strength of interaction between the gas and the solid.

In a typical BET measurement, the known amount of N_2 gas is released into the sample chamber. Relative pressures less than atmospheric pressure can be achieved by creating conditions of partial vacuum. After the saturation pressure, no more adsorption occurs regardless

of any further increase in pressure. Highly precise and accurate pressure transducers monitor the pressure changes due to the adsorption process. After the adsorption layers are formed, the sample is removed from the nitrogen atmosphere and heated to cause the adsorbed nitrogen to be released from the material and thereby quantified.

The data collected are displayed in the form of a BET isotherm, which plots the amount of gas adsorbed as a function of the relative pressure.[14] The surface area of the sample is determined from the BET equation, illustrated in Equation 2.2, which utilizes the information from the isotherm. 'X' is the weight of nitrogen adsorbed at a given relative pressure (P/P_o) as a function of the incident pressure P_o, 'X_m' is the monolayer capacity, which is the volume of gas adsorbed at standard temperature and pressure (STP), and 'C' is a constant.

$$\frac{1}{X[(P_0/P)-1]} = \frac{1}{X_m C} + \frac{C-1}{X_m C}\left(\frac{P}{P_0}\right) \quad \text{[Equation 2.2]}$$

2.2.5. Atomic force microscopy (AFM)

The atomic force microscope (AFM) is a scanning near-field tool, and was invented by Binnig in 1986 for nanoscale investigation.[15] The basic design of an AFM (left-hand image in Figure 2.5) includes the use of a sharp tip scanning over the surface of a sample, while sensing the interactions between the tip and the sample.[16] The tip with a cantilever is mounted onto a piezoelectric scanner, which can move in three dimensions. During the measurement, a laser beam is bounced upon the back of the cantilever associated with the tip, which subsequently deflects the laser in an angular fashion. The movement of the reflected laser beam is detected with a position-sensitive photodiode. The intensity of the beam deflection changes in response to the interaction force between the tip and sample, which provides the relevant details in terms of the surface topography of the sample. AFM usually provides for two imaging modes, known as

contact mode (right-hand image in Figure 2.5, panel A) and dynamic mode (right-hand image in Figure 2.5, panel B), in order to visualize the sample topography. In contact mode, the AFM tip continuously scans over the sample, which causes significant lateral forces in the sample. In the dynamic mode, the cantilever is oscillated either near or slightly above its resonance frequency during the scan, which significantly reduces the lateral force between the tip and sample.[17]

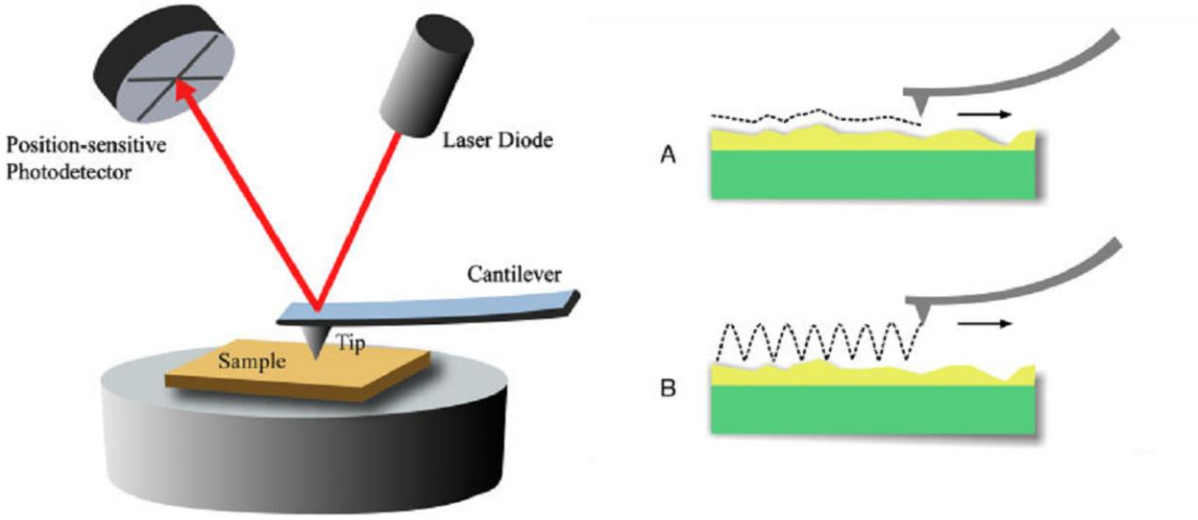

Figure 2.5. Work principle (left) as well as operating modes (right) of the AFM (A. contact mode and B. dynamic mode) (Adapted in part from ref. 16).

2.2.6. Fourier transform infrared (FT-IR) spectroscopy

FT-IR is the preferred method of infrared spectroscopy. In infrared spectroscopy, IR radiation is passed through a sample. Some of the infrared radiation is absorbed by the sample, and some of it is transmitted. IR spectroscopy records the molecular absorption and transmission, corresponding to the unique signature frequencies of vibrations between the bonds of the atoms making up the material, thereby creating a molecular fingerprint of the sample.[18] FT-IR spectrometry was developed in order to overcome the limitations encountered with dispersive IR instruments, which measure all of the infrared frequencies individually, thereby resulting in a

slow scanning process. In order to achieve the goal of measuring IR frequencies simultaneously, an optical device called an interferometer is employed, which includes a beam splitter that takes the incoming infrared beam and divides it into two optical beams. Because the subsequent analysis requires a spectrum of the intensity at each individual frequency in order to enable an identification of a certain compound, the measured interferogram signal cannot be interpreted directly. A well-known mathematical technique called the Fourier transformation was used to decode the individual frequencies. This transformation process is performed by computer which then provides the user with the desired spectral information for analysis.[19]

2.2.7. Raman

Raman spectroscopy is a spectroscopic technique based on inelastic scattering of monochromatic light, usually from a laser source. Inelastic scattering means that the frequency of photons in monochromatic light changes upon interaction with a sample. Photons of the laser light are absorbed by the sample and then re-emitted. The frequency of the re-emitted photons is shifted either up or down by comparison with the original monochromatic frequency, which provides information about the vibrational, rotational, and other low-frequency transitions in molecules.[20] Raman spectroscopy has provided for an exceedingly powerful tool for the characterization of carbon nanotubes.[21]

In this thesis, Raman spectra have been acquired on both DWNT and DWNT-CdSe heterostructures in order to reveal details about potential charge transfer in between these two constituent components. Three different Raman regions are generally investigated with respect to CNTs, namely, the lower frequency radial breathing mode (RBM) region, the D-band, and the G-band at higher frequency. The study of the RBM frequencies associated with various laser energy values can be used for characterizing the diameter distributions of SWNTs within SWNT

bundles. For example, the D band carries important information about the crystalline quality of the samples. The disorder-induced D band is only activated in the Raman spectrum of sp^2 carbons in the presence of hetero-atoms, vacancies, grain boundaries, or any other defects that can potentially lower the crystal symmetry of the quasi-infinite lattice. The D-band intensity and linewidth can be used as a handy probe for measuring the degree of disorder in SWNTs.[22]

The G-band lineshape can be used to distinguish between metallic from semiconducting nanotubes within SWNT bundles. The charge transfer is monitored by a shift of the G line. Upon doping, the G line shifts to higher frequencies for the outer tubes and to lower frequencies for the inner tubes. Usually, charge transfer from the dopant happens predominantly to the outer tubes at low doping. Charge transfer to the inner tubes occurs at higher doping levels. Depending on the type of doping involved, the Fermi level can be shifted either upwards with n-type doping or downwards with p-type doping.[23]

2.2.8. Ultraviolet–visible spectroscopy (UV-Vis)

UV-visible refers to absorption spectroscopy in the UV (200-400 nm) and visible (400-700) portion of the electromagnetic spectrum. When a molecule containing electrons typically starting out in a singlet ground state absorbs a photon, the electrons will be excited to higher anti-bonding orbitals. A UV/Vis spectrophotometer measures the intensity of the transmitted light passing through a sample (I) as well as the intensity of the incident light at a given wavelength (I_0). The transmittance, T, is defined as the ratio I/I_0, and is usually expressed as a percentage ($\%T$). The absorbance, A, can be derived from transmittance using A= -log ($\%T$/100%). The Beer-Lambert law (Equation 2.3) states that A is directly proportional to the concentration of the absorbing species in the solution and the path length.[24] Therefore, UV-Visible spectroscopy can be used to determine the concentration of the absorbing species, using Equation 2.3.

$$A == -\log(\%T/100\%) = \varepsilon cL \quad \text{[Equation 2.3]},$$

wherein L is the path length through the sample, ε is the extinction coefficient, and c is the concentration of the absorbing species.

2.2.9. Photoluminescence spectroscopy

Photoluminescence spectroscopy involves the excitation of the sample with incident light and the detection of the emitted light from the sample. Photoluminescence is divided into two categories: fluorescence and phosphorescence. A pair of electrons occupying the same electronic ground state, i.e. a singlet spin state, possesses opposite spins. When the sample absorbs either an ultraviolet or visible photon, one of its valence electrons moves from the ground state to an excited state with a conservation of the electron's spin. Fluorescence is one of many relaxation processes by which a photon is emitted from the singlet excited state to the singlet ground state with the same spin, and the average lifetime of an electron in the excited state is only 10^{-5}–10^{-8} s. In some cases, an electron in a singlet excited state is transformed to a triplet excited state, in which its spin is opposite to that of the electron in the ground state. The emission between the triplet excited state and the singlet ground state is defined as phosphorescence with an average lifetime ranging from 10^{-4} to 10^{4} s.[25]

2.2.10. Near-edge X-ray absorption fine structure spectroscopies (NEXAFS)

As a means of probing interfacial interactions among nanocomposites, the use of near-edge X-ray absorption fine structure (*NEXAFS*) spectroscopy has been extensively investigated,[26-29] as it characterizes the electronic transitions from a particular core level of an atom to its unoccupied (i.e. bound or continuum) states. Therefore, NEXAFS spectroscopy is element specific and is also very sensitive to the local chemical environment. Upon core−hole decay, two processes can occur, namely either fluorescence emission (i.e. bulk-sensitive)[30] or

Auger electron emission (i.e. surface-sensitive, as probed using the partial electron yield (PEY) mode).[31] By observing these processes, information about the occupancy of the low-lying unoccupied electronic states specific to the absorbing atom can be derived, and these data have been productively used to investigate the chemical bonding, electronic structure, and surface chemistry of many disparate types of nanomaterials.[32]

Furthermore, as compared with other techniques, such as but not limited to infrared spectroscopy (IR), NEXAFS (i) places fewer demands on the actual physico-chemical characteristics of the substrates analyzed (such as optical transparency), a finding which is advantageous for *in situ* analysis, and (ii) provides for high sensitivity upon chemical changes.[32] Moreover, by contrast with X-ray photoelectron spectroscopy (XPS) and ultraviolet photoelectron spectroscopy (UPS) which determines the presence of occupied states in the core region and the valence region, respectively, NEXAFS probes unoccupied states, and is thus complementary to both XPS and UPS.[26]

2.2.11. Field-effect transistors (FETs) for electrical transport measurement

The field-effect transistor (FET) is a transistor that uses an electric field to control the electrical conductivity of one type of charge carrier (i.e. either an electron or hole) in a semiconductor material in an active channel from the source to the drain. The conductivity of the channel is a function of the potential applied across the gate and source terminals. A FET usually includes the following components (illustrated in Figure 2.6):[33] a thin semiconducting layer, which is separated from a gate electrode by the insulating gate dielectric as well as source and drain electrodes of width W(channel width), separated by a distance L (channel length) that are in ohmic contact with the semiconducting layer.

The semiconducting layer in the FET is usually deposited using either spin-coating or the drop-cast method. The gate electrode can be either a metal or a conducting polymer, but very often, highly doped silicon serves as the substrate and the gate electrode at once. Inorganic insulators, such as SiO_2, are often either thermally grown or sputtered onto Si to serve as the gate dielectrics. The source and drain electrodes, usually high work functional metals, such as Au or Ag, inject charges into the semiconductor.[34] Voltages that are applied to the gate and drain electrode are referred to as V_g and V_d, respectively. The source electrode is normally grounded ($V_s = 0$). The potential difference between the source and the gate electrodes is usually just called the gate voltage (V_g), while the potential difference between the source and the drain is referred to as the source-drain voltage (V_{ds}). The source is the charge-injecting electrode, as it is always more negative than the gate electrode when a positive gate voltage is applied (i.e. electrons are injected) and more positive than the gate electrode when a negative gate voltage is applied (i.e. holes are injected).

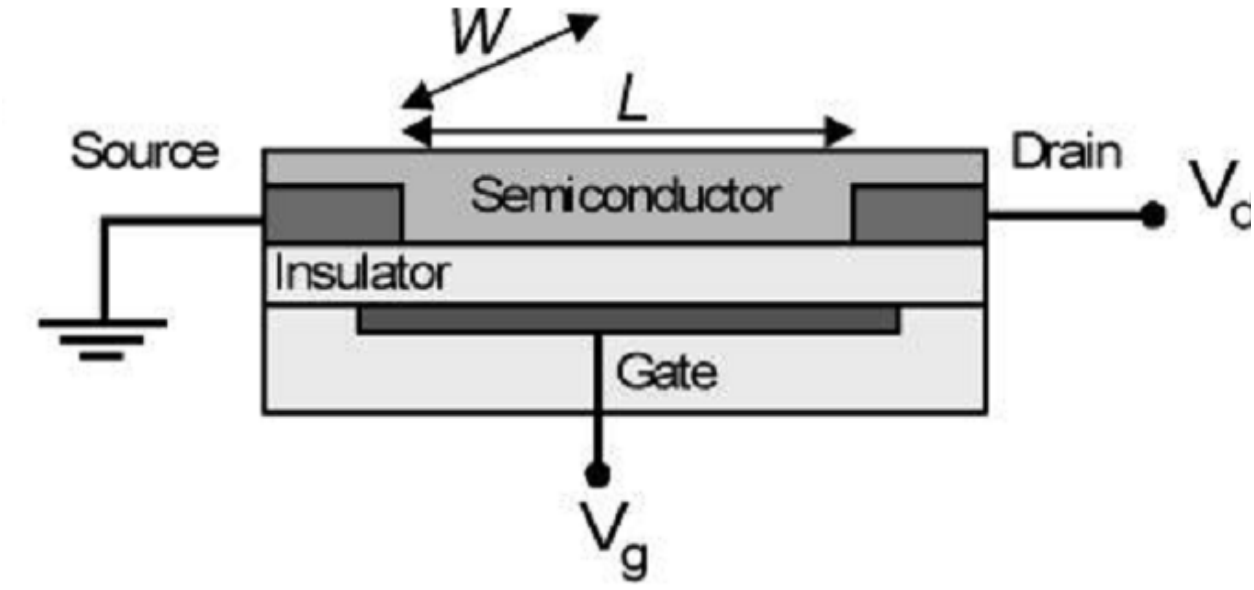

Figure 2.6 Schematic structure of a field-effect transistor with applied voltages: L = channel length; W = channel width; V = drain voltage; V_g = gate voltage; V_{Th} = threshold voltage; I_d = drain current (Adapted in part from Ref. 33).

2.2.12. Theoretical modeling methods for simulated X-ray absorption spectra (XAS)

In this thesis, we have simulated theoretical X-ray absorption spectra (XAS) results, calculated using density functional theory (DFT) calculations,[35-38] based on Fermi's Golden Rule, to compare and ultimately to correlate computed results with measured NEXAFS experimental data in order to potentially test for and verify predictions from experiments. DFT is a relatively efficient and unbiased computational quantum mechanical modelling approach used in physics, chemistry, and materials science in order to investigate the electronic structure (principally the ground state) of many-body systems, in particular atoms, molecules, and solids to nuclei in addition to quantum and classical fluids. DFT predicts a great variety of molecular properties, such as molecular structures, vibrational frequencies, atomization energies, ionization energies as well as electric and magnetic properties.[39]

In the current thesis, the electronic ground state calculations was computed using NorthWest computational Chemistry (NWChem),[40] which is a code developed in the W.R. Wiley Environmental Molecular Sciences Laboratory (EMSL) at the Pacific Northwest National Laboratory (PNNL). Such a software package offers a wide range of capabilities and it is able to take advantage of massively parallel computer architectures, which fully realize the potential of computational modeling in answering key scientific questions.

2.3. Structural characterization protocols used in this thesis

2.3.1. XRD

For the CdSe QDs, we characterized the crystallinity and crystallographic profile of our variously processed CdSe QDs using powder XRD. To analyze these materials, as-prepared samples were sonicated, dispersed in ethanol for about 2 min, and after deposition, finally air-dried onto transparent glass slides. Diffraction patterns for all of these materials were recorded

using a Scintag diffractometer, operating in the Bragg configuration with Cu Kα radiation (λ = 1.54 Å) and scanning in the range from 20 to 80° at a rate of 0.25° per minute.

In terms of the flower-like LTO and the resulting LTO-MWNT composites, crystallographic data on as-prepared LTO micron-scale spheres as well as various LTO-MWNT composites were obtained using a Rigaku Miniflex II diffractometer, operating in the Bragg configuration using Cu Kα radiation (1.54 Å). Specifically, diffraction data were collected in a range of 10°-70° at a scanning rate of 1° per minute using a zero-background holder. A Rietveld refinement has been performed on as-obtained XRD profiles using the EXPGUI interface in the Match! (Crystal Impact GbR) software, thereby allowing for phase identification from powder diffraction data.

2.3.2. Electron Microscopy

The structure, morphology, and size of the as-prepared LTO micron-scale spheres were observed by using a field-emission scanning electron microscope (FE-SEM Leo 1550) operating at 2.5 kV. LTO-MWNT micron-scale spheres were probed using an analytical high resolution SEM (JEOL 7600F) instrument, operating at an accelerating voltage of 15 kV and equipped with EDX capabilities. To prepare these samples for subsequent characterization, fixed quantities were dispersed in ethanol and sonicated for ~1 min, prior to their deposition onto an underlying silicon (Si) wafer.

Low-magnification TEM images were collected using an accelerating voltage of 120 kV on a JEOL JEM-1400 instrument, with a 2048 x 2048 Gatan CCD Digital Camera. High resolution TEM (HR-TEM) images coupled with SAED patterns were recorded using a JEOL JEM-3000F microscope, equipped with a Gatan image filter (GIF) spectrometer, operating at an accelerating voltage of 300 kV. Specimens for all of these TEM runs were prepared by

dispersing as-prepared samples in ethanol, sonicating for 2 min in order to ensure adequate dispersion, and finally depositing a drop of solution onto a 300 mesh Cu grid, coated with a lacey carbon film. Microtomed LTO samples analyzed by using transmission electron microscopy were processed by using standard techniques. Briefly, samples of as-prepared LTO were dehydrated by using ethyl alcohol and then embedded in a low-viscosity Spurr's resin (Electron Microscopy Sciences, Fort Washington PA). A series of ultrathin sections of 80 nm were serially prepared by using a Leica EM UC7 ultramicrotome instrument and then placed onto formvar-coated Cu grids. Sections were then stained with uranyl acetate and lead citrate, and viewed by using a FEI Tecnai12 BioTwinG^2 electron microscope. Digital images were acquired with an AMT XR-60 CCD digital camera system.

2.3.3. Thermo-gravimetric Analysis (TGA)

To test the thermal behavior as well as the MWNT loading ratio in the heterostructures, thermogravimetric analysis (TGA) data were collected using a TGA Q500 instrument over a relatively broad temperature range spanning from 30 to 800°C under an air atmosphere, using a heating rate of 10°C/min.

2.3.4. BET (Brunauer–Emmett–Teller) surface area

Multipoint BET surface area data were acquired by using a Quantachrome Nova 4200e instrument with N_2 gas as the adsorbent.

2.3.5. FT-IR spectra

To obtain FT-mid-IR data on solid samples, we used a Nexus 670 (Thermo Nicolet) spectrometer, equipped with a single-reflectance zinc selenide (ZnSe) ATR accessory, a KBr beam splitter, and a DTGS KBr detector. A series of as-prepared, PPD-, AET-, and ATP-capped CdSe QD samples as well as MWNT-LTO and DWNT-CdSe heterostructures were then dried in

a vacuum oven, prior to measurement. Solid samples were physisorbed onto a ZnSe crystal. Measurements were then taken in reflectance mode by using the Smart Orbit module.

2.3.6. Atomic force microscopy (AFM)

AFM height images were obtained in tapping mode in air at resonant frequencies of 50–75 kHz with oscillating amplitudes of 10 to 100 nm. The magnitude of the tip oscillation amplitude was kept at a minimal level for each sample to minimize potential sample damage. The samples were spin coated from a methanolic solution onto a mica substrate, and imaged with Si tips ($k = 1–5\ Nm^{-1}$) using a Multimode Nanoscope IIIa (Digital Instruments, Santa Barbara, CA) instrument. All AFM images were taken at the center of the sample substrate, measuring $500 \times 500\ nm^2$ in area, and were normalized to a vertical height scale of 150 nm in order to permit for self-consistency and comparison within our data set.

2.4. Opto-electronic characterization techniques used in this thesis

2.4.1. UV-visible spectra.

UV-visible spectra of the CdSe QDs were gathered at high resolution by using a Thermospectronics UV1 instrument on sample dispersions within quartz cells, maintaining a 10 mm path length. Specifically, as-prepared QDs were suspended in hexane, while the ligand-exchanged QDs were dispersed in dimethyl sulfoxide (DMSO). Collected data were corrected in order to account for and subtract away the presence of the solvent background. Ensemble extinction spectra were collected on a PerkinElmer Lambda25 apparatus.

2.4.2. Photoluminescence spectra.

Ensemble photoluminescence (PL) spectra were collected on samples under continuous stirring utilizing an SC 450-PP Fianium supercontinuum laser and interference filters for excitation. Steady-state PL was collected using 2MHz pulses. Excitation fluences were kept near

<N> = 1E-5. A long wave pass emission filter was used in conjunction with a JY-Horiba monochromator and CCD camera for steady-state detection. Photoluminescence quantum yields (QY) were calculated using Rhodamine B as a relative standard which has a quantum yield of 0.7.[41] Quantum dot concentrations were kept low, with attenuation values between 0.2 and 0.02 so as to avoid errors in QY calculations. Nonetheless, the lower limit for our PL QY detection is of the order of 1×10^{-5} %.

2.4.3. Raman.

Raman spectra were accumulated from our samples using a Renishaw inVia high resolution confocal Raman microscope that had been outfitted with a Leica DM2500 upright microscope using a 514.5 nm (2.41 eV) in line laser. The microscope stage was equipped with an automated *xyz*-motorized stage. Wavelength and intensity calibrations were completed by using an internal silicon standard, based upon a reference peak at 520 cm^{-1}.

Spectra from the samples were acquired using an 1800 line/mm grating, thereby resulting in a spectral resolution of ~0.5 cm^{-1}, with a 10 s integration time per spectrum using a CCD array. Raw spectra were subsequently processed and analyzed using the WiRE 4.1 software. Baselines were subtracted from all of the spectra, and the integrated spectral areas were normalized to an area of 1. The resulting peaks were then fitted with Lorentzian curves in order to determine the requisite peak positions, integrated areas (intensity), and peak widths.

2.4.4. Near-edge X-ray absorption fine structure spectroscopies (NEXAFS).

We were able to perform carbon *K*-, oxygen *K*-, and cadmium M_3-edge NEXAFS measurements at the NIST U7A beamline at the National Synchrotron Light Source located at Brookhaven National Laboratory. Specifically, NEXAFS spectra were achieved by using a horizontally polarized X-ray beam incident at 55^o (i.e. magic angle) and a channeltron electron

multiplier equipped with a variable entrance grid bias. For the various elements studied, the entrance grid bias was set to –150 V in order to enhance surface sensitivity and to reduce the low-energy electron background. A toroidal spherical grating monochromator, comprised of a 600 lines/mm grating for the C *K*-edge data as well as a 1200 lines/mm grating for the Cd M_3 & O *K*-edges, was used. Slit openings of 30 μm × 30 μm along the beamline provided for an energy resolution of ~0.1 eV for all measured spectra. An electron flood gun set at 60 μA was used to mitigate for the possibility of surface charging.

The partial electron yield (PEY) signals were normalized to the incident beam intensity using the photoemission signal from a freshly evaporated Au mesh located along the incident beam path. The spectra were calibrated in terms of energy by analyzing the photoemission current from an amorphous carbon mesh also located along the path of the incident beam. Spectra were calibrated and normalized using standard routines from the Athena software.[42]

2.4.5. Electrical transport.

Electrical transport measurements have been used to complement the NEXAFS and Raman data as well as to gain additional insights into the impacts of QD size, coverage density as well as ligand identities. To this extent, devices have been fabricated onto a highly *p*-doped silicon substrate with a 90 nm silicon dioxide layer on top. Next, carbon nanotubes either with or without functionalization are spun out of solution onto the substrate, and the three-terminal transistor structure is finalized by e-beam lithography and lift-off of titanium / gold (30 nm / 30 nm) source/drain contacts. A probe station set up in conjunction with a parameter analyzer is then used to determine the current through the device, i.e. I_{DS}, as a function of the drain V_{DS} and the gate voltage V_{GS}. To reduce any hysteresis effect on the device characteristics, a pulse measurement set up was used. In a typical pulse measurement, the Hewlett Packard (HP)

parameter analyzer) is turned off between each data point taken instead of being operated continuously. In total, more than 180 discrete and distinctive double-wall carbon nanotube (DWNT) field-effect transistors (FETs) were characterized in this fashion, giving rise to a decent statistical trend, that have allowed us to observe trends between variously treated devices, in spite of the presence of possible device-to-device variations arising from different DWNT chiralities and diameters as well as general experimental non-reproducibilities. All data presented in this article were obtained at room temperature under a vacuum of about 10^{-5} Torr.

2.5. Theoretical modeling methods used in this thesis

Since the DWNTs used in our experiments possess outer diameters of about 10 nm and have tendency to form larger bundles, curvature and reduced dimension effects should be quite small, and thus, the outer surface of the DWNTs can be approximated by graphene in our theoretical modeling endeavors.[43] A finite model with a 3 nm square (410 carbon atoms) sheet of graphene was employed for the analysis. Electronic ground state calculations for the various complexes were computed using the NWChem[40] version 6.3, and specifically, the self-consistent density functional theory (DFT) calculations were achieved using the PBE-0 functional[44, 45] within the 6-31G*[46] basis set. Full details associated with the construction of the differentially functionalized systems will be discussed later.

Since relaxed core-hole calculations were too expensive on these systems with so many distinctive carbon atoms present, the theoretical X-ray absorption spectra (XAS) were calculated, according to Fermi's Golden Rule, using the dipole approximation as well as using unrelaxed orbitals and energies, following established practices.[47] Gaussian numerical broadening was used with a half width of 0.1 eV to model beam width and finite temperature effects. Since the core energies are not accurately predicted by DFT, theoretical spectra when compared with their

experimental counterparts were shifted in order to align the large peak, attributed to the σ* transition. When comparing theory to theory, no shift was deemed to be necessary.

In a complex system characterized by a large population of polydisperse nanotubes, unforeseen numbers and types of defects and binding sites, as well as differential amounts of ligands and QD coverages, generating precise quantitative agreement with experimental results may be an unreasonable expectation. Nevertheless, herein we have employed standard, widely accepted methods in our analysis to acquire a basic, well-grounded qualitative understanding of the experimental behavior. In so doing, we have attempted to make sense of and to potentially de-convolute the acquired experimental results by systematically and separately identifying the independent contributions of the defects, the ligands, and the quantum dots, respectively. Details regarding the construction of the various model systems as well as a representative image of a typical graphene-ATP-CdSe QD composite, which is illustrative of our approach and captured in Vesta,[48] are displayed in Figure 2.10.[3]

A flat graphene sheet measuring 3 nm x 3 nm and a carbon - carbon bond length of 1.418 Å was created using the VMD software.[49] The sheet was hydrogen-terminated using the Avogadro software.[50] The 'defected' system was created from this graphene sheet by adding in 20 defects, randomly spaced around the interior of the sheet. The localized geometries of the 'defected' carboxyl groups as well as that of the local environment in the graphene sheet were each individually allowed to relax using Avogadro's force field optimization with the UFF force field. The linker molecules were subsequently built into this 'defected' system, with the linker molecules attached at the same 'defected' sites in the graphene sheet. Identical relaxation techniques were also applied to the various atoms in the ligands, followed by a geometry

relaxation using NWChem for all systems. Detailed coordinates of each ligand-bound graphene system can be found in separate 'xyz' files, attached herein.

For systems with a CdSe quantum dot, the dot was generated as follows: a würtzite[51] unit cell with a stoichiometric ratio of 1:1 cadmium to selenium was replicated many times along each spatial dimension. Then all atoms outside the desired radius of 0.75 nm were discarded. A sphere of $(CdSe)_{33}$ (i.e. a magic number[52]) was subsequently attached to either the relevant S or N atom after removing the capping hydrogen atom of the linker, and the entire system was subsequently relaxed in NWChem using the identical parameters, as stated above. Full images of these systems, captured in Vesta, are displayed in Figure 2.7.

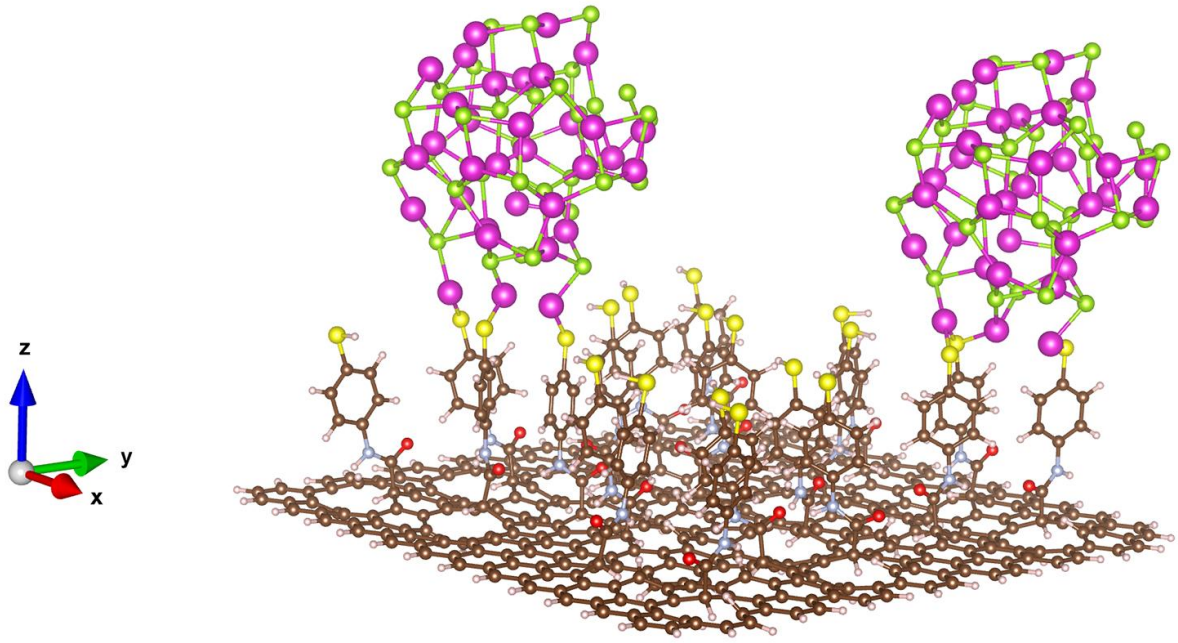

Figure 2.7. Representative model used in theoretical NEXAS calculations of typical graphene-bound ATP-CdSe QD heterostructures. The atoms are labeled as follows: brown - carbon; white – hydrogen; red – oxygen; gray – nitrogen; yellow – sulfur; pink – cadmium; and green – selenium (Reprinted with permission from *Nanoscale*, **2016**, DOI**:** 10.1039/C6NR03091B. Copyright 2016 Royal Society of Chemistry.).

2.6. Electrochemical characterization techniques used in this thesis

Details associated with coin cell assembly and electrochemical characterizations will be discussed in the thesis from Yiman Zhang (Takeuchi Group, Stony Brook University).

2.7. References

1. Qu, L. H.; Peng, X. G. Control of photoluminescence properties of CdSe nanocrystals in growth. *J. Am. Chem. Soc.* **2002**, *124*, 2049-2055.
2. Wang, L.; Han, J. K.; Zhu, Y. Q.; Zhou, R. P.; Jaye, C.; Liu, H. Q.; Li, Z. Q.; Taylor, G. T.; Fischer, D. A.; Appenzeller, J.; Wong, S. S. Probing the Dependence of Electron Transfer on Size and Coverage in Carbon Nanotube-Quantum Dot Heterostructures. *J. Phys. Chem. C* **2015**, *119*, 26327-26338.
3. Wang, L.; Han, J.; Sundahl, B.; Thornton, S.; Zhu, Y.; Zhou, R.; Jaye, C.; Liu, H.; Li, Z. Q.; Taylor, G. T.; Fischer, D. A.; Appenzeller, J.; Harrison, R. J.; Wong, S. S. Ligand-induced dependence of charge transfer in nanotube-quantum dot heterostructures. *Nanoscale* **2016,** *in press*.
4. Byrappa, K.; Adschiri, T. Hydrothermal technology for nanotechnology. *Prog. Cryst. Growth Charact. Mater.* **2007**, *53*, 117-166.
5. Sankaraiah, S.; Lee, J. M.; Kim, J. H.; Choi, S. W. Preparation and characterization of surface-functionalized polysilsesquioxane hard spheres in aqueous medium. *Macromolecules* **2008**, *41*, 6195-6204.
6. Noda, I.; Kamoto, T.; Yamada, M. Size-controlling synthesis of narrowly distributed particles of methylsilsesquioxane derivatives. *Chem. Mater.* **2000**, *12*, 1708-1714.
7. Asenath-Smith, E.; Chen, W. How To Prevent the Loss of Surface Functionality Derived from Aminosilanes. *Langmuir* **2008**, *24*, 12405-12409.
8. Stanjek, H.; Hausler, W. Basics of X-ray diffraction. *Hyperfine Interact.* **2004**, *154*, 107-119.
9. Nellist, P. Seeing with electrons. *Physics World* **2005**, *18*, 24-29.
10. An Introduction to Electron Microscopy booklet, *FEI company*.
11. A Beginners Guide Thermogravimetric Analysis (TGA). *PerkinElmer*, 1-19.
12. Brunauer, S.; Emmett, P. H.; Teller, E. Adsorption of gases in multimolecular layers. *J. Am. Chem. Soc.* **1938**, *60*, 309-319.
13. Langmuir, I. THE ADSORPTION OF GASES ON PLANE SURFACES OF GLASS, MICA AND PLATINUM. *J. Am. Chem. Soc.* **1918**, *40*, 1361-1403.
14. Brunauer, S.; Deming, L. S.; Deming, W. E.; Teller, E. On a theory of the van der Waals adsorption of gases. *J. Am. Chem. Soc.* **1940**, *62*, 1723-1732.
15. Giessibl, F. J. Advances in atomic force microscopy. *Rev. Mod. Phys.* **2003**, *75*, 949-983.
16. Dufrene, Y. F. AFM for nanoscale microbe analysis. *Analyst* **2008**, *133*, 297-301.
17. Zhong, Q.; Inniss, D.; Kjoller, K.; Elings, V. B. Fractured Polymer Silica Fiber Surface Studied by Tapping Mode Atomic-Force Microscopy. *Surf. Sci.* **1993**, *290*, L688-L692.
18. Schultz, C. P. Precision infrared spectroscopic imaging: The future of FT-IR spectroscopy. *Spectroscopy* **2001**, *16*, 24.
19. Brault, J. W. New approach to high-precision Fourier transform spectrometer design. *Appl. Opt.* **1996**, *35*, 2891-2896.

20. Kloprogge, J. T. Short introduction to infrared and Raman spectroscopy. *Application of Vibrational Spectroscopy to Clay Minerals and Layered Double Hydroxides* **2005**, *13*, 1-7.
21. Dresselhaus, M. S.; Dresselhaus, G.; Saito, R.; Jorio, A. Raman spectroscopy of carbon nanotubes. *Physics Reports-Review Section of Physics Letters* **2005**, *409*, 47-99.
22. Souza, A. G.; Jorio, A.; Samsonidze, G. G.; Dresselhaus, G.; Saito, R.; Dresselhaus, M. S. Raman spectroscopy for probing chemically/physically induced phenomena in carbon nanotubes. *Nanotechnology* **2003**, *14*, 1130-1139.
23. Rauf, H.; Pichler, T.; Pfeiffer, R.; Simon, F.; Kuzmany, H.; Popov, V. N. Detailed analysis of the Raman response of n-doped double-wall carbon nanotubes. *Phys. Rev. B* **2006**, *74*, 235419.
24. Mayerhöfer, T. G.; Mutschke, H.; Popp, J. Employing Theories Far beyond Their Limits—The Case of the (Boguer-) Beer–Lambert Law. *ChemPhysChem* **2016**, *17*, 1948-1955.
25. Gilliland, G. D. Photoluminescence spectroscopy of crystalline semiconductors. *Materials Science & Engineering R-Reports* **1997**, *18*, 99-399.
26. Hahner, G. Near edge X-ray absorption fine structure spectroscopy as a tool to probe electronic and structural properties of thin organic films and liquids. *Chem. Soc. Rev.* **2006**, *35*, 1244-1255.
27. De Jesus, L. R.; Dennis, R. V.; Depner, S. W.; Jaye, C.; Fischer, D. A.; Banerjee, S. Inside and Outside: X-ray Absorption Spectroscopy Mapping of Chemical Domains in Graphene Oxide. *J. Phys. Chem. Lett.* **2013**, *4*, 3144-3151.
28. Kuznetsova, A.; Popova, I.; Yates, J. T.; Bronikowski, M. J.; Huffman, C. B.; Liu, J.; Smalley, R. E.; Hwu, H. H.; Chen, J. G. G. Oxygen-containing functional groups on single-wall carbon nanotubes: NEXAFS and vibrational spectroscopic studies. *J. Am. Chem. Soc.* **2001**, *123*, 10699-10704.
29. Wang, Z.; Wu, L.; Zhou, J.; Cai, W.; Shen, B.; Jiang, Z. Magnetite Nanocrystals on Multiwalled Carbon Nanotubes as a Synergistic Microwave Absorber. *J. Phys. Chem. C* **2013**, *117*, 5446-5452.
30. Perez-Dieste, V.; Castellini, O. M.; Crain, J. N.; Eriksson, M. A.; Kirakosian, A.; Lin, J. L.; McChesney, J. L.; Himpsel, F. J.; Black, C. T.; Murray, C. B. Thermal decomposition of surfactant coatings on Co and Ni nanocrystals. *Appl. Phys. Lett.* **2003**, *83*, 5053-5055.
31. Hemraj-Benny, T.; Banerjee, S.; Sambasivan, S.; Balasubramanian, M.; Fischer, D. A.; Eres, G.; Puretzky, A. A.; Geohegan, D. B.; Lowndes, D. H.; Han, W. Q.; Misewich, J. A.; Wong, S. S. Near-edge X-ray absorption fine structure spectroscopy as a tool for investigating nanomaterials. *Small* **2006**, *2*, 26-35.
32. Winter, A. D.; Larios, E.; Alamgir, F. M.; Jaye, C.; Fischer, D. A.; Omastova, M.; Campo, E. M. Thermo-Active Behavior of Ethylene-Vinyl Acetate I Multiwall Carbon Nanotube Composites Examined by in Situ near-Edge X-ray Absorption Fine-Structure Spectroscopy. *J. Phys. Chem. C* **2014**, *118*, 3733-3741.
33. Zaumseil, J.; Sirringhaus, H. Electron and ambipolar transport in organic field-effect transistors. *Chem. Rev.* **2007**, *107*, 1296-1323.
34. Cai, X. Y.; Burand, M. W.; Newman, C. R.; da Silva, D. A.; Pappenfus, T. M.; Bader, M. M.; Bredas, J. L.; Mann, K. R.; Frisbie, C. D. N- and P-channel transport behavior in thin film transistors based on tricyanovinyl-capped oligothiophenes. *J. Phys. Chem. B* **2006**, *110*, 14590-14597.

35. Warszawski, E.; Adler, J.; Hoffman, A.; Silverman, A. Experiment (NEXAFS) versus simulation (DOS) for carbon allotropes. *Proceedings of the 22th Workshop on Computer Simulation Studies in Condensed Matter Physics (Csp 2009)* **2010**, *3*, 1381-1385.
36. Qian, X.; Sambe, H.; Ramaker, D. E. Theoretical study on Cl L_{23} NEXAFS and UV absorption data for metal chlorides. *Phys. Rev. B* **1995**, *52*, 15115-15121.
37. Voloshina, E.; Ovcharenko, R.; Shulakov, A.; Dedkov, Y. Theoretical description of X-ray absorption spectroscopy of the graphene-metal interfaces. *J. Chem. Phys.* **2013**, *138*, 154706.
38. Schultz, B. J.; Jaye, C.; Lysaght, P. S.; Fischer, D. A.; Prendergast, D.; Banerjee, S. On chemical bonding and electronic structure of graphene-metal contacts. *Chem. Sci.* **2013**, *4*, 494-502.
39. Harrison, N. A. An introduction to density functional theory. *Comput. Mater. Sci.* **2003**, *187*, 45-70.
40. Valiev, M.; Bylaska, E. J.; Govind, N.; Kowalski, K.; Straatsma, T. P.; Van Dam, H. J. J.; Wang, D.; Nieplocha, J.; Apra, E.; Windus, T. L.; de Jong, W. A. NWChem: A comprehensive and scalable open-source solution for large scale molecular simulations. *Comput. Phys. Commun.* **2010**, *181*, 1477-1489.
41. Brouwer, A. M. Standards for photoluminescence quantum yield measurements in solution (IUPAC Technical Report). *Pure Appl. Chem.* **2011**, *83*, 2213-2228.
42. Ravel, B.; Newville, M. ATHENA, ARTEMIS, HEPHAESTUS: data analysis for X-ray absorption spectroscopy using IFEFFIT. *J. Synchrotron Rad.* **2005**, *12*, 537-541.
43. Azoz, S.; Jiang, J.; Keskar, G.; McEnally, C.; Alkas, A.; Ren, F.; Marinkovic, N.; Haller, G. L.; Ismail-Beigi, S.; Pfefferle, L. D. Mechanism for strong binding of CdSe quantum dots to multiwall carbon nanotubes for solar energy harvesting. *Nanoscale* **2013**, *5*, 6893-6900.
44. Ernzerhof, M.; Scuseria, G. E. Assessment of the Perdew-Burke-Ernzerhof exchange-correlation functional. *J. Chem. Phys.* **1999**, *110*, 5029-5036.
45. Adamo, C.; Barone, V. Toward reliable density functional methods without adjustable parameters: The PBE0 model. *J. Chem. Phys.* **1999**, *110*, 6158-6170.
46. Rassolov, V. A.; Pople, J. A.; Ratner, M. A.; Windus, T. L. 6-31G* basis set for atoms K through Zn. *J. Chem. Phys.* **1998**, *109*, 1223-1229.
47. Prendergast, D.; Galli, G. X-ray absorption spectra of water from first principles calculations. *Phys. Rev. Lett.* **2006**, *96*, 215502.
48. Momma, K. I., F. VESTA 3 for three-dimensional visualization ofcrystal, volumetric and morphology data. *J. Appl. Cryst.* **2011**, *44*, 1272-1276.
49. Humphrey, W.; Dalke, A.; Schulten, K. VMD: Visual molecular dynamics. *J. Mol. Graphics* **1996**, *14*, 33-38.
50. Hanwell, M. D.; Curtis, D. E.; Lonie, D. C.; Vandermeersch, T.; Zurek, E.; Hutchison, G. R. Avogadro: an advanced semantic chemical editor, visualization, and analysis platform. *J. Cheminformatics* **2012**, *4*, 17-33.
51. Xu, Y. N.; Ching, W. Y. Electronic, Optical, and Structural-Properties of Some Wurtzite Crystals. *Phys. Rev. B* **1993**, *48*, 4335-4351.
52. Kasuya, A.; Sivamohan, R.; Barnakov, Y. A.; Dmitruk, I. M.; Nirasawa, T.; Romanyuk, V. R.; Kumar, V.; Mamykin, S. V.; Tohji, K.; Jeyadevan, B.; Shinoda, K.; Kudo, T.; Terasaki, O.; Liu, Z.; Belosludov, R. V.; Sundararajan, V.; Kawazoe, Y. Ultra-stable nanoparticles of CdSe revealed from mass spectrometry. *Nat. Mater.* **2004**, *3*, 99-102.

Chapter 3: Probing Differential Optical and Coverage Behavior in Nanotube-Nanocrystal Heterostructures Synthesized by Covalent versus Non-covalent Approaches

3.1. Introduction

In our group, we have successfully demonstrated not only a covalent but also an *in situ* route towards the site-selective synthesis of single-walled carbon nanotube (SWNT) and multiwalled carbon nanotube (MWNT) – nanoparticle-based conjugates containing two different types of nanoscale species, i.e. Au nanoparticles and CdSe/CdTe quantum dots (QDs).[1-4] Although *in situ* techniques can potentially achieve a higher level of control over spatial coverage as well as the degree of clustering of QDs onto the nanotubes (NTs), as-formed nanoparticles often lack homogeneity in terms of size and shape.[5] By contrast, chemical bonding protocols, such as covalent and non-covalent-inspired schemes, are inherently more flexible, since nanoparticles with desired shape, size, and morphology can in theory be pre-synthesized with excellent monodispersity prior to their attachment onto the NT templates. Nevertheless, the key point of our findings is that we have the synthetic capability of not only spatially controlling where we place our nanoparticles (e.g. ends versus sidewalls) but also their size, density, and numbers on the CNT surface. Recently, using covalent chemistry, we have quantitatively probed the effects of varying oxidation treatments, precursor concentrations, and incubation times in order to rationally affect the spatial coverage and distribution of either Au nanoparticles or semiconducting QDs on the MWNT sidewalls and tips.[6]

Moreover, in previous work, the formation of these heterostructures has consequences for their overall optical behavior. Specifically, we have found that the emission of CdSe QDs appears to be obviously quenched when bound covalently to the MWNT, suggesting a strong excited state interaction with the NTs. The featureless fluorescence signal for MWNT-CdSe conjugates is in agreement with prior literature on these types of heterostructures.[7, 8] That is, to

explain the observed emission quenching, the deactivation process of photo-excited CdSe nanoparticles can be attributed to an appreciable and rapid electron transfer and charge injection from the excited semiconductors into the MWNT platform.[9, 10] Specifically, photoinduced electrons upon illumination of CdSe formed electron-hole pairs which could then undergo a normal radiative recombination process. However, once MWNTs were brought into contact with these excited QDs, a non-radiative quenching process became competitive with the intrinsic radiative decay process, thereby resulting in the observed decrease in the PL intensity of the CdSe.[11] The quenching of the excitonic emission of QDs has also been previously observed in SWNT-QD composites by our group and many others,[4, 7, 8, 12, 13] especially when the nanotube and QD are in close spatial contact with one another. This phenomenon has been ascribed to the electron-acceptor behavior of SWNTs. That is, photoexcited electrons produced upon illumination of QDs can conceivably flow into SWNTs, nonradiatively, prior to their recombination with photogenerated holes in QDs. The overall point is that efficient charge separation and transport can be achieved in these nanoscale conjugate systems but needs to be more fully understood.

The question therefore we wish to address in this work is how to more precisely tune and potentially optimize that optical 'cross-talk', 'cross-communication', and interaction between the QD and the NT motif in a more deterministic and controlled way. The *first strategy* we have taken in this Chapter has been to use double-walled carbon nanotubes (DWNTs)[14, 15] as opposed to SWNTs. We recognize that the sp^2–hybridized structure of single nanotube sidewalls can be potentially destroyed during the oxidation treatment associated with their purification, a step which may result in a corresponding and unwanted decrease in the favorable electronic transport properties of the SWNTs that render them so appealing in the first place. By contrast, with

DWNTs, consisting of two coaxial single tubes, we can potentially and selectively functionalize only the outer walls so as to enable selective chemical attachment of quantum dots without necessarily damaging and degrading the inner tubes, a consequence of which is that one can envision possibly retaining the desired electronic properties of the overall material. For instance, it has been demonstrated that preferential functionalization of the outer wall of DWNTs has a much less profound influence upon their carrier transport ability as compared with the analogous functionalization of SWNTs.[16] Our group[17] has already shown that the synthesis of DWNT-CdSe QD heterostructures using a conventional covalent protocol mediated by 2-aminoethanethiol (AET) is not only possible but also that there is some degree of charge transfer from the CdSe QDs to DWNTs.

The *second strategy* we have employed in this Chapter is to consider alternatives to covalent attachment that do not necessarily depend on either high-temperature, *in situ*, electrodeposition, or reduction reactions. The approach that we have chosen in this Chapter is to immobilize our QDs onto the underlying NTs through non-covalent π-π stacking interactions, a process which takes advantage of the extended, delocalized conjugated π-electron system inherent to NTs. It is a method which has already been exploited by a number of groups, due to the simplicity, relative non-destructiveness, and effectiveness of this technique;[18-20] in essence, both the intrinsic morphology and electronic structure of the NTs tend to be preserved. In addition, the 'π-π stacking' method is attractive, because it may take as little as 10 minutes of sonication to complete, which is significantly more time-efficient and facile as compared with certain conventional covalent attachment approaches, which may involve as much as 1 day of vigorous stirring under zero illumination conditions to finalize.[6] More importantly, this noncovalent protocol may potentially mitigate for some of the deficiencies associated with

covalent attachment approaches, namely (i) the relatively low efficiency and degree of resulting chemical functionalization on the NT surface, (ii) the potentially unpredictable effect of such a treatment upon the electronic properties of the NTs, and (iii) the resulting non-uniform spatial distribution of QDs on the NT surface.[19] However, it has been reported[21] that heterostructures formed through the 'π-π stacking' approach are not necessarily stable over the long term, may be highly sensitive to the changes in pH and ionic strength, and can be difficult to tailor in terms of relative percentages of constituent QDs and NTs. Nonetheless, to highlight the feasibility of this approach for our particular experiments, an analogous SWNT-pyrene-CdTe heterostructure has been generated through this π-π stacking methodology; in terms of optical characterization, steady-state measurements and luminescence lifetimes were used to analyze the resulting charge transfer process.[20]

It is somewhat surprising that while these distinctive attachment approaches to create nanotube-based heterostructures have been known for years, there has not been any systematic effort (either qualitatively or quantitatively) to correlate morphology as well as the optical properties (and specifically the charge transfer behavior) of these composites with the corresponding chemical treatment process used to synthesize these composite materials in the first place. Therefore, in this Chapter, we aim to perform such a structure-property correlation by focusing on comparing morphology as well as the charge transfer behavior in DWNT-CdSe heterostructures created through the mediation of 4-aminothiophenol (4-ATP) as a linker, using complementary covalent and π-π stacking attachment approaches. 4-aminothiophenol (4-ATP) is relatively a short linker with a terminal –SH group with a strong affinity for CdSe QDs; the $–NH_2$ group at the other end of the molecule can be potentially utilized to initiate possible amide formation with acid-functionalized CNTs in order to covalently generate the desired

heterostructures. Conversely, the aryl ring within the 4-ATP molecule can also be exploited to initiate heterostructure formation through π-π stacking interactions with the nanotube sidewall. To highlight the potential of our work, we note that there have already been reports about the use of 4-ATP as a linker, specifically in the context of as-prepared graphene-4-ATP-CdSe heterostructures, which gave rise to effective PL quenching.[22]

The morphology and specifically the QD coverage density on the DWNT surface were characterized by transmission electron microscopy (TEM) in order to compare the relative attachment efficiency of the two protocols we have tested herein. In terms of charge transfer properties and to probe the optical behavior of heterostructures generated by different chemical strategies, photoluminescence measurements and quantum yield calculation were carried out. Meanwhile, in order to further confirm the charge transfer properties, Raman spectra of both constituent NTs and QDs as well as of the resulting heterostructures were obtained with a focus on analyzing and understanding relative changes in certain distinctive bands associated with both NTs and QDs. Specifically, the high-frequency Raman-active vibrations of sp^2 carbon are sensitive to chemical doping,[23] and there has been a concomitant increase in interest in studying the resonance Raman spectra of DWNTs, doped with electron donors and acceptors, with the hope and expectation of being able to modulate their electronic properties in a deterministic manner.[24-27] In particular, the tangential mode (TM) region of the Raman spectrum provides information about the metallicity of the tubes and even minute changes in these features are often induced by charge transfer between the dopants and the tubes themselves.[26,28] In this respect, in our work, for our heterostructures, we are treating our attached CdSe QDs as a ‘dopant’ for our DWNTs. Hence, our Raman measurements will enable us to better understand charge transfer in our as-prepared heterostructures as a function of their attachment chemistry.

3.2. Results and Discussion

3.2.1. Structural Characterization

Low magnification TEM data in Figure 3.1A highlights the formation of a heterostructure formed by covalent attachment with the mediation of DCC as a coupling agent. On the basis of statistical measurements of 20 distinctive and discrete as-formed heterostructures, QDs possessing an average diameter of 3.2 nm were clearly visible on the outer surfaces of our purified DWNT bundles. The corresponding average coverage density was found to be 88 ± 15 dots for DWNTs, measuring 1 μm in length and 40 nm in diameter for a typical bundle. This coverage density figure of CdSe QDs immobilized on the DWNT surface was estimated by dividing the total number of QDs attached onto the CNT surface by the corresponding length of the DWNTs in microns. However, the spatial coverage of QDs on DWNTs was non-uniform, an observation which could be attributed to the initial non-uniform precursor distribution of carboxylic functional groups on the outer surfaces of the DWNTs.

The corresponding HRTEM image in Figure 3.1B further confirmed the successful chemical conjugation of DWNTs with CdSe QDs. Lattice fringes associated with CdSe QDs as well as with the interface between the QDs and the DWNT surface were clearly discernible. Specifically, the measured 3.51 Å value corresponded to the *d*-spacing of the (002) lattice plane of the hexagonal CdSe, whereas the measured 3.41 Å spacing could be ascribed to the interlayer spacing of graphite layers within the DWNT themselves. The concentric rings in the SAED pattern in Figure 3.1C have been enumerated as 1 through 8, moving from the inner center to the outside rim, and these can likely be assigned to successive features associated with the (100) and (002) lattice planes of hexagonal CdSe, the (002) lattice plane of DWNTs, as well as the (101), (110), (103), (112), and (213) lattice planes of hexagonal CdSe, respectively.

Analogous TEM and HRTEM images of QDs immobilized onto DWNTs by non-covalent coupling are shown in Figure 3.1 D and E. In this case, the coverage density was calculated to be 1273 ± 70 dots for DWNT bundles, measuring 1 μm in length and 60 nm in diameter, a finding suggesting that substantially larger numbers of QDs could be attached onto DWNT surfaces with this non-covalent synthetic technique. Moreover, we noted a far more uniform nanoparticle coverage on the sidewalls of the DWNT bundles as compared with the covalent coupling approach. These cumulative observations can be explained by the fact that in a covalent reaction, QDs can be attached to DWNT practically only where the –COOH functional groups in DWNT are spatially located, whereas in the π-π stacking mechanism, QDs can be anchored essentially anywhere along the conjugated π system in the DWNTs.

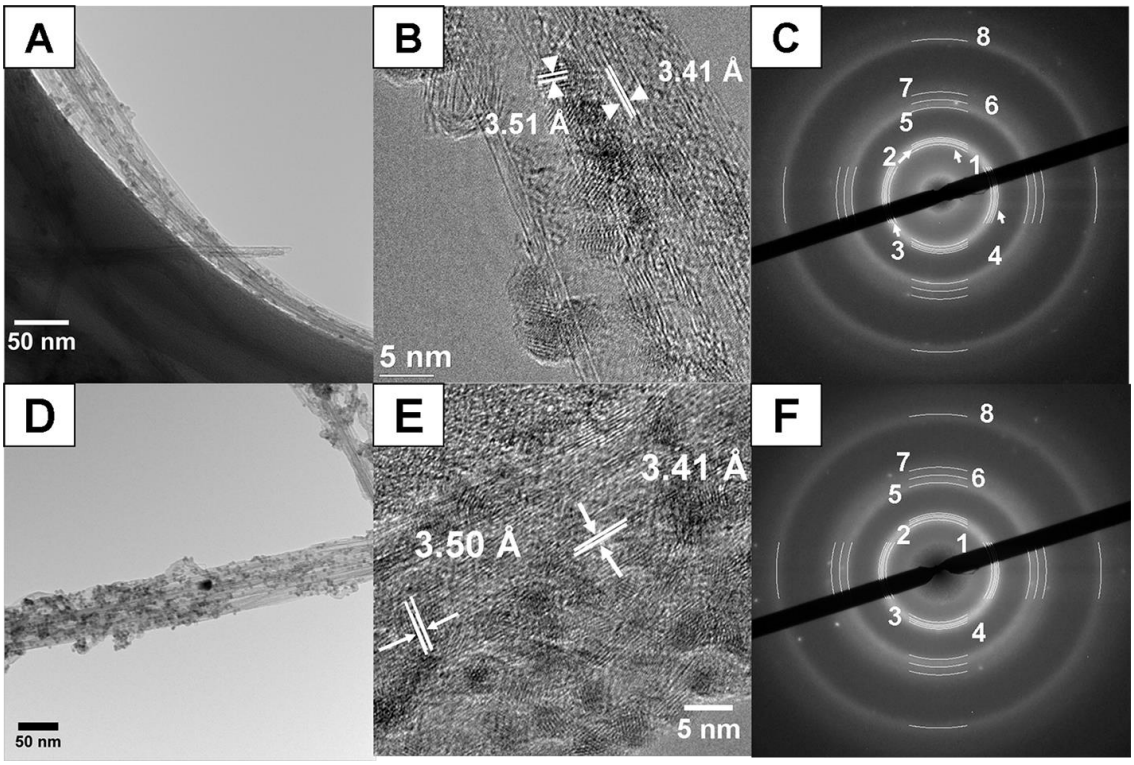

Figure 3.1. A, B, and C. TEM image, HRTEM image, and SAED pattern, respectively, of DWNT-4-ATP-CdSe heterostructures synthesized by covalent attachment. **D, E, and F.** Corresponding TEM image, HRTEM image, and SAED pattern, respectively, of DWNT-4-ATP-CdSe heterostructures fabricated through π-π stacking effects. (Reprinted with permission from *Dalton Trans.*, **2014**, *43*, 7480 – 7490. Copyright 2014 Royal Society of Chemistry.)

The *d*-spacings of 3.51 Å and 3.41 Å measured from Figure 3.1E were ascribed to the *d*-spacing of the (002) lattice plane of hexagonal CdSe as well as to the interlayer spacing of the graphite layer in DWNTs, respectively. The SAED pattern in Figure 1F highlighted similar results to what had been observed with covalently bound analogues. Specifically, the ring pattern from the inner core to the outside rim could be assigned to successive features associated with hexagonal CdSe (100) and (002), DWNT (002), as well as with hexagonal CdSe (101), (110), (103), (112), and (213) lattice planes, respectively. The morphologies of representative heterostructures generated using both covalent and non-covalent protocols were further probed and corroborated by atomic force microscopy (AFM) height images, shown in Figure 3.2. These data are suggestive of a slightly more uniform and homogeneous coverage of QDs on the surfaces of heterostructures produced non-covalently as compared with their covalently synthesized counterparts, a finding which is consistent with our TEM observations.

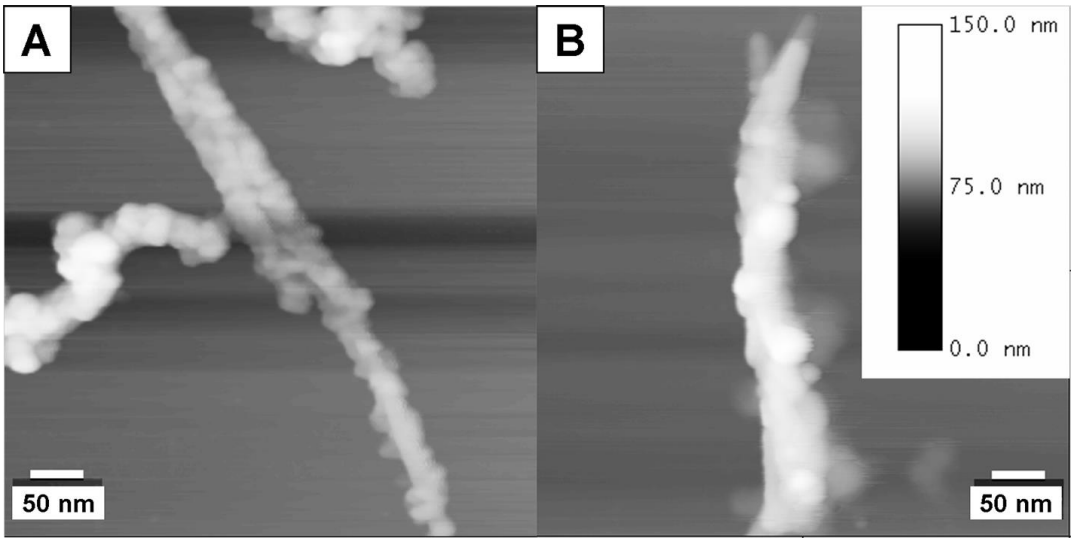

Figure 3.2. AFM height images (same z-scale), obtained in air of purified DWNT-4-ATP-CdSe heterostructures, derived using non-covalent (A) and covalent (B) methodologies. (Reprinted with permission from *Dalton Trans.*, **2014**, *43*, 7480 – 7490. Copyright 2014 Royal Society of Chemistry.)

In a non-covalent reaction process, the extended conjugated π system in DWNTs essentially reacts non-specifically with the phenyl rings of 4-ATP linkers immobilized on the surfaces of the QDs. We postulated therefore that an acid pre-treatment for DWNTs should not be a necessary pre-requisite for fabricating DWNT-QD heterostructures in a non-covalent manner. In order to prove that hypothesis, we substituted pristine DWNTs for their functionalized analogues in our work in order to directly attach QDs with the objective of creating our desired heterostructures. The TEM image (Figure 3.3B) illustrated a typical smaller DWNT bundle, possessing a diameter consistent with that of fewer bound individual constituent DWNTs, as compared with the larger DWNT bundles noted in Figure 3.3A. We note parenthetically that the number of individual DWNTs within a bundle is a function of the degree of chemical functionalization since greater quantities of oxygenated functional groups such as carboxylic acid moieties on the outer wall can facilitate nanotube aggregation and clumping; hence, purified DWNTs are associated with more tubes than their pristine counterparts.

The point is that after reaction with QDs, our pristine DWNTs were noted to be uniformly covered with CdSe QDs. The average coverage density was measured to be 437 ± 20 dots for a structure measuring 1 μm in length and 10 nm in diameter. This coverage density value was subsequently normalized to 2622 ± 120 dots for a 1-μm long, 60 nm diameter bundle, which represented over 2 times higher spatial coverage density as compared with the use of purified, functionalized DWNT analogues (i.e. 1273 ± 70 dots, as per Figure 3.1 analysis). This result can potentially be attributed to a higher degree of structural preservation in the extended conjugated carbon network in pristine DWNTs as compared with processed DWNTs. The implication therefore is that there is a higher quantity of available active sites present in pristine DWNTs for potential QD attachment through π-π stacking interactions.

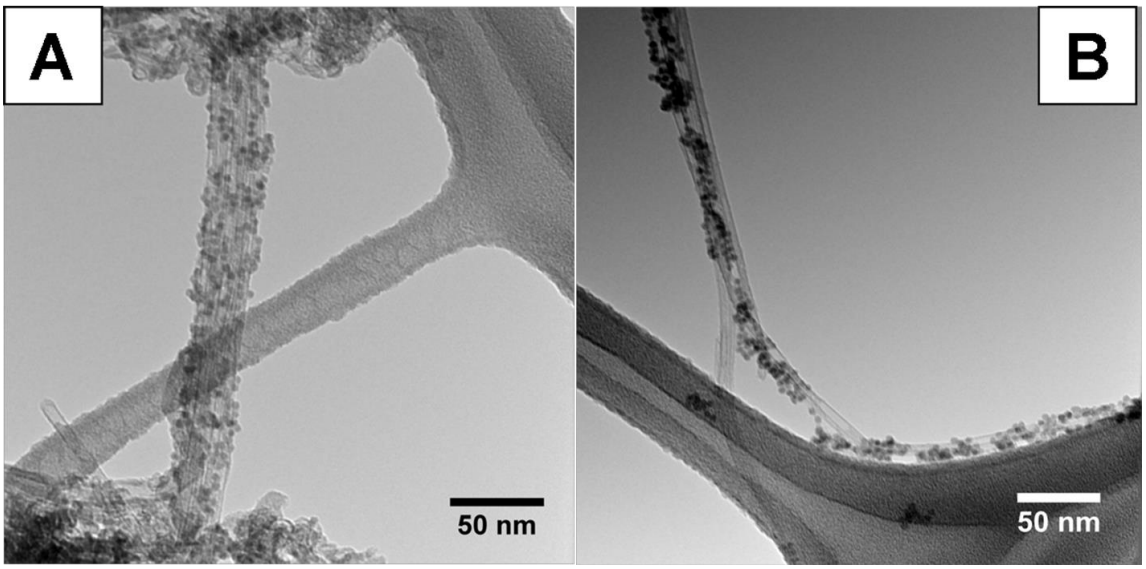

Figure 3.3. DWNT-4-ATP-CdSe heterostructures formed from π-π stacking effects, derived from purified (A) and pristine (B) DWNTs, respectively. (Reprinted with permission from *Dalton Trans.*, **2014**, *43*, 7480 – 7490. Copyright 2014 Royal Society of Chemistry.)

The IR spectra of pristine DWNTs, purified DWNTs, covalently-formed DWNT-ATP-CdSe heterostructures, and π-π stacking-derived purified DWNT-ATP-CdSe heterostructures are respectively shown in Figure 3.4. The major peak (feature 'a') located at 1700 cm^{-1} in Figure 3.4B can be assigned to the asymmetric stretching mode of carboxylic acid groups, which had been absent in the spectrum of the pristine DWNTs (Figure 3.4A), and its presence is suggestive evidence of a successful surface functionalization process. After the attachment of amine-terminated CdSe QDs to the purified DWNTs, the amide group appeared (features 'b' through 'd' in Figure 3.4C). Specifically, the peak at 1677 cm^{-1} could be ascribed to the C=O stretching mode of a secondary amide, whereas the peak at 1510 cm^{-1} could be assigned to the N-H bending stretch of a secondary amide as well. The peak at 1255 cm^{-1} might originate from the the C-N stretching from the unreacted ATP linker. No distinctive peaks or features were noteworthy in the IR spectrum of DWNT-ATP-CdSe QD heterostructures, synthesized non-covalently through π-π stacking interactions (Figure 3.4D).

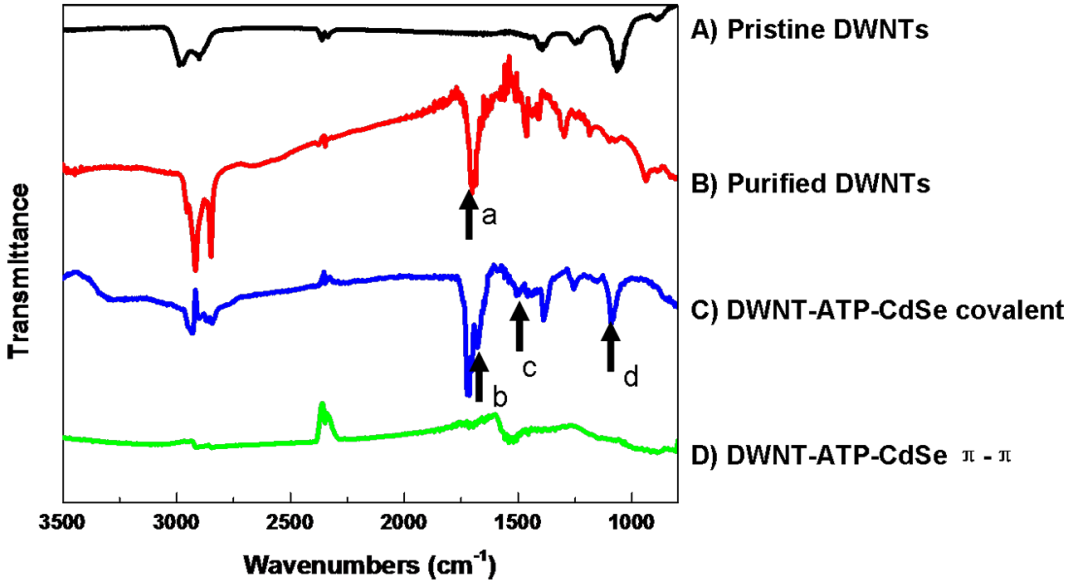

Figure 3.4. Infrared spectra of (A) pristine DWNTs, (B) purified DWNTs, (C) covalently-derived DWNT-4-ATP-CdSe QD heterostructures, and (D) non-covalently-derived DWNT-4-ATP-CdSe QD heterostructures. (Reprinted with permission from *Dalton Trans.*, **2014**, *43*, 7480 – 7490. Copyright 2014 Royal Society of Chemistry.)

3.2.2. Optical Characterization

To probe the optical properties of different types of DWNT-4-ATP-CdSe QD heterostructures, UV-visible and photoluminescence (PL) spectra were collected in Figure 3.5. The UV-Vis spectra (black curves in Figure 3.5) indicate the presence of CdSe on the DWNTs. The first exciton feature is present in all extinction spectra, with the feature appearing at 570 nm in as-prepared CdSe(A) and ATP-CdSe (B). The extinction spectra from the heterostructure materials are prominently show non-resonant scattering from all DWNT species and resonant absorption of metallic DWNTs, potentially resulting in less photons being absorbed by the 4-ATP-CdSe QDs themselves and therefore less overall signal, leading to a masking and shifting of the CdSe band edge features 565 nm (C), 567 nm (D), and 571 nm (E).

Moreover, another factor is that the CdSe QD concentration likely decreased in the final, resulting, as-prepared composites, with the implication that the measured signal would therefore became less featured.

Even with elevated concentrations the emission intensity was quite low (red curves in Figure 3.5). Calculating the PL QY value validated that indeed the emission efficiency had been reduced for the PL of the ligand exchanged dots but the most severely reduced in the heterostructure systems. Despite the exceedingly low values, the lower limit of detection for our system coupled with longer integration times, allowed us to obtain the following PL quantum yield (QY) values in order from highest to lowest PL QY: (A) 28.333% (± 0.2) (as-prepared CdSe), (B) 0.0185% (± 2E-4) (ATP-CdSe), (C) 0.0023% (± 2E-5) (pristine DWNT-ATP-CdSe using π-π stacking method), (E) 0.0014% (±8E-6) (purified DWNT-ATP-CdSe using covalent method), and (D) 0.0009% (±6E-6) (purified DWNT-ATP-CdSe using π-π stacking method). This order indicates that functionalization of the DWNT promotes additional PL quenching and indicates more efficient quenching for (E) and (D) than for (C) with the most efficient charge transfer being attained for the functionalized π-π stacking method. Another signature of the efficient electronic coupling is the absence of the deep trap emission (730 nm in ATP-CdSe) for the heterostructure samples indicating charges are successfully transferred to the DWNT instead of being trapped.

The high-energy (roughly 500 nm) emission seen in Figure 3.5(C), is consistent with previous observations of hot carrier emission being prominent in time integrated emission spectra under conditions of efficient energy transfer in QD-NT heterostructures[29]. The loss of deep trap emission at 730 nm and absence of band edge recombination is characteristic of ultrafast electronic interactions. In the absence of covalent interactions which lead to efficient

carrier trapping, it is reasonable to assume that energy transfer will dominate. We note that Figure 3.5(D) and 3.5(E) display distinct emission spectra from (C), despite similar levels of PL quenching. It is likely that the introduction of surface states via functionalization of the DWNTs (D) and covalent attachment (E) leads to a different mechanism for charge transfer.

The differences between the covalent and π-π methods of the acid functionalized DWNT heterostructures, while minor, can attributed to the distance dependence of charge and energy transfer interactions, resulting in slightly improved charge transfer efficiency (slightly lower PL QY) for a sample with decreased distance for charges to travel.

The lifetime data for the ligand exchanged/heterostructure samples was dominated by the instrument response function, not enough photons could be detected under this excitation wavelength, which is consistent with significantly decreased PL QY. For CdSe quantum dots with charge trapping ligands on the surface and little-to-no trap emission this extremely shortened PL lifetime is expected. [29-32]

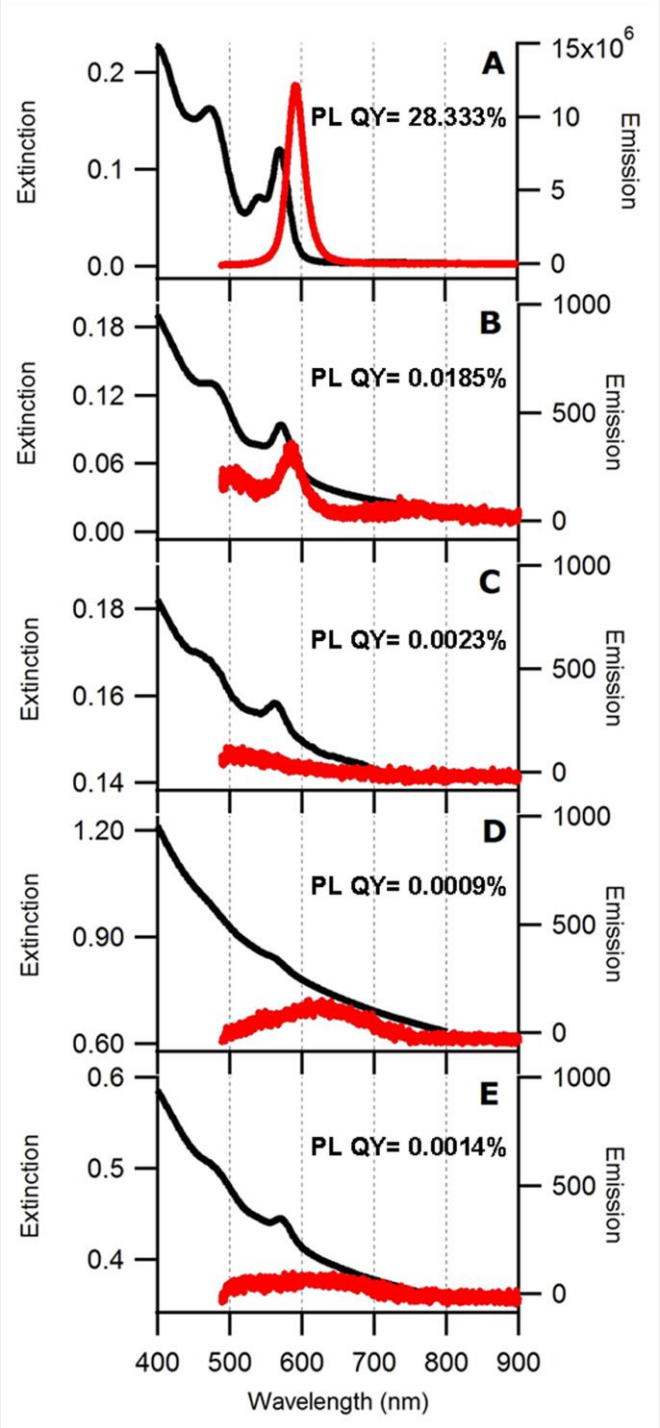

Figure 3.5 Extinction and Emission spectra for As-prepared CdSe (A), 4-ATP-CdSe (B), pristine DWNT-ATP-CdSe generated by noncovalent method (C), purified DWNT-ATP-CdSe derived from non-covalent method (D), and covalent method (E). All emission spectra were obtained by exciting the samples at 415 nm. The extinction spectra in (C) – (E) are offset by a roughly constant non-resonant scattering background due to the presence of DWNTs. (Reprinted with permission from *Dalton Trans.*, **2014**, *43*, 7480 – 7490. Copyright 2014 Royal Society of Chemistry.)

The Raman spectra for (i) DWNTs, (ii) as-prepared CdSe QDs, as well as (iii) DWNT-CdSe heterostructures synthesized by both covalent and non-covalent (π-π stacking) means are shown in Figure 3.6 and Figure 3.7. All samples have been excited at energies of 2.41 eV (Figure 3.6) and 1.58 eV (Figure 3.7), respectively. Specifically, the spectra associated with pristine and purified DWNTs were displayed in Figure 3.6A. The intensity ratio of the D band near 1340 cm^{-1} to the tangential mode (G band) near 1580 cm^{-1} (I_D/I_G) dramatically increases after the purification process (i.e. I_D/I_G = 0.04 for pristine DWNTs and 0.50 for purified DWNTs). The increase in the I_D/I_G ratio due to the purification process is understandable, since the increased peak intensity of D band is typically attributed to damage and distortion of the conjugated sp^2 carbon lattice, as well as to the presence of amorphous carbon[33] and other symmetry-breaking defects in the DWNTs generated during the oxidation and concomitant surface functionalization of DWNTs (i.e., formation of –COOH and other oxygenated species on the surfaces of our tubes).[34, 35] The Raman spectra (Figure 3.6B) of CdSe dots anchored onto the sidewalls of pristine DWNTs by non-covalent π-π stacking interactions were broadly similar to that of pristine DWNTs themselves, thereby suggesting that the inherent electronic structures of pristine DWNTs were likely preserved to a large extent by this relatively non-destructive protocol. Similar phenomena in terms of a lack of shift or distortion in G peaks after non-covalent attachment were observed in SWNTs modified with pyridine-coated QDs.[18]

The tangential modes (G bands) of purified DWNT-4-ATP-CdSe composite heterostructures synthesized by covalent and π-π stacking methods together with their starting analogues are collectively displayed in Figure 3.6C. The asymmetry of the lines shapes of certain peaks, i.e. G^- peaks, in our data is consistent with the idea that metallic tubes are being excited at 2.41 eV. Each individual G band was interpreted as being composed of a convolution of 4

Gaussian and Lorentzian functions (i.e. the dashed curves). For the purified DWNTs, the peak at 1580 cm^{-1} is associated with the A_1 tangential G^+ mode for the inner tubes, while the peak located at the higher frequency, i.e. 1605 cm^{-1}, can be ascribed to the unresolved A_1 and E_1 tangential G^+ modes for the outer tubes.[36] It has been reported in previous literature that shifts of the G band are opposite for *n*-and *p*-doping of DWNTs;[37] for example, the G-band of nitrogen-doped DWNTs often appears at a lower frequency as compared with undoped DWNTs, whereas the G band of boron-doped DWNTs appears at a higher frequency.[38]

In our case, the peak of the G band in our DWNT-ATP-CdSe heterostructures formed by covalent chemistry was up-shifted by 4 cm^{-1} to 1583 cm^{-1} as compared with purified DWNTs (1579 cm^{-1}). This up-shift of the G band position through covalent QD attachment onto the DWNTs can potentially be attributed to a photoinduced hole transfer from CdSe QDs to the DWNT (or conversely electron transfer from the DWNTs to the CdSe acceptor, resulting in a depletion in the occupation of electron states from the nanotube valence bands as the Fermi level is lowered)[28] through the ATP linker. The hole transfer process results in an effective shortening of the C-C bond distance and therefore, a stiffening of the G mode.[39] A similar explanation has also been noted to explain the peak shift of the G band in Br_2-doped DWNT systems, wherein the observed up-shift of the G band intensity in the Raman spectra appeared, due to electron transfer from the CNTs to Br_2, leaving holes on the CNTs.[27] Analogous G band upshifts have also been observed in thiolation reactions of DWNTs.[40]

By contrast with the heterostructure synthesized by covalent means, the G band of QDs attached to DWNTs by π-π interactions gave rise to a downshift to 1576 cm^{-1}. One possible explanation for this observation could be the injection of excess charge carriers from the linker molecule present, coating the QDs. More specifically, we observed that the G band of 4-ATP-

linked DWNTs (i.e. nanotubes functionalized with ligands only) was down-shifted 11 cm^{-1} to 1568 cm^{-1} as compared with that of purified DWNTs (i.e. 1579 cm^{-1}), as shown in Figure 3.6C. The ligand, 4-ATP, possesses a strong electron donating group (i.e. $-NH_2$ connected to the phenyl ring),[41] which allows for an increase of the electron density in the carbon nanotube backbone and a corresponding expansion in the C-C bond distance associated with a G band downshift.[38] As compared with the G band of 4-ATP-capped DWNTs (i.e. 1568 cm^{-1}) alone, the G band associated with the subsequent addition of CdSe, i.e. CdSe-4-ATP-DWNT heterostructures, created by π-π stacking interactions, is located at 1576 cm^{-1} and is upshifted by 8 cm^{-1}, indicating that the photoinduced holes from the CdSe QDs are indeed still being transferred to DWNTs. That is, this hole transfer process from the CdSe to the DWNTs compensates to some degree for the primary countervailing down-shift phenomenon associated with the ATP linker itself.

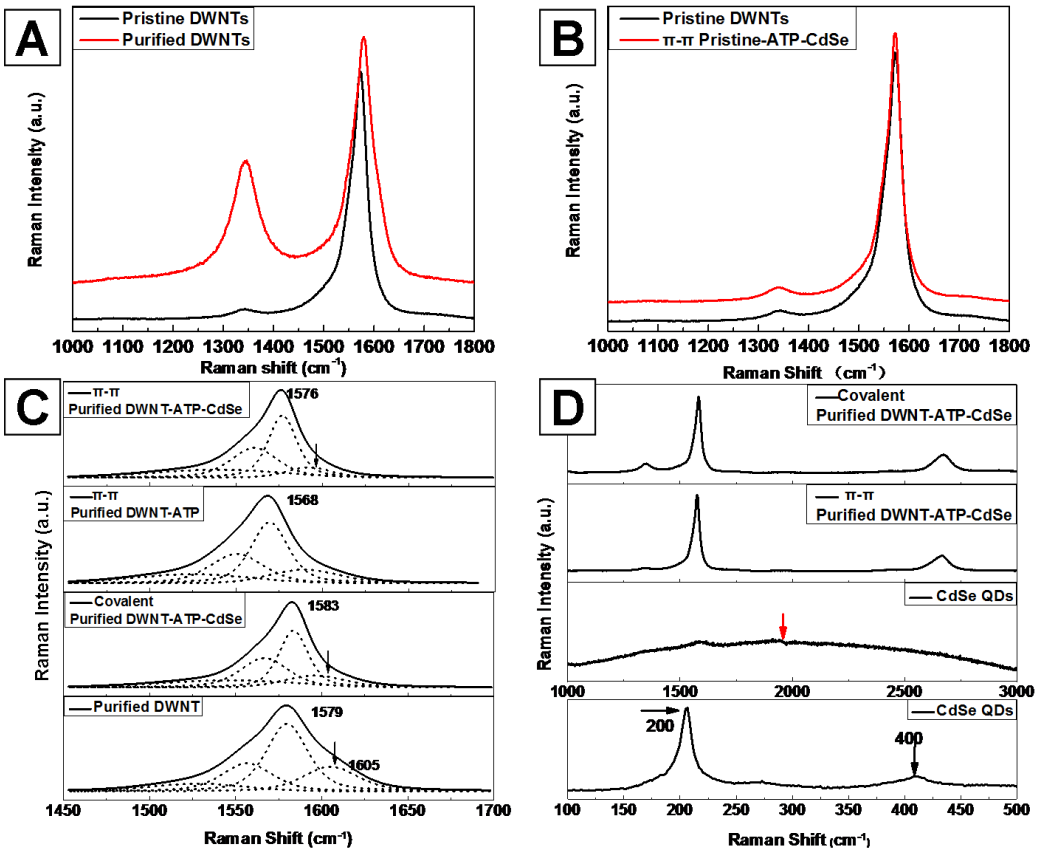

Figure 3.6. Raman spectra measured at an excitation wavelength of 514 nm (2.41 eV) of (A) pristine and purified DWNTs, (B) pristine DWNT as well as pristine DWNT-4-ATP-CdSe heterostructures, generated by non-covalent π-π stacking, (C) G-band analysis of purified DWNT-4-ATP-CdSe heterostructures, derived both covalently and non-covalently, as well as of purified DWNTs. (D) D and G band regions of purified DWNT-4-ATP-CdSe heterostructures, derived using covalent and non-covalent methods. Raman profile of as-prepared CdSe QDs. (Reprinted with permission from *Dalton Trans.*, **2014**, *43*, 7480 – 7490. Copyright 2014 Royal Society of Chemistry.)

Hence, as compared with the relevant control samples, the observed Raman upshifts associated with heterostructures generated both covalently and non-covalently provide evidence for a charge transfer process occurring between CdSe QDs and DWNTs. Though we emphasize that our results are merely suggestive, we did indeed observe a larger upshift of the G band with heterostructures fabricated by π-π stacking interactions (i.e. 8 cm^{-1} upshift) as compared with their counterparts produced by covalent binding (i.e. 4 cm^{-1} upshift), implying a more efficient

charge transfer process[42] in the non-covalently generated composite. This observation could be attributed in part to the order-of-magnitude higher coverage densities of QDs noted in heterostructures created using non-covalent (i.e. 1000s of particles) versus covalent (i.e. 100s of particles) protocols.

This Raman study about charge transfer properties further supported the aforementioned QY yield comparison with non-covalently derived heterostructures maintaining a lower QY, which also indicated a more efficient transfer process happening in this system as compared with its covalent counterparts. Nevertheless, an evident decrease in the intensity of the G^+ peak for outer tubes (near 1605 cm^{-1}) was observed in heterostructures generated by both chemical methodologies as compared with purified DWNTs alone (see arrows in Figure 3.6C), providing for additional evidence of 'charge flow' between the nanotube and the proximal QDs.[43]

A comparison between unbound CdSe QDs and the corresponding CdSe-DWNT heterostructures is shown in Figure 3.6D. From the CdSe QD spectrum, two discernible peaks (bottom figure) attributed to the longitudinal optical phonon mode (1-LO) and its overtone (2-LO) of the CdSe QDs core are clearly visible in the region of 200 cm^{-1} and 400 cm^{-1}, respectively.[44,45] The broad peak in the region spanning from 1000 cm^{-1} to 3000 cm^{-1} likely corresponds to the fluorescence peak of CdSe QDs due to photoexcitation. The disappearance of this distinctive broad peak after CdSe QD attachment onto the DWNT template surface suggests that the charge transfer process takes place in both non-covalently and covalently-derived heterostructures. This result is consistent with what has been previously observed with pyridine-capped QDs self-assembled onto individual SWNTs.[19]

By means of comparison, Raman spectra of the aforementioned samples were also collected and measured at 785 nm (1.58 eV), and these data are shown in Figure 3.7.

Specifically, spectra associated with pristine and purified DWNTs (Figure 3.7A) are similar to the analogous results measured at 514 nm (Figure 3.6A) with a perceptible increase in the I_D/I_G ratio after the acid treatment process (i.e. I_D/I_G = 0.04 for pristine DWNTs and 0.11 for the corresponding purified DWNTs). In order to probe the potential for charge transfer in these systems, the G band was studied prior to and after 'doping' with CdSe QDs at an excitation wavelength of 785 nm. Our G band profiles obtained at this particular wavelength appeared to be mainly associated with semiconducting nanotubes, based on the line shape, and are likely strongly influenced by small diameter inner semiconducting tubes [27, 46] It is interesting to note that unlike at 514 nm excitation, we did not observe any appreciable shift in the positions of the Raman peaks at 785 nm excitation for all of the heterostructures analyzed (Figure 3.7B and C) upon CdSe QD attachment, using either noncovalent or covalent strategies.

We attribute the absence of shifts in the G bands noted at 785 nm excitation to either the total absence of or very minimal charge transfer, which could possibly have occurred for the following two reasons. First, shielding of the semiconducting inner tubes by the outer metallic tubes may have resulted in a very weak interaction between the inner semiconducting tubes and the attached CdSe QD 'dopants' and hence, a correspondingly smaller charge transfer effect between the two. That is, the inner semiconducting tubes are in stronger resonance and more prominent at this wavelength, and this fact contributes more to the observed line shape profile as opposed to any more nuanced charge transfer effect.[46] Second, the Raman spectrum of unbound CdSe QDs at 785 nm (Figure 3.7D) gave rise to a substantially noisier profile as compared with the results obtained at 514 nm (Figure 3.6D). Only a longitudinal optical phonon mode (1-LO) was clearly visible in the region of 200 cm^{-1}. No obvious fluorescence peak in the 1000-3000 cm^{-1} range was visible in the spectrum. These observations are not surprising, considering that

excitation either at 785 nm or at 1.58 eV represents an energy level which was far below the energy level necessary for CdSe QDs to become photoexcited (Figure 3.5). Hence, the intrinsically low probability of finding charge carriers at 785 nm would have contributed to low charge transfer observed. By contrast, at 514 nm, our observation of charge transfer was likely due in part to photoexcitation of CdSe QDs.

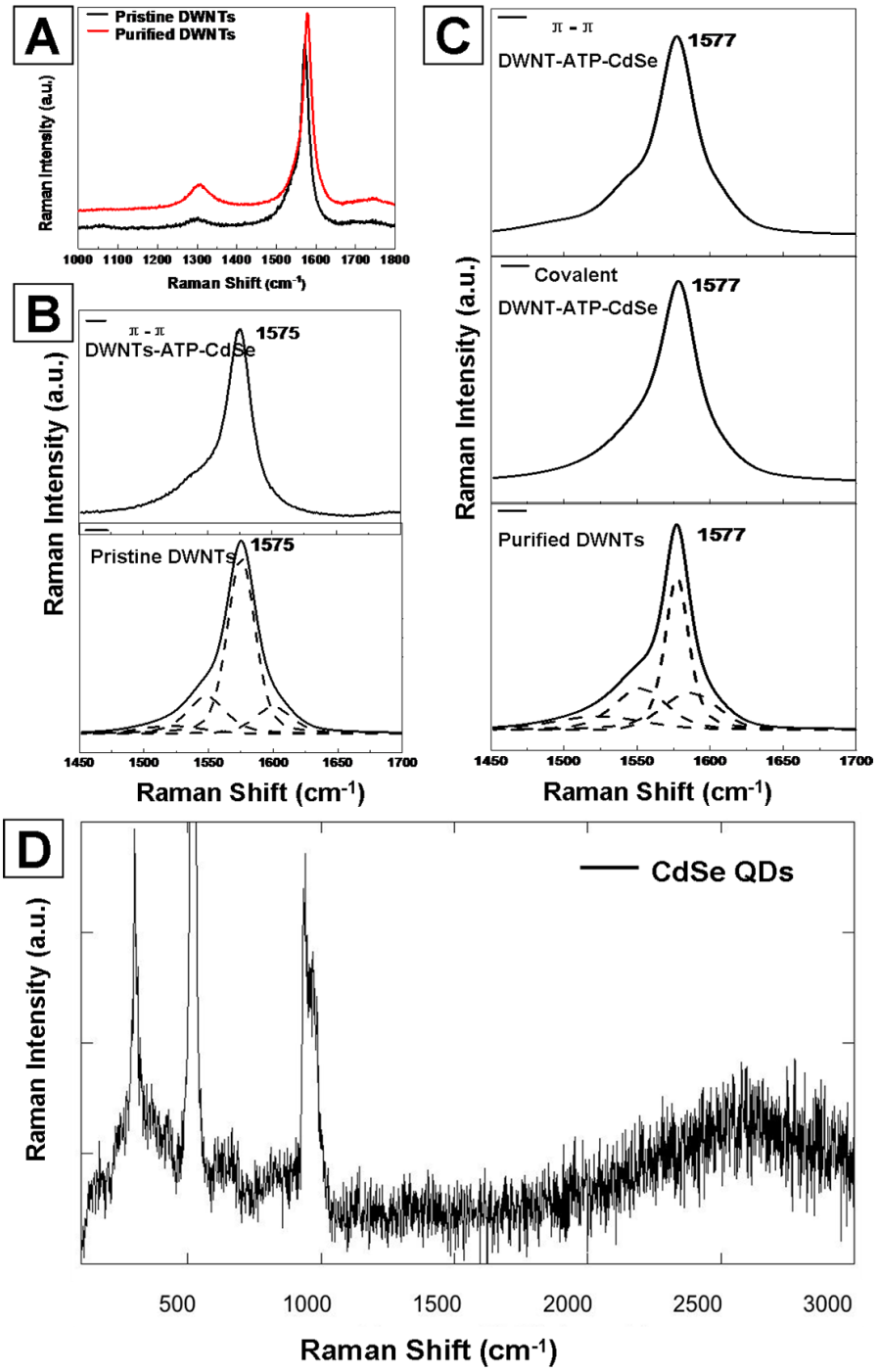

Figure 3.7. Raman spectra measured at an excitation wavelength of 785 nm (1.58 eV) of (A) pristine and purified DWNTs, (B) G band analysis of pristine DWNT as well as pristine DWNT-4-ATP-CdSe heterostructures, generated by non-covalent π-π stacking, (C) G-band analysis of purified DWNT-4-ATP-CdSe heterostructures, derived both covalently and non-covalently, as well as of purified DWNTs.(D) Raman profile of as-prepared CdSe QDs. (Reprinted with permission from *Dalton Trans.*, **2014**, *43*, 7480 – 7490. Copyright 2014 Royal Society of Chemistry.)

3.3. Conclusions

In this manuscript, DWNT-4-ATP-CdSe heterostructures have been successfully synthesized by both covalent and non-covalent attachment approaches, as confirmed by AFM height images. TEM and HRTEM images indicated that the non-covalent attachment was quantitatively more efficient in terms of coverage density of CdSe QDs on the DWNT surface. Furthermore, the non-covalent method is significantly more time-efficient and facile as compared with analogous covalent attachment approaches. Moreover, the non-covalent π-π stacking method can be carried using pristine DWNTs without additional surface functionalization, an experimental possibility which can preserve the inherent electronic structure of DWNTs. Further investigation of PL quantum yield and Raman spectra suggests that both covalent and non-covalent attachments of 4-ATP-functionalized CdSe QDs lead to observable charge transfer behavior with the latter non-covalent protocols appearing to be more efficient, possibly due to the resulting higher coverage density of discrete QDs on the DWNT surface.

3.4. References

1. S. Banerjee and S. S. Wong, *Nano Lett.*, 2002, **2**, 195-200.
2. S. Banerjee and S. S. Wong, *J. Am. Chem. Soc*, 2003, **125**, 10342-10350.
3. S. Banerjee and S. S. Wong, *Adv. Mater.*, 2004, **16**, 34-37.
4. S. Banerjee and S. S. Wong, *Chem. Commun.*, 2004, **(16)**, 1866-1867.
5. C. Schulz-Drost, V. Sgobba, C. Gerhards, S. Leubner, R. M. K. Calderon, A. Ruland and D. M. Guldi, *Angew. Chem. Int. Ed.*, 2010, **49**, 6425-6429.
6. X. Peng and S. S. Wong, *Chem. Mater.*, 2009, **21**, 682-694.
7. I. Robel, B. A. Bunker and P. V. Kamat, *Adv. Mater.*, 2005, **17**, 2458-2463.
8. N. Cho, K. R. Choudhury, R. B. Thapa, Y. Sahoo, T. Ohulchanskyy, A. N. Cartwright, K. S. Lee and P. N. Prasad, *Adv. Mater.*, 2007, **19**, 232-236.
9. A. Kongkanand, R. M. Dominguez and P. V. Kamat, *Nano Lett*, 2007, **7**, 676-680.
10. F. Vietmeyer, B. Seger and P. V. Kamat, *Adv. Mater.*, 2007, **19**, 2935-2940.
11. M. Olek, T. Busgen, M. Hilgendorff and M. Giersig, *J. Phys. Chem. B*, 2006, **110**, 12901-12904.
12. S. Banerjee and S. S. Wong, *Adv. Mater.*, 2004, **16**, 34-37.
13. V. Biju, T. Itoh, Y. Baba and M. Ishikawa, *J. Phys. Chem. B*, 2006, **110**, 26068-26074.

14. Y. Tison, C. E. Giusca, V. Stolojan, Y. Hayashi and S. R. P. Silva, *Adv. Mater.*, 2008, **20**, 189.
15. A. Hashimoto, K. Suenaga, K. Urita, T. Shimada, T. Sugai, S. Bandow, H. Shinohara and S. Iijima, *Phys. Rev. Lett.*, 2005, **94**, 45504.
16. D. Bouilly, J. Cabana, F. Meunier, M. Desjardins-Carriere, F. Lapointe, P. Gagnon, F. L. Larouche, E. Adam, M. Paillet and R. Martel, *ACS Nano*, 2011, **5**, 4927-4934.
17. X. Peng, M. Y. Sfeir, F. Zhang, J. A. Misewich and S. S. Wong, *J. Phys. Chem. C* 2010, **114**, 8766-8733.
18. S. Jeong, H. C. Shim, S. Kim and C. S. Han, *ACS Nano*, 2010, **4**, 324-330.
19. Q. Li, B. Sun, I. A. Kinloch, D. Zhi, H. Sirringhaus and A. H. Windle, *Chem. Mater.*, 2005, **18**, 164-168.
20. C. Schulz-Drost, V. Sgobba, C. Gerhards, S. Leubner, R. M. Krick Calderon, A. Ruland and D. M. Guldi, *Angew. Chem. Int. Ed.*, 2010, **49**, 6425-6429.
21. R. J. Williams, M. Lipowska, G. Patonay and L. Strekowski, *Anal. Chem.*, 1993, **65**, 601-605.
22. J. Debgupta and V. K. Pillai, *Nanoscale*, 2013, **5**, 3615-3619.
23. G. G. Chen, S. Bandow, E. R. Margine, C. Nisoli, A. N. Kolmogorov, V. H. Crespi, R. Gupta, G. U. Sumanasekera, S. Iijima and P. C. Eklund, *Phys. Rev. Lett.*, 2003, **90**, 257403.
24. G. M. do Nascimento, T. Hou, Y. A. Kim, H. Muramatsu, T. Hayashi, M. Endo, N. Akuzawa and M. S. Dresselhaus, *Nano Lett.*, 2008, **8**, 4168-4172.
25. G. M. do Nascimento, T. Hou, Y. A. Kim, H. Muramatsu, T. Hayashi, M. Endo, N. Akuzawa and M. S. Dresselhaus, *J. Phys. Chem. C* 2009, **113**, 3934-3938.
26. J. Cambedouzou, J. L. Sauvajol, A. Rahmani, E. Flahaut, A. Peigney and C. Laurent, *Phys. Rev. B*, 2004, **69**, 235422.
27. G. M. do Nascimento, T. Hou, Y. A. Kim, H. Muramatsu, T. Hayashi, M. Endo, N. Akuzawa and M. S. Dresselhaus, *Carbon*, 2011, **49**, 3585-3596.
28. A. G. Souza, M. Endo, H. Muramatsu, T. Hayashi, Y. A. Kim, E. B. Barros, N. Akuzawa, G. G. Samsonidze, R. Saito and M. S. Dresselhaus, *Phys. Rev. B* , 2006, **73**, 235413.
29. A. J. Akey, C. G. Lu, L. J. Wu, Y. M. Zhu and I. P. Herman, *Phys. Rev. B*, 2012, **85**.
30. P. Guyot-Sionnest, B. Wehrenberg and D. Yu, *J. Chem. Phys.*, 2005, **123**.
31. X. Y. Wang, L. H. Qu, J. Y. Zhang, X. G. Peng and M. Xiao, *Nano Lett.*, 2003, **3**, 1103-1106.
32. X. H. Peng, J. A. Misewich, S. S. Wong and M. Y. Sfeir, *Nano Lett.*, 2011, **11**, 4562-4568.
33. S. Osswald, E. Flauhaut, H. Ye and Y. Gogotsi, *Chem. Phys. Lett.*, 2005, **402**, 422-427.
34. J. Gyeong Bok, M. Yoon, J. Park, M. Inhee and S. Joo-Hiuk, in 34th International Conference on Infrared, Millimeter, and Terahertz Waves, Busan, Sept. 21–25, 2009, pp. 1–2.
35. S. Campidelli, C. Sooambar, E. Lozano Diz, C. Ehli, D. M. Guldi and M. Prato, *J Am Chem Soc*, 2006, **128**, 12544-12552.
36. A. Rahmani, J. L. Sauvajol, S. Rols and C. Benoit, *Phys. Rev. B*, 2002, **66**.
37. L. S. Panchakarla, A. Govindaraj and C. N. R. Rao, *ACS Nano*, 2007, **1**, 494-500.
38. L. S. Panchakarla, A. Govindaraj and C. N. R. Rao, *Inorg. Chim. Acta.*, 2010, **363**, 4163-4174.

39. M. T. Martinez, M. A. Callejas, A. M. Benito, M. Cochet, T. Seeger, A. Anson, J. Schreiber, C. Gordon, C. Marhic, O. Chauvet, J. L. G. Fierro and W. Maser, *Carbon*, 2003, **41**, 2247-2256.
40. A. V. Ellis and A. Bubendorfer, *Chem. Phys. Lett.*, 2005, **412**, 449-453.
41. J. Kong and H. Dai, *J. Phys. Chem. B*, 2001, **105**, 2890-2893.
42. G. M. do Nascimento, T. Hou, Y. A. Kim, H. Muramatsu, T. Hayashi, M. Endo, N. Akuzawa and M. S. Dresselhaus, *Nano Lett.*, 2008, **8**, 4168-4172.
43. G. G. Chen, S. Bandow, E. R. Margine, C. Nisoli, A. N. Kolmogorov, V. H. Crespi, R. Gupta, G. U. Sumanasekera, S. Iijima and P. C. Eklund, *Phys. Rev. Lett.*, 2003, **90**.
44. X. Li, Y. Jia and A. Cao, *ACS Nano*, 2009, **4**, 506-512.
45. A. V. Baranov, Y. P. Rakovich, J. F. Donegan, T. S. Perova, R. A. Moore, D. V. Talapin, A. L. Rogach, Y. Masumoto and I. Nabiev, *Phys. Rev. B*, 2003, **68**, 165306.
46. A. G. Souza, M. Endo, H. Muramatsu, T. Hayashi, Y. A. Kim, E. B. Barros, N. Akuzawa, G. G. Samsonidze, R. Saito and M. S. Dresselhaus, *Phys. Rev. B*, 2006, **73,** 235413.

Chapter 4: Probing the Dependence of Electron Transfer on Size and Coverage in Carbon Nanotube−Quantum Dot Heterostructures

4.1. Introduction

Carbon nanotube (CNT) - quantum dot (QD) heterostructures, which merge the favorable charge transport properties of CNTs with the interesting size-tunable optoelectronic properties of QDs into an integrated whole, represent not only a conceptually unusual architectural paradigm but also a practically functional nanocomposite in the field of photovoltaic cells.[1-5] In our group, we have successfully demonstrated various synthetic methods including but not limited to covalent attachment, π-π stacking, as well as an *in situ* route towards the simple, site-selective, and coverage-controllable synthesis of single-walled carbon nanotube (SWNT), double-walled carbon nanotube (DWNT), and multiwalled carbon nanotube (MWNT) - CdSe/CdTe quantum dot (QD) conjugates.[6-8]

In this thesis, we have specifically chosen to use DWNTs as opposed to SWNTs. One rationale is that the acid purification process developed to remove the metal catalysts and amorphous carbon impurities from the pristine carbon nanotubes often involves the breaking of the sp^2 structure of the nanotube sidewall, thereby diminishing the attractive electronic transport characteristics we seek to exploit when utilizing SWNTs. Moreover, with DWNTs, consisting of two coaxial tubules, we can selectively functionalize the outer tube while retaining the desirable electronic properties of the inner tube.[1]

Nevertheless, the crucial step in understanding the nature of QD-based photovoltaic cells involves control over the effective interfacial charge transfer, which is often inefficient due to the spatial confinement of the electron and the hole to the interior of the QDs as well as to the unavoidable recombination process caused by the Coulombic interaction.[9] This issue can be

potentially tackled by rational chemical design. Specifically, by properly choosing linker molecules and the subsequent chemical modification of the external surfaces of these QDs through a ligand exchange reaction in order to passivate surface defects, we can do much towards controlling surface-related emission and reducing recombination losses.[10] In fact, the fabrication of conductive QD films for optimum operation within a solar cell regime often relies on replacing the long alkyl ligands used in colloidal QD synthesis with short organic bidentate linkers, such as either ethanedithiol or mercaptopropionic acid (MPA), for instance.[11, 12 13] These specific short bidentate linkers not only reduce the interdot separation to less than the carrier tunneling distance, thereby facilitating exciton dissociation and enabling carrier transport towards the collecting contacts[14, 15] but also serve as a bridge with which to connect QDs with CNTs through either covalent or non-covalent attachment strategies.[6, 16]

The specific linker molecule we have deliberately chosen here is 4-mercaptophenol (MTH) with the terminal thiol –SH group, possessing a strong affinity for Cd sites on the QD surface. The presence of the aromatic aryl ring moiety within the MTH molecule can be manipulated in order to initiate heterostructure formation through facile non-covalent π-π stacking interactions with the CNT sidewalls. It has been previously reported that the presence of thiol functional groups within MTH can serve as 'hole – scavengers' and thereby act as effective acceptors for photogenerated holes from the CdSe QDs. These photogenerated holes from CdSe can efficiently convert thiols into disulfides by means of a photocatalytic reaction. [17, 18]

Due to the conduction band alignment of CdSe QDs with either adjacent DWNTs or metal oxides, interfacial electron transfer has been extensively studied.[19, 20] Specifically, Hines *et al.* have reported on electron tunneling from CdSe to TiO_2, a process facilitated by various thiol linkers, which possessed higher LUMO levels as compared with both QDs and TiO_2 and which

served as energy barriers.[21] Additional examples exist. For example, Weaver *et al.* investigated the photoinduced electron and hole transfer within a complex nanocomposite, consisting of CNTs, thiol derivatives of perylene compounds, and CdSe QDs.[22] Herein, in our experiments, due to the presence of the energetic barrier created by the existence of bridging MTH linker molecules located at the interface, the linkers maintain a higher LUMO level as compared with both CdSe QDs and DWNTs. Hence, electrons from QDs need to tunnel through the linkers themselves, prior to their localization onto adjoining DWNTs, whereas the associated holes are expected to be trapped by the terminal thiol groups inherent to the MTH.

Understanding of interfacial charge transport mechanisms are therefore essential towards realizing the optimal design and construction of high-performance QD-based solar energy conversion systems.[23] As a means of probing interfacial interactions among nanocomposites, the use of near-edge X-ray absorption fine structure (*NEXAFS*) spectroscopy has been extensively investigated,[24-27] as it characterizes the electronic transitions from a particular core level of an atom to its unoccupied (bound or continuum) states. With respect to relevant, prior results, the Sn $M_{5,4}$ edge, O *K*-edge, and C *K*-edge have been successfully measured and analyzed with the goal of elucidating the synergistic interactions between crystalline SnO_2 nanoparticles (NPs) and CNTs through bonding, and the study noted that this interaction involved a charge redistribution between C 2*p*-derived states with the valence and conduction bands in SnO_2 NPs via an interfacial interaction facilitated by oxidative treatment of the CNTs, prior to composite formation.[28] Additional examples abound. Koroteev *et al.* reported a decrease of the π^* resonance intensity in the C *K*-edge spectrum upon MoS_2 deposition onto the CNT surface, signifying the likelihood of charge transfer between the two components.[29] Yueh *et al.* investigated the local electronic structure associated with 'Fe-catalyzed and stabilized' CNTs of

various diameters, and they noted that an enhancement of the C *K*-edge and a corresponding reduction of the Fe L_3-edge features, thereby denoting observations indicative of a charge transfer taking place from C 2p to Fe 3d orbitals.[30]

In terms of charge transfer properties, the *Raman* spectra of both constituent CNTs and the resulting heterostructures have been collected with a focus towards analyzing and understanding relative changes in the presence of certain distinctive bands associated with CNTs. Specifically, the high-frequency Raman-active vibrations of sp^2 carbon are sensitive to chemical doping,[31] and there has been a concomitant increase in interest in studying the resonance Raman spectra of DWNTs, doped with electron donors and acceptors, with the hope and expectation of being able to modulate their electronic properties in a deterministic manner.[32-35] In particular, the tangential mode (TM) region (G-band) of the Raman spectrum provides information about the metallicity of the tubes and even minute changes in these features are often a consequence of charge transfer between the dopants and the tubes themselves.[34] Moreover, shifts in the Raman frequencies for the tangential G^+ modes and the corresponding alterations in their intensities can provide for further evidence for charge transfer between CNTs and the dopants themselves.[36] For example, Li *et al.* have reported a large downshift of the G-band, which is likely indicative of substantial electron transfer between Fe atoms and DWNTs.[37] In another manifestation of the sensitivity of this technique, Rauf *et al.* observed G band shifts to higher frequencies for the outer tubes and corresponding shifts to lower frequencies for the inner tubes, when charge transfer occurred through potassium intercalation into the DWNTs.[38]

In order to monitor the charge carrier mobility in our heterostructures, *electrical transport* measurements have been collected by constructing field effect transistor (FET) devices. Owing to their suitable direct bandgap (E_g = 1.74 eV), which yields a measurable

response upon exposure to visible light, CdSe QDs have attracted extensive attention as promising candidates for applications in photovoltaic and photoelectronic devices.[39, 40] Moreover, CNTs also yield respectable field-effect mobility and therefore represent a promising architecture for electronic devices.[41] There have been reports focusing on FETs, created using CNT-QD heterostructures. For example, Zhao *et al.* noted that CdSe QDs formed in situ on the carbon nanobelt matrix could give rise to the formation of a nanoscale *p–i–n* junction, possessing *p*-type conductivity with hole mobility values as high as 1.4×10^4 $cm^2 V^{-1}s^{-1}$.[42]

Therefore, it is interesting to note that while NEXAFS, Raman, and electrical transport measurements have been separately applied as tools to investigate charge transfer in various types of nanotube-based heterostructures for years, there have been comparatively fewer papers published about utilizing these unique characterization protocols within the context of DWNT-QD heterostructures in order to study the nature of interfacial charge transfer. There have been even fewer deliberative and systematic efforts (either qualitatively or quantitatively) to use a cumulative combination of all of these techniques in CNT-QD systems with the focus on probing and correlating the effect of varying QD sizes and coverage densities with the resulting charge transfer properties of as-prepared nanocomposites.

Hence, in the current Chapter, our efforts are focused on gaining fundamental insights into charge transfer behavior across nanoscale interfaces in composite heterostructures as a function of QD size and coverage density. Specifically, our efforts are directed towards comparing and understanding charge transfer behavior, i.e. specifically electron transfer trends, at the interfaces of a number of different DWNT-CdSe heterostructures, possessing various QD average diameters (2.3 nm, 3.0 nm, and 4.1 nm), created through the mediation of 4-mercaptophenol (MTH) using a non-covalent π-π stacking attachment approach. The structure,

morphology, and specifically the QD coverage density on the DWNT surface were characterized by transmission electron microscopy (TEM). Meanwhile, data from NEXAFS and Raman spectroscopies coupled with electrical transport measurements were acquired on both constituent CNTs and the resulting heterostructures with a focus towards analyzing and understanding the nature of nuanced but reproducible data trends, governing charge transfer (and specifically electron tunneling) from QDs with various sizes and coverage densities to DWNTs within heterostructures.

4.2. Results and Discussion

With the amount of DWNTs and the concentration of the MTH-CdSe solution kept constant in order to ensure data reliability, the resulting DWNT-MTH-CdSe heterostructures, possessing QD diameters measuring 2.3, 3.0, and 4.1 nm, respectively, were generated by utilizing a facile non-covalent π-π stacking strategy (Scheme 2.1 in Chapter 2). TEM was utilized to characterize the QD sizes and coverage densities on the DWNT surface in the resulting heterostructures. Meanwhile, charge transfer (and specifically electron tunneling) from QDs with various sizes and coverage densities to DWNTs in heterostructures was probed by using NEXAFS and Raman spectroscopies coupled with electrical transport measurements.

4.2.1. Electron Microscopy Studies.

Low magnification TEM data in Figure 4.1 highlighted the formation of all three heterostructures, formed by π-π stacking, with the presence of QDs clearly visible on the outer surfaces of our purified DWNT bundles, created through the mediation of MTH linker. On the basis of statistical measurements of 20 distinctive and discrete as-formed DWNT-QD bundles within each heterostructure sample, the corresponding average coverage density was found to be 14 ± 10 dots for MTH-QDs, possessing diameters of 2.3 ± 0.4 nm (Figure 4.1A); 16 ± 8 dots for

MTH-QDs, with diameters of 3.0 ± 0.4 nm (Figure 4.1B); and 27 ± 5 dots for MTH-QDs, measuring 4.1 ± 0.6 nm in diameter (Figure 4.1C), respectively. All measurements were based on typical DWNT bundles with lengths of 100 nm and diameters of 20 nm.

This average coverage density of CdSe QDs immobilized onto the DWNT surface was estimated by dividing the total number of QDs attached onto the CNT surface by the corresponding length of the DWNTs normalized to 100 nm intervals. We found that the 4.1 nm CdSe QDs evinced a notably higher coverage density (almost two times) as compared with their 2.3 and 3.0 nm diameter analogues, possibly due to the presence of additional ligand molecules at the surface, which would have contributed to more effective bonding with the underlying DWNT framework.

The corresponding HRTEM images in Figure 4.1D-F further confirmed the successful chemical conjugation of DWNTs with CdSe QDs. Lattice fringes associated with CdSe QDs as well as with the interface between the QDs and the DWNT surface were clearly discernible. Specifically, the measured 3.51 Å and 3.72 Å values corresponded to the *d*-spacings of the (002) and (100) lattice planes of the hexagonal CdSe, respectively, whereas the measured 3.41 Å spacing could be ascribed to the interlayer spacing between the graphitic layers within the DWNT themselves.

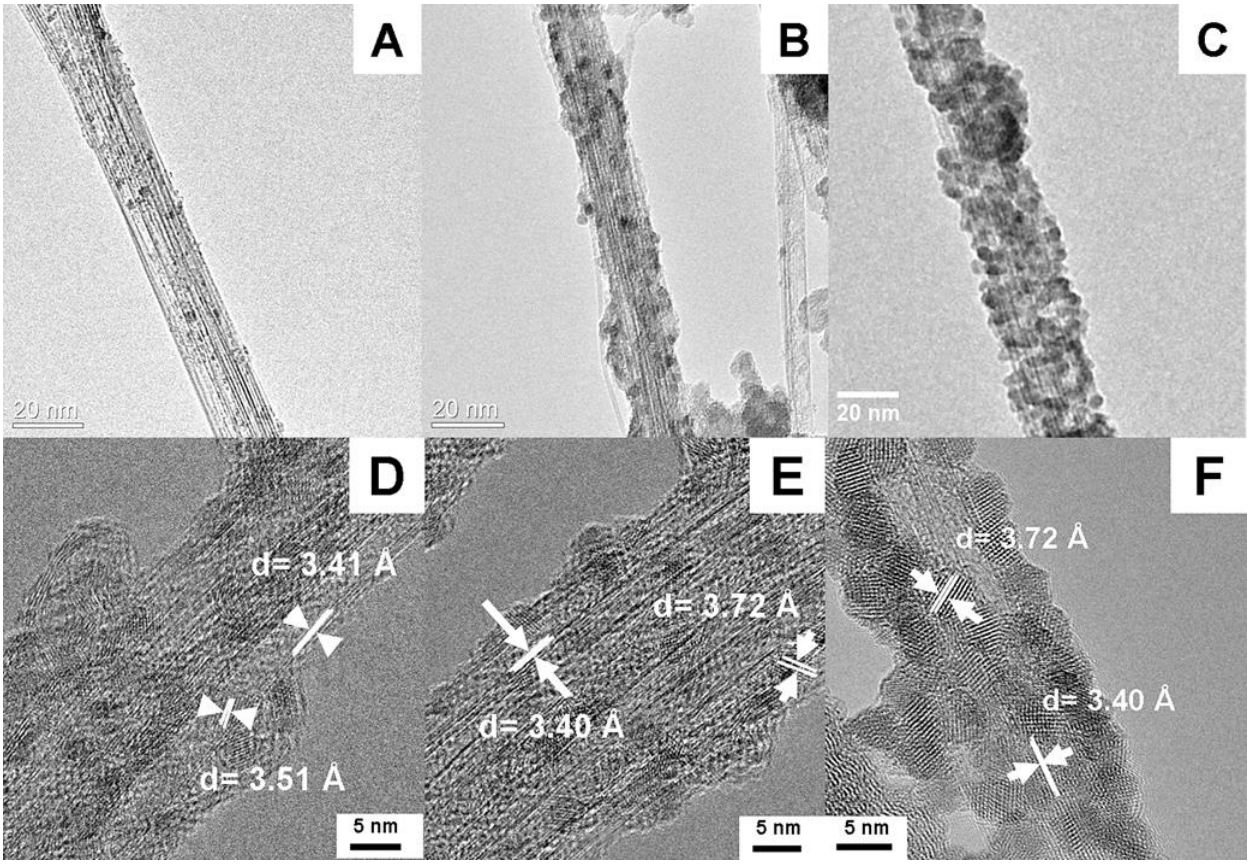

Figure 4.1 (A, B, and C). TEM images and **(D, E, and F).** HRTEM images of DWNT-MTH-CdSe QD (with average constituent QD diameters of 2.3, 3.0, and 4.1 nm, respectively) heterostructures, respectively, synthesized by a non-covalent strategy, taking advantage of π-π stacking effects. (Reprinted with permission from *J. Phys. Chem. C*, **2015**, *119*, 26327–26338. Copyright 2015 American Chemical Society.)

4.2.2 NEXAFS Spectra.

Explanation of Physical Meaning of Edge Data: Specifically, the C *K*-edge spectral features arise from dipole transitions from C 1s core states to 2p-derived electronic states. The sharp peak at around 285.4 eV represents a C 1s to the C=C 2p π* transition; the broad peak at 292-294 eV is composed of three C 1s to C-C σ* transitions.[27, 43] Furthermore, the peaks at ~288.1 eV and ~289.1 eV can be attributed to the π* C=O and σ* states, respectively, associated with C-O functionalities.[26, 46] Moreover, the areas under resonance (or peak intensity) of these π* and σ* features are approximately proportional to the electronic density of the unoccupied C 2p derived

states, whereas the increased intensities of these features can be correlated either with the increased numbers of unoccupied C 2p orbitals or with a charge transfer process taking place between the C 2p orbital and the dopant at the interface.[27, 28, 30]

Two well-separated absorption features are observed in the O *K*-edge with a sharp peak located at 531.8 eV and a broader peak centered at around 539−546 eV. The feature at ~531 eV can be assigned to transitions from the O 1s core levels to π* C=O states derived from carboxylic acid moieties, whereas the broad absorption feature centered at around 539−546 eV can be attributed to the superposition of transitions from the O 1s core levels to the final states possessing σ* symmetry, localized on the O−H, C−O, and C=O bonds. The small peak at ~534.6 eV likely originates from the -OH π* transition associated with carboxylic acid species.[25, 44, 47]

The Cd M_3 edge originates from transitions between the Cd 3p initial state and unoccupied 5s states. The projected electronic density of states (DOS) generated from theory demonstrates that the bottom of the conduction band of CdSe is composed of Cd 5s states. If the bottom of the CdSe conduction band were to shift by an energy interval, ΔE_c, then the corresponding M_3 absorption edge would shift by an equivalent amount, thereby representing the quantum confinement induced shift in the conduction band.[48, 49] Although the *M* edges are known to suffer from weak signals and a large background[48] by contrast with the Cd L_3 edge, the former can be readily probed within the operational energy range (180-1200 eV) of the U7A beam line. Therefore, in order to render these M_3 edges useful for quantitative analysis, we collected multiple replicates of the spectra and increased data integration times in order to obtain higher signal-to-noise ratios and therefore data interpretability.

Actual Results Obtained: The C *K*-edge and O *K*-edge spectra of the pristine and oxidized DWNTs (Figures 4.2A and B) were consistent with the successful purification and

functionalization of DWNTs by acid-treatment which generated oxygenated functionalities, e.g. –COOH groups, on their external surfaces. C *K*-edge data gave rise to prominent transitions at 285 eV, 292-294 eV, and 301–309 eV, respectively, corresponding to a sharp C 1s to C=C π* (ring) transition, three C 1s to C-C σ* (ring) transitions,[27, 43] as well as broad (π + σ) transitions, respectively.[44] After oxidation of the DWNTs, specific transitions at ~288.1 and 289.1 eV, which can attributed to the π* states of carbonyl groups associated with –COOH as well as of σ* states associated with C-O functionalities,[26] became more prominent. The corresponding O *K*-edge data associated with the oxidized DWNTs evinced several distinctive peaks. Specifically, the peak at 531.6 eV corresponds to the C=O π* transition, which originates from the carbonyl oxygen atom, while the peak at 534.8 eV can be assigned to the "-OH" moiety from the carboxylic group. The two broader peaks located at 539.6 and 543.8eV can be ascribed to the presence of inequivalent σ* C-O bonds within the carboxylic acid group.[44, 45]

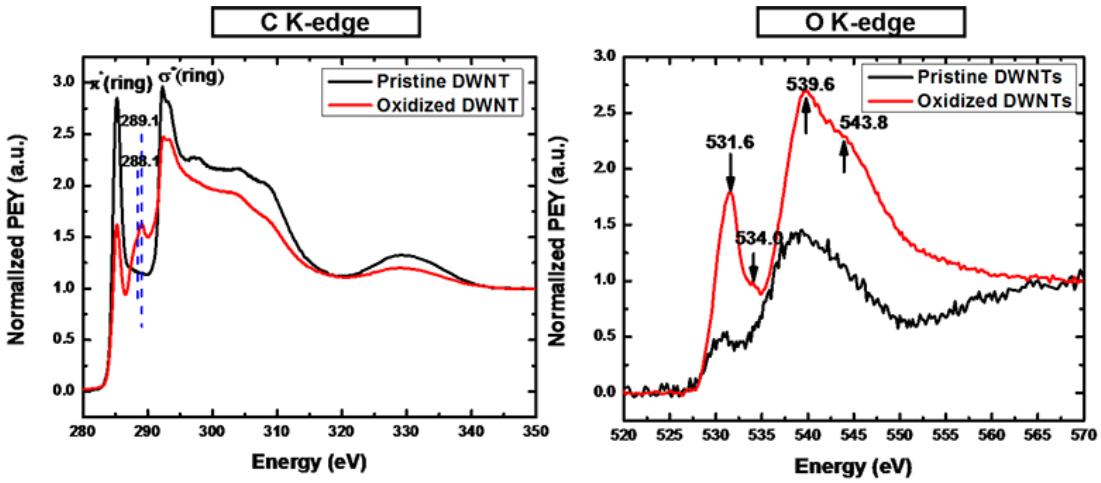

Figure 4.2. C *K*-edge and O *K*-edge NEXAFS spectra of pristine and oxidized DWNTs. (Reprinted with permission from *J. Phys. Chem. C*, **2015**, *119*, 26327–26338. Copyright 2015 American Chemical Society.)

The C and O *K*-edge NEXAFS spectra of the DWNTs, of the DWNT-MTH control sample, and of the DWNT-MTH-CdSe heterostructures are shown in Figure 4.3, panels A and B,

respectively, whereas the Cd M_3-edge spectra of free-standing MTH-CdSe QDs as well as of all three DWNT-MTH-CdSe heterostructures are highlighted in Figure 4.4.

On the basis of the C *K*-edge NEXAFS analysis (Figure 4.3A), several features are worthy of note. *First*, the π* transition intensity, which reflects the unoccupied DOS corresponding to π* character, is enhanced when MTH linkers were attached onto oxidized MWNTs, which might be due to the presence of the sp^2 carbon from the aromatic MTH linker. This π* transition intensity is subsequently strongly reduced within DWNT-MTH-CdSe heterostructures; the composites incorporating 2.3 nm diameter QDs gives rise to the largest observed reduction, suggestive of possible electron transfer from CdSe conduction bands to the C 2p-derived π* states.

Second, the appearance of a slightly enhanced C *K*-edge peak at ~289 eV coupled with shoulder features near this peak within the heterostructures, as compared with the DWNT-MTH nanohybrid control alone, suggests the presence of slightly perturbed bonding between carbon and oxygen after the QD deposition process. That is, the presence of an oxidized C environment at the interface of the heterostructures may result in a localized and higher density of the unoccupied state possessing C 2p character, thereby indicating that DWNTs may have the opportunity of possibly back donating a small amount of charge to the immobilized CdSe QDs through the mediation of Cd−O−C bonding.[27, 50]

In the O *K*-edge data (Figure 4.3B), the C=O π* transition intensity appears to be suppressed in all three heterostructures after the QD deposition as compared with the DWNT-MTH control sample. The heterostructure incorporating the smallest 2.3 nm diameter QDs gives rise to the strongest reduction in the C=O π* transition, suggesting that the carbonyl oxygen atom within the carboxylic group on the surface of the DWNTs is withdrawing charge after QD

deposition, whereas the C-O or -OH σ* transition intensity is apparently enhanced the most in the heterostructure incorporating 2.3 nm diameter QDs, thereby implying that the oxygen atoms in the –OH and C-O bonds from the MTH ligands are donating charge.

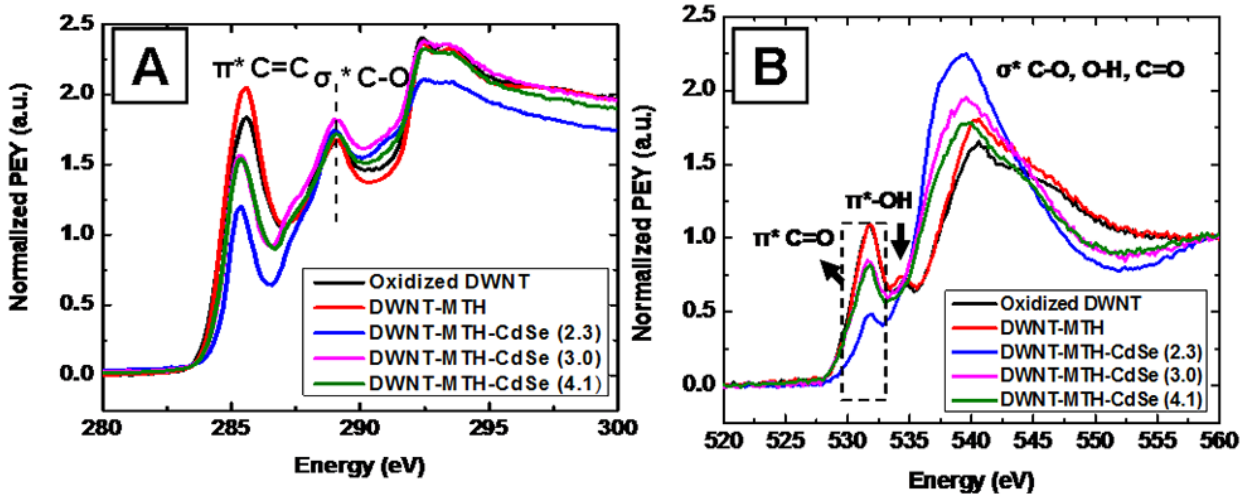

Figure 4.3. C *K*-edge **(A)** and O *K*-edge **(B)** spectra of oxidized DWNTs (black), DWNT-MTH composite control samples (red), and DWNT-MTH-CdSe QD (with constituent QD average diameters of 2.3 (blue), 3.0 (pink), and 4.1 (green) nm, respectively) heterostructures. (Reprinted with permission from *J. Phys. Chem. C*, **2015**, *119*, 26327–26338. Copyright 2015 American Chemical Society.)

We found that all three DWNT-MTH-CdSe heterostructures evince enhanced intensities of the Cd M_3-edge relative to that of free-standing MTH-CdSe QDs (Figure 4.4), thereby implying an increased level of unoccupied DOS in the conduction band of CdSe and providing for direct evidence of an electron transfer process taking place from CdSe QDs to DWNTs. By analogy with the C and O *K*-edge features previously discussed, we have noted that the heterostructure incorporating 2.3 nm diameter QDs gave rise to the largest enhancement of the peak intensity, thereby indicating the potential for the largest amount of electron transfer in this system.

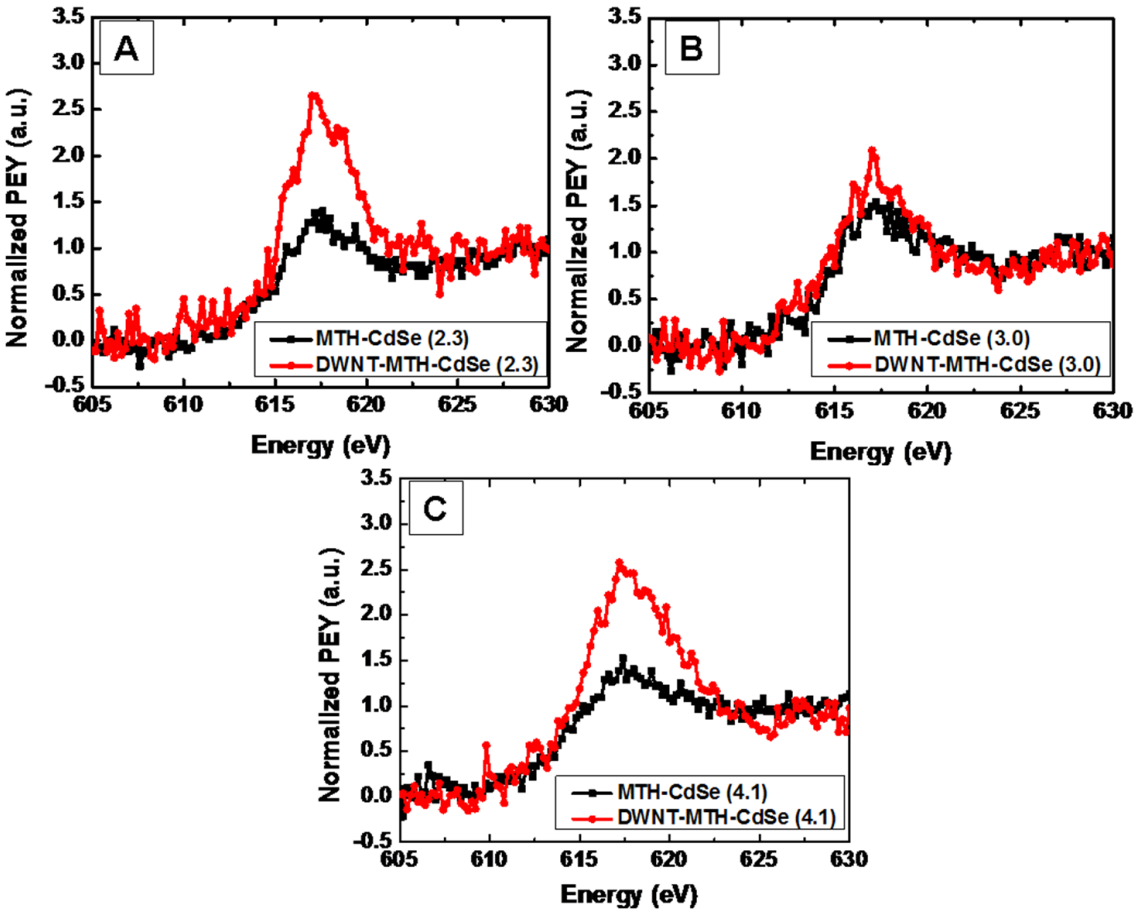

Figure 4.4 (**A, B, and C).** Cd M_3-edge spectra of MTH-functionalized CdSe QDs (black) and of DWNT-MTH-CdSe (red; with average constituent QD diameters of 2.3, 3.0, and 4.1 nm, respectively) heterostructures. (Reprinted with permission from *J. Phys. Chem. C*, **2015**, *119*, 26327–26338. Copyright 2015 American Chemical Society.)

All NEXAFS spectra have yielded spectroscopic evidence that charge redistribution involving the CdSe QDs and C 2p-derived states likely has occurred. Specifically, upon close inspection of the C and O *K*-edge together with the Cd M_3-edge data, these entailed *(i)* an intensity reduction in the π* C=O and –OH signal of the O *K*-edge and the π* C=C response of the C *K*-edge transitions coupled with *(ii)* an intensity enhancement in the Cd M_3-edge as well as the σ* C-O or –OH signal associated with the O *K*-edge. Hence, it is plausible to propose a possible directional electron transfer process, as follows. Upon excitation, the electrons tunnels

from the conduction band of the CdSe QDs to the π^* states of the DWNT C=C carbonaceous network as well as the C=O π^* states of surface carboxylic functional moieties. This charge interaction was mediated between the π- π conjugated system associated with the DWNTs and the MTH-capped CdSe QDs, as manifested in discernible but interpretable changes.

Therefore, we have shown that the DWNT-MTH-CdSe heterostructures incorporating the smallest 2.3 nm diameter QDs gives rise to the largest amount of electron transfer, an observation which can be potentially explained by the Marcus theory, which is commonly used to describe the interfacial charge transfer process and to quantitatively probe the dependence of the transfer rate on the driving force.[51-53] Previous studies have indicated that electron transfer from photoexcited QDs lies in the so-called 'normal' region, where the charge transfer rate increases with and is proportional to the driving force.[54, 55] For example, the Kamat group reported[56] that by systematic reduction of the QD size, the electron transfer from CdSe QDs to the adjoining TiO_2 particles could be enhanced, and it was subsequently concluded that this transfer resides within the 'normal' region of Marcus theory.

A potential charge transfer model for our DWNT-MTH-bound-CdSe systems, possessing discrete energy levels associated with each component, is proposed in Figure 4.5. The energy levels of CdSe QDs possessing different sizes as well as of the DWNTs have been calculated, based on previous papers.[57-60] The redox energy level of the thiophenol linker has been previously reported to be -0.006 V vs. NHE,[61] which is situated at a higher energy as compared with the valence bands of all three CdSe QDs; hence, the linker is energetically favorable for hole trapping. Upon excitation and photon absorption, an electron–hole pair exciton will form within the CdSe QDs. The photogenerated holes will then be efficiently trapped by the thiol groups within the MTH linker that is strongly adsorbed onto the CdSe surface, resulting in the

creation of a thiol-based radical with the implication that two thiol-based radicals can be combine to form a disulfide.[18] Due to the previously reported higher LUMO levels associated with these various thiol molecules,[21, 62, 63] electron transfer should occur at the interface between the CdSe QDs and the DWNTs, in which the intervening MTH linker molecule serves as an energetic barrier through which electrons can tunnel.[64, 65] Hence, the difference between the conduction band energy levels of the CdSe QDs and of the DWNTs serves as a driving force for interfacial electron transfer.[66] Therefore, it is expected that the QDs, possessing higher conduction band energy levels, i.e. ever smaller sizes of quantum confined QDs, should induce additional electron transfer.

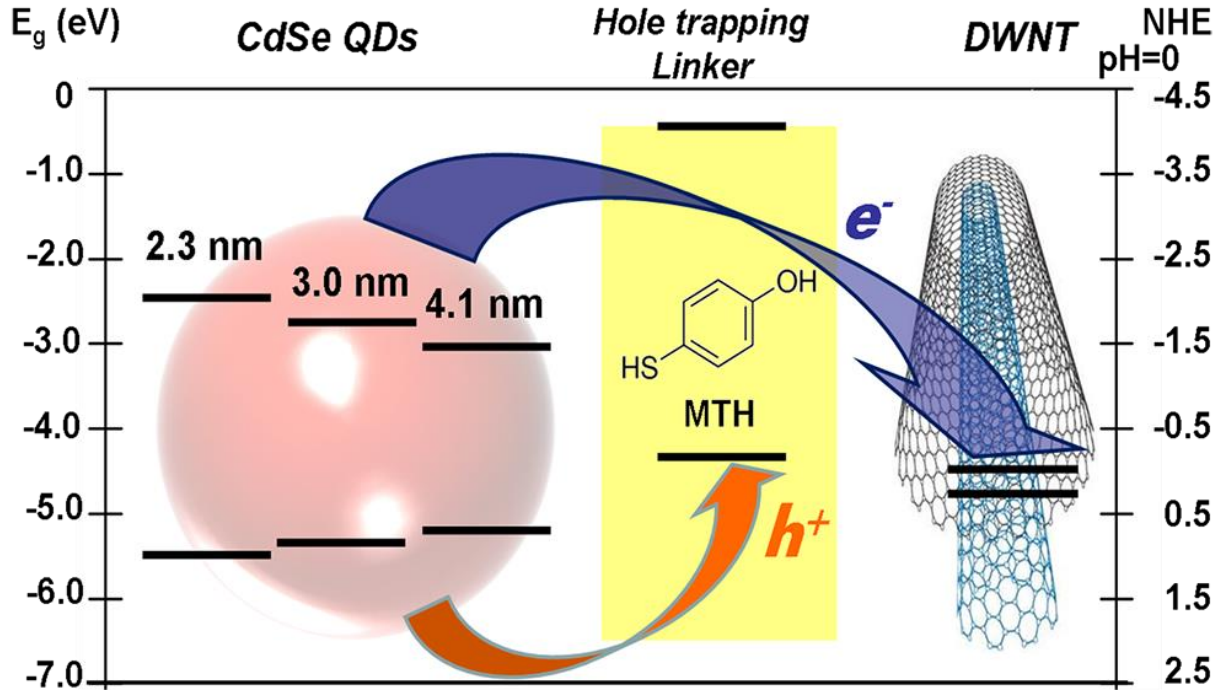

Figure 4.5. Energy diagram of the various sizes of the CdSe QDs probed, the MTH linkers themselves, and the DWNTs, respectively. e^-: electron, h^+: hole. (Reprinted with permission from *J. Phys. Chem. C*, **2015**, *119*, 26327–26338. Copyright 2015 American Chemical Society.)

Nevertheless, it was noted that there was not a significant difference between the 3.0 and 4.1 nm diameter QD-based systems in terms of the C and O *K*-edges. Furthermore, we appeared

to observe more charge transfer in the Cd M_3-edge for the composites incorporating 4.1 nm diameter QDs as opposed to 3.0 nm diameter QDs, although the smaller 3.0 nm diameter QDs with their higher conduction bands supposedly were more amenable to charge transfer.

One possible explanation for this aberration is the fact that we observed different QD coverage densities within these two systems. Specifically, as shown in Figure 4.1, the 4.1 nm diameter CdSe QDs evinced a noticeably higher coverage density (i.e. ~1.5 times) as compared with their 3.0 nm diameter counterparts on the outer DWNT surface, thereby providing for greater interfacial contact areas as well as the potential possibility for additional pathways and channels for charge flow to occur from QDs to DWNTs with the net result that this intrinsic spatial, geometric consideration would dominate over the inherent electronic driving force associated with quantum confinement. The impact of QD coverage density upon the electron transfer properties has been specifically investigated using electrical transport measurements, as described later.

4.2.3. Raman Spectra.

Raman spectra associated with pristine and oxidized DWNTs are displayed in Figure 4.6. The intensity ratio of the D band near 1340 cm^{-1} to the tangential mode (G band) near 1580 cm^{-1} (I_D/I_G) dramatically increases after the purification process (i.e. I_D/I_G = 0.04 for pristine DWNTs and 0.50 for purified DWNTs). The increase in the I_D/I_G ratio due to the purification process is expected, since the increased peak intensity associated with the D band can typically be attributed to damage and distortion of the intrinsic conjugated sp^2 carbon lattice, as well as to the presence of amorphous carbon[67] and other symmetry-breaking defects in the DWNTs generated during the oxidation and concomitant surface functionalization of DWNTs (i.e., formation of –COOH and other oxygenated species on the surfaces of our tubes).[68, 69]

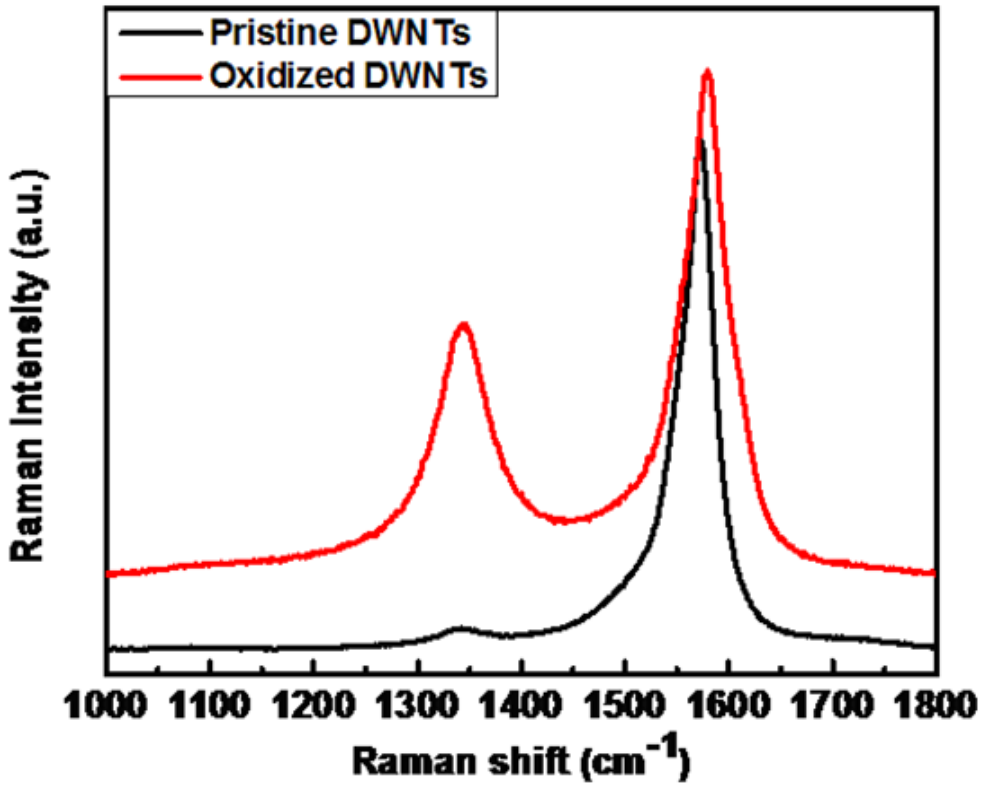

Figure 4.6. Raman D and G-band data of pristine (black) and oxidized (red) DWNTs, respectively. (Reprinted with permission from *J. Phys. Chem. C*, **2015**, *119*, 26327–26338. Copyright 2015 American Chemical Society.)

The tangential modes (G-bands) of the DWNT-MTH-CdSe composite heterostructures together with that of the DWNT-MTH control sample are collectively displayed in Figure 4.7. Each individual G band was treated as a convolution of 4 Lorentzian components (i.e. the dashed curves). The two peaks at higher frequencies can be attributed to the G^+ and G^- bands of the semiconducting outer tube, whereas the other two peaks at lower frequencies correspond to the G^+ and G^- bands of the semiconducting inner tube. According to the Kataura plot,[70] the 2.41 eV excitation energy of the laser is in resonance with the E_{33}^S transition of a semiconducting (S) outer tube as well as with the E_{33}^S transition of a semiconducting (S) inner tube. The fits of the

sum of the Lorentzian peaks match well with previously reported G-band deconvolution data on DWNTs, possessing a S@S configuration.[71, 72]

Upon deposition of CdSe QDs, all of the outer tube G^+ sub-bands (i.e. the peak with the highest frequency), which can be ascribed to the unresolved A_1 and E_1 tangential G^+ modes for the outer tubes,[73] evince an apparent peak down-shift, an observation which can be potentially attributed to the G-band 'softening', indicative of the expansion of C-C bonds upon *n*-type doping and suggestive of the presence of electron transfer from QDs in all three linker systems.[37, 38] The observed downshifts in the frequency of the outer tube G^+-band of DWNT-MTH-CdSe heterostructures possessing QD sizes of 2.3, 3.0, and 4.1 nm are 15, 3, and 8 cm^{-1}, respectively. Moreover, the behavior associated with downshift in the G^+_{outer} peak frequency evinces a similar trend to electron transfer that had been previously observed with the C *K*-edge and Cd M_3-edge NEXAFS spectra (i.e. QD diameters of 2.3 > 4.1 > 3.0 nm), again confirming the presence and extent of charge transfer. The fact that the inner outer tube G sub-bands barely alter after QD deposition is also consistent with a picture in which the charge from the QD donor is transferred to the outer tubes within the DWNT acceptor, which leads to a filling of those van Hove singularities (VHS) in the conduction band responsible for the observed Raman resonance.

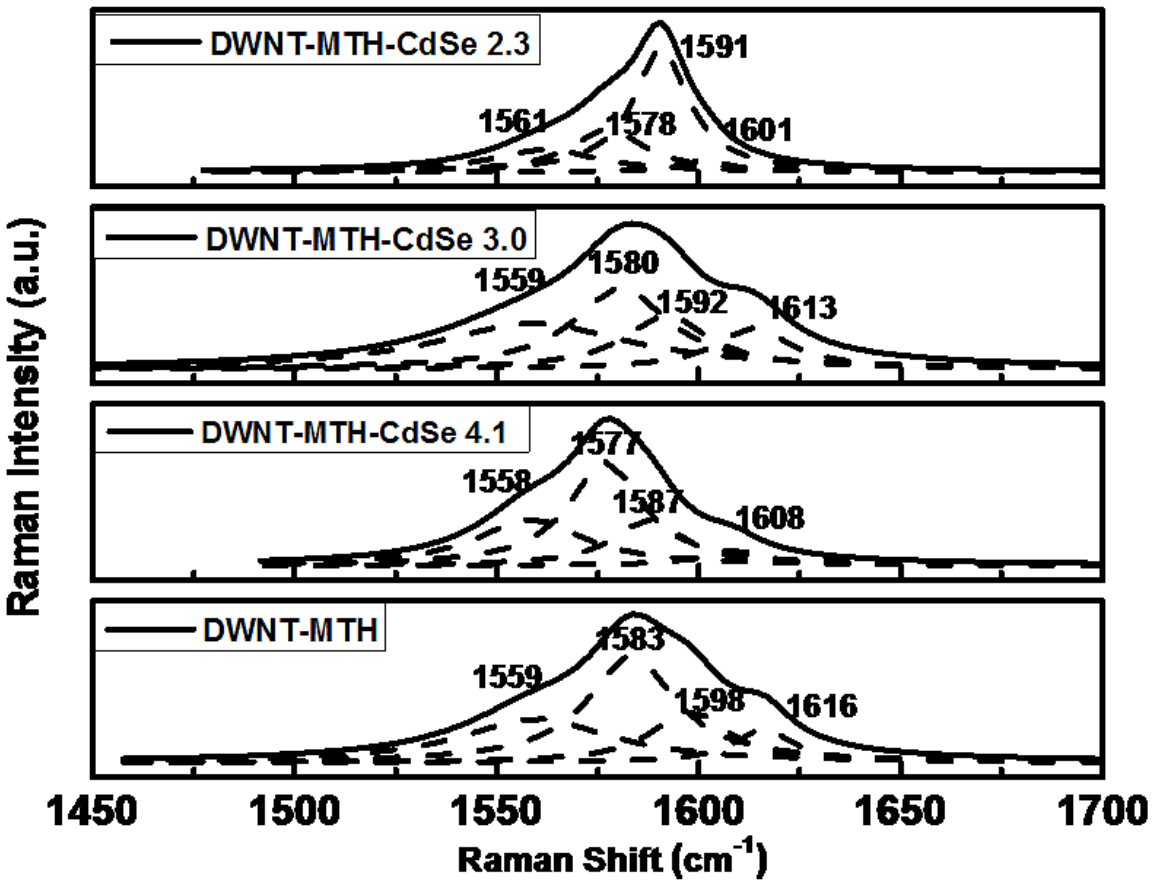

Figure 4.7. Raman G-band spectra measured at an excitation wavelength of 514 nm (2.41 eV) of a DWNT-MTH control sample as well as of DWNT-MTH-CdSe (with constituent QD diameters of 2.3, 3.0, and 4.1 nm, respectively) heterostructures, generated by non-covalent π-π stacking. (Reprinted with permission from *J. Phys. Chem. C*, **2015**, *119*, 26327–26338. Copyright 2015 American Chemical Society.)

4.2.4. Electrical Transport Measurements.

Both NEXAFS and Raman spectroscopy data have confirmed the presence of electron transfer between CdSe QDs and the underlying DWNTs. Electrical transport measurements have been used to complement the optical data as well as to achieve additional insights into the impact of individual reaction parameters such as acid functionalization, QD sizes, and QD coverage densities. In total, more than 180 DWNT-MTH-CdSe heterostructure field-effect transistors

(FETs) were characterized by a pulse measurement set-up in order to reduce any hysteresis effect on the device as well as to provide decent statistics that would allow for detecting any evident trends between variously chemically treated devices.

Specifically, exemplary subthreshold characteristics of a pristine DWNT and of an MTH-CdSe functionalized device obtained at V_{DS} = -0.5 V were shown in Figure 4.8 in order to illustrate the extraction process that was used to acquire insights into the impact of QD size and coverage density on the doping stage of DWNTs. For otherwise similar devices, the threshold voltage holds critical information about the doping stage of an FET and/or the amount of charge in the vicinity of the channel. Since extracting the actual threshold voltage V_{th} that defines the transition from the device off-state (where the current depends exponentially on the gate voltage) to the on-state that typically shows more of a power law dependence from experimental data is often challenging, we have used herein a more robust approach that utilizes the ambipolar nature of most nanotube device characteristics.

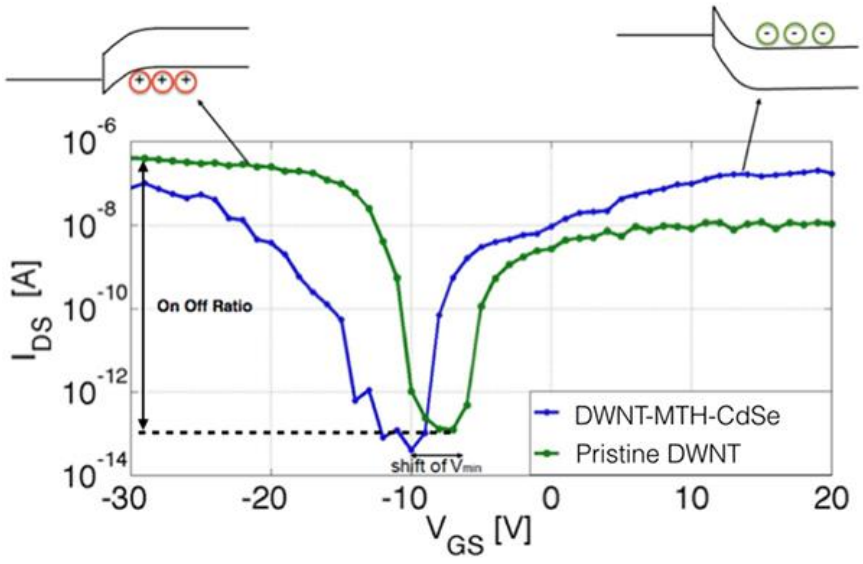

Figure 4.8. Sub-threshold characteristics of a pristine and MTH-functionalized DWNT FET measured at V_{DS} = -0.5 V. A clear shift of the minimum current point is observed. (Reprinted with permission from *J. Phys. Chem. C*, 2015, *119*, 26327–26338. Copyright 2015 American Chemical Society.)

So-called ambipolar device characteristics are a result of electron transport through the nanotube conduction band at positive gate voltages and hole transport for negative gate voltages through the valence band. Of the above mentioned total number of devices, those that show clear ambipolar behavior were selected for the extraction process that determines the gate voltage at which minimum current is reached as a qualitative measure of V_{th}. The process was discretely used for (a) pristine DWNTs, (b) DWNTs functionalized with MTH and CdSe QDs measuring 2.3 nm, (c) DWNTs functionalized with MTH and CdSe QDs possessing a diameter of 3.0 nm, as well as for (d) DWNTs functionalized with MTH and CdSe QDs with a diameter of 4.1 nm. It is worth mentioning here that all of the measurements have been carried out under dark conditions. Hence, the observed charge transfer behavior is not associated with the photo-induced excitons,[74] but rather with possible work function differences amongst the various individual components in the system.

The trend of a shifted minimum current V_{min} for pristine and various DWNT-MTH-CdSe heterostructures is summarized in Figure 4.9. We note that while individual devices may show a similar V_{min}, indicating a similar doping level, the large number of devices characterized in this study provides clear evidence of a doping trend between transistors of type (a) through (d). In fact, our data suggest an increase in the *n*-doping level from (a) to (d) with the highest *n*-doping achieved in the DWNT-MTH-CdSe, measuring 4.1 nm, suggestive of the presence of the highest amount of charge generated in spatial proximity to the DWNTs. As has been pointed out before, the coverage of DWNTs varies with the choice of the QD size. We find that our transport results are consistent with the TEM supported observation (Figure 4.1) that the average QD density varies from 14 QDs/100 nm in case (b) to 16 QDs/100 nm in case (c) to 27 QDs/100 nm in case (d). We submit that it is the charge transfer process from the MTH-CdSe QD system to the

DWNT due to a smaller work function of the functionalized group as compared with the DWNT itself that creates the observed *n*-doping level, a finding that had not been previously reported before. We also re-emphasize that the above statements are not related to the amount of charge transfer under illumination. Since all measurements were performed in the dark, no photo-induced electron transfer can be observed. Instead, the data indicate that the QD-ligand system once attached to the DWNT is no longer 'charge neutral', an important fact that needs to be considered in the context of solar cell applications. To summarize, in the absence of laser illumination, systems possessing higher QD coverage densities lead to more charge transport. Measurements of this series of DWNT-MTH-CdSe heterostructures in the presence of laser illumination are still under investigation in order to reveal additional insights into photo-induced charge transport.

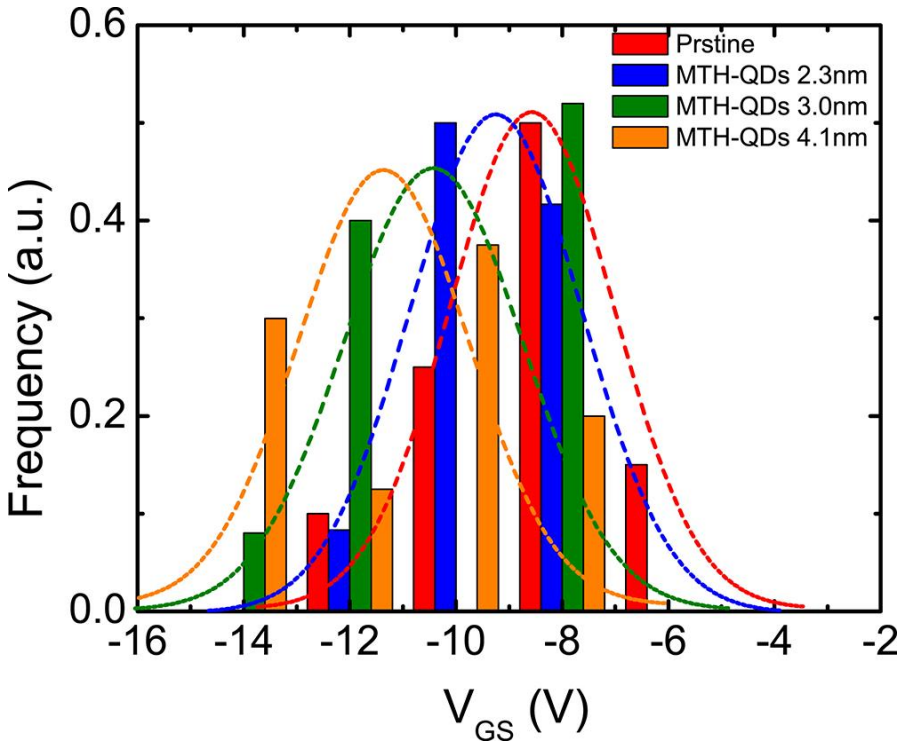

Figure 4.9. Distribution plot showing the trend of a shifted minimum current V_{min} for pristine and MTH-QD functionalized DWNTs. The higher the level of QD-decoration, the more negative the V_{min}. (Reprinted with permission from *J. Phys. Chem. C*, **2015**, *119*, 26327–26338. Copyright 2015 American Chemical Society.)

It is also worth reinforcing our findings about DWNT functionalization from data associated with 'on/off current ratios'. When functionalizing DWNTs as opposed to single-wall carbon nanotubes (SWNTs) with the MTH-QD complex, the idea was to ensure the structural and electronic integrity of the inner carbon nanotube shell, while only breaking bonds associated with and attaching the ligands onto the outer shell of the DWNT. This approach appears to be a promising strategy for solar cell applications, since it ensures that excellent transport of charges through the inner shell of the system is preserved, even after functionalization of the outer tube shell has occurred. While the various optical methods presented above clearly indicate the successful attachment of the ligand-QD system, these measurements cannot unambiguously provide the desired information about the quality of transport through the DWNT system after functionalization. Therefore, herein we present for the first time a statistical study of on/off current ratios (see illustration in Figure 4.10) that provides initial insights into this topic.

Figure 4.10 highlights the distribution of experimentally measured I_{on}/I_{off} values for a large number of three-terminal devices. For pristine DWNT FETs, the expectation is that on/off current ratios are rather small, consistent with the notion that the outer shell of a DWNT with its larger diameter exhibits a smaller band gap that results in a higher off-current as compared with a SWNT. Groups have recently reported[75, 76] on/off current ratios of about 3 and 4 respectively, consistent with this statement. Our results indicate that pristine DWNT FETs exhibit in only about 13% of all cases, I_{on}/I_{off}-values larger than 2, and none of these devices characterized achieved an on/off ratio of 8. On the other hand, a much larger number of devices, i.e. 22% of MTH-capped CdSe QD-functionalized DWNTs exhibited $I_{on}/I_{off} > 2$ and a small number of these devices even attained on/off current ratios of as large as 8 (c.f. Figure 4.10). This interesting observation can be understood in the context of the above intuitive argument of breaking only

the outer, external carbon nanotube shell when attaching the MTH-capped CdSe QDs onto the DWNT structure. In fact, we find that in 34% of all SWNT FETs, on/off-current ratios larger than 2 are obtained and values as high as 8 are achievable in some FETs (see lower distribution plot in Figure 4.10). Our experimental data clearly suggest that the device behavior of DWNTs is becoming more similar to pristine SWNT FETs after functionalization, thereby confirming the validity of the intuitive picture.

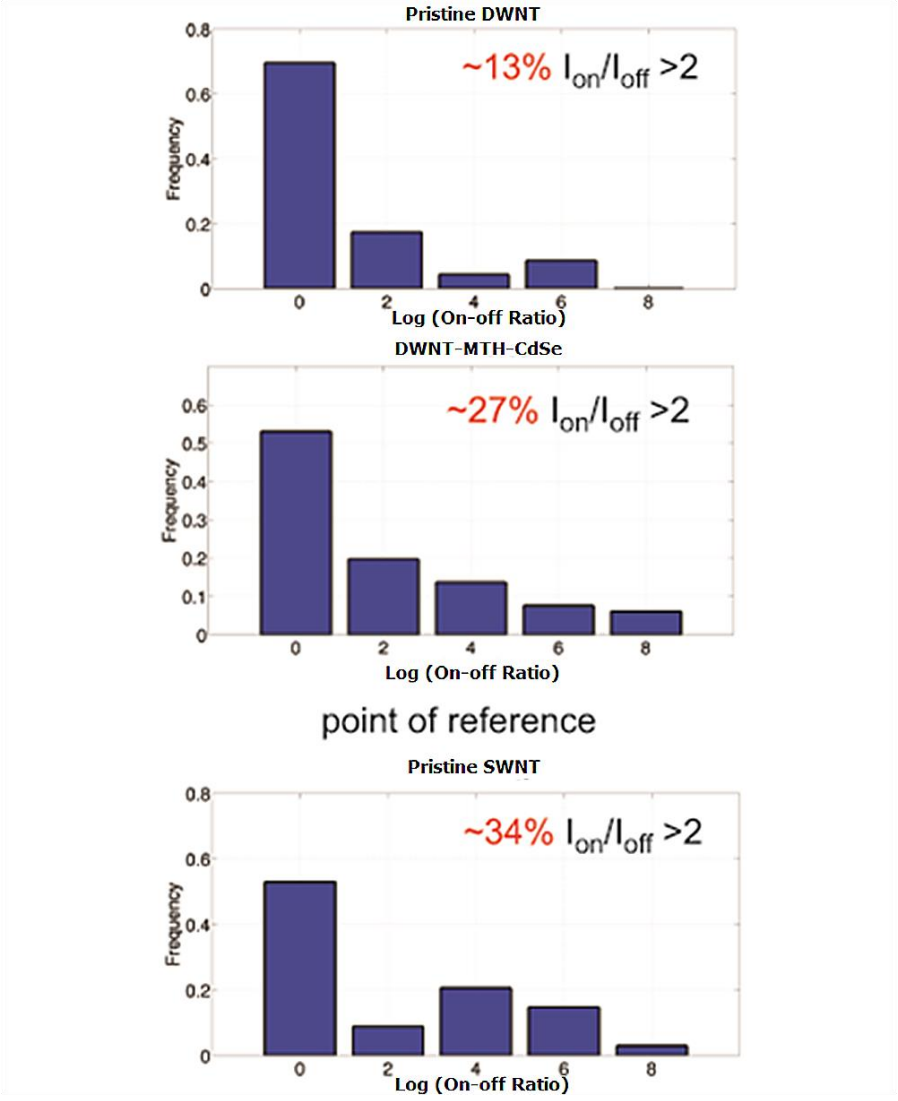

Figure 4.10. On / off-current distribution for pristine and functionalized carbon nanotubes. A larger portion of functionalized DWNTs shows an on/off-current ratio larger than 2 as compared with pristine DWNTs. (Reprinted with permission from *J. Phys. Chem. C*, 2015, *119*, 26327–26338. Copyright 2015 American Chemical Society.)

4.3. Conclusions

In this manuscript, DWNT-MTH-CdSe heterostructures, possessing average QD diameters ranging from 2.3, 3.0, and 4.1 nm, have been successfully synthesized using a facile non-covalent π-π attachment approach through the mediation of MTH linker. TEM and HRTEM images have indicated that the 4.1 nm diameter MTH-CdSe QDs are quantitatively more numerous as compared with their smaller-sized counterparts in terms of coverage density on the underlying DWNT surface.

With a collective analysis of both NEXAFS and Raman spectra, plausible evidence for electron transfer has been proposed for all the DWNT-MTH-CdSe heterostructures. Specifically, NEXAFS spectra of DWNT-MTH-CdSe heterostructures incorporating different QD sizes confirms that the interfacial electron transfer falls within the 'normal' Marcus theory region, wherein the heterostructure possessing the smallest QD size (i.e. 2.3 nm) gives rise to the largest driving force for charge transfer. The heterostructure possessing larger 4.1 nm diameter QDs yielded anomalously greater charge transfer behavior with respect to that containing 3.0 nm diameter QDs, an observation which can be ascribed to differential coverage densities onto the underlying DWNT templates.

Complementary Raman investigation at 2.41 eV excitation evinced an evident down shift of the outer tube G^+-band, thereby suggesting that CdSe QDs serve as electron donors, wherein electrons are predominantly transferred to the outer tubes in DWNTs in all three as-synthesized DWNT-MTH-CdSe QDs heterostructures, which led not only to a filling of the Van Hove singularities of the conduction band but also to a further 'softening' of the C-C bond, thereby shifting the G^+-band to lower frequencies. We note that this downshift in the G^+_{outer} peak frequency evinces a similar trend to what has been previously noted with electron transfer in the

NEXAFS spectra (QD diameters of 2.3 > 4.1 > 3.0 nm), again confirming the presence and extent of charge transfer.

The electrical transport measurements obtained in the absence of illumination, which serves as complementary measurement to the aforementioned optical data, indicated that the MTH-capped QDs once attached onto the DWNTs are no longer 'charge neutral' and further correlated the idea of *n*-doping, i.e. the presence of electron transfer under 'dark' conditions from the QDs to DWNTs which is essentially dependent upon the QD coverage densities, as corroborated by interpretable changes in threshold voltage characteristics. The on-off ratios from the FETs further confirmed that the acid treatment used selectively functionalizes the outer tubes of the DWNTs and hence preserves the electronic integrity of the inner tubes.

Therefore, the cumulative NEXAFS, Raman, and electrical transport studies present in this work have highlighted the presence of electron transfer in the DWNT-MTH-CdSe heterostructures both under photonic excitation as well as under 'dark' illumination conditions. Moreover, our studies offer a reasonable capability and path forward to tune and facilitate charge transfer of DWNTs via size and coverage density control of immobilized CdSe QDs. Such findings should shed light upon the connection between architectural design and control of charge separation within the context of QD-based solar cell regimes.

4.4. References

1. Peng, X.; Sfeir, M. Y.; Zhang, F.; Misewich, J. A.; Wong, S. S. Covalent Synthesis and Optical Characterization of Double-walled Carbon Nanotube-Nanocrystal Heterostructures. *J. Phys. Chem. C* **2010**, *114*, 8766-8733.
2. Schulz-Drost, C.; Sgobba, V.; Gerhards, C.; Leubner, S.; Calderon, R. M. K.; Ruland, A.; Guldi, D. M. Innovative Inorganic-Organic Nanohybrid Materials: Coupling Quantum Dots to Carbon Nanotubes. *Angew. Chem. Int. Ed.* **2010**, *49*, 6425-6429.
3. Wang, D. F.; Baral, J. K.; Zhao, H. G.; Gonfa, B. A.; Truong, V. V.; El Khakani, M. A.; Izquierdo, R.; Ma, D. L. Controlled Fabrication of PbS Quantum-Dot/Carbon-Nanotube Nanoarchitecture and its Significant Contribution to Near-Infrared Photon-to-Current Conversion. *Adv. Funct. Mater.* **2011**, *21*, 4010-4018.
4. Reiss, P.; Protiere, M.; Li, L. Core/Shell Semiconductor Nanocrystals. *Small* **2009**, *5*, 154-168.
5. Zhang, L. H.; Shi, E. Z.; Li, Z.; Li, P. X.; Jia, Y.; Ji, C. Y.; Wei, J. Q.; Wang, K. L.; Zhu, H. W.; Wu, D. H.; Cao, A. Y. Wire-supported CdSe nanowire array photoelectrochemical solar cells. *Phys. Chem. Chem. Phys.* **2012**, *14*, 3583-3588.
6. Peng, X. H.; Wong, S. S. Controlling Nanocrystal Density and Location on Carbon Nanotube Templates. *Chem. Mater.* **2009**, *21*, 682-694.
7. Peng, X. H.; Sfeir, M. Y.; Zhang, F.; Misewich, J. A.; Wong, S. S. Covalent Synthesis and Optical Characterization of Double-Walled Carbon Nanotube-Nanocrystal Heterostructures. *J. Phys. Chem. C* **2010**, *114*, 8766-8773.
8. Banerjee, S.; Wong, S. S. Formation of CdSe nanocrystals onto oxidized, ozonized single-walled carbon nanotube surfaces. *Chem. Commun.* **2004**, 1866-1867.
9. Peng, X. H.; Misewich, J. A.; Wong, S. S.; Sfeir, M. Y. Efficient Charge Separation in Multidimensional Nanohybrids. *Nano Lett.*. **2011**, *11*, 4562-4568.
10. Newton, J. C.; Ramasamy, K.; Mandal, M.; Joshi, G. K.; Kumbhar, A.; Sardar, R. Low-Temperature Synthesis of Magic-Sized CdSe Nanoclusters: Influence of Ligands on Nanocluster Growth and Photophysical Properties. *J. Phys. Chem. C* **2012**, *116*, 4380-4389.
11. Ning, Z.; Voznyy, O.; Pan, J.; Hoogland, S.; Adinolfi, V.; Xu, J.; Li, M.; Kirmani, A. R.; Sun, J.-P.; Minor, J.; Kemp, K. W.; Dong, H.; Rollny, L.; Labelle, A.; Carey, G.; Sutherland, B.; Hill, I.; Amassian, A.; Liu, H.; Tang, J.; Bakr, O. M.; Sargent, E. H. Air-stable n-type colloidal quantum dot solids. *Nat. Mater.* **2014**, *13*, 822-828.
12. Fischer, A.; Rollny, L.; Pan, J.; Carey, G. H.; Thon, S. M.; Hoogland, S.; Voznyy, O.; Zhitomirsky, D.; Kim, J. Y.; Bakr, O. M.; Sargent, E. H. Directly Deposited Quantum Dot Solids Using a Colloidally Stable Nanoparticle Ink. *Adv. Mater.* **2013**, *25*, 5742.
13. Anderson, N. C.; Hendricks, M. P.; Choi, J. J.; Owen, J. S. Ligand Exchange and the Stoichiometry of Metal Chalcogenide Nanocrystals: Spectroscopic Observation of Facile Metal-Carboxylate Displacement and Binding. *J. Am. Chem. Soc.* **2013**, *135*, 18536-18548.
14. Mora-Sero, I.; Bertoluzzi, L.; Gonzalez-Pedro, V.; Gimenez, S.; Fabregat-Santiago, F.; Kemp, K. W.; Sargent, E. H.; Bisquert, J. Selective contacts drive charge extraction in quantum dot solids via asymmetry in carrier transfer kinetics. *Nat. Commun.* **2013**, *4*, 2272.
15. Tang, J.; Kemp, K. W.; Hoogland, S.; Jeong, K. S.; Liu, H.; Levina, L.; Furukawa, M.; Wang, X. H.; Debnath, R.; Cha, D. K.; Chou, K. W.; Fischer, A.; Amassian, A.; Asbury, J. B.; Sargent, E. H. Colloidal-quantum-dot photovoltaics using atomic-ligand passivation. *Nat. Mater.* **2011**, *10*, 765-771.

16. Wang, L.; Han, J.; Hoy, J.; Hu, F.; Liu, H. Q.; Gentleman, M. M.; Sfeir, M. Y.; Misewich, J. A.; Wong, S. S. Probing differential optical and coverage behavior in nanotube-nanocrystal heterostructures synthesized by covalent versus non-covalent approaches. *Dalton Trans.* **2014**, *43*, 7480-7490.
17. Liu, I. S.; Lo, H.-H.; Chien, C.-T.; Lin, Y.-Y.; Chen, C.-W.; Chen, Y.-F.; Su, W.-F.; Liou, S.-C. Enhancing photoluminescence quenching and photoelectric properties of CdSe quantum dots with hole accepting ligands. *J. Mater. Chem.* **2008**, *18*, 675-682.
18. Wuister, S. F.; de Mello Donegá, C.; Meijerink, A. Influence of Thiol Capping on the Exciton Luminescence and Decay Kinetics of CdTe and CdSe Quantum Dots. *J. Phys. Chem. B* **2004**, *108*, 17393-17397.
19. Yu, K.; Lu, G.; Chen, K.; Mao, S.; Kim, H.; Chen, J. Controllable photoelectron transfer in CdSe nanocrystal-carbon nanotube hybrid structures. *Nanoscale* **2012**, *4*, 742-746.
20. Robel, I.; Bunker, B. A.; Kamat, P. V. Single-walled carbon nanotube-CdS nanocomposites as light-harvesting assemblies: Photoinduced charge-transfer interactions. *Adv. Mater.* **2005**, *17*, 2458.
21. Hines, D. A.; Forrest, R. P.; Corcelli, S. A.; Kamat, P. V. Predicting the Rate Constant of Electron Tunneling Reactions at the CdSe-TiO_2 Interface. *J. Phys. Chem. B* **2015,** *119*, 7439–7446.
22. Weaver, J. E.; Dasari, M. R.; Datar, A.; Talapatra, S.; Kohli, P. Investigating Photoinduced Charge Transfer in Carbon Nanotube-Perylene-Quantum Dot Hybrid Nanocomposites. *ACS Nano* **2010**, *4*, 6883-6893.
23. Zhu, N.; Zheng, K.; Karki, K. J.; Abdellah, M.; Zhu, Q.; Carlson, S.; Haase, D.; Žídek, K.; Ulstrup, J.; Canton, S. E.; Pullerits, T.; Chi, Q. Sandwiched confinement of quantum dots in graphene matrix for efficient electron transfer and photocurrent production. *Sci. Rep.* **2015**, *5*, 9860.
24. Hahner, G. Near edge X-ray absorption fine structure spectroscopy as a tool to probe electronic and structural properties of thin organic films and liquids. *Chem. Soc. Rev.* **2006**, *35*, 1244-1255.
25. De Jesus, L. R.; Dennis, R. V.; Depner, S. W.; Jaye, C.; Fischer, D. A.; Banerjee, S. Inside and Outside: X-ray Absorption Spectroscopy Mapping of Chemical Domains in Graphene Oxide. *J. Phys. Chem. Lett.* **2013**, *4*, 3144-3151.
26. Kuznetsova, A.; Popova, I.; Yates, J. T.; Bronikowski, M. J.; Huffman, C. B.; Liu, J.; Smalley, R. E.; Hwu, H. H.; Chen, J. G. G. Oxygen-containing functional groups on single-wall carbon nanotubes: NEXAFS and vibrational spectroscopic studies. *J. Am. Chem. Soc.* **2001**, *123*, 10699-10704.
27. Wang, Z.; Wu, L.; Zhou, J.; Cai, W.; Shen, B.; Jiang, Z. Magnetite Nanocrystals on Multiwalled Carbon Nanotubes as a Synergistic Microwave Absorber. *J. Phys. Chem. C* **2013**, *117*, 5446-5452.
28. Zhou, J. G.; Fang, H. T.; Maley, J. M.; Ko, J. Y. P.; Murphy, M.; Chu, Y.; Sammynaiken, R.; Sham, T. K. An X-ray Absorption, Photoemission, and Raman Study of the Interaction between SnO_2 Nanoparticle and Carbon Nanotube. *J. Phys. Chem. C* **2009**, *113*, 6114-6117.
29. Koroteev, V. O.; Bulusheva, L. G.; Asanov, I. P.; Shlyakhova, E. V.; Vyalikh, D. V.; Okotrub, A. V. Charge Transfer in the MoS_2/Carbon Nanotube Composite. *J. Phys. Chem. C* **2011**, *115*, 21199-21204.
30. Yueh, C. L.; Jan, J. C.; Chiou, J. W.; Pong, W. F.; Tsai, M. H.; Chang, Y. K.; Chen, Y. Y.; Lee, Y. F.; Tseng, P. K.; Wei, S. L.; Wen, C. Y.; Chen, L. C.; Chen, K. H. Electronic

structure of the Fe-layer-catalyzed carbon nanotubes studied by x-ray-absorption spectroscopy. *Appl. Phys. Lett.* **2001**, *79*, 3179-3181.
31. Chen, G. G.; Bandow, S.; Margine, E. R.; Nisoli, C.; Kolmogorov, A. N.; Crespi, V. H.; Gupta, R.; Sumanasekera, G. U.; Iijima, S.; Eklund, P. C. Chemically doped double-walled carbon nanotubes: Cylindrical molecular capacitors. *Phys. Rev. Lett.* **2003**, *90*, 257403.
32. do Nascimento, G. M.; Hou, T.; Kim, Y. A.; Muramatsu, H.; Hayashi, T.; Endo, M.; Akuzawa, N.; Dresselhaus, M. S. Double-wall carbon nanotubes doped with different Br_2 doping levels: a resonance Raman study. *Nano Lett.* **2008**, *8*, 4168-4172.
33. do Nascimento, G. M.; Hou, T.; Kim, Y. A.; Muramatsu, H.; Hayashi, T.; Endo, M.; Akuzawa, N.; Dresselhaus, M. S. Comparison of the Resonance Raman Behavior of Double-Walled Carbon Nanotubes Doped with Bromine or Iodine Vapors. *J. Phys. Chem. C* **2009**, *113*, 3934-3938.
34. Cambedouzou, J.; Sauvajol, J. L.; Rahmani, A.; Flahaut, E.; Peigney, A.; Laurent, C. Raman spectroscopy of iodine-doped double-walled carbon nanotubes. *Phys. Rev. B* **2004**, *69*, 235422.
35. do Nascimento, G. M.; Hou, T.; Kim, Y. A.; Muramatsu, H.; Hayashi, T.; Endo, M.; Akuzawa, N.; Dresselhaus, M. S. Behavior of the high frequency Raman modes of double-wall carbon nanotubes after doping with bromine or iodine vapors. *Carbon* **2011**, *49*, 3585-3596.
36. Souza, A. G.; Endo, M.; Muramatsu, H.; Hayashi, T.; Kim, Y. A.; Barros, E. B.; Akuzawa, N.; Samsonidze, G. G.; Saito, R.; Dresselhaus, M. S. Resonance Raman scattering studies in Br_2-adsorbed double-wall carbon nanotubes. *Phys. Rev. B* **2006**, *73*, 235413.
37. Li, Y. F.; Hatakeyama, R.; Kaneko, T.; Izumida, T.; Okada, T.; Kato, T. Synthesis and electronic properties of ferrocene-filled double-walled carbon nanotubes. *Nanotechnology* **2006**, *17*, 4143-4147.
38. Rauf, H.; Pichler, T.; Pfeiffer, R.; Simon, F.; Kuzmany, H.; Popov, V. N. Detailed analysis of the Raman response of n-doped double-wall carbon nanotubes. *Phys. Rev. B* **2006**, *74, 235419*.
39. Zhang, L. H.; Jia, Y.; Wang, S. S.; Li, Z.; Ji, C. Y.; Wei, J. Q.; Zhu, H. W.; Wang, K. L.; Wu, D. H.; Shi, E. Z.; Fang, Y.; Cao, A. Y. Carbon Nanotube and CdSe Nanobelt Schottky Junction Solar Cells. *Nano Lett.* **2010**, *10*, 3583-3589.
40. Bang, J. H.; Kamat, P. V. Quantum Dot Sensitized Solar Cells. A Tale of Two Semiconductor Nanocrystals: CdSe and CdTe. *ACS Nano* **2009**, *3*, 1467-1476.
41. Bolotin, K. I.; Sikes, K. J.; Jiang, Z.; Klima, M.; Fudenberg, G.; Hone, J.; Kim, P.; Stormer, H. L. Ultrahigh electron mobility in suspended graphene. *Solid State Commun.* **2008**, *146*, 351-355.
42. Zhao, J.; Cao, M.; Cheng, B.; Wu, G.; Guo, H.; Ai, Y.; Su, X.; Xiao, Y.; Lei, S. Carbon-encapsulated CdSe quantum dot inorganic hybrid nanobelts for high performance photoelectronic devices based on the efficient separation and transfer of photoinduced holes. *J. Mater. Chem. C* **2015**, *3*, 2471-2478.
43. Liu, C.; Lee, S.; Su, D.; Zhang, Z.; Pfefferle, L.; Haller, G. L. Synthesis and Characterization of Nanocomposites with Strong Interfacial Interaction: Sulfated ZrO2 Nanoparticles Supported on Multiwalled Carbon Nanotubes. *J. Phys. Chem. C* **2012**, *116*, 21742-21752.
44. Banerjee, S.; Hemraj-Benny, T.; Balasubramanian, M.; Fischer, D. A.; Misewich, J. A.; Wong, S. S. Surface Chemistry and Structure of Purified, Ozonized, Multiwalled Carbon

Nanotubes Probed by NEXAFS and Vibrational Spectroscopies. *ChemPhysChem* **2004**, *5*, 1416-1422.
45. Leon, V.; Parret, R.; Almairac, R.; Alvarez, L.; Babaa, M. R.; Doyle, B. P.; Ienny, P.; Parent, P.; Zahab, A.; Bantignies, J. L. Spectroscopic study of double-walled carbon nanotube functionalization for preparation of carbon nanotube / epoxy composites. *Carbon* **2012**, *50*, 4987-4994.
46. Winter, A. D.; Larios, E.; Alamgir, F. M.; Jaye, C.; Fischer, D. A.; Omastova, M.; Campo, E. M. Thermo-Active Behavior of Ethylene-Vinyl Acetate I Multiwall Carbon Nanotube Composites Examined by in Situ near-Edge X-ray Absorption Fine-Structure Spectroscopy. *J. Phys. Chem. C* **2014**, *118*, 3733-3741.
47. Leon, V.; Parret, R.; Almairac, R.; Alvarez, L.; Babaa, M. R.; Doyle, B. P.; Ienny, P.; Parent, P.; Zahab, A.; Bantignies, J. L. Spectroscopic study of double-walled carbon nanotube functionalization for preparation of carbon nanotube/epoxy composites. *Carbon* **2012**, *50*, 4987-4994.
48. Lee, J. R. I.; Meulenberg, R. W.; Hanif, K. M.; Mattoussi, H.; Klepeis, J. E.; Terminello, L. J.; van Buuren, T. Experimental observation of quantum confinement in the conduction band of CdSe quantum dots. *Phys. Rev. Lett.* **2007**, *98, 146803*.
49. Wright, J. T.; Meulenberg, R. W. Modification of the conduction band edge energy via hybridization in quantum dots. *Appl. Phys. Lett.* **2012**, *101, 193104*.
50. Liang, Y.; Wang, H.; Zhou, J.; Li, Y.; Wang, J.; Regier, T.; Dai, H. Covalent Hybrid of Spinel Manganese–Cobalt Oxide and Graphene as Advanced Oxygen Reduction Electrocatalysts. *J. Am. Chem. Soc.* **2012**, *134*, 3517-3523.
51. Marcus, R. A. On the Theory of Oxidation-Reduction Reactions Involving Electron Transfer .1. *J. Chem. Phys.* **1956**, *24*, 966-978.
52. Marcus, R. A. Chemical + Electrochemical Electron-Transfer Theory. *Annu. Rev. Phys. Chem.* **1964**, *15*, 155.
53. Tarafder, K.; Surendranath, Y.; Olshansky, J. H.; Alivisatos, A. P.; Wang, L. W. Hole Transfer Dynamics from a CdSe/CdS Quantum Rod to a Tethered Ferrocene Derivative. *J. Am. Chem. Soc.* **2014**, *136*, 5121-5131.
54. Tafen, D.; Prezhdo, O. V. Size and Temperature Dependence of Electron Transfer between CdSe Quantum Dots and a TiO_2 Nanobelt. *J. Phys. Chem. C* **2015**, *119*, 5639-5647.
55. Tvrdy, K.; Frantsuzov, P. A.; Kamat, P. V. Photoinduced electron transfer from semiconductor quantum dots to metal oxide nanoparticles. *Proc. Natl. Acad. Sci.* **2011**, *108*, 29-34.
56. Robel, I.; Kuno, M.; Kamat, P. V. Size-dependent electron injection from excited CdSe quantum dots into TiO2 nanoparticles. *J. Am. Chem. Soc.* **2007**, *129*, 4136.
57. Meulenberg, R. W.; Lee, J. R.; Wolcott, A.; Zhang, J. Z.; Terminello, L. J.; van Buuren, T. Determination of the exciton binding energy in CdSe quantum dots. *ACS Nano* **2009**, *3*, 325-330.
58. Mintmire, J. W.; White, C. T. Electronic and structural properties of carbon nanotubes. *Carbon* **1995**, *33*, 893-902.
59. Shan, B.; Cho, K. First-principles study of work functions of double-wall carbon nanotubes. *Phys. Rev. B* **2006**, *73*, 081401.
60. Jasieniak, J.; Califano, M.; Watkins, S. E. Size-Dependent Valence and Conduction Band-Edge Energies of Semiconductor Nanocrystals. *ACS Nano* **2011**, *5*, 5888-5902.

61. Liu, I. S.; Lo, H. H.; Chien, C. T.; Lin, Y. Y.; Chen, C. W.; Chen, Y. F.; Su, W. F.; Liou, S. C. Enhancing photoluminescence quenching and photoelectric properties of CdSe quantum dots with hole accepting ligands. *J. Mater. Chem.* **2008**, *18*, 675-682.
62. Li, J.; Zhang, M. Atomic insights into adsorption of thiophenol derivatives as corrosion inhibitors for mild steel in hydrochloric acid solution. *Mater. Res. Innovations* **2014**, *18*, 38-42.
63. Kalimuthu, P.; Sivanesan, A.; John, S. A. Charge-transfer interaction of aromatic thiols with 2,3-dichloro-5,6-dicyano-p-benzoquinone: Spectral and quantum mechanical studies. *J. Phys. Chem. A* **2007**, *111*, 12086-12092.
64. Liu, Y.; Gibbs, M.; Puthussery, J.; Gaik, S.; Ihly, R.; Hillhouse, H. W.; Law, M. Dependence of Carrier Mobility on Nanocrystal Size and Ligand Length in PbSe Nanocrystal Solids. *Nano Lett.* **2010**, *10*, 1960-1969.
65. Wang, H.; McNellis, E. R.; Kinge, S.; Bonn, M.; Canovas, E. Tuning Electron Transfer Rates through Molecular Bridges in Quantum Dot Sensitized Oxides. *Nano Lett.* **2013**, *13*, 5311-5315.
66. Kongkanand, A.; Tvrdy, K.; Takechi, K.; Kuno, M.; Kamat, P. V. Quantum dot solar cells. Tuning photoresponse through size and shape control of CdSe-TiO_2 architecture. *J. Am. Chem. Soc.* **2008**, *130*, 4007-4015.
67. Osswald, S.; Flauhaut, E.; Ye, H.; Gogotsi, Y. Elimination of D-band in Raman spectra of double-wall carbon nanotubes by oxidation. *Chem. Phys. Lett.* **2005**, *402*, 422-427.
68. Gyeong Bok, J.; Yoon, M.; Park, J.; Inhee, M.; Joo-Hiuk, S. In *Terahertz spectroscopy of platinum, copper sulfide, and tin oxide nanocrystals-carbon nanotube hybrid nanostructures*, Infrared, Millimeter, and Terahertz Waves, 2009. IRMMW-THz 2009. 34th International Conference on, 21-25 Sept. 2009; 2009; pp 1-2.
69. Campidelli, S.; Sooambar, C.; Lozano Diz, E.; Ehli, C.; Guldi, D. M.; Prato, M. Dendrimer-Functionalized Single-Wall Carbon Nanotubes: Synthesis, Characterization, and Photoinduced Electron Transfer. *J. Am. Chem. Soc.* **2006**, *128*, 12544-12552.
70. Kataura, H.; Kumazawa, Y.; Maniwa, Y.; Umezu, I.; Suzuki, S.; Ohtsuka, Y.; Achiba, Y. Optical properties of single-wall carbon nanotubes. *Synth. Met.* **1999**, *103*, 2555-2558.
71. Bandow, S.; Chen, G.; Sumanasekera, G. U.; Gupta, R.; Yudasaka, M.; Iijima, S.; Eklund, P. C. Diameter-selective resonant Raman scattering in double-wall carbon nanotubes. *Phys. Rev. B* **2002**, *66*, 075416.
72. Villalpando-Paez, F.; Son, H.; Nezich, D.; Hsieh, Y. P.; Kong, J.; Kim, Y. A.; Shimamoto, D.; Muramatsu, H.; Hayashi, T.; Endo, M.; Terrones, M.; Dresselhaus, M. S. Raman Spectroscopy Study of Isolated Double-Walled Carbon Nanotubes with Different Metallic and Semiconducting Configurations. *Nano Lett.* **2008**, *8*, 3879-3886.
73. Rahmani, A.; Sauvajol, J. L.; Rols, S.; Benoit, C. Nonresonant Raman spectrum in infinite and finite single-wall carbon nanotubes. *Phys. Rev. B* **2002**, *66*, 125404.
74. Huynh, W. U.; Dittmer, J. J.; Teclemariam, N.; Milliron, D. J.; Alivisatos, A. P.; Barnham, K. W. J. Charge transport in hybrid nanorod-polymer composite photovoltaic cells. *Phys. Rev. B* **2003**, *67*,115326.
75. Green, A. A.; Hersam, M. C. Properties and application of double-walled carbon nanotubes sorted by outer-wall electronic type. *ACS Nano* **2011**, *5*, 1459-1467.
76. Liu, K.; Wang, W.; Xu, Z.; Bai, X.; Wang, E.; Yao, Y.; Zhang, J.; Liu, Z. Chirality-dependent transport properties of double-walled nanotubes measured in situ on their field-effect transistors. *J. Am. Chem. Soc.* **2009**, *131*, 62-63.

Chapter 5. Ligand-induced dependence of charge transfer in nanotube–quantum dot heterostructures

5.1. Introduction

Semiconducting quantum dots (QDs) have been considered as candidate materials for the next generation of photovoltaic devices as a result of their unique attributes including (a) size-dependent opto-electronic properties, (b) a potential to maximize the production of hot photogenerated carriers through a multi-exciton generation effect, which would increase photoconversion efficiency, (c) a remarkable photostability, including resistance to photoinduced quenching, as well as (d) high extinction coefficients.[1] Double-walled carbon nanotubes (DWNTs), consisting of two coaxial tubules, represent a particularly interesting variation on the carbon-based anisotropic motif. By contrast with single-walled carbon nanotubes (SWNTs), in DWNTs, the outer shell of these structures can be selectively chemically functionalized while maintaining the physical integrity and hence, the favorable opto-electronic properties of the inner shell.[2-4] As such, DWNT - QD heterostructures, which merge the desirable properties of individual nanoscale constituent components into an integrated whole, embody a conceptually unusual architectural design in the field of photovoltaic cells.[5-8]

Typically, as-prepared QDs are capped with organic bulky long-chain, alkyl-based ligands, such as but not limited to trioctylphosphine oxide, tri-*n*-butylphosphine, oleylamine, hexadecylamine, and oleic acid. The presence of these molecular capping agents stabilizes QDs within a colloidal dispersion and allows for reproducible and precise control over QD size and by extension, the corresponding tuning of the QD bandgap.[9, 10] However, by their very structure, these unwieldy, bulky, and often non-conjugated ligands can effectively hamper charge transport and flow, which are inherently critical parameters to optimize for improving upon photovoltaic

cell efficiency. Moreover, due to the insulating properties of these ligands, they often act as a potential barrier to the charge transport capability between adjacent nanoparticles and nanostructures.[11, 12]

This issue can be potentially tackled by properly choosing electroactive ligand molecules and by performing the subsequent ligand exchange processes with the native ligands, in order to chemically modify and coat the external surfaces of these QDs with more conductive entities.[13] In this light, to tailor QDs for desirable photovoltaic behavior, a wide variety of ligands have been studied as candidates for potential capping agents of these nanoparticles, including bidentate aliphatic and aromatic thiols,[14] primary amines,[15] carboxylic acids,[16] and halide ions.[17] The judicious choice of ligands and the chemical modification of the outer surfaces of QDs through ligand exchange reactions are crucial for a number of reasons.

First, ligands can help to passivate surface defects, which play an important role in the surface-related emission and corresponding photostability of QDs. *Second*, on a relevant device level, the electronic properties of coupled colloidal QD solids can be precisely tuned through modification of the QD surface chemistry *via* ligand exchange, and such an approach designates a complementary strategy to control the QD bandgap through predictable variation of nanocrystal size.[18] *Third*, specific short bidentate ligands, such as ethanedithiol, not only reduce the interdot separation, thereby facilitating exciton dissociation and subsequent carrier transport towards the collecting contacts,[17, 19] but also serve as a molecular ligand bridge with which to connect QDs with other charge transporting components, such as the DWNTs herein, through either covalent or non-covalent attachment strategies.[20] Recently, our group has already shown that the synthesis of DWNT-CdSe QD heterostructures, using both covalent and non-covalent π-π conjugation protocols, mediated by specially chosen, short-chain ligands, 2-aminoethanethiol[21]

and 4-aminothiophenol,[22] is not only chemically feasible but also that there is a degree of charge transfer from the CdSe QDs to the DWNTs with the heterostructure itself.

Therefore, by deliberatively altering the identity of the ligands, we can vary the ligand length, the nature of the chemical binding groups, and the associated dipole moments, thereby leading to a shift in the positions of the QD valence band maximum and conduction band minimum. In doing so, we can potentially tune for efficient charge transfer, which is crucial to the development of QD-based photovoltaics.

With respect to previous and relevant studies on probing photo-induced charge transfer process in the CNT-QD systems, Weaver *et al.* reported on both electron and hole transfer from both CdSe QDs and the thiol-containing perylene compound (ETPTCDI) molecular linkers to the underlying CNTs, denoting processes which effectively increased the overall photon harvesting efficiency of the resulting nanocomposite.[23] In a separate work, based upon steady state and time resolved photoluminescence studies, rapid electron transport was observed between QDs and CNTs within ligand-free CdSe QD - CNT composites that had been fabricated using ultrasonication.[24] Additional examples abound. For example, Guo *et al.* designed graphene-CdSe QD composites bridged together by pyridine linkers, which not only enhanced the adhesion of QDs onto the graphene surface but also provided for good electronic coupling between the CdSe QDs and the underlying two-dimensional carbon allotrope, thereby leading to injection of *n*-type carriers within the graphene phase.[25]

Yet, although substantial research efforts have been expended with respect to analyzing charge transfer within CNT-QD composites, the precise role and function of the ligand molecules in this process is not entire clear. To the best of our knowledge, there have been very few if any systematic efforts, involving either qualitative or quantitative studies, with the

objective of exploiting a cumulative combination of both experimental and theoretical techniques within the context of carbon nanotube (CNT)-QD systems to correlate the effect of varying ligand molecules with interfacial charge transfer in these nanocomposites.

Hence, in the current Chapter, our efforts are focused on gaining fundamental insights into charge transfer behavior across nanoscale interfaces within covalently bound DWNT-CdSe composite heterostructures as a function of the chemical nature of mediating ligand molecules, i.e. *p*-phenylenediamine (PPD), 2-aminoethanethiol (AET), and 4-aminothiophenol (ATP), respectively. The 3 ligand molecules we have deliberately chosen here are relatively short structures, with either a terminal –SH or $–NH_2$ group, possessing a strong affinity for Cd sites on the QD surface; the pendant $–NH_2$ group at the other end of the molecule can be potentially utilized to initiate possible amide formation with acid-functionalized CNTs in order to covalently generate the desired heterostructures. It is worth noting that these -SH or $–NH_2$ capped ligands are 'hole –scavengers'[26] and can act as effective acceptors for photogenerated holes.

Our group has previously reported on the presence of effective hole transfer from CdSe QDs to underlying DWNT networks, connected through ligands, i.e. using both the AET[27] and the ATP[22] ligands in separate studies. Nevertheless, despite the well-studied hole transfer behavior, electron transfer also exists in these types of systems, due to the band alignment of CdSe QDs with either adjacent DWNTs or metal oxides.[28, 29]

Therefore, in the current manuscript, the electron transfer processes in the DWNT-ligand-CdSe QD heterostructures will be probed through a unique combination of data acquired from complementary experimental techniques such as (i) transmission electron microscopy (*TEM*) images in order to nail down morphology and heterostructure formation as well as the corresponding QD coverage density within our various CNT-CdSe QD nanocomposites; (ii)

near-edge X-ray absorption fine structure (*NEXAFS*) spectroscopy, which will provide information about the occupancy of the low-lying unoccupied electronic density of states, specific to the CdSe QDs and DWNTs;[30] (iii) *Raman* spectra of both constituent CNTs and the resulting heterostructures, with a focus towards analyzing and understanding relative changes in the positions and intensities of distinctive CNT-specific, Raman-active vibrational modes, which are sensitive to chemical doping;[31-34] and (iv) *electrical transport* measurements of heterostructures as manifested through the construction of field-effect transistor (FET) devices in order to monitor the effect of the 'doping' of DWNTs, induced by the presence of QDs. We emphasize that rarely if ever have all of these experimental techniques been collectively and advantageously used in a constructive, synergistic combination to analyze and to fundamentally understand the opto-electronic behavior of nanoscale composites of any composition.

As a unique corroboration for our insights, we have used theoretical X-ray absorption spectra (XAS) results, calculated based on Fermi's Golden Rule, to simulate, compare, and ultimately correlate computed results with measured NEXAFS experimental data in order to potentially test for and verify predictions from experiments. Although there are several papers that already deal with a comparison between DFT theoretical calculations and NEXAFS experimental data,[35-38] this current effort herein represents, to the best of our knowledge, the first attempt to comprehensively model a complex CNT-QD nanoscale heterostructure composite system generated using various ligands, through the interpretation of (i) an ensemble of theoretical molecular modeling and DFT calculations, buttressed by (ii) a suite of microscopy and spectroscopy measurements in addition to (iii) device data. That is, we seek a holistic picture and understanding of linker-mediated charge interactions between the CdSe QDs and DWNTs.

5.2. Results and Discussion

We have chosen to organize our discussion on the key scientific issue of how systematically varying QD ligands alters charge transfer within composite nanoscale motifs through the 'prism' of particular data sets obtained from various complementary characterization techniques. Nonetheless, it is worth pointing out that to specifically deduce the effect of ligand identity, i.e. with all other parameters kept constant to ensure consistency, DWNT-CdSe heterostructures incorporating QDs with average diameters of ~4.1 nm *only* were generated by a covalent attachment strategy through the mediation of intervening PPD, AET, and ATP ligand molecules, respectively (Scheme 2.2 in Chapter 2).

5.2.1. Structural Characterization.

Low magnification TEM data in Figure 5.1 depicted the formation of all three, as-prepared heterostructures. The corresponding average coverage density on the underlying DWNT surface was noted to be 40 ± 12 dots for PPD-capped QDs, possessing an average diameter of 4.1 ± 0.9 nm (Figure 5.1A); 450 ± 55 dots for AET-capped QDs, maintaining average diameters of 4.1 ± 0.7 nm (Figure 5.1B); and 430 ± 30 dots with ATP-capped QDs, associated with average diameters of 3.9 ± 0.5 nm (Figure 5.1C), respectively. The DWNTs used measured 500 nm in length and 30 nm in diameter for a typical bundle.

The use of 4.1 nm average diameter, AET and ATP-capped CdSe QDs resulted in substantially larger quantities of QDs attached onto the underlying DWNT surfaces (i.e. about 10 times as much as compared with their PPD analogues). Moreover, we noted a far more uniform nanoparticle coverage for these specific functionalized QDs on the sidewalls of the DWNT bundles as compared with heterostructures synthesized using PPD-CdSe QDs. These collective observations can be explained by the fact that the –SH group associated with the AET and ATP

ligands possesses a stronger affinity for the CdSe QD surface by contrast with the -NH_2 group, thereby resulting in a greater coverage of these thiol-based ligands and consequently a higher probability and accessibility for QDs to be attached onto the DWNT surface frameworks.[39, 40] The measured *d*-spacings of 3.52 Å and 3.41 Å in Figure 5.1 D-F could be ascribed to the *d*-spacing of the (002) lattice plane of the hexagonal phase of CdSe as well as to the interlayer spacing of the graphitic layer within DWNTs, respectively. One other feature worthy of note is that AET-QDs (Figure 5.1E) appear to have a larger tendency to aggregate as compared with their PPD-QD (Figure 5.1D) and ATP-QD (Figure 5.1F) counterparts, a finding which could possibly be ascribed to the shorter interdot distance as a result of the shorter ligand length associated with AET.

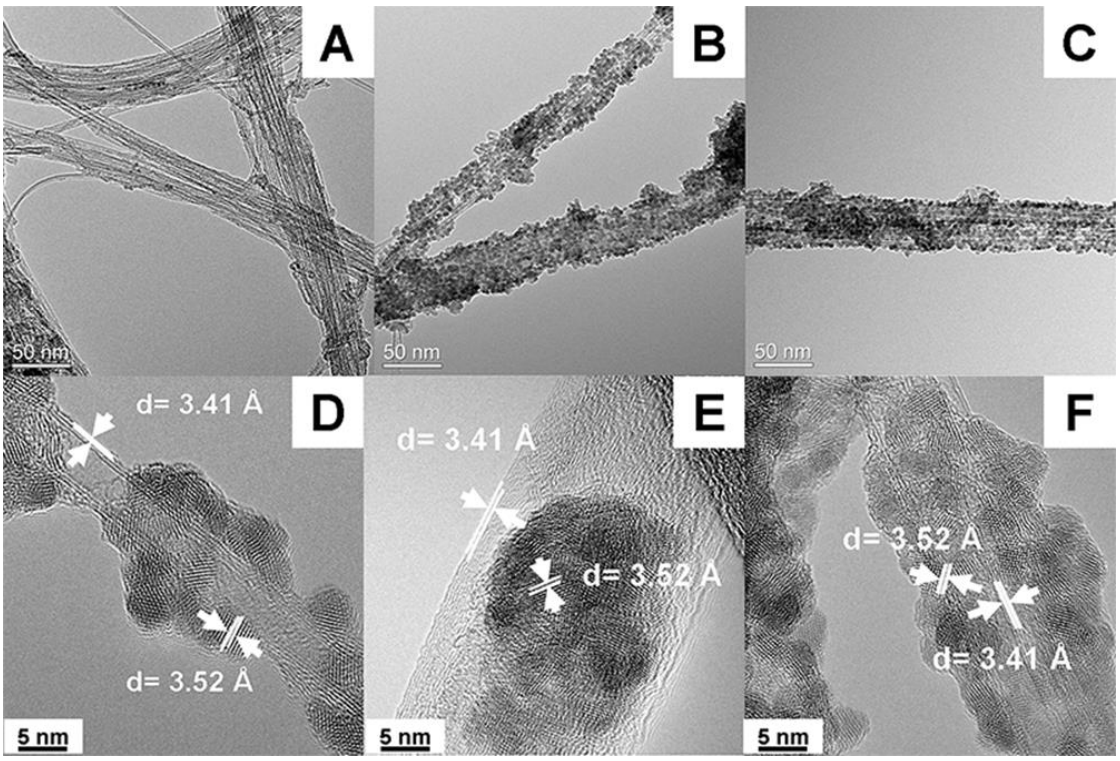

Figure 5.1. (**A, B, and C).** TEM images and (**D, E, and F)** HRTEM images of DWNT-PPD-CdSe QD, DWNT-AET-CdSe QD, and DWNT-ATP-CdSe QD heterostructures, respectively, synthesized by an amide-mediated covalent attachment strategy. (Reprinted with permission from *Nanoscale*, **2016**, DOI**:** 10.1039/C6NR03091B. Copyright 2016 Royal Society of Chemistry.)

To further confirm this observation, TEM and HRTEM images of various ligand-capped CdSe QDs have been provided in Figure 5.2. We confirm that the AET-QDs, highlighted by the yellow circles, tend to be more clustered, as compared with their other two analogues.

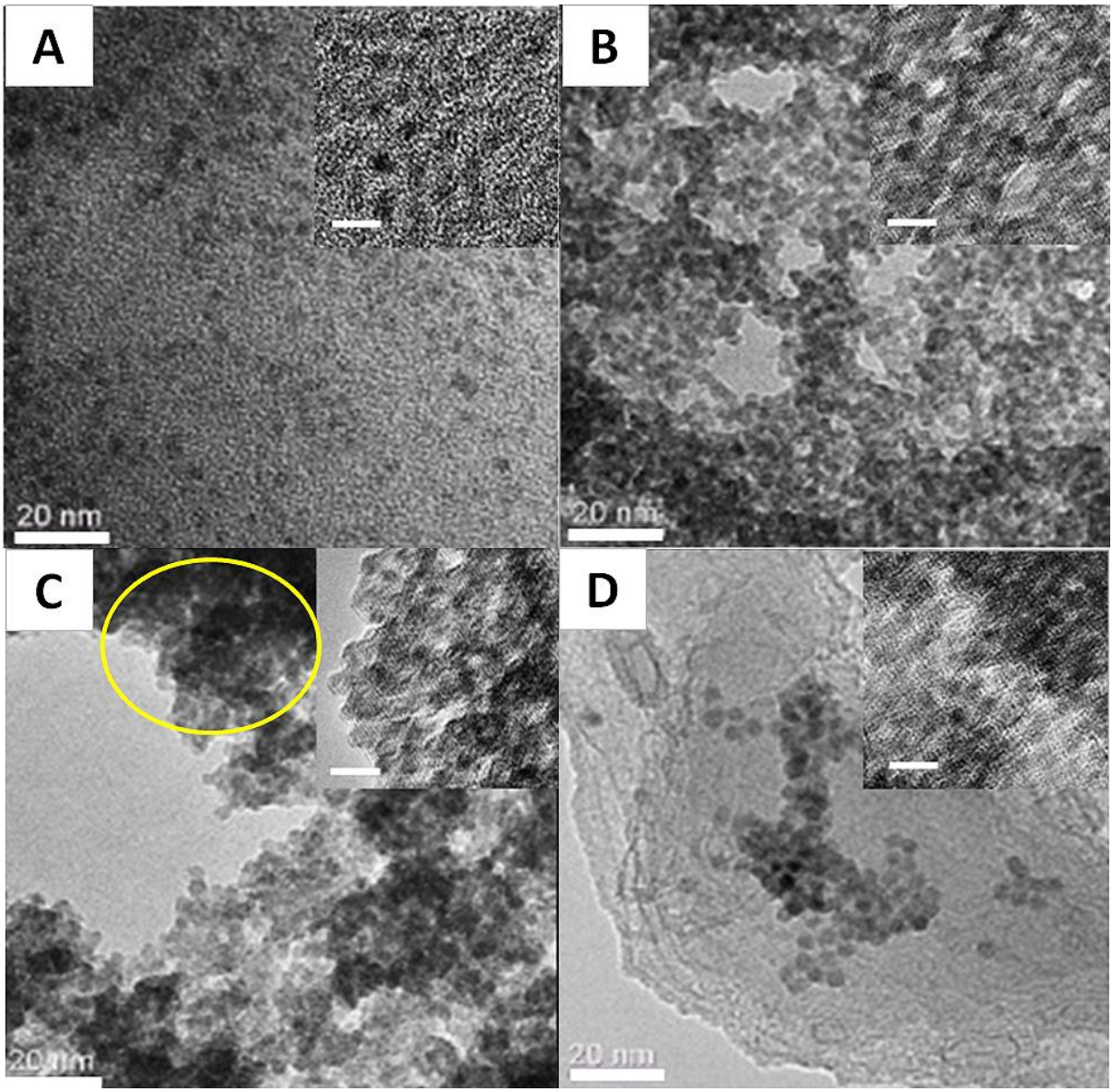

Figure 5.2. TEM images of (A) as-prepared, (B) PPD-capped, (C) AET-capped, and (D) ATP-capped CdSe QDs. Insets shows corresponding HRTEM images and the scale bar in insets are 5 nm. The aggregated AET-capped CdSe QDs are highlighted in yellow circle. (Reprinted with permission from *Nanoscale*, **2016**, DOI**:** 10.1039/C6NR03091B. Copyright 2016 Royal Society of Chemistry.)

To further investigate the surface functionalities as well as confirm the successful ligand exchange process, FT-IR data are present in Figure 5.3. The presence of the various ligand terminated moieties (i.e. PPD, AET and ATP) on the CdSe QD surfaces expected after ligand exchange was confirmed by FTIR analysis, as shown in Figure 5.3. Specifically, for the as-prepared CdSe QDs, the surface capping agent is TOPO.[41] The sharp P=O stretch of the TOPO near 1147 cm^{-1} is red-shifted to 1070 cm^{-1} and is strongly broadened, which could imply the presence of multidentate coordination through the occupation of bridging sites on the Cd surface.[42, 43] Significantly, in the case of CdSe QDs capped with thiol ligands such as AET and ATP, after the respective ligand exchange reactions involved, the absence of a distinctive R-SH peak near 2400-2500 cm^{-1} suggests that all thiol pendant moieties in these ligands are likely to be completely bound onto the surfaces of the CdSe QDs.[44] Moreover, the two N-H stretching bands for free PPD species initially located near 3400-3300 and 3330-3250 cm^{-1}, respectively, are distinctly absent in the corresponding spectra of the capped dots, thereby confirming that PPD is likely bound onto the CdSe QD surface.

In terms of other noticeable peaks, aromatic ligands such as PPD and ATP give rise to characteristic peaks for aromatic rings near the 1530-1600 cm^{-1}, 1400-1500 cm^{-1}, and 1160-1175 cm^{-1} regions for the C=C asymmetric stretching mode, the C=C symmetric stretching mode, and the C-H bending mode, respectively. The broad OH vibration peak located at 3430 cm^{-1} and found in the AET-CdSe QDs likely emanates from water. Water adsorbs onto the surfaces of CdSe quantum dots, because of their high surface-to volume ratio. The bands located at around 2925 cm^{-1} and 2850 cm^{-1} in the ligand-exchanged QDs can be assigned to a C–C–H stretching mode, implying that there are still small, remnant amounts of TOPO immobilized onto the surfaces of the CdSe quantum dots, even after the ligand exchange process.

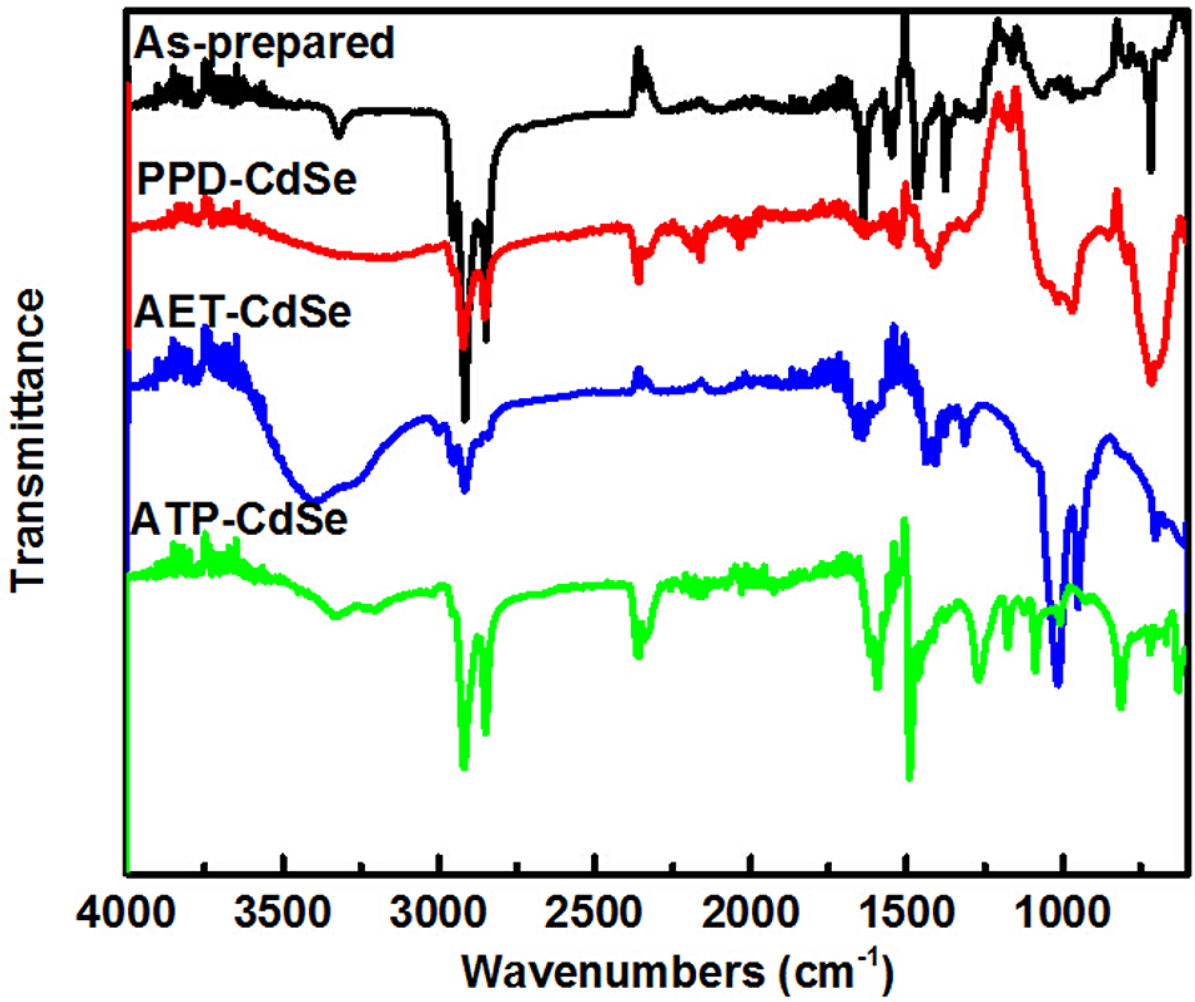

Figure 5.3 FT-IR spectra of as-prepared, PPD, AET, and ATP-capped CdSe QDs possessing average diameters of 4.1 nm, respectively. (Reprinted with permission from *Nanoscale*, **2016**, DOI**:** 10.1039/C6NR03091B. Copyright 2016 Royal Society of Chemistry.)

5.2.2. NEXAFS Spectra.

Figures 5.4 highlighted the corresponding C and O *K*-edges as well as the Cd M_3-edge associated with the DWNT-PPD/AET/ATP capped-CdSe QD heterostructures. By means of comparison, all of the data associated with the various edges within the three ligand systems tested have been plotted on the same scale.

C *K*-edge. In principle, the C *K*-edge spectra correspond to the dipole transitions from C 1s core states to 2p-derived electronic states. The sharp peak at around 285.4 eV can be ascribed

to a C 1s to the C=C 2p π* transition. The broad peak at 292-294 eV can be assigned to a convolution of three C 1s to C-C σ* transitions.[45, 46] In addition, the peaks at ~288.1 eV and ~289.1 eV can be attributed to the π* C=O and σ* C-O functionalities, respectively.[30, 47] Moreover, the areas under resonance (or peak intensity) of the various π* and σ* features are approximately proportional to the extent of the electronic density of the unoccupied C 2p derived states. Hence, the increased intensities of these features can be correlated either with the increased numbers of unoccupied C 2p states or with a charge transfer process taking place between the C 2p orbital and the dopant at the interface.[46, 48, 49]

Experimentally, when the ligands are attached onto the oxidized DWNTs (i.e. red spectra), the C *K*-edge (Figure 5.4A, D, and G) C=C π* transition intensity was found to be enhanced in the AET and ATP systems (black spectra), while no obvious change was observed for the PPD system. The reason for this enhancement will be discussed in the theory section.

After the QD deposition (i.e. blue spectra), we note that in all three of these heterostructures, the C *K*-edge π* transition intensity is either barely affected or perceptibly reduced in magnitude, whereas the σ * C-O transition evinced an enhanced intensity and a narrower peak as compared with the DWNT-PPD / AET / ATP nanoscale hybrid control sample prior to CdSe QD deposition (i.e. red spectra). These data suggest that the CdSe QDs donate charge onto the DWNT C=C π* states, while the sp^3 carbons in the σ* C-O states on the DWNTs may also back donate some charges to the CdSe QDs, possibly through the formation of a C-O-Cd link.[46, 50] One hypothesis consistent with our later theoretical analysis is that the conjugated π* carbons are accepting electrons from the QDs, thereby resulting in a decrease in the unoccupied electronic density of states and giving rise to a suppressed signal, associated with the C=C π* transitions. By contrast, the σ* carbons associated with the oxygenated species are

donating charges to the QDs, thereby causing an increase in the unoccupied electronic density of states and hence, an enhanced peak.

Nevertheless, the amount of charge transfer from DWNTs to CdSe QDs is expected to be negligible as compared with charge transfer in the reverse direction from CdSe QDs to DWNTs, within the CdSe QD – DWNT heterostructures. We hypothesize that the slight increase in the π* C=O band intensity observed with AET-capped QDs may also denote possible evidence for electron transfer from the DWNTs to the QDs through the mediation of the C=O linkage in the derivatized DWNTs, because the absence of a conjugated aromatic system associated with the attached AET ligand itself renders a small, albeit finite, probability for this particular 'back donation' scenario. The broad σ* C-O peak (present in the oxidized and ligand-attached DWNTs) may be ascribed to the presence of σ conjugated structures of varying sizes, i.e. a superposition of σ* resonances. Upon addition of (interaction with) the QDs, some of these structures are chemically eliminated, thereby resulting in the narrowing of the peak.

Cd *M*$_3$-edge. In principle, the Cd M_3-edge is associated with transitions between the Cd 3p initial state and the unoccupied 5s states, which comprise the bottom of the conduction band of CdSe, based on the projected electronic density of states (DOS) proposed by theory. Hence, if the bottom of the CdSe conduction band were to shift by an energy interval, ΔE_c, then the corresponding M_3 absorption edge would shift by an equivalent amount, thereby representing the quantum confinement induced shift in the conduction band.[51, 52] The *M*-edges are known to suffer from weak signals and a large background[51] by contrast with the Cd L_3-edge. Therefore, in order to render these M_3-edges useful for quantitative analysis, multiple replicates of the spectra were collected with increased data integration times in order to obtain higher signal-to-noise ratios and therefore data interpretability.

Experimentally, within the heterostructure data set, the enhanced intensity of the Cd M_3-edge (Figure 5.4B, E, and H) provides direct evidence for charges being withdrawn from CdSe QDs upon deposition onto the DWNTs. Moreover, the heterostructures incorporating AET-QDs appeared to give rise to the largest enhancements observed, as noted by the drastic changes in the Cd M_3 edge (Figure 5.4E), as compared with their aromatic PPD and ATP analogues. This situation may possibly be ascribed to the shorter lengths of the aliphatic ligands, thereby resulting in a more extensive and favorable intermolecular charge transfer as compared with that of analogous bulkier aromatic ligands.[53] Another viable contributive factor is the electron affinity of –SH, which has been calculated to be 2.23 and significantly, is higher in magnitude than that of -NH_2, i.e. 0.71.[54] The implication is that ligands with pendant thiol groups can potentially withdraw more charge from CdSe QDs as compared with their amine-terminating analogues.

Furthermore, it is also worth recalling from the TEM data (Figure 5.1) that the AET-based heterostructure possesses a higher coverage density (about 10 times) as compared with its PPD counterpart, a situation which might contribute to a larger amount of the observed charge transfer. Hence, because the Cd *M* edge spectra of each linker (5.4B, E and H) are pre-to-post edge normalized (to unity), on an atom-by-atom basis, we emphasize that the greatest enhancement of the Cd M_3-edge is detected with the AET-based heterostructure, an observation implying that the highest amount of charge transfer ascribed to the CdSe QDs is associated with the AET-capped CdSe QD system. To gain additional insights into the precise effect of QD coverage density associated with various ligands upon the resulting charge transfer, we have collected and interpreted complementary electrical transport measurements in Section 5.2.5.

O *K*-edge. In terms of the O *K*-edge, the two well-separated absorption features observed can be ascribed to a sharp peak located at 531.8 eV and a broader peak centered at around

539−546 eV. Specifically, the feature at ~531 eV can be potentially assigned to transitions from the O 1s core levels to the π* C=O states derived from carboxylic acid moieties, whereas the broad absorption feature centered at around 539−546 eV can possibly be attributed to the superposition of transitions arising from the O 1s core levels to the final states possessing σ* symmetry, localized on the O−H and C−O bonds. The small peak centered at ~534.6 eV likely derives from the -OH π* transition associated with carboxylic acid species.[55-57]

Experimentally, the π* -OH (534.6 eV) transition in the O *K*-edges (Figure 5.4C, F, and I) originating from carboxylic groups on the DWNT surface diminishes in all three of the heterostructures tested, suggestive of the formation of an amide bond upon QD deposition. Significant increases in both the π* and σ * transitions associated with the O *K*-edge spectra were also observed in all three of the heterostructures analyzed (i.e. blue spectra) as compared with the oxidized DWNT controls (i.e. red spectra), a likely consequence of electrons being withdrawn from the oxygenated functional moieties on the DWNTs after chemical attachment of the adjoining QDs.

From all of the NEXAFS results associated with the C *K*-edge, O *K*-edge, and Cd M_3-edge data, it is reasonable to assert that charge is being transferred from CdSe (i.e. enhanced Cd M_3-edge intensity) to the surface oxidized C-O functionalities (such as carboxylic acid moieties), and finally onto the C=C conjugated network of the ligand-functionalized DWNTs (i.e. as evidenced by an increase in the O *K*-edge π* C=O and σ* C-O transition intensities and a corresponding reduction in the C *K*-edge π* C=C transition intensity). We also expect a minor degree of charge back donation from DWNTs to QDs, as manifested by alterations in the σ* C-O bond transitions (i.e. an enhanced C *K*-edge σ* C-O intensity after QD deposition).

It is also noteworthy that although the AET system demonstrates the largest enhancement in the Cd M_3-edge data, in the corresponding C *K*-edge spectra, the ATP system appears to evince the largest suppression in the π^* C=C transition (Figure 5.4G), while comparable changes within AET and PPD-based systems are similar to each other. Hence, the C *K*-edge data would seem to suggest that the largest amount of charge transferred from the QDs to the underlying DWNTs occurs within the ATP-based heterostructures. Therefore, in order to further probe the effect of the intrinsic properties of each ligand upon the individual charge transfer processes observed, to normalize for the effect of QD coverage density, and to reveal more detailed insight into the charge transfer process from the QDs to the DWNTs as manifested by changes in the experimental C *K*-edge data, theoretical calculations of the C *K*-edge NEXAFS spectra have been performed on these various ligand systems, possessing identical QD coverage.

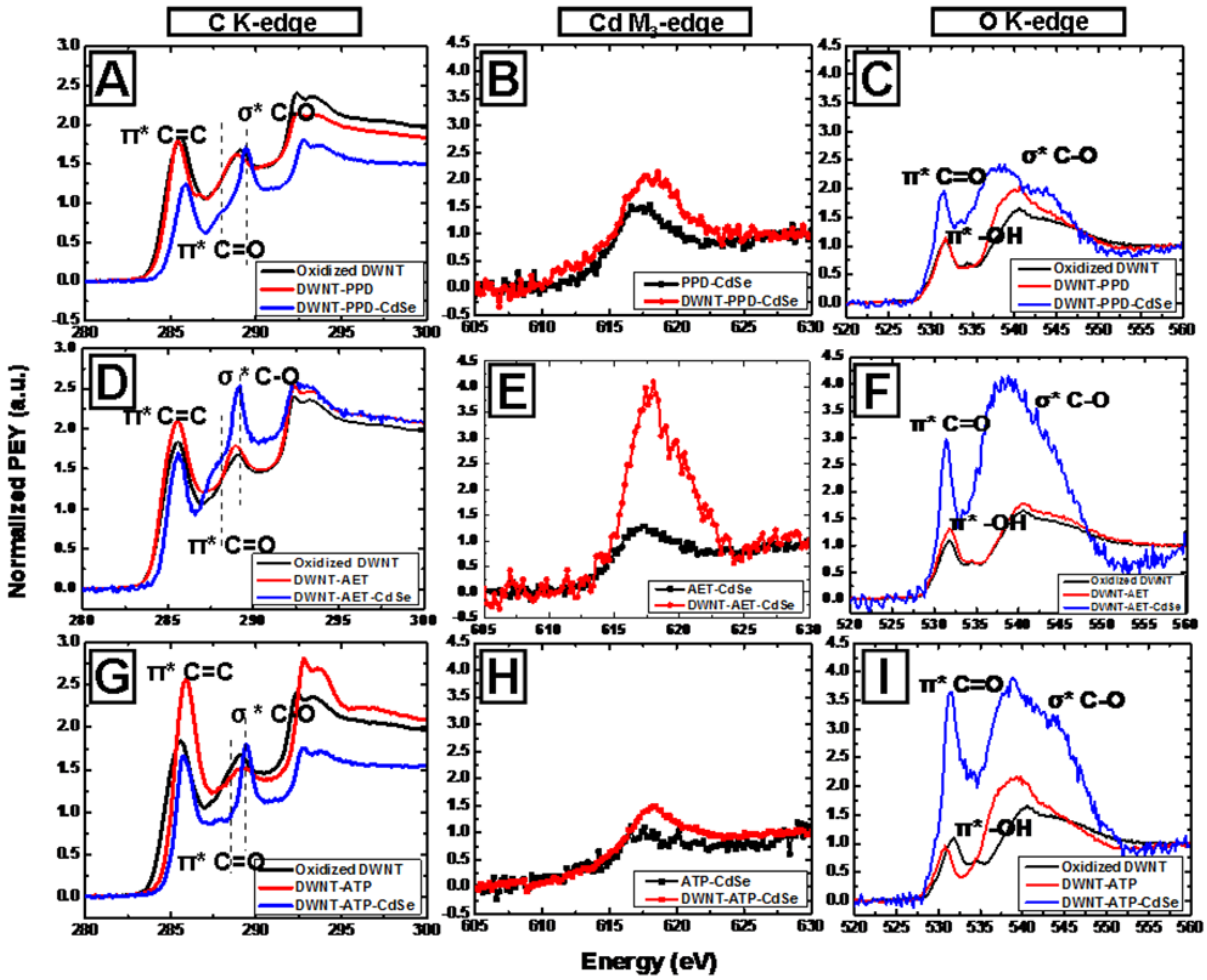

Figure 5.4. Probing the effect of varying ligands. Experimental (**A, D, and G)** C *K*-edge, (**B, E, and H**) Cd M_3-edge, and (**C, F, and I**) O *K*-edge spectra of DWNT-PPD-CdSe QD, DWNT-AET-CdSe QD, and DWNT-ATP-CdSe QD systems, respectively. (Reprinted with permission from *Nanoscale*, **2016**, DOI**:** 10.1039/C6NR03091B. Copyright 2016 Royal Society of Chemistry.)

5.2.3. Theoretical Modeling.

In the theoretical models (see Chapter 2 for full details), a flat graphene sheet measuring 3 nm x 3 nm, with 20 carboxyl group defects randomly spaced around the interior of the sheet, was created. The presence of the linker molecules was subsequently built into this 'defected' system, with the ligand molecules attached at the same 'defected' sites in the graphene sheet. QDs possessing a relaxed geometry of 1.3 nm were subsequently attached onto the ligand-

capped graphene. Figure 5.5 overlays the experimental (purple) with theoretical (green) C *K*-edge NEXAFS spectra of various linker-modified graphene species (Figure 5.5A, C and E) as well as of the corresponding linker-derivatized graphene-CdSe QD heterostructures (Figure 5.5B, D and F), with theory shifted to align with the experimental σ* peak located at 293 eV. Both data sets have been normalized, such that the σ* peak located at 293 eV has a spectral intensity of 1. A comparison highlights the overall agreement in terms of the relative positions and intensities of the π^* and σ* peaks associated with the various species. The calculated C *K*-edge spectra of pristine graphene (red), of defect-ridden (oxidized) graphene (blue), of various ligand species bound to graphene (green), as well as of heterostructures characterized by CdSe QDs attached to various ligand-modified graphene species (purple) are displayed in Figure 5.6.

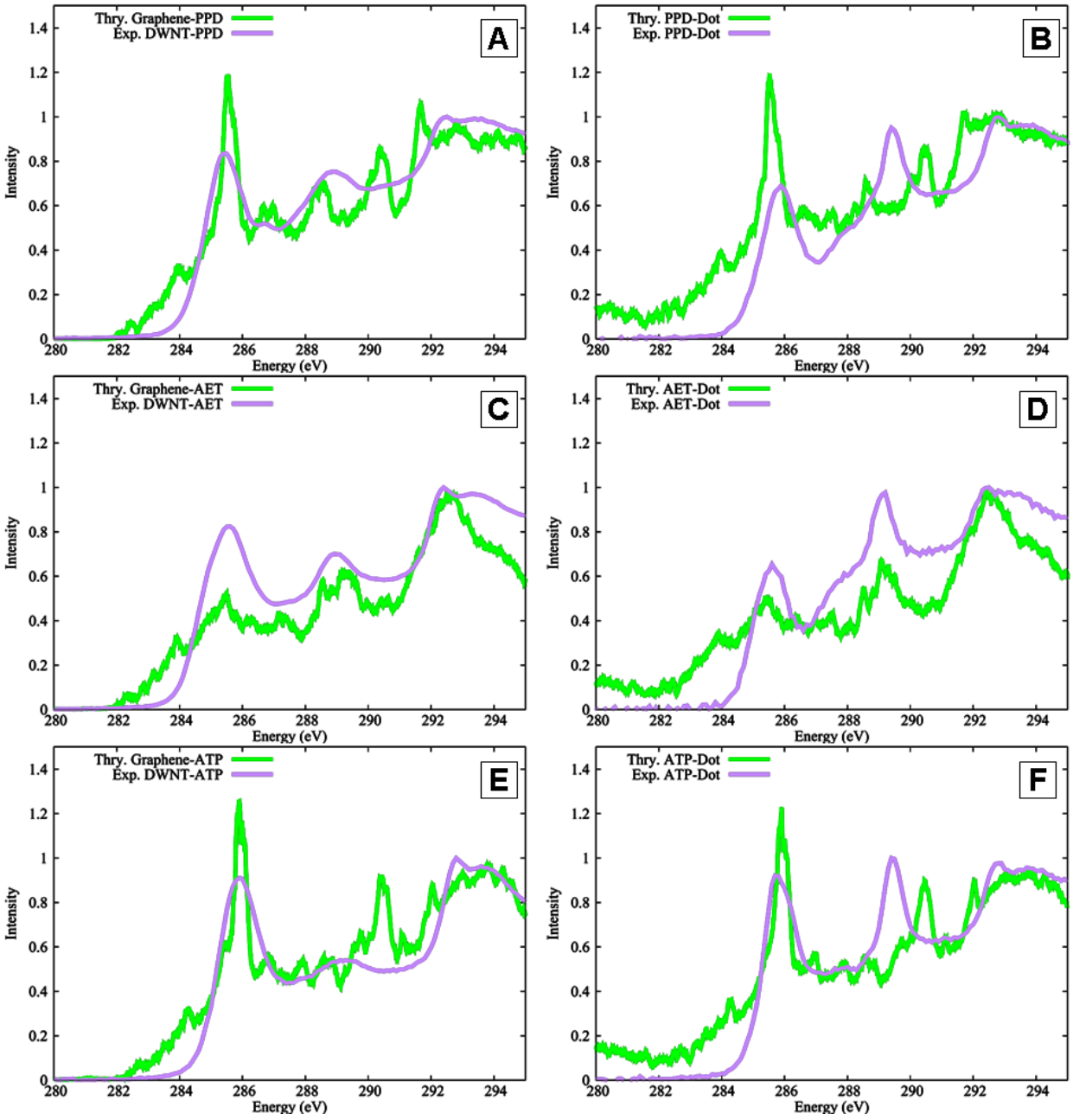

Figure 5.5. Comparisons of theoretically calculated versus experimental C *K*-edge NEXAFS spectra for the graphene-bound PPD/AET/ATP composites (**A, C, and E**), as well as for the graphene-bound PPD/AET/ATP-CdSe QD heterostructures (**B, D, and F**), respectively. (Reprinted with permission from *Nanoscale*, **2016**, DOI**:** 10.1039/C6NR03091B. Copyright 2016 Royal Society of Chemistry.)

Before QD deposition (ligand bound to graphene systems). As previously mentioned, with respect to the experimental NEXAFS data connected with AET/ ATP-bound DWNTs (i.e.

red curves in Figure 5.4D and G), the C=C π^*(~279 eV) intensity appears to be enhanced relative to that of oxidized graphene alone (i.e. black curves in Figure 5.4D and G). Such an enhancement was observed as well with the simulated spectra for both calculated AET and ATP-bound graphene (i.e. green curves in Figure 5.6B and C) as compared with the oxidized graphene alone (i.e. blue curves in Figure 5.6B and C). It is noted that both in the experimental and theoretical systems, the ATP-bound graphene evinced a more obvious enhancement as compared with its AET-linked analogue. It is also worth mentioning that the enhancement is most obvious with the calculated PPD-bound graphene system (i.e. green curve) as compared with oxidized graphene alone (i.e. blue curve in Figure 5.6A). Such a scenario was not necessarily confirmed by the experimental NEXAFS data (i.e. red curve as compared with black in Figure 5.4A), and this discrepancy might have been possibly ascribed to the much lower coverage density of PPD within the experimental PPD-bound DWNT system.

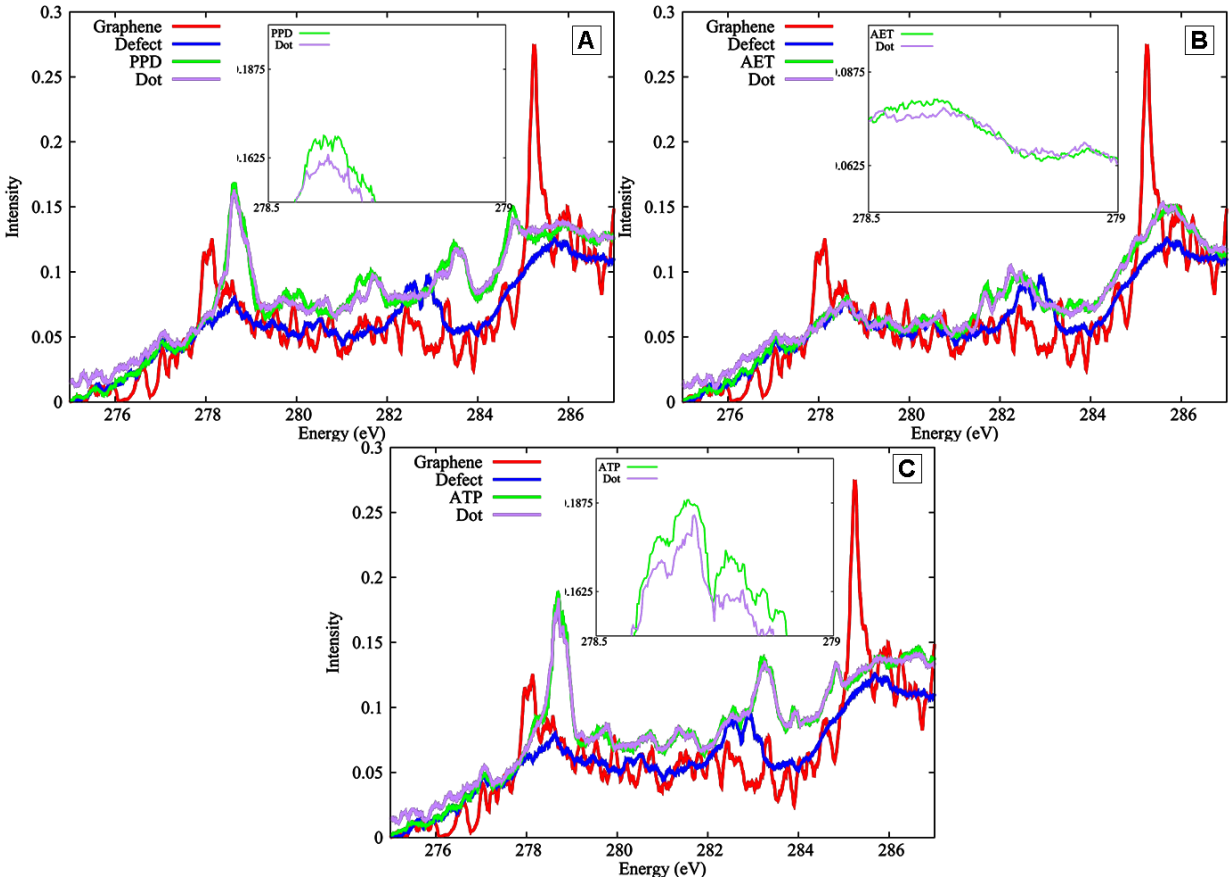

Figure 5.6. Theoretically calculated C *K*-edge NEXAFS spectra of pristine graphene (red), of defect-ridden (i.e. oxidized) graphene (blue), of various ligands bound to graphene (green), as well as of graphene-bound ligand-CdSe QD heterostructures (purple). (Reprinted with permission from *Nanoscale*, **2016**, DOI**:** 10.1039/C6NR03091B. Copyright 2016 Royal Society of Chemistry.)

In order to further investigate this enhancement, Figure 5.7 delineates the contribution of the various constituent groups of carbons to the total spectrum associated with the PPD, AET, and ATP-bound graphene systems, including (1) the C=C backbone carbons within the graphene layer (i.e. the carbon atoms in the plane of the graphene sheet, labeled as the "sheet" carbon, herein) and (2) the carbon atoms associated with the ligands themselves (i.e. the carbon atoms out of the plane of the graphene, labeled as the "linker" carbon, herein). It is apparent that the origin of the large increase in the C=C π^* peak near 279 eV for the PPD and ATP-bound graphene systems (i.e. green curves) as compared with oxidized graphene alone (i.e. blue curves)

in Figure 5.6A and C) can be ascribed to the aromatic carbon atoms present within the ligands themselves, which constitute the major component of the total C=C π^* peak signal in Figure 5.7A and C. Such an enhancement in the experimental data associated with ATP-bound DWNTs (i.e. red curve) relative to that of the oxidized DWNTs itself (i.e. black curve) is also apparent in Figure 5.4G, but it is not as evident with the PPD-bound DWNT system in Figure 5.4A, an observation possibly due to the much lower coverage density of PPD within the experimental PPD-bound DWNT system. The corresponding lack of a large increase in the C=C π^* peak intensity near 279 eV for AET-bound graphene (i.e. green curve, Figure 5.6B) can be attributed to the fact AET does not possess aromatic carbons within the ligand itself (Figure 5.7B). Hence, the spectra for the AET, ATP, and PPD-bound graphene systems are very similar with respect to the carbon atoms within the sheet itself, with only a slight increase in the intensity of the peak located at 278 eV for the AET-bound graphene system (i.e. blue curve in Figure 5.7B).

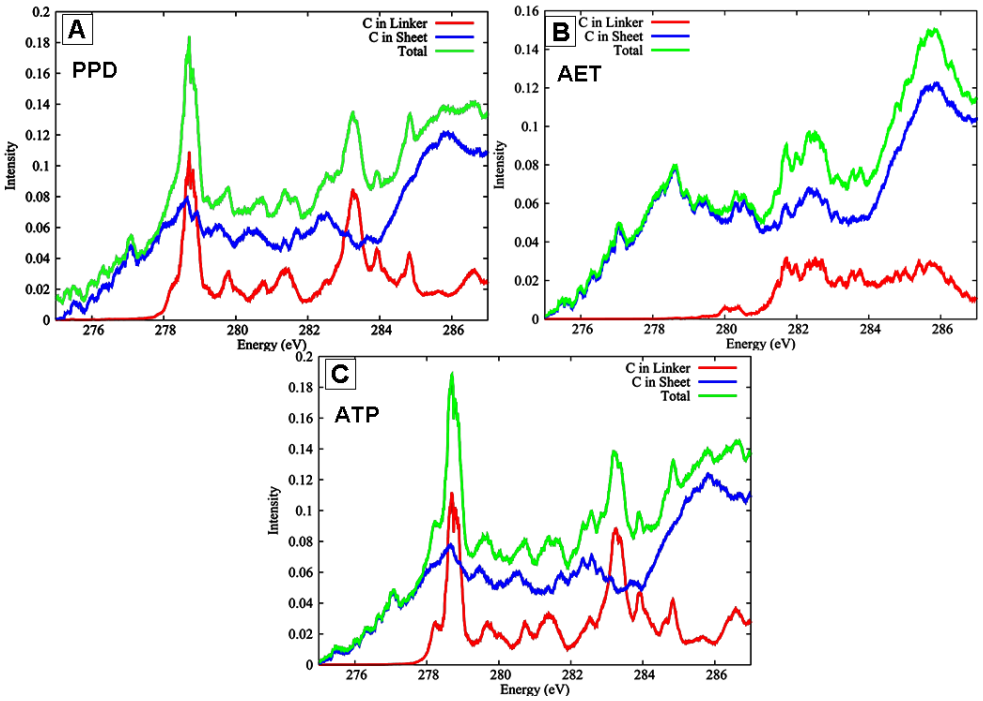

Figure 5.7. (A, B, and C). Breakdown of the NEXAFS spectra associated with graphene-bound PPD, AET, and ATP composites, respectively. (Reprinted with permission from *Nanoscale*, **2016**, DOI**:** 10.1039/C6NR03091B. Copyright 2016 Royal Society of Chemistry.)

After QD deposition (CdSe QDs chemically attached onto ligand-bound graphene systems). After CdSe QD deposition, a reduction of the C=C π^* transition was observed for the CdSe-ATP-graphene system as compared with ATP-graphene itself (i.e. purple curve as compared with green curve in the Figure 5.6C inset), denoting behavior which is consistent with the corresponding experimental data shown in Figure 5.4G (blue as compared with red curves). A smaller reduction was noted in the C=C π^* transition of the CdSe-PPD-graphene composite as compared with PPD-graphene itself (i.e. purple curve as compared with green curve in the Figure 5.6A inset). Only a marginal diminution was observed with the CdSe-AET-graphene heterostructure as compared with AET-graphene itself (i.e. purple curve as compared with green curve in the Figure 5.6B inset).

In particular with the CdSe-ATP-graphene heterostructures, the total decrease in the C=C π^* peak intensity appears to be much larger than what has observed for both the AET and PPD-based analogues. In order to further investigate the suppression in the C=C π^* transition after QD deposition, the various 'differential' carbon contributions to the simulated C *K*-edge NEXAFS spectra associated with the CdSe QD-ligand-graphene heterostructures as compared with the analogous ligand-bound graphene system are highlighted in Figure 5.8.

The largest suppression was noted with the CdSe-ATP-graphene system after the QD deposition (i.e. purple curve) as compared with ATP-graphene itself (i.e. green curve in Figure 5.8G and Figure 5.6C inset). In effect, the ligand carbons (Figure 5.8H) contribute to the largest reduction in the π^* peak amongst all three of the ligand systems tested. We have also observed that the C=C π^* peak associated with the "sheet" carbon atoms (Figure 5.8I) remain relatively unchanged when the QD is added. The smallest reduction was actually observed in the C=C π^* peak near 279 eV for the CdSe-AET-graphene system (i.e. purple curve) as compared with AET-

graphene itself (i.e. green curve in Figure 5.8D and Figure 5.6B inset). This decrease can be attributed to the carbon atoms within the graphene sheet, likely experiencing suppression in their intensity at this energy level (Figure 5.8F). There is a corresponding noticeable enhancement of the peak attributed to the "ligand" carbons at 282 eV (Figure 5.8E), which is consistent with experimental data presented in Figure 5.4D.

For the graphene carbon atoms in the CdSe-PPD-graphene system (i.e. purple curve), a reduction is noted in the π^* peak intensity as compared with the analogous PPD-graphene system (i.e. green curve in Figure 5.8A and Figure 5.6A inset)**.** This decrease can be attributed to the sp^2 carbons within the ligand (Figure 5.8B). The first thing to note is that the addition of QDs can reduce the intensity of nearly all energies, with the only exceptions being around 281 and 282 eV, associated with the σ* C-O functionalities, which yielded a small amount of enhancement from the carbon atoms in the graphene sheet and the ligand region (Figure 5.8B and C). The suppression of nearly every peak and the corresponding enhancement of the peak at 282 eV in the CdSe-PPD-graphene system are consistent with experiment (Figure 5.4A). The locations of both calculated π^* and σ* peaks also correlate well with experiment (Figure 5.4A), though the intensity of the theoretical CdSe-PPD-graphene system was found to be different from what experiment yielded. This latter discrepancy may be due to the higher coverage of the PPD ligands in the simulated system as compared with the corresponding coverage of the PPD ligands within the experimental CdSe-PPD-DWNT system.

Our calculated C *K*-edge NEXAFS spectra imply that when normalized to the same amount of QD coverage density, the CdSe-ATP-graphene heterostructure gave rise to the largest decrease in the C=C π^* peak. Successively lower reductions in the C=C π^* peak intensities were

noted for the CdSe-graphene-PPD and AET-based systems, respectively, with the AET-associated composite yielding the least amount of π^* peak reduction.

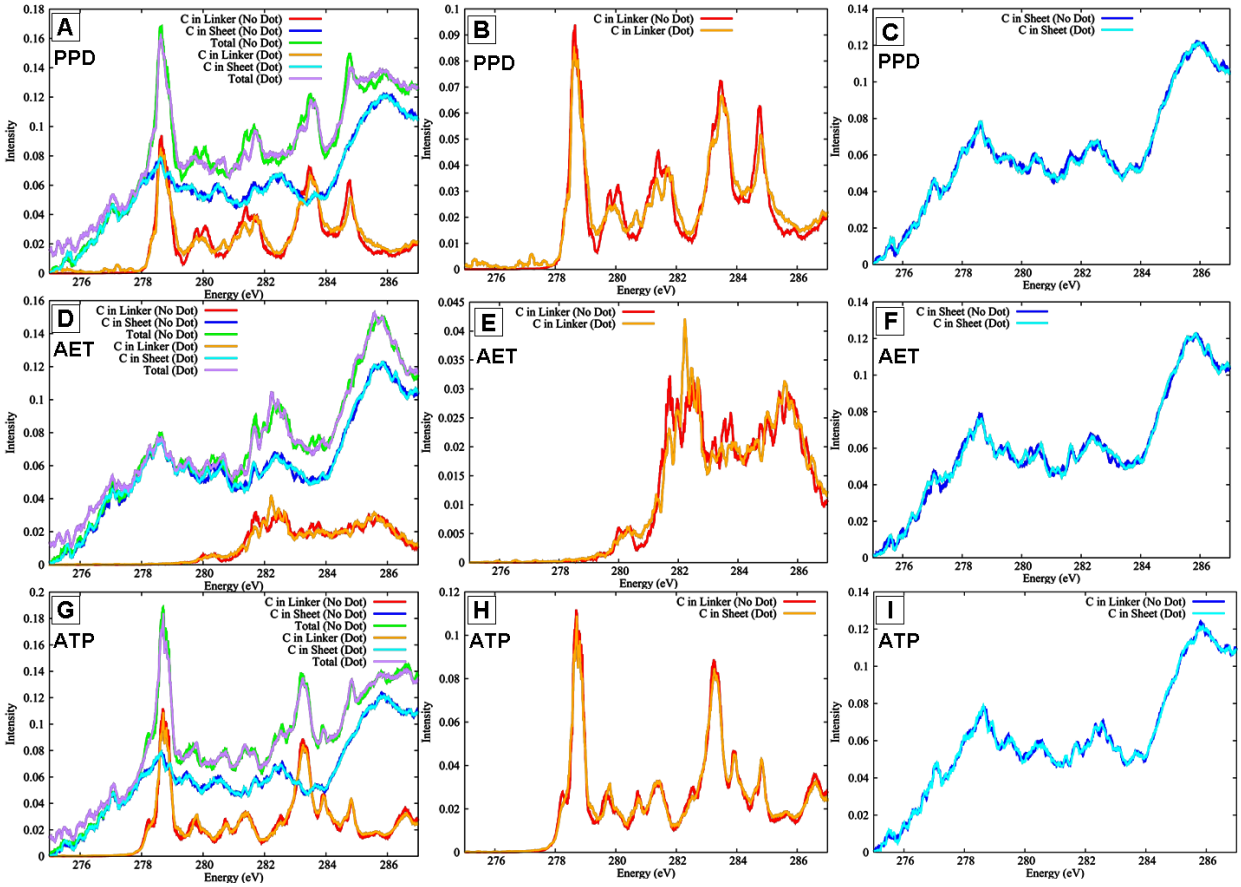

Figure 5.8. Differential carbon contributions to the C *K*-edge NEXAFS spectra associated with the graphene-bound PPD-QD heterostructures as compared with the graphene-bound PPD system (A-C), graphene-bound AET-QD heterostructures as compared with the graphene-bound AET system (D-F), and graphene-bound ATP-QD heterostructures as compared with graphene-bound ATP composites (G-I), respectively. (Reprinted with permission from *Nanoscale*, **2016**, DOI**:** 10.1039/C6NR03091B. Copyright 2016 Royal Society of Chemistry.)

Summation. To recapitulate, despite differences between theory and experiment in terms of ligand coverage and QD size, theory reproduces the overall experimental trends observed. With respect to the ligand-bound graphene systems, theory and experiment mutually confirm the presence of the largest enhancement in the C=C π^* peak of the ATP-derivatized graphene, and the least enrichment for the AET-functionalized graphene. Theory explains these trends on the

basis that the sp^2 carbon atoms within the ATP ligand share a similar chemical environment with the carbon atoms of the graphene sheet and can therefore add onto the C=C π^* peak intensity directly, whereas the analogous sp^3 carbons within the AET ligand do not. Experimentally, the PPD ligands maintained such a low spatial coverage that this trend was not observed.

When analyzing the extent of the C=C π^* peak suppression occurring upon the addition of QDs, theory and experiment both were in agreement that use of the ATP ligand gave rise to the strongest decline, whereas the AET linker yielded significantly less peak intensity decrease. Indeed, theory explains the overall observed 'suppression' as arising primarily from a diminution in the intensity emanating from the carbons in the ligands themselves in the aromatic ligand systems. These data are consistent with the experimental results presented in Figure 5.4A and G, and the calculated XAS shown in Figure 5.6A and C. This finding moreover corroborates previous published results which suggest that electron-rich, conjugated systems are more efficacious at enabling the charge transfer process as compared with their non-conjugated counterparts.[58]

5.2.4. Raman.

The tangential modes (G bands) typical of DWNT-PPD / AET / ATP-CdSe heterostructures together with the corresponding DWNT-PPD / AET / ATP control samples are highlighted in Figure 5.9A-C. Each individual G band was treated as a convolution of 4 Lorentzian functions (i.e. the dashed curves). The two peaks located at the higher frequencies can be attributed to the G^+ and G^- bands of the semiconducting outer tube, whereas the other two peaks associated with the lower frequencies correspond to the G^+ and G^- bands of the semiconducting inner tube. According to the Kataura plot,[59] the 2.41 eV excitation energy of the laser is in resonance with the E_{33}^S transition of a semiconducting (S) outer tube as well as with

the E_{33}^{S} transition of a semiconducting (S) inner tube. The fits of the sum of the Lorentzian peaks match well with previously reported G-band deconvolution data on DWNTs, possessing a S@S configuration.[60, 61] In particular, the peak located at higher frequency can be ascribed to the unresolved A_1 and E_1 tangential G^+ modes for the outer tubes.[62]

Upon deposition of CdSe QDs, all of the outer tube G^+ sub-bands evince an apparent peak down-shift and a corresponding intensity decrease, an observation which can be potentially attributed to the G-band 'softening', indicative of the expansion of C-C bonds upon *n*-type doping and suggestive of the presence of electron transfer from QDs in all three of the ligand systems analyzed.[63, 64] ATP-based heterostructures gave rise to the largest down shift in the peak position recorded of 16 cm^{-1}, as compared with 2 cm^{-1} and 7 cm^{-1} associated with PPD and AET-based analogues, respectively. These data are consistent with complementary observations from both experimental and calculated NEXAFS data, indicating the largest amount of electron transfer with ATP-centric systems. Although the observed changes in the PPD and AET-based systems are reasonably comparable in terms of the measured peak downshift, as a result of the much higher coverage density of AET-CdSe QDs as compared with PPD-CdSe QDs within our heterostructures (Figure 5.1A and B), the use of aromatic PPD might actually be a more promising and efficient ligand choice in terms of promoting charge transfer.

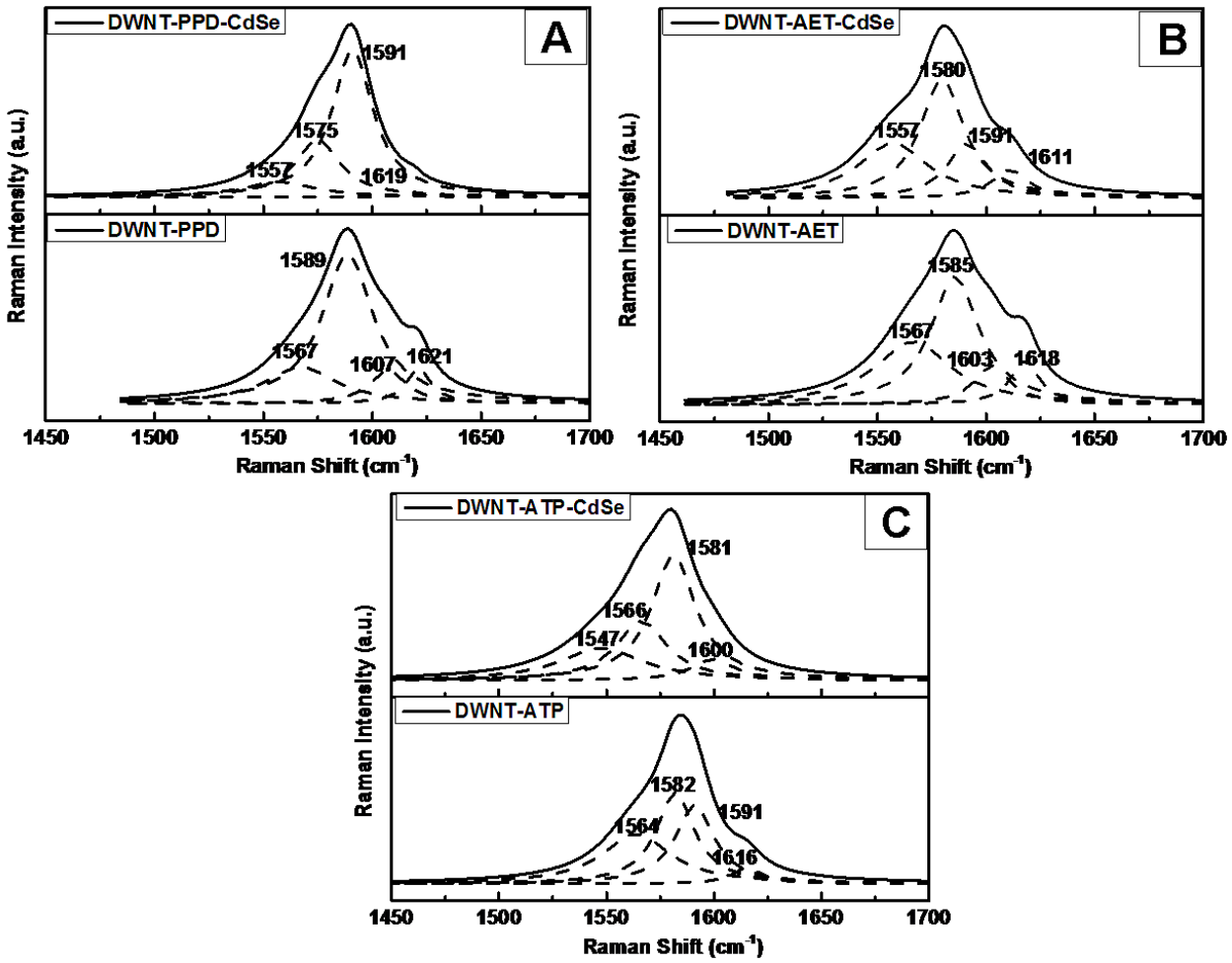

Figure 5.9 (A, B, and C). Raman G-band spectra, measured at an excitation wavelength of 514 nm (2.41 eV), of DWNT-PPD-CdSe QD, DWNT-AET-CdSe QD, and DWNT-ATP-CdSe QD heterostructures, respectively, by comparison with their respective controls. Reduced chi-square of the fitting is 3.2, 1.6, 2.7, 2.8, 1.3, and 1.7 for DWNT-PPD-CdSe QD, DWNT-PPD, DWNT-AET-CdSe QD, DWNT-AET, DWNT-ATP-CdSe QD, and DWNT-ATP structures, respectively. (Reprinted with permission from *Nanoscale*, **2016**, DOI**:** 10.1039/C6NR03091B. Copyright 2016 Royal Society of Chemistry.)

5.2.5. Electrical Transport Measurements.

The combination of NEXAFS and Raman spectroscopy data has experimentally confirmed the presence of charge transfer between immobilized CdSe QDs and the underlying DWNTs. In order to further probe the potential device capabilities of our as-generated DWNT-CdSe QD heterostructures for photoelectronic applications, additional electrical transport

measurements of associated FETs have been acquired. When performing electrical transport measurements within a three-terminal FET geometry, critical information about the charge state of the pristine and ligand-QD decorated carbon nanotubes can be gathered from the gate voltage dependence of the respective devices.[65] It is worth mentioning here that all of the measurements have been carried out under 'dark' conditions, meaning the ligand-capped CdSe QDs themselves are not being excited. Hence, the observed charge-transfer behavior is not associated with photoinduced excitons, but rather with possible work function differences among the various individual components in the system.

All measurements were performed at room-temperature at a pressure of ~$1 \cdot 10^{-5}$ torr. Device characteristics obtained in this way are very similar in appearance (inset of Figure 5.10) but exhibit their current minima at distinctly different gate voltages, depending on the particular type of ligand analyzed (Figure 5.10). In fact, in these CNT devices, it is this unique fingerprint characterized by a shift in the threshold voltage (relative to V_{gs}) that holds information about the amount of charge transfer that can occur between the ligand-QD system and the attached DWNTs, due to their different work functions.

Figure 5.10 highlights the gate voltage at which the current through the device is minimum (V_{min}) with the relevant transfer characteristics obtained for four different types of samples: (a) pristine DWNTs; (b) DWNTs coupled with ~4.1 nm diameter AET-QDs; (c) DWNTs immobilized with ~4.1 nm diameter ATP-QDs; and (d) DWNTs connected to ~4.1 nm diameter PPD-QDs. To obtain a decent statistical distribution, about 40 devices were fabricated and measured for each functionalization type. Only devices showing clear ambipolar behavior, i.e. electron currents for positive gate voltages and hole currents for negative gate voltages, have been included in the analysis. Relative to pristine CNT FETs, all functionalized tube devices

show a clear negative shift of V_{min}, which indicates that electrons are being transferred from the ligand-QD system to the DWNTs. Indeed, the performance of the CNT FET devices is indicative of electron transfer both to and from DWNTs. Nevertheless, it is obvious that the electron transfer from QDs to DWNTs is the predominant effect as compared with possible electron back-donation from the DWNTs to the QDs, since the FET devices tested herein primarily demonstrated the presence of an *n*-doping effect after QD decoration.

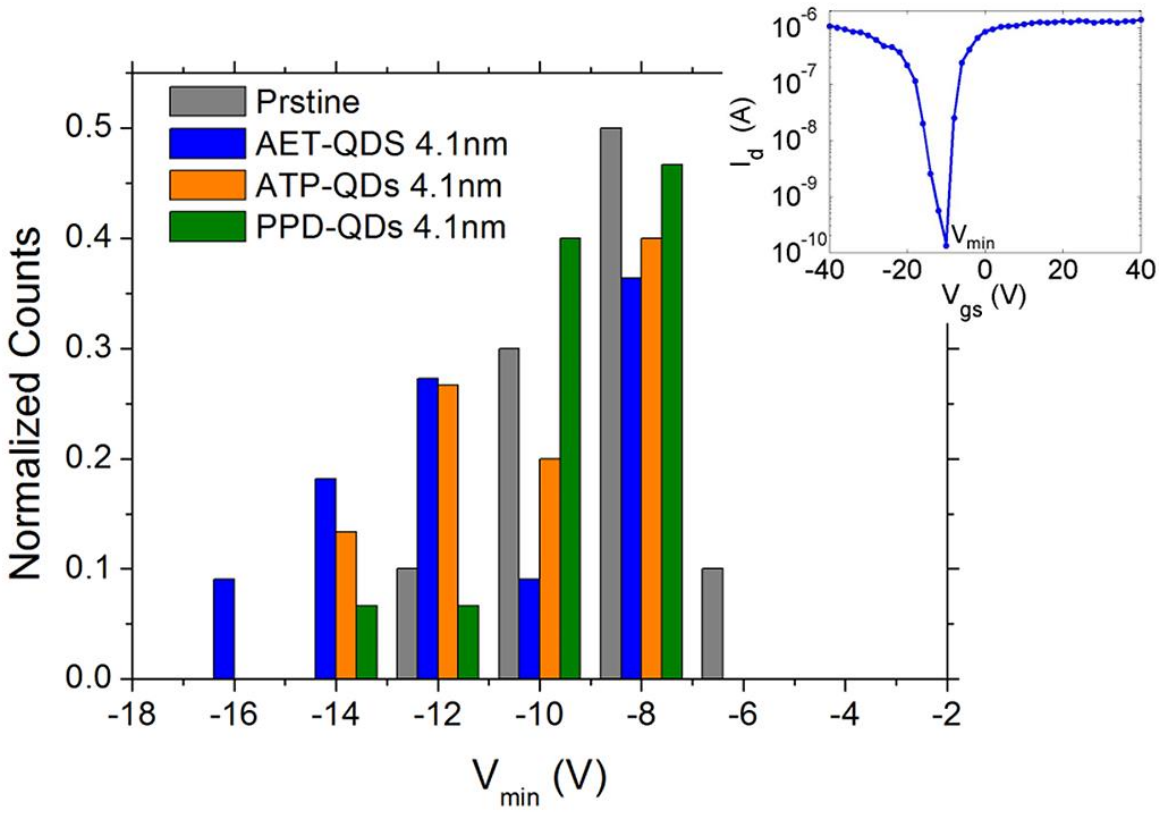

Figure 5.10. V_{gs} values, at which the current versus gate voltage characteristics of individual devices showed their minimum, for the various ligands tested. The inset shows a representative measurement for a device with ATP functionalization at a drain voltage of V_{ds} = -1 V. The channel length is 1 μm. (Reprinted with permission from *Nanoscale*, **2016**, DOI**:** 10.1039/C6NR03091B. Copyright 2016 Royal Society of Chemistry.)

Figure 5.11 summarizes the distribution of V_{min} values for the various ligand-QD CNT devices as a function of the respective QD coverage densities on the underlying DWNTs, as extracted from TEM. To summarize, the data suggest that in the absence of laser illumination, the QD-ligand system once attached to the DWNT is no longer "charge neutral" and in fact, systems possessing higher QD coverage densities lead to more charge transfer to the DWNT (Table 5.1). Measurements of the various DWNT−ligand-capped CdSe QD heterostructures in the presence of laser illumination are still under investigation in order to reveal additional insights into photoinduced charge transport.

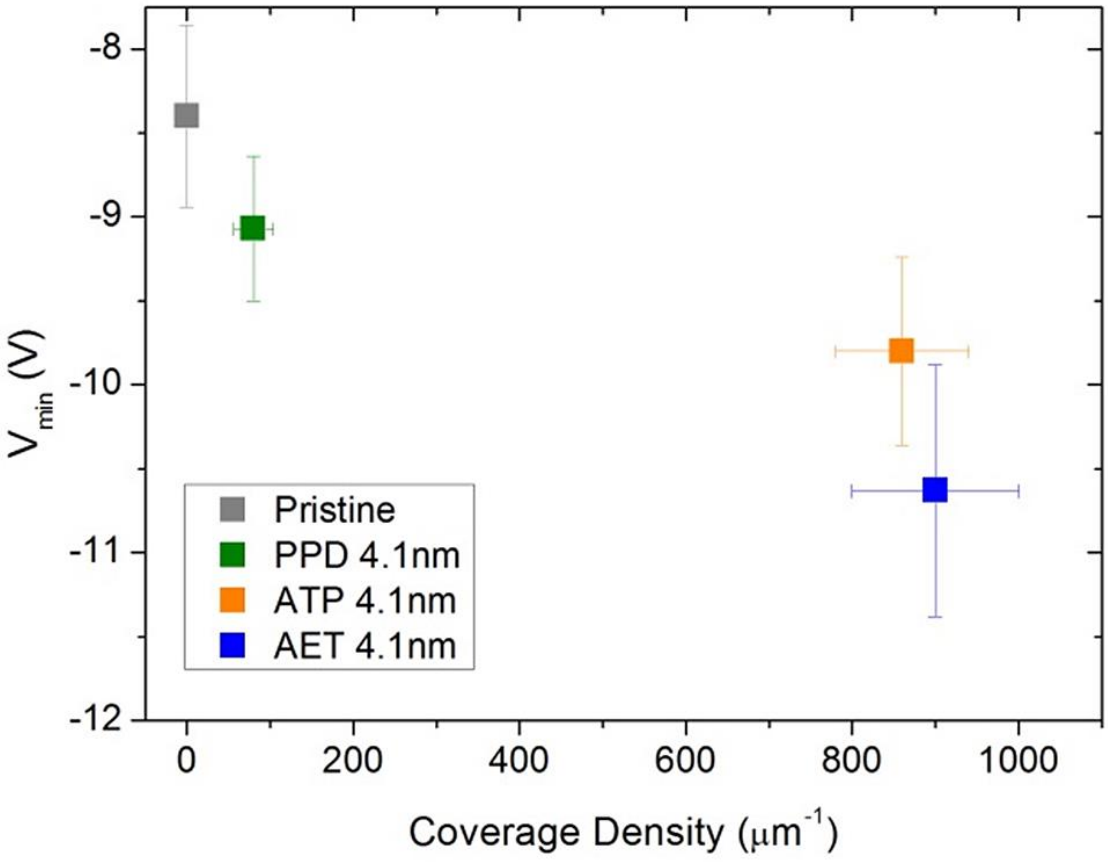

Figure 5.11. V_{min} vs. coverage density for various ligand-bound QD-CNT heterostructured samples. (Reprinted with permission from *Nanoscale*, **2016**, DOI**:** 10.1039/C6NR03091B. Copyright 2016 Royal Society of Chemistry.)

Table 5.1. Summary of transport results for various functionalized ligand-QD CNT samples. (Reprinted with permission from *Nanoscale*, **2016**, DOI**:** 10.1039/C6NR03091B. Copyright 2016 Royal Society of Chemistry.)

	PPD 4.1nm	ATP 4.1nm	AET 4.1nm
Shift of V_{min} [V]	-0.67±0.69	-1.4±0. 78	-2.23±0. 92
Coverage [μm^{-1}]	80±24	860±80	900±100

5.3. Conclusions

In this manuscript, various DWNT-CdSe heterostructures, with average QD diameter of 4.1 nm, have been successfully synthesized using a covalent attachment approach through the mediation of PPD, AET, and ATP ligands, respectively. With a collective analysis of both experimental and theoretical data sets, plausible evidence for charge transfer has been proposed for heterostructures generated through the mediation of various ligands.

Focusing on the role of the *pendant functional group* within the ligand, TEM and HRTEM images have indicated that the PPD-capped CdSe QDs gave rise to a lower coverage density as compared with AET and ATP-based heterostructures, possibly due to the weaker binding strength of $–NH_2$ as compared with the –SH groups with respect to the Cd sites of the QD surface. Specifically, the larger experimental NEXAFS enhancement associated with the Cd *M_3-edge* transition intensity for the AET-based (versus PPD-bound) heterostructures was likely a consequence not only of their greater QD coverages but also of the higher electron affinity of the AET's terminal –SH groups as compared with PPD's pendant $–NH_2$ moieties. The net consequence was an overall increased charge withdrawal and charge transfer from the immobilized CdSe QDs within the AET-mediated heterostructures. Subsequent electrical transport measurements suggest that in the absence of laser illumination, the QD-ligand system

once attached to the DWNT is no longer "charge neutral", and *systems possessing higher QD coverage densities lead to more charge transfer* to the underlying DWNTs.

Concentrating on the function of the carbon-rich *π-conjugated system* within the ligand structure, analysis of the experimental C *K*-edge spectra, specifically the C=C π* transition, as well as of the Raman spectra of the DWNT G^+-band down-shift have unambiguously suggested a more nuanced picture in which the ATP-based heterostructures actually gave rise to the largest amount of charge transfer observed from the QDs to the underlying DWNTs. We hypothesize that although both ligands similarly possess pendant –SH functional groups as well as similar QD coverage densities, the presence of the ATP's intrinsic π-conjugated aromatic system mediates and facilitates greater charge transfer as compared with its aliphatic AET counterpart. Nonetheless, the aromatic PPD-based system yielded a smaller amount of charge transferred to DWNTs as compared with their aliphatic ATP-based analogues, possibly due to the much lower QD coverage density and concentrations, i.e. 1/10 for PPD versus ATP-based composites.

Our overall data point to the presence of the π-conjugated carbon system as well as the pendant groups within the ligands as important contributive factors governing the resulting charge transfer to the underlying CNTs. Theoretical NEXAFS data reproduced the overall experimental trends in terms of enhancement/suppression behavior of the C=C π* peak (Figure 5.5). In particular, the use of theory explained the origin of the C=C π* peak enhancement in the graphene-linker systems as arising from the nature of carbon atoms within the linker (Figure 5.7) and the suppression of the C=C π* peak is stronger within the conjugated systems (Figure 5.6). Theory could not conclusively ascribe the C=C π* peak suppression to the effect of charge transfer. However, it is crucial to note that whereas by virtue of creating a computationally tractable and doable system, the theory calculations necessarily focused upon a QD with a

relaxed geometry of 1.3 nm, experimental QDs were actually substantially larger (4 nm) and often aggregated, a scenario which would be expected to transfer more charge. In other words, theory could effectively and qualitatively account for all of the observed phenomena and behavior at the smallest of dimensions. Hence, future work will explore the idea of scaling these size-dependent effects to macroscopic regimes involving larger-sized and greater numbers of quantum dots.

5.4. References

1. Carey, G. H.; Abdelhady, A. L.; Ning, Z.; Thon, S. M.; Bakr, O. M.; Sargent, E. H. Colloidal Quantum Dot Solar Cells. *Chem. Rev.* **2015**, *115*, 12732–12763.
2. Tison, Y.; Giusca, C. E.; Stolojan, V.; Hayashi, Y.; Silva, S. R. P. The inner shell influence on the electronic structure of double-walled carbon nanotubes. *Adv. Mater.* **2008**, *20*, 189-194.
3. Hashimoto, A.; Suenaga, K.; Urita, K.; Shimada, T.; Sugai, T.; Bandow, S.; Shinohara, H.; Iijima, S. Atomic correlation between adjacent graphene layers in double-wall carbon nanotubes. *Phys. Rev. Lett.* **2005**, *94*, 045504/1-4.
4. Saito, R.; Matsuo, R.; Kimura, T.; Dresselhaus, G.; Dresselhaus, M. S. Anomalous potential barrier of double-wall carbon nanotube. *Chem. Phys. Lett.* **2001**, *348*, 187-193.
5. Schulz-Drost, C.; Sgobba, V.; Gerhards, C.; Leubner, S.; Calderon, R. M. K.; Ruland, A.; Guldi, D. M. Innovative Inorganic-Organic Nanohybrid Materials: Coupling Quantum Dots to Carbon Nanotubes. *Angew. Chem. Int. Ed.* **2010**, *49*, 6425-6429.
6. Wang, D. F.; Baral, J. K.; Zhao, H. G.; Gonfa, B. A.; Truong, V. V.; El Khakani, M. A.; Izquierdo, R.; Ma, D. L. Controlled Fabrication of PbS Quantum-Dot/Carbon-Nanotube Nanoarchitecture and its Significant Contribution to Near-Infrared Photon-to-Current Conversion. *Adv. Funct. Mater.* **2011**, *21*, 4010-4018.
7. Reiss, P.; Protiere, M.; Li, L. Core/Shell Semiconductor Nanocrystals. *Small* **2009**, *5*, 154-168.
8. Zhang, L. H.; Shi, E. Z.; Li, Z.; Li, P. X.; Jia, Y.; Ji, C. Y.; Wei, J. Q.; Wang, K. L.; Zhu, H. W.; Wu, D. H.; Cao, A. Y. Wire-supported CdSe nanowire array photoelectrochemical solar cells. *Phys. Chem. Chem. Phys.* **2012**, *14*, 3583-3588.
9. Yu, W. W.; Peng, X. Formation of high-quality CdS and other II-VI semiconductor nanocrystals in noncoordinating solvents: tunable reactivity of monomers. *Angew. Chem. Int. Ed.* **2002**, *41*, 2368-2371.
10. Peng, Z. A.; Peng, X. G. Formation of high-quality CdTe, CdSe, and CdS nanocrystals using CdO as precursor. *J. Am. Chem. Soc.* **2001**, *123*, 183-184.
11. Virgili, T.; López, I. S.; Vercelli, B.; Angella, G.; Zotti, G.; Cabanillas-Gonzalez, J.; Granados, D.; Luer, L.; Wannemacher, R.; Tassone, F. Spectroscopic Signature of Trap States in Assembled CdSe Nanocrystal Hybrid Films. *J. Phys. Chem. C* **2012**, *116*, 16259-16263.

12. Querner, C.; Reiss, P.; Sadki, S.; Zagorska, M.; Pron, A. Size and ligand effects on the electrochemical and spectroelectrochemical responses of CdSe nanocrystals. *Phys. Chem. Chem. Phys.* **2005**, *7*, 3204-3209.
13. Newton, J. C.; Ramasamy, K.; Mandal, M.; Joshi, G. K.; Kumbhar, A.; Sardar, R. Low-Temperature Synthesis of Magic-Sized CdSe Nanoclusters: Influence of Ligands on Nanocluster Growth and Photophysical Properties. *J. Phys. Chem. C* **2012**, *116*, 4380-4389.
14. Klem, E. J. D.; MacNeil, D. D.; Cyr, P. W.; Levina, L.; Sargent, E. H. Efficient solution-processed infrared photovoltaic cells: Planarized all-inorganic bulk heterojunction devices via inter-quantum-dot bridging during growth from solution. *Appl. Phys. Lett.* **2007**, *90*, 183113.
15. Talapin, D. V.; Murray, C. B. PbSe nanocrystal solids for n- and p-channel thin film field-effect transistors. *Science* **2005**, *310*, 86-89.
16. Pattantyus-Abraham, A. G.; Kramer, I. J.; Barkhouse, A. R.; Wang, X.; Konstantatos, G.; Debnath, R.; Levina, L.; Raabe, I.; Nazeeruddin, M. K.; Gratzel, M.; Sargent, E. H. Depleted-heterojunction colloidal quantum dot solar cells. *ACS Nano* **2010**, *4*, 3374-3380.
17. Tang, J.; Kemp, K. W.; Hoogland, S.; Jeong, K. S.; Liu, H.; Levina, L.; Furukawa, M.; Wang, X.; Debnath, R.; Cha, D.; Chou, K. W.; Fischer, A.; Amassian, A.; Asbury, J. B.; Sargent, E. H. Colloidal-quantum-dot photovoltaics using atomic-ligand passivation. *Nat. Mater.* **2011**, *10*, 765-771.
18. Brown, P. R.; Kim, D.; Lunt, R. R.; Zhao, N.; Bawendi, M. G.; Grossman, J. C.; Bulovic, V. Energy level modification in lead sulfide quantum dot thin films through ligand exchange. *ACS Nano* **2014**, *8*, 5863-5872.
19. Mora-Sero, I.; Bertoluzzi, L.; Gonzalez-Pedro, V.; Gimenez, S.; Fabregat-Santiago, F.; Kemp, K. W.; Sargent, E. H.; Bisquert, J. Selective contacts drive charge extraction in quantum dot solids via asymmetry in carrier transfer kinetics *Nat. Commun.* **2013**, *4*, 3272.
20. Peng, X. H.; Wong, S. S. Controlling Nanocrystal Density and Location on Carbon Nanotube Templates. *Chem. Mater.* **2009**, *21*, 682-694.
21. Peng, X.; Sfeir, M. Y.; Zhang, F.; Misewich, J. A.; Wong, S. S. Covalent Synthesis and Optical Characterization of Double-walled Carbon Nanotube-Nanocrystal Heterostructures. *J. Phys. Chem. C* **2010**, *114*, 8766-8733.
22. Wang, L.; Han, J.; Hoy, J.; Hu, F.; Liu, H.; Gentleman, M. M.; Sfeir, M. Y.; Misewich, J. A.; Wong, S. S. Probing differential optical and coverage behavior in nanotube-nanocrystal heterostructures synthesized by covalent versus non-covalent approaches. *Dalton Trans.* **2014**, *43*, 7480-7490.
23. Weaver, J. E.; Dasari, M. R.; Datar, A.; Talapatra, S.; Kohli, P. Investigating Photoinduced Charge Transfer in Carbon Nanotube-Perylene-Quantum Dot Hybrid Nanocomposites. *ACS Nano* **2010**, *4*, 6883-6893.
24. Azoz, S.; Jiang, J.; Keskar, G.; McEnally, C.; Alkas, A.; Ren, F.; Marinkovic, N.; Haller, G. L.; Ismail-Beigi, S.; Pfefferle, L. D. Mechanism for strong binding of CdSe quantum dots to multiwall carbon nanotubes for solar energy harvesting. *Nanoscale* **2013**, *5*, 6893-6900.
25. Guo, S. R.; Bao, D. D.; Upadhyayula, S.; Wang, W.; Guvenc, A. B.; Kyle, J. R.; Hosseinibay, H.; Bozhilov, K. N.; Vullev, V. I.; Ozkan, C. S.; Ozkan, M. Photoinduced Electron Transfer Between Pyridine Coated Cadmium Selenide Quantum Dots and Single Sheet Graphene. *Adv. Funct. Mater.* **2013**, *23*, 5199-5211.
26. Liu, I. S.; Lo, H. H.; Chien, C. T.; Lin, Y. Y.; Chen, C. W.; Chen, Y. F.; Su, W. F.; Liou, S. C. Enhancing photoluminescence quenching and photoelectric properties of CdSe quantum dots with hole accepting ligands. *J. Mater. Chem.* **2008**, *18*, 675-682.

27. Peng, X. H.; Misewich, J. A.; Wong, S. S.; Sfeir, M. Y. Efficient Charge Separation in Multidimensional Nanohybrids. *Nano Lett.* **2011**, *11*, 4562-4568.
28. Yu, K.; Lu, G.; Chen, K.; Mao, S.; Kim, H.; Chen, J. Controllable photoelectron transfer in CdSe nanocrystal-carbon nanotube hybrid structures. *Nanoscale* **2012**, *4*, 742-746.
29. Robel, I.; Bunker, B. A.; Kamat, P. V. Single-walled carbon nanotube-CdS nanocomposites as light-harvesting assemblies: Photoinduced charge-transfer interactions. *Adv. Mater.* **2005**, *17*, 2458.
30. Winter, A. D.; Larios, E.; Alamgir, F. M.; Jaye, C.; Fischer, D. A.; Omastova, M.; Campo, E. M. Thermo-Active Behavior of Ethylene-Vinyl Acetate I Multiwall Carbon Nanotube Composites Examined by in Situ near-Edge X-ray Absorption Fine-Structure Spectroscopy. *J. Phys. Chem. C* **2014**, *118*, 3733-3741.
31. do Nascimento, G. M.; Hou, T.; Kim, Y. A.; Muramatsu, H.; Hayashi, T.; Endo, M.; Akuzawa, N.; Dresselhaus, M. S. Double-wall carbon nanotubes doped with different Br_2 doping levels: a resonance Raman study. *Nano Lett.* **2008**, *8*, 4168-4172.
32. do Nascimento, G. M.; Hou, T.; Kim, Y. A.; Muramatsu, H.; Hayashi, T.; Endo, M.; Akuzawa, N.; Dresselhaus, M. S. Comparison of the Resonance Raman Behavior of Double-Walled Carbon Nanotubes Doped with Bromine or Iodine Vapors. *J. Phys. Chem. C* **2009**, *113*, 3934-3938.
33. Cambedouzou, J.; Sauvajol, J. L.; Rahmani, A.; Flahaut, E.; Peigney, A.; Laurent, C. Raman spectroscopy of iodine-doped double-walled carbon nanotubes. *Phys. Rev. B* **2004**, *69*, 235422.
34. do Nascimento, G. M.; Hou, T.; Kim, Y. A.; Muramatsu, H.; Hayashi, T.; Endo, M.; Akuzawa, N.; Dresselhaus, M. S. Behavior of the high frequency Raman modes of double-wall carbon nanotubes after doping with bromine or iodine vapors. *Carbon* **2011**, *49*, 3585-3596.
35. Warszawski, E.; Adler, J.; Hoffman, A.; Silverman, A. Experiment (NEXAFS) versus simulation (DOS) for carbon allotropes. *Proceedings of the 22th Workshop on Computer Simulation Studies in Condensed Matter Physics* **2010**, *3*, 1381-1385.
36. Qian, X.; Sambe, H.; Ramaker, D. E. Theoretical study on Cl L_{23} NEXAFS and UV absorption data for metal chlorides. *Phys. Rev. B* **1995**, *52*, 15115-15121.
37. Voloshina, E.; Ovcharenko, R.; Shulakov, A.; Dedkov, Y. Theoretical description of X-ray absorption spectroscopy of the graphene-metal interfaces. *J. Chem. Phys.* **2013**, *138*, 154706.
38. Schultz, B. J.; Jaye, C.; Lysaght, P. S.; Fischer, D. A.; Prendergast, D.; Banerjee, S. On chemical bonding and electronic structure of graphene-metal contacts. *Chem. Sci.* **2013**, *4*, 494-502.
39. Munro, A. M.; Jen-La Plante, I.; Ng, M. S.; Ginger, D. S. Quantitative Study of the Effects of Surface Ligand Concentration on CdSe Nanocrystal Photoluminescence. *J. Phys. Chem. C* **2007**, *111*, 6220-6227.
40. Park, C.; Yoon, T. L-cysteine adsorption on thiol-coated quantum dot (QD) in aqueous solution: An implication on the QD speciation in biological media. *Toxicology and Environmental Health Sciences* **2009**, *1*, 151-158.
41. Qu, L.; Peng, X. Control of photoluminescence properties of CdSe nanocrystals in growth. *J. Am. Chem. Soc.* **2002**, *124*, 2049-2055.
42. Liu, I. S.; Lo, H.-H.; Chien, C.-T.; Lin, Y.-Y.; Chen, C.-W.; Chen, Y.-F.; Su, W.-F.; Liou, S.-C. Enhancing photoluminescence quenching and photoelectric properties of CdSe quantum dots with hole accepting ligands. *J. Mater. Chem.* **2008**, *18*, 675-682.

43. Katari, J. E. B.; Colvin, V. L.; Alivisatos, A. P. X-ray Photoelectron Spectroscopy of CdSe Nanocrystals with Applications to Studies of the Nanocrystal Surface. *J. Phys. Chem.* **1994**, *98*, 4109-4117.
44. Young, A. G.; McQuillan, A. J.; Green, D. P. In Situ IR Spectroscopic Studies of the Avidin−Biotin Bioconjugation Reaction on CdS Particle Films. *Langmuir* **2009**, *25*, 7416-7423.
45. Liu, C.; Lee, S.; Su, D.; Zhang, Z.; Pfefferle, L.; Haller, G. L. Synthesis and Characterization of Nanocomposites with Strong Interfacial Interaction: Sulfated ZrO_2 Nanoparticles Supported on Multiwalled Carbon Nanotubes. *J. Phys. Chem. C* **2012**, *116*, 21742-21752.
46. Wang, Z.; Wu, L.; Zhou, J.; Cai, W.; Shen, B.; Jiang, Z. Magnetite Nanocrystals on Multiwalled Carbon Nanotubes as a Synergistic Microwave Absorber. *J. Phys. Chem. C* **2013**, *117*, 5446-5452.
47. Kuznetsova, A.; Popova, I.; Yates, J. T.; Bronikowski, M. J.; Huffman, C. B.; Liu, J.; Smalley, R. E.; Hwu, H. H.; Chen, J. G. G. Oxygen-containing functional groups on single-wall carbon nanotubes: NEXAFS and vibrational spectroscopic studies. *J. Am. Chem. Soc.* **2001**, *123*, 10699-10704.
48. Yueh, C. L.; Jan, J. C.; Chiou, J. W.; Pong, W. F.; Tsai, M. H.; Chang, Y. K.; Chen, Y. Y.; Lee, Y. F.; Tseng, P. K.; Wei, S. L.; Wen, C. Y.; Chen, L. C.; Chen, K. H. Electronic structure of the Fe-layer-catalyzed carbon nanotubes studied by x-ray-absorption spectroscopy. *Appl. Phys. Lett.* **2001**, *79*, 3179-3181.
49. Zhou, J. G.; Fang, H. T.; Maley, J. M.; Ko, J. Y. P.; Murphy, M.; Chu, Y.; Sammynaiken, R.; Sham, T. K. An X-ray Absorption, Photoemission, and Raman Study of the Interaction between SnO_2 Nanoparticle and Carbon Nanotube. *J. Phys. Chem. C* **2009**, *113*, 6114-6117.
50. Liang, Y.; Wang, H.; Zhou, J.; Li, Y.; Wang, J.; Regier, T.; Dai, H. Covalent Hybrid of Spinel Manganese–Cobalt Oxide and Graphene as Advanced Oxygen Reduction Electrocatalysts. *J. Am. Chem. Soc.* **2012**, *134*, 3517-3523.
51. Lee, J. R. I.; Meulenberg, R. W.; Hanif, K. M.; Mattoussi, H.; Klepeis, J. E.; Terminello, L. J.; van Buuren, T. Experimental observation of quantum confinement in the conduction band of CdSe quantum dots. *Phys. Rev. Lett.* **2007**, *98*, 146803.
52. Wright, J. T.; Meulenberg, R. W. Modification of the conduction band edge energy via hybridization in quantum dots. *Appl. Phys. Lett.* **2012**, *101*, 193104.
53. Si, H. Y.; Liu, C. H.; Xu, H.; Wang, T. M.; Zhang, H. L. Shell-Controlled Photoluminescence in CdSe/CNT Nanohybrids. *Nanoscale Research Letters* **2009**, *4*, 1146-1152.
54. Ortiz, J. V. Electron-Affinity Calculations on NH_2-, PH_2-, CN-, SH-, OH-, Cl-, and F- - Basis-Sets and Direct Vs Indirect Methods. *J. Chem. Phys.* **1987**, *86*, 308-312.
55. De Jesus, L. R.; Dennis, R. V.; Depner, S. W.; Jaye, C.; Fischer, D. A.; Banerjee, S. Inside and Outside: X-ray Absorption Spectroscopy Mapping of Chemical Domains in Graphene Oxide. *J. Phys. Chem. Lett.* **2013**, *4*, 3144-3151.
56. Banerjee, S.; Hemraj-Benny, T.; Balasubramanian, M.; Fischer, D. A.; Misewich, J. A.; Wong, S. S. Surface chemistry and structure of purified, ozonized, multiwalled carbon nanotubes probed by NEXAFS and vibrational spectroscopies. *ChemPhysChem* **2004**, *5*, 1416-1422.
57. Leon, V.; Parret, R.; Almairac, R.; Alvarez, L.; Babaa, M. R.; Doyle, B. P.; Ienny, P.; Parent, P.; Zahab, A.; Bantignies, J. L. Spectroscopic study of double-walled carbon nanotube functionalization for preparation of carbon nanotube/epoxy composites. *Carbon* **2012**, *50*, 4987-4994.
58. Metzger, R. M. Unimolecular electrical rectifiers. *Chem. Rev.* **2003**, *103*, 3803-3834.

59. Kataura, H.; Kumazawa, Y.; Maniwa, Y.; Umezu, I.; Suzuki, S.; Ohtsuka, Y.; Achiba, Y. Optical properties of single-wall carbon nanotubes. *Synth. Met.* **1999**, *103*, 2555-2558.
60. Bandow, S.; Chen, G.; Sumanasekera, G. U.; Gupta, R.; Yudasaka, M.; Iijima, S.; Eklund, P. C. Diameter-selective resonant Raman scattering in double-wall carbon nanotubes. *Phys. Rev. B* **2002**, *66*, 075416.
61. Villalpando-Paez, F.; Son, H.; Nezich, D.; Hsieh, Y. P.; Kong, J.; Kim, Y. A.; Shimamoto, D.; Muramatsu, H.; Hayashi, T.; Endo, M.; Terrones, M.; Dresselhaus, M. S. Raman Spectroscopy Study of Isolated Double-Walled Carbon Nanotubes with Different Metallic and Semiconducting Configurations. *Nano Lett.* **2008**, *8*, 3879-3886.
62. Rahmani, A.; Sauvajol, J. L.; Rols, S.; Benoit, C. Nonresonant Raman spectrum in infinite and finite single-wall carbon nanotubes. *Phys. Rev. B* **2002**, *66*, 125404.
63. Rauf, H.; Pichler, T.; Pfeiffer, R.; Simon, F.; Kuzmany, H.; Popov, V. N. Detailed analysis of the Raman response of n-doped double-wall carbon nanotubes. *Phys. Rev. B* **2006**, *74*, 235419.
64. Li, Y. F.; Hatakeyama, R.; Kaneko, T.; Izumida, T.; Okada, T.; Kato, T. Synthesis and electronic properties of ferrocene-filled double-walled carbon nanotubes. *Nanotechnology* **2006**, *17*, 4143-4147.
65. Wang, L.; Han, J.; Zhu, Y.; Zhou, R.; Jaye, C.; Liu, H.; Li, Z.-Q.; Taylor, G. T.; Fischer, D. A.; Appenzeller, J.; Wong, S. S. Probing the Dependence of Electron Transfer on Size and Coverage in Carbon Nanotube–Quantum Dot Heterostructures. *J. Phys. Chem. C* **2015**, *119*, 26327-26338.

Chapter 6. Enhanced Performance of "Flower-like" $Li_4Ti_5O_{12}$ Motifs as Anode Materials for High-rate Li-ion Batteries

6.1. Introduction

Lithium ion batteries (LIBs) have achieved commercial success in the field of portable electronic devices due to their outstanding properties, such as high energy density, light weight, long lifespan, and ambient temperature operation.[1-3] With the growing demand for applications in energy storage stations and modern electric vehicles, the development of LIBs possessing a desirable mixture of positive attributes, such as high energy and power densities, superior durability, long cycling performance, as well as favorable environmental sustainability remains a highly sought-after objective.[4, 5] Conventional LIBs utilize carbon-based anode materials (typically graphite), which suffer greatly from effects associated with volume expansion and shrinkage during Li-ion intercalation and extraction processes. These phenomena can potentially lead to a loss in electrical contact between graphitic particles and in turn, a decrease in overall capacity. Another limitation arises from the potential for deleterious lithium dendrite formation during the overcharge process, owing to a low Li-intercalation potential of the graphite anode, approaching 0 V (versus Li/Li^+).[3, 5, 6]

Spinel $Li_4Ti_5O_{12}$, known as the 'zero-strain' material, has been extensively studied as an excellent alternative anode material, due to several intrinsic advantages, including (i) its outstanding structural stability due to its 'zero-volume' change during electrochemical cycling; (ii) its high and stable potential plateau value (i.e. 1.55 V *versus* Li/Li^+), which circumvents solid electrolyte interphase (SEI) formation and avoids the possibility for a battery short circuit issue, triggered by the formation of lithium dendrite deposition on the surface of the electrode; as well as (iii) its fast electrode kinetics enhanced by possible 3-dimensional Li^+-ion diffusion pathways

within the spinel structure.[5, 7] However, the inherently sluggish lithium ion diffusion coefficient of bulk $Li_4Ti_5O_{12}$ (10^{-9} to 10^{-13} cm^2/s)[8, 9] coupled with its low intrinsic electronic conductivity (10^{-13} S/cm)[10,11] greatly limit its rate capability.

Two strategies have been typically employed to improve the rate performance of $Li_4Ti_5O_{12}$ anodes. One strategy has been to improve the electron transfer via ion doping, surface modification, and/or incorporation of carbon. The other strategy is to reduce the electron and Li-ion diffusion lengths by producing nanostructured analogues of $Li_4Ti_5O_{12}$ itself.[12, 13] Recently, the synthesis of nanostructured motifs of $Li_4Ti_5O_{12}$, including zero-dimensional (0D) nanoparticles,[14, 15] one-dimensional (1D) nanowires and nanotubes,[16, 17] as well as other three-dimensional (3D) structural architectures,[3, 4, 18] has been widely adopted to address and overcome these issues, as these unique structures often lead to improved kinetic performance by reducing the overall lithium diffusion distance. Among various unique structural manifestations, the 3D nano-/micro- hierarchical structure in particular represents an ideal host for lithium storage, since it combines the merits of nanometer-sized building blocks (i. e., shortened diffusion distances and high electrode/electrolyte contact surface areas) with the benefits of either micrometer- or sub-micrometer-sized assemblies (i. e., thermodynamic stability and high tap-density).[18, 19]

For instance, Kim *et al*. reported on $Li_4Ti_5O_{12}$ microspheres assembled from nanosheets, synthesized by mixing titanium tetraisopropoxide (TTIP), LiOH, and H_2O_2 at 130°C for 20 h under hydrothermal conditions; these nanosheets evinced stable cycling performances, with a high capacity retention (140 mAh g^{-1}) at a current density of 10^4 mA/g, even after 4000 cycles.[20] Tang *et al*. created flower-like $Li_4Ti_5O_{12}$, consisting of nanosheets fabricated using a hydrothermal reaction, run at 170°C for 36 h; these structures exhibited a high reversible capacity and an excellent rate capability of 165.8 mAh g^{-1} at 8 C.[21] Wu *et al*. prepared petal-like

$Li_4Ti_5O_{12}$-TiO_2 nanosheets by boiling a lithium titanium peroxide - ammonium solution in an oil bath followed by a low temperature, short duration solid-state calcination. The resulting nanosheets gave rise to excellent performance with a remarkably high discharge capacity of 175.8 mAh g^{-1} after 450 cycles, representing ~94.8% of the initial discharge capacity at a 0.1 C rate.[22] Sha *et al*. fabricated well-crystallized $Li_4Ti_5O_{12}$ nanoplates through a two-step hydrothermal preparation using benzyl alcohol–$NH_3{\cdot}H_2O$ as the solvent at 180°C for 6 h followed by subsequent calcination in air; these nanoplates retained a superior discharge capacity of 153 mAh g^{-1} after 1000 charge–discharge cycles at 10 C.[23]

Therefore, herein, we have constructed novel three-dimensional $Li_4Ti_5O_{12}$ flower-like micron-scale spheres through a facile and rapid hydrothermal reaction, which possesses the following novel synthetic attributes: (i) use of a Ti foil instead of an organic titanium precursor to synthesize a 3D hierarchical $Li_4Ti_5O_{12}$ material; (ii) no other solvents except for water were needed for the hydrothermal reaction; and (iii) the hydrothermal reaction was carried out at 130°C for 4 h, which effectively shortened the reaction time and lowered the overall reaction temperature as compared with previous reported experiments.[4, 18, 24] Subsequent experiments showed that the Ti foil itself can be repeatedly recycled and re-used without either a noticeable alteration in sample morphology and quality or a drop-off in the yield of the resulting product.

The as-prepared $Li_4Ti_5O_{12}$ described herein possesses outstanding advantages that can assist in improving the measured anode performance. *First*, the flower-like $Li_4Ti_5O_{12}$ microspheres assembled by thin nanosheets can contribute to a reduced lithium ion diffusion distance. *Second*, the roughened exposed surfaces of the thin petal-like nanosheets can provide for an enhanced active surface area available for reaction and are beneficial for the interaction of the electrolyte with $Li_4Ti_5O_{12}$, thereby ultimately providing for improved voltage profiles and

charge/discharge dynamics. Herein, the as-prepared nanostructured $Li_4Ti_5O_{12}$ material was tested as an anode material for lithium ion batteries, and yielded an excellent reversible capacity and good cycling performance, even under conditions of high current densities. Specifically, at the highest discharge rate of 100 C tested, our flower-like motifs provided ~3X the discharge capacity of spherical commercial material analogues, thereby demonstrating their significantly improved rate capability.

6.2. Results and Discussion

6.2.1. Structure and Morphology of as-prepared $Li_4Ti_5O_{12}$ materials

The intermediate $Li_4Ti_5O_{12}$ precursor first obtained from the initial hydrothermal reaction can be ascribed to a ternary Li–Ti–O phase. Specifically, the XRD pattern shown in Figure 6.1A can be assigned to an orthorhombic lithium titanium oxide hydrate: $Li_{1.8}H_{0.19}Ti_2O_5 \cdot x\ H_2O$ (i.e. JCPDS card No. 47-0123) phase.[3, 18, 23] The peak possessing a relatively high intensity at $2\theta = 10.5°$ (i.e. $d_{200} = 0.84$ nm) suggests that this product possesses a layered titanate structure, an assertion which can be confirmed with SEM (Figure 6.2). Nonetheless, though the as-prepared $Li_4Ti_5O_{12}$ precursor exists as a flower-like motif, it is covered with a coating composed of a low atomic number element, possibly excess LiOH precursor, as indicated in Figure 6.2.

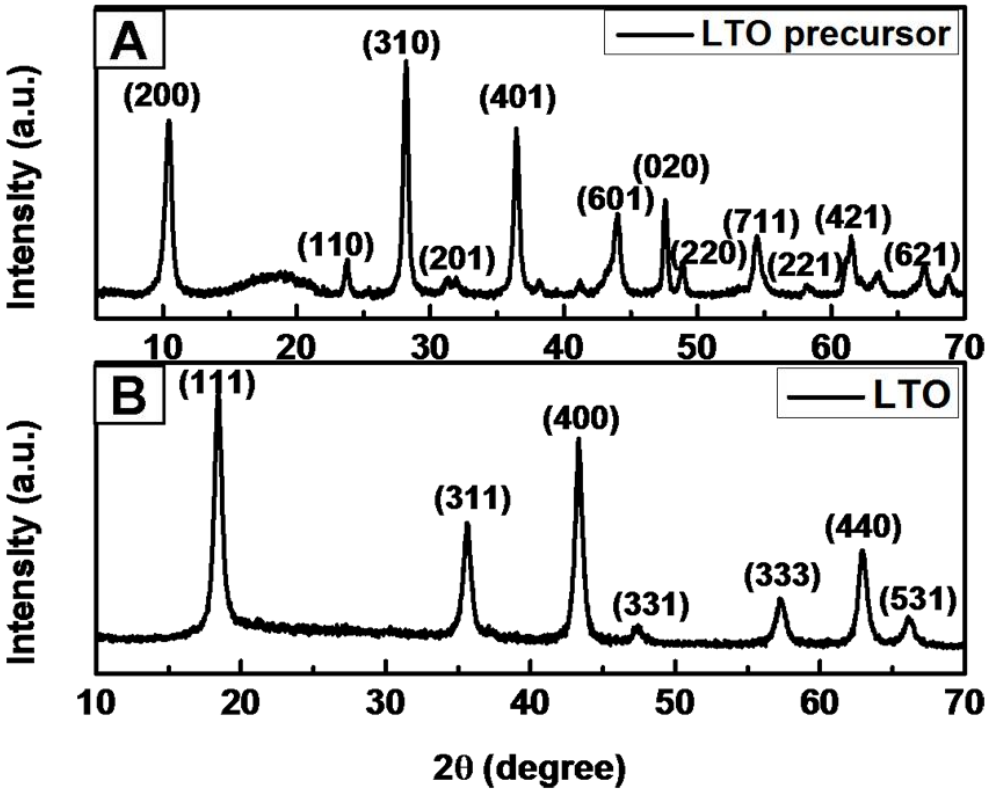

Figure 6.1. XRD patterns associated with (A) an as-prepared $Li_4Ti_5O_{12}$ (LTO) precursor as well as (B) the product of the calcination of the as-synthesized LTO precursor at 500°C. (Reprinted from *ChemSusChem* **2015**, *8*, 3304 –3313. Copyright 2015 John Wiley & Sons, Inc.).

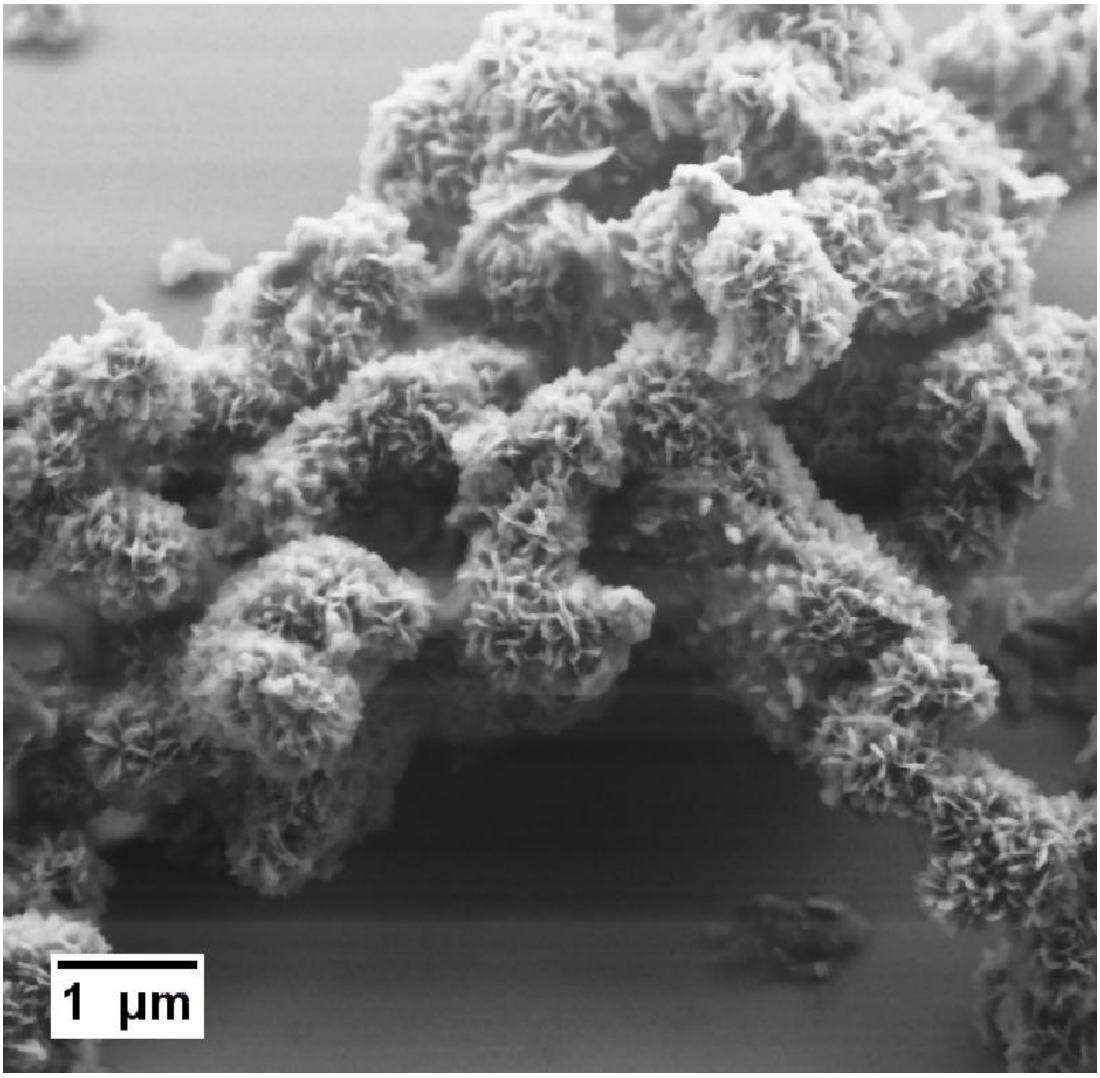

Figure 6.2. SEM image of the $Li_4Ti_5O_{12}$ precursor intermediate, obtained immediately after the hydrothermal reaction. (Reprinted from *ChemSusChem* **2015**, *8*, 3304 –3313. Copyright 2015 John Wiley & Sons, Inc.).

The TGA profile in Figure 6.3 corresponding to the layered hydrous lithium titanate indicates that it can be transformed into the $Li_4Ti_5O_{12}$ spinel phase by removing water molecules intercalated between the gaps of the lithium-titanate oxide layers, after heat treatment above 400°C. In this light, the precursor was annealed at 500°C for 3 h in order to ensure adequate transformation. The final product can be indexed to the pure cubic spinel structure of $Li_4Ti_5O_{12}$ (i.e. JCPDS card No. 49-0207) (Figure 6.1B). The broad peaks in the XRD pattern suggest that

the $Li_4Ti_5O_{12}$ possesses a small crystallite size, whose presence has been previously reported to favor enhanced rate properties of the material;[25] in fact, the mean crystallite size of our sample was calculated to be ~13.3 nm using the Debye - Scherrer equation.

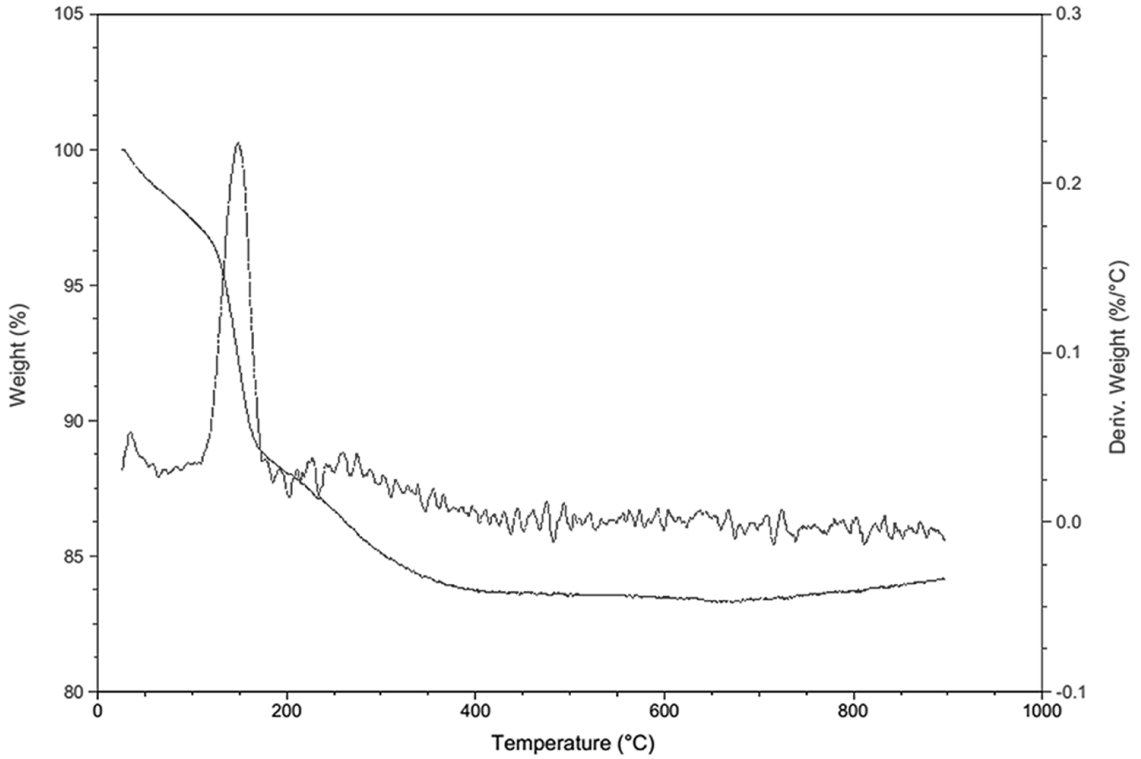

Figure 6.3. TGA curve of the $Li_4Ti_5O_{12}$ precursor intermediate, obtained immediately after the hydrothermal reaction. (Reprinted from *ChemSusChem* **2015**, *8*, 3304 –3313. Copyright 2015 John Wiley & Sons, Inc.).

The morphology and structure of as-synthesized flower-like $Li_4Ti_5O_{12}$ microspheres have been investigated using scanning electron microscopy (SEM). The overall morphology is clearly flower-like in shape with an overall diameter of 1 μm, as can be seen in Figure 6.4. At higher magnification (i.e. Figure 6.4B), the product is characterized as a hierarchical architecture, composed of an assemblage of many fine petal-like nanosheets, possessing a thickness of about 12.5 ± 2.6 nm. The presence of such a grouping of both nanoscale and micron-scale structures should increase the active, accessible surface area of the electrode material, which in turn should

contribute to an enhanced electrode performance by reducing the overall diffusion path lengths necessary for efficient ionic and electronic mobility.

More detailed structural information and morphology data were provided by transmission electron microscopy (TEM) and selected area electron diffraction (SAED). Typical TEM images of $Li_4Ti_5O_{12}$ microspheres in Figure 6.4C show that the $Li_4Ti_5O_{12}$ microspheres possess an average uniform diameter of ca. 0.9 ± 0.1 μm. A higher magnification image of the nanosheets (Figure 6.4D), corresponding to the region indicated in the inset figure in Figure 6.4C, confirms the overall layer-by-layer stacking framework as well as the roughened surfaces of the constituent component petals of the flower-like $Li_4Ti_5O_{12}$ microspheres, which could render a more efficient contact interfacial area between the active material and the intervening, surrounding electrolyte. HRTEM images of the individual petals are shown in Figure 6.4E (top-view) and Figure 6.4F (side-view), respectively. The lattice fringes with *d*-spacings of 2.09 and 4.84 Å can be respectively attributed to the (400) and (111) planes of spinel $Li_4Ti_5O_{12}$. It is also worth noting that the (400) surface has been reported to be the most energetically favorable for Li insertion,[26] suggesting that its exposure represents another possible contributor to the enhanced rate performance observed for our samples herein. The corresponding SAED pattern (inset to Figure 6.4E) can be indexed to the (111), (311), (400), (333), and (531) lattice planes, respectively. A side-view image of the petal highlights a 'sawtooth' shape, confirming the roughened surfaces of the petals (Figure 6.4F).

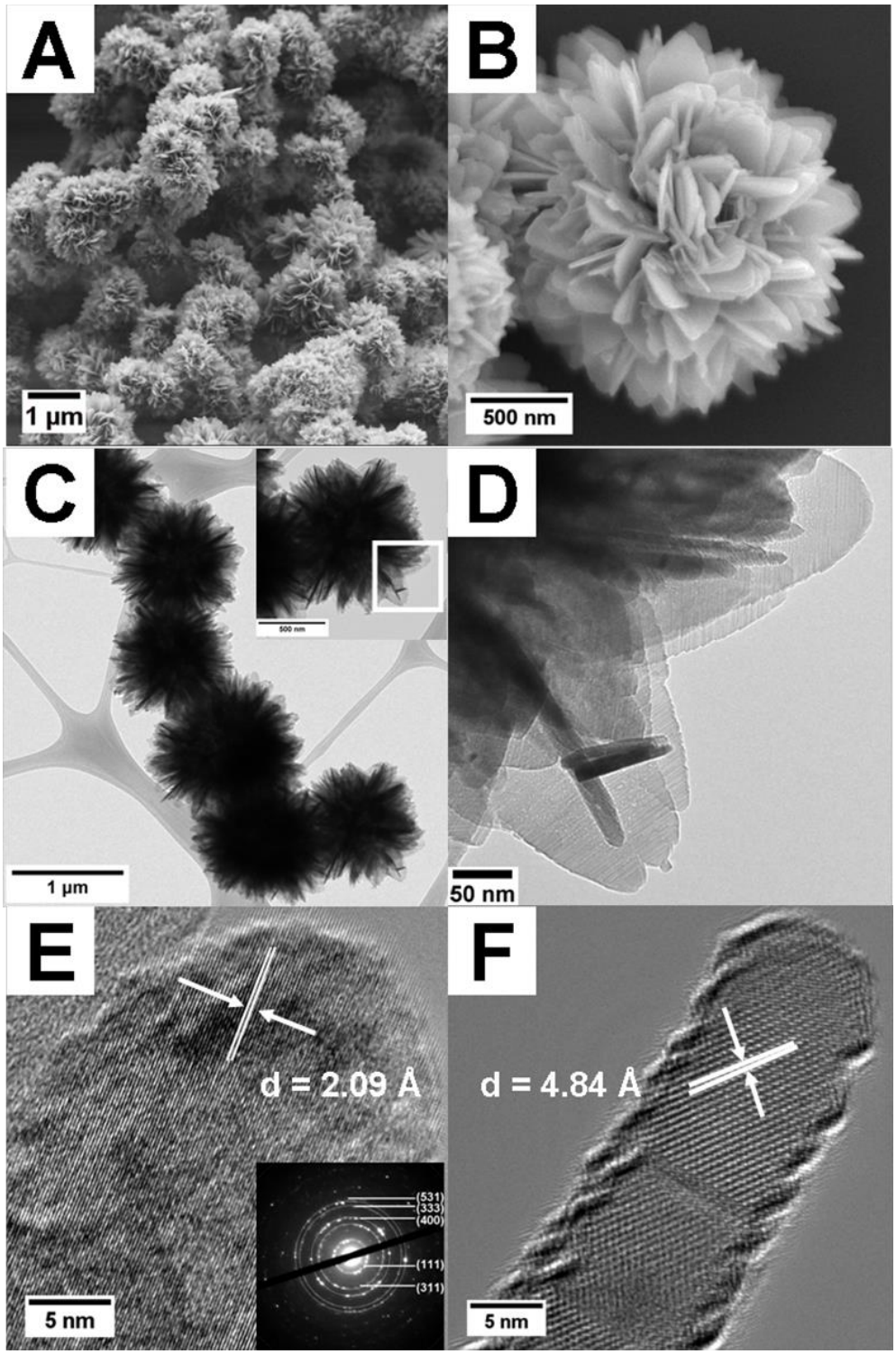

Figure 6.4. SEM (A and B) and TEM (C and D) images of as-synthesized $Li_4Ti_5O_{12}$ nanostructures at various magnifications. HRTEM image and an inset corresponding to the SAED pattern of an individual constituent petal-like nanosheet (E: top-view and F: side-view). (Reprinted from *ChemSusChem* **2015**, *8*, 3304 –3313. Copyright 2015 John Wiley & Sons, Inc.).

To obtain greater structural insights into our as-prepared 3D hierarchical $Li_4Ti_5O_{12}$ microspheres, samples were physically microtomed for subsequent TEM analysis. In particular, a series of successive radial cross-sections, obtained by serially 'cutting' through a sample of such microspheres, was collected. Each 'slice' measured ~80 nm in thickness; our goal was to analyze the overall spherical structure of an individual flower-like aggregate, commencing from its external 'petals' at one 'pole', proceeding inwards through to its innermost core, and ultimately terminating at its opposite 'pole'. A representative sequence of images collected from visualizing a series of 9 consecutive, evenly spaced sections obtained from a specific microtomed flower-shape $Li_4Ti_5O_{12}$ microsphere is depicted in Figure 6.5.

In the first two outermost sections, only exposed, loosely interconnected nanosheets can be observed, and these appear to be randomly packed. The outlines of the aggregate 'core' composed of discrete nanoparticles begin to materialize by section C. As the sectioning process progresses further inwards, the core comes into greater structural definition and focus. The core diameter itself attains an ostensible maximum value in section E with an average dimension of 444 ± 20 nm, and its individual constituent nanoparticles possess an apparent diameter of ~11.9 ± 1.8 nm. The other key structural motif present in section E, i.e. nanosheets, are characterized by average lengths of 242.7 ± 25 nm, and are arranged and aligned radially, like spokes of a wheel, around the central particulate core. Due to the inherent symmetry of the spherical microsphere, the core understandably begins to disappears from view from section F onwards, and is replaced by a growing preponderance of ever more disorganized nanosheets upon reaching the opposite 'end' of the 'flower-like' structure.

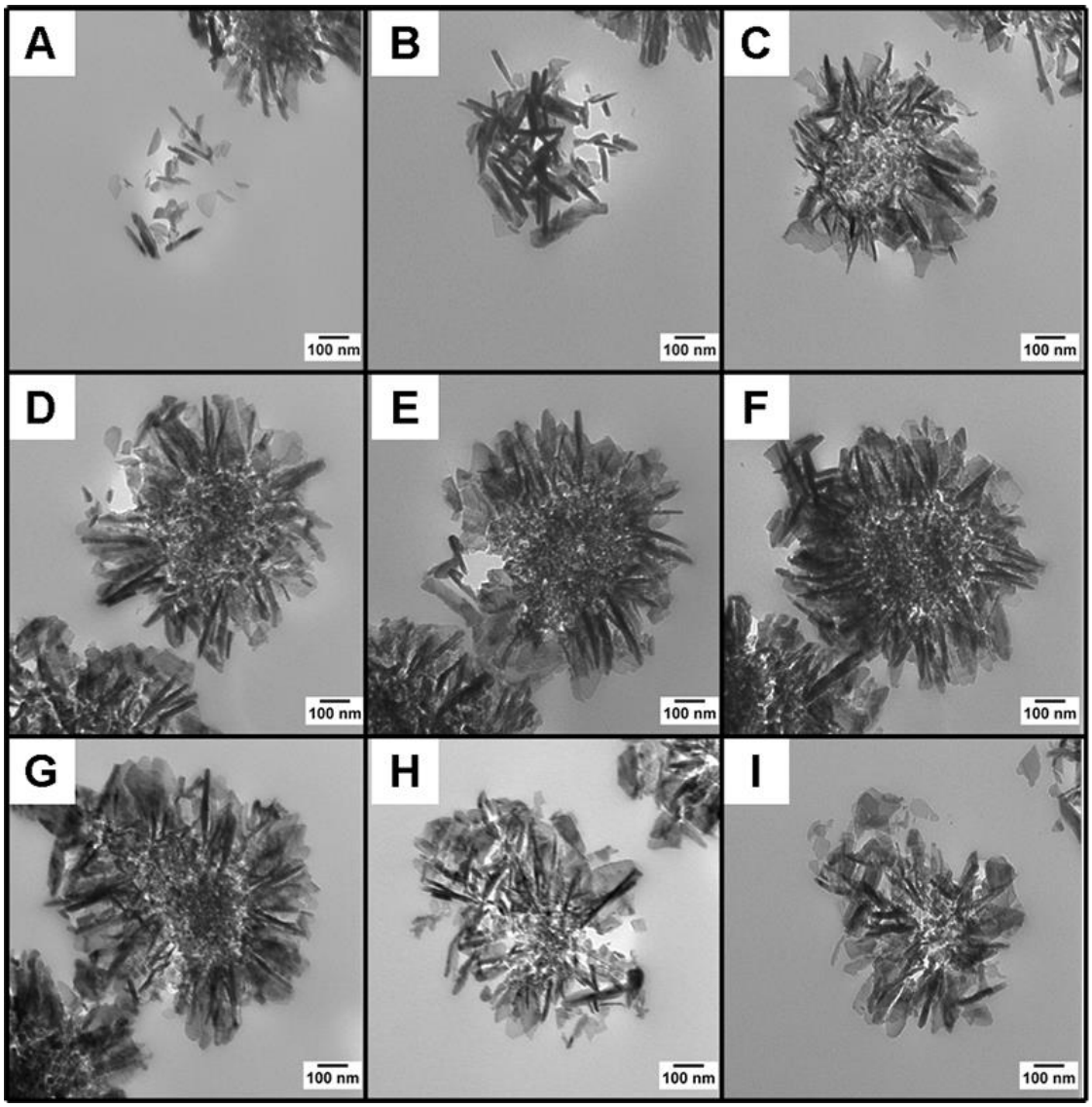

Figure 6.5 (A) through (I). Serial sections of microtomed $Li_4Ti_5O_{12}$ flowers, processed from one end to the other. (Reprinted from *ChemSusChem* **2015**, *8*, 3304 –3313. Copyright 2015 John Wiley & Sons, Inc.).

In order to fully understand the structural evolution and temporal formation of the 'flower-like' $Li_4Ti_5O_{12}$ microspheres, the effect of the reaction time upon the resulting morphology has been carefully investigated using SEM, as presented in Figure 6.6. It was observed that the morphology of the $Li_4Ti_5O_{12}$ precursor (Figure 6.2) and of the final product after further calcination at 500°C exhibited no significant differences; that is, the loss of water in $Li_{1.8}H_{0.19}Ti_2O_5 \cdot x\ H_2O$ as well as its phase transformation to spinel-type $Li_4Ti_5O_{12}$ did not induce

any obvious changes in the structure of the material. In the following analysis, only samples obtained after further calcination at 500°C are presented, due to the greater facility of obtaining interpretable SEM images of these specific samples.[23]

Over the reaction time course of 12 h, as shown in Figure 6.6, titanium foil oxidation proceeded through an H_2O_2-enhanced oxidation in aqueous LiOH solution to create the $Li_4Ti_5O_{12}$ precursor. Such a redox strategy combined with a hydrothermal reaction involving a titanium source (e.g., either Ti foil or Ti powder), a basic NaOH or KOH solution, and an oxidizing H_2O_2 solution has been previously developed by our group to generate the 3D sea-urchin TiO_2 assemblies.[27]

In the early stages of the reaction, i.e. a reaction time of 1 h (Figure 6.6A), irregularly-shaped bulk materials were observed, possessing a relatively smooth surface. Approximately 15 min later (Figure 6.6B), small, ultrafine nanoparticles were generated by a rapid nucleation process,[28] and these particles later aggregated to produce the core of the 'flower-like' structure. At this initial reaction stage, products collected after hydrothermal reaction maintained a very low yield.

When the reaction time was increased to 1.5 h (Figure 6.6C), evidence of the appearance of closely packed, layered nanoplatelets comprising more defined edges and smooth surfaces was noted, as if the shapeless bulk were being deftly 'chiseled' and 'molded' by the hydrogen peroxide solution into more recognizable morphologies. These plate-like architectures further evolved into aggregates of thinner nanosheets with average thicknesses of 30.8 ± 6.5 nm, and these appeared to freely self assemble to generate a larger, more complex, and more ordered 6.6D hierarchical motif with little if any nanoparticles present, upon a reaction time of 1 h and 45 min (Figure 6.6D).

Additionally, after a reaction time of 2 h (Figure 6.6E), unbound, detached 'flower-like' $Li_4Ti_5O_{12}$ microspheres started to appear, possessing an overall diameter of 1.3 ± 0.1 μm with their individual constituent petals measuring 25.4 ± 3.3 nm in thickness. As the reaction time was prolonged to 4 h (Figure 6.6F), the microspheres became somewhat smaller with overall dimensions of 0.9 ± 0.1 μm in diameters, and the individual constituent petals thinned by approximately half to 12.5 ± 2.6 nm. The simultaneous decrease in not only the diameter of the flower-like microspheres but also the thicknesses of the petals can reasonably be attributed to additional etching from the surrounding, enveloping H_2O_2 solution. We believe this unique, relatively uniform morphology to be beneficial for an enhancement in electrode performance, due to the potential for shortened ion diffusion distances and enhanced contact surface area with the electrolyte. As the reaction proceeded onwards to 8 h, a more polydisperse mixture of flower-like microspheres and aggregated particles was noted, as shown in Figure 6.6G. At a reaction time of 12 h and beyond (Figure 6.6H), the 3D flower-like structures appeared to ostensibly fall apart and disintegrate with the concomitant formation of smaller, more plentiful motifs comprised of nanoparticles and nanosheets.

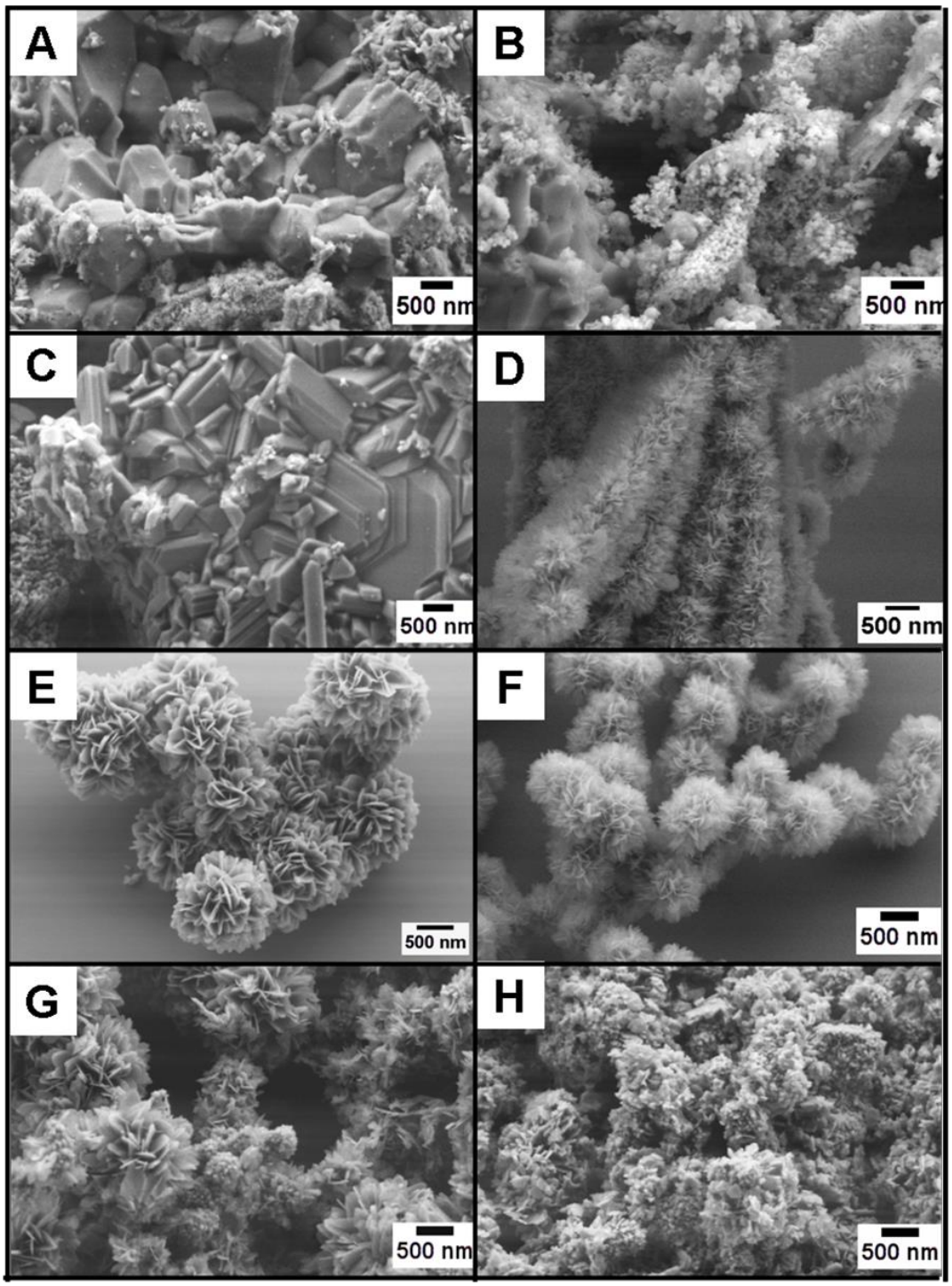

Figure 6.6. SEM images of precursor $Li_4Ti_5O_{12}$ micron-scale spheres, grown at various reaction stages with successively increasing reaction times of (A) 1 h, (B) 1 hour 15 min, (C) 1 hour 30 min, (D) 1 h 45 min, (E) 2 h, (F) 4 h, (G) 8 h, and (H) 12 h, respectively. (Reprinted from *ChemSusChem* **2015**, *8*, 3304 –3313. Copyright 2015 John Wiley & Sons, Inc.).

Based on the SEM and TEM analyses discussed above, we have devised a plausible scheme to clearly illustrate the growth procedures of the flower-like $Li_4Ti_5O_{12}$ precursor. As mentioned, our initial step was to generate from a redox strategy combined with a hydrothermal reaction, as a function of increasing hydrothermal reaction time (presented in Scheme 6.1). The oxidation of Ti foil proceeded through an H_2O_2-enhanced oxidation process in the presence of LiOH aqueous solution. In the initial stages of the reaction, we noted bulk-like in addition to rapidly nucleated, small particulate morphologies of Li-Ti-O. Particularly after 1.5 h of reaction time, the surface of the bulk material continued to roughen with the concomitant formation of layered sheets. It has been previously reported that the addition of a large amount of H_2O_2 can induce the formation of distinctive layered hydrous lithium titanate nanosheets, which are precursors to particular morphological motifs of $Li_4Ti_5O_{12}$.[18, 29] Moreover, a similar 'evolution' of structures has been previously reported by Tang *et al.* during the analogous synthesis of TiO_2 microspheres using H_2O_2 under alkaline reaction conditions.[30] All of these observations can be reasonably attributed to the fact that regions of the bulk material undergo localized dissolution–precipitation followed by an in-situ transformation during the hydrothermal reaction.[31, 32]

When the reaction time was prolonged to 1 h and 45 min, the ongoing H_2O_2 etching 'sculpted' the underlying bulk material into hierarchical aggregates of individual thinner nanosheets. The driving force favoring spherical 3D architectures can be presumably ascribed to factors such as but not limited to van der Waals attractive forces, hydrogen bonding,[32] interfacial tension, the postulated hydrophilicity of adjacent titanate surfaces,[27] as well as the minimization of the overall total energy of the system.[33] After a longer growth and etching process to 2 h, the larger nanosheet aggregates started to break up into smaller individual, discrete 3D 'flower-shape' motifs. Additional reaction to 4 h resulted in a continued thinning of the individual

constituent ‘petals’ and a perceptible decrease in the overall sizes of our ‘flowers’. When the reaction time was further extended to 8 h and beyond, the desired 3D hierarchical structure itself began to disintegrate into less organized, individual discrete ‘petals’ and particles with a polydisperse size distribution. We should note that all of the resulting products from the hydrothermal reaction were likely encapsulated with unreacted LiOH precursor, present in excess in order to compensate for Li volatilization during the calcination process.

From the electrochemically desirable vantage point of exploiting an Li-Ti-O precursor intermediate, possessing attributes of an optimized surface area, size monodispersity, chemical purity, morphological definition, as well as structural integrity, our products isolated after 4 h represented the ‘best’ choice. After the subsequent annealing process in air, the initial flower motif was successfully retained, and the intermediate Li-Ti-O phase was transformed into the desired spinel $Li_4Ti_5O_{12}$ structure.

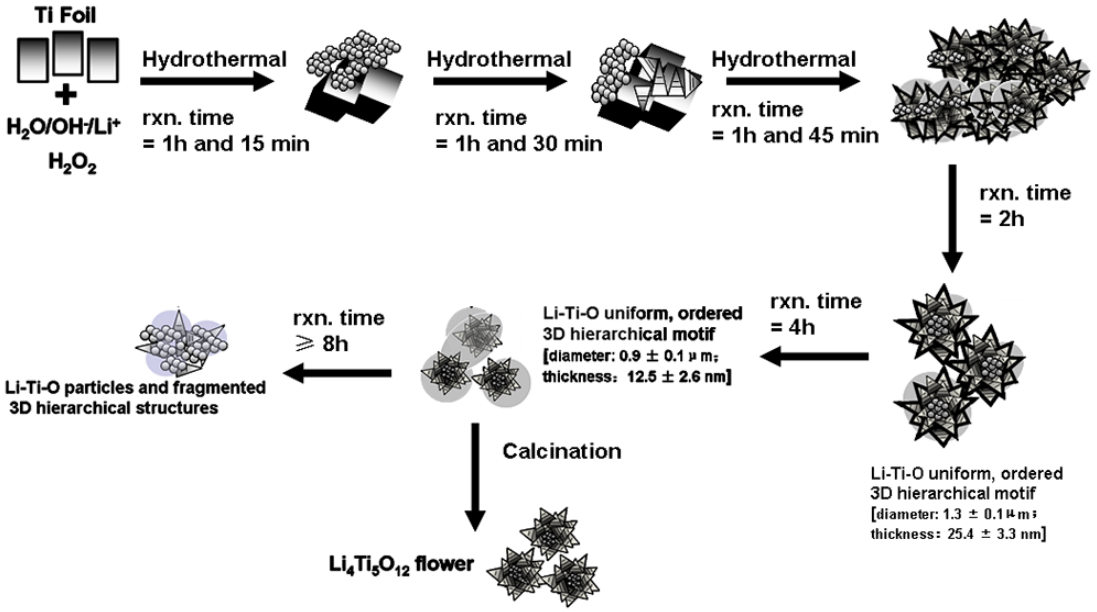

Scheme 6.1. Proposed formation process of LTO precursors and ‘flower-like’ $Li_4Ti_5O_{12}$ motifs. (Reprinted from *ChemSusChem* **2015**, *8*, 3304 –3313. Copyright 2015 John Wiley & Sons, Inc.).

The surface area of our $Li_4Ti_5O_{12}$ materials was determined using the BET gas adsorption method. We found that our as-synthesized 'flower-like' materials possess a surface area of 44 m^2/g as compared with 10 m^2/g for the spherically-shaped control samples. Presumably, the high surface area can be attributed to a combination of the 3D hierarchical structure and the roughened surfaces of the 'sawtooth' shape petals, which lead to an enlarged interfacial contact area between the electrolyte and the $Li_4Ti_5O_{12}$ sample, thereby providing for the superior high-rate capacities and charge/discharge dynamics observed.

6.2.2. Electrochemical performance

Figures associated with the following discussions will be presented in the thesis from Yiman Zhang (Takeuchi Group, Stony Brook University). The electrochemical cells were tested in galvanostatic mode. In total, the flower-like and spherical $Li_4Ti_5O_{12}$ materials were subjected to 100 discharge-charge cycles at different discharge rates, ranging from 0.2 C to 100 C, with a moderate rate of a 0.2 C charge for cycles 1-50 and 71-100, respectively; a 0.5 C charge was used for the intervening interval consisting of cycles 51 to 70. This unusual regimen provided the opportunity to effectively assess both the rate capability and the capacity retention of our samples. In effect, our special motifs evinced excellent rate capability, delivering 148, 141, 137, 123, and 60 mAh g^{-1} under discharge rates of 0.2 C, 10 C, 20 C, 50 C, and 100 C, at cycles 50, 55, 60, 65, and 70, respectively. By contrast, the spherical $Li_4Ti_5O_{12}$ control material only delivered 148, 114, 106, 80, and 20 mAh g^{-1} under identical circumstances. Thus, the realized capacity was similar under low rate discharge conditions but very different under high rates of discharge, with an evidently higher delivered capacity from our as-prepared 'flower-like' $Li_4Ti_5O_{12}$.

The capacity retention behavior was assessed by considering the capacity under a lower rate 0.2 C discharge as a function of cycle number. At cycles 10, 30, 50, and 100, the capacities for the spherical control were 150, 148, 148, and 148 mAh g^{-1}, respectively, whereas the capacities for our unique flower-like architectures were 151, 149, 148, and 147 mAh g^{-1}, respectively. Thus, both materials exhibited a similar capacity retention of 97% from cycles 10 – 100 and ~99% from cycles 20 - 100.

The voltage profiles of both as-synthesized flower-like $Li_4Ti_5O_{12}$ and commercial spherical $Li_4Ti_5O_{12}$ were consistent with prior reports for $Li_4Ti_5O_{12}$, i.e. showing a long single plateau followed by a steep voltage transition for discharge at rates ≤ 50 C. The voltage versus capacity curves were generated at cycles 50, 55, 60, 65, and 70, respectively, in order to assess the relative polarization of the two $Li_4Ti_5O_{12}$ materials tested under various discharge rates. Under the 0.2 C, 10 C, and 20 C rates, the two $Li_4Ti_5O_{12}$ materials, i.e. the spherical as well as the 'flower-like' morphologies, evinced voltages plateaus at 1.56 (1.57), 1.45 (1.48), and 1.39 (1.41) respectively, all within 20-30 mV of each other. At the higher rate discharge (50 C), additional polarization was evident in the spherical control, with a 60 mV lower voltage, relative to our flower-like motifs (i.e. 1.23 versus 1.29 V). At the highest discharge rate of 100 C, our as-prepared flower-like structures provided for ~3X the discharge capacity of the spherical control, thereby clearly highlighting demonstrating the significantly improved rate capability of the products of our synthesis-driven designs.

To further evaluate the rate capability of the material, 200 additional discharge-charge cycles were performed under perceptibly higher and more rigorous 20 C discharge and 20 C charge rates. The flower-like $Li_4Ti_5O_{12}$ material delivered 134 mAh g^{-1} on cycle 101 and 117 mAh g^{-1} on cycle 300 (i.e. 87% capacity retention), whereas the commercial spherical $Li_4Ti_5O_{12}$

only gave rise to 103 mAh g^{-1} on cycle 101 and 77 mAh g^{-1} on cycle 300 (i.e. 66% capacity retention). Thus, our 'flower-like' materials exhibited both a significantly improved capacity and a superior capacity retention (~20% reduced fade) as compared with commercial spherical analogues under 'high rate' conditions.

In order to further investigate the structural stability of the electrodes, pre- and post-cycling SEM images of electrodes containing commercial $Li_4Ti_5O_{12}$ (Figure 6.7 A and B) and the as-synthesized flower-like $Li_4Ti_5O_{12}$ (Figure 6.7C and D) are analyzed. Both pre-cycling electrodes evince reasonable surface uniformity with particles (Figure 6.7A) and 3D hierarchical microspheres (Figure 6.7C) of $Li_4Ti_5O_{12}$ active materials mixed with carbon black spheres. After 300 discharge-charge cycles, the morphology of the commercial $Li_4Ti_5O_{12}$ electrode retains intact. It is worth to mention that the flower-like $Li_4Ti_5O_{12}$ materials with nanosheet constituents are still discernible in the electrode after cycling (Figure 6.7D), indicating the high structural stability of our synthesized 3D hierarchical $Li_4Ti_5O_{12}$ motifs.

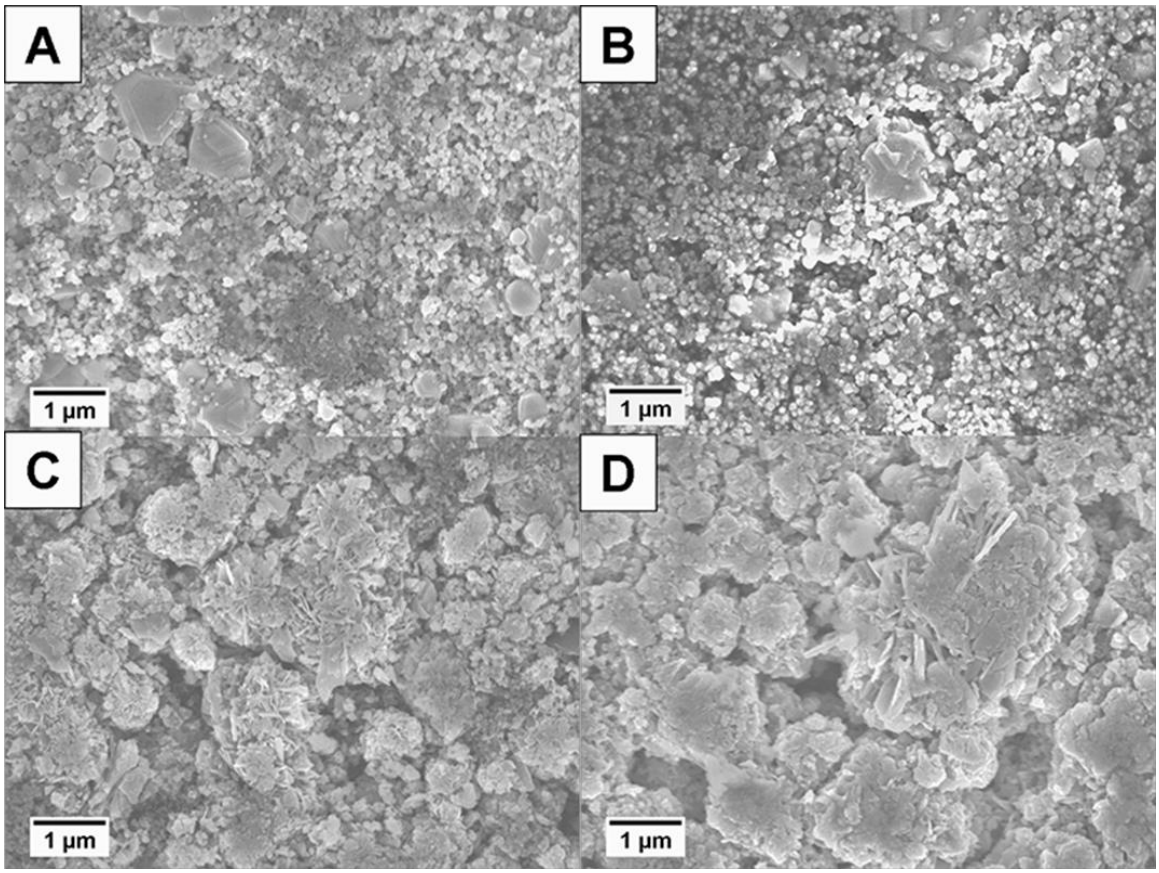

Figure 6.7. SEM images of electrodes taken both before (A and C) and after (B and D) electrochemical cycling. (A) and (B) correspond to the commercial $Li_4Ti_5O_{12}$ whereas (C) and (D) are associated with the as-synthesized flower-like $Li_4Ti_5O_{12}$, both active materials are coupled with carbon black. (Reprinted from *ChemSusChem* **2015**, *8*, 3304 –3313. Copyright 2015 John Wiley & Sons, Inc.).

These electrochemical results for our flower-like $Li_4Ti_5O_{12}$ prepared were considered in light of prior reports for materials of similar structure (summarized in Table 6.1). We should state at the outset that our synthesis protocol is relatively more simplistic and less time-consuming as compared with the strategies used for other previously reported structures. In terms of a direct comparison of electrochemical results, after ~50 cycles of testing, herein we observed a discharge capacity of ~140 mAh g^{-1} under 10 C discharge, whereas a previously reported 'flower-like' $Li_4Ti_5O_{12}$ structure gave rise to ~150 mAh g^{-1} under 8 C,[34] and a different 'peony-like' $Li_4Ti_5O_{12}$ material yielded merely ~100 mAh g^{-1} under 10 C discharge.[35] As another

example, after ~65 cycles of testing, we noted a discharge capacity of 123 mAh g^{-1} observed at 50 C, whereas a similar porous hierarchical $Li_4Ti_5O_{12}$ architecture reported in the literature only delivered 121 mAh g^{-1} at a 30 C discharge rate.[25] Finally, another analogous urchin-like $Li_4Ti_5O_{12}$ motif gave rise to 120.8 mAh g^{-1} at 20 C rate.[31]

Notably, our as-prepared structures have been tested under high rate discharge conditions, and it is worth mentioning that our as-prepared flower-like $Li_4Ti_5O_{12}$ maintained a capacity of ≥60 mAh g^{-1} at 100 C. Furthermore, after 300 total cycles including >200 cycles at anomalously high discharge rates ≥ 20 C, our 'flower-like' $Li_4Ti_5O_{12}$ material delivered 117 mAh g^{-1}. To the best of our knowledge, this represents one of the more strenuous tests incorporating $Li_4Ti_5O_{12}$ material of this specific hierarchical morphology. In terms of capacity retention, the behavior of our flower-like $Li_4Ti_5O_{12}$ structure compares favorably with that of other previously reported flower-like $Li_4Ti_5O_{12}$ materials. For instance, after 100 cycles, our capacity was 147 mAh g^{-1} under 0.2 C (i.e. 97% relative to cycle 10 and ~99% from cycles 20 - 100), and 117 mAh g^{-1} after 300 cycles under a relatively high discharge rate of 20 C, demonstrating not only comparable performance, relative to a prior flower-like $Li_4Ti_5O_{12}$ motif,[34] but also, importantly, significant capacity retention improvement, relative to prior dandelion-like[36] and peony-like $Li_4Ti_5O_{12}$ materials.[35] Moreover, it has been previously reported[28] that the favorable cyclic retention can be attributed to the 3D motif itself, which can effectively accommodate the drastic volume changes associated with Li insertion and extraction.

Table 6.1. Comparison of Synthesis Methods and Corresponding Electrode Performances of $Li_4Ti_5O_{12}$ prepared in this work and in prior cited literature. (Reprinted TOC figure from *ChemSusChem* **2015**, *8*, 3304 –3313. Copyright 2015 John Wiley & Sons, Inc.).

Material	***Method***	***Rate Capability***	***Cycling Performance***	**Ref.**
Flower-like $Li_4Ti_5O_{12}$ (discharge range: 3.0-1.0 V)	Hydrothermal: 130°C for 4 h Anneal: 500°C for 3 h	For cycles 55, 60, 65, and 70: 10 C: 141 mA h g^{-1}; 20 C: 137 mA h g^{-1}; 50 C: 123 mA h g^{-1}; 100 C: 60 mA h g^{-1}	For cycles 20-100: 0.2 C: 99% retention; For cycles 101-300: 20 C: 87% retention	This work
Flower-like $Li_4Ti_5O_{12}$ (discharge range: 2.5-1.5 V)	Hydrothermal: 170°C for 36 h with ammonia and ethylene glycol. Anneal: 500°C for 2 h	First discharge 8 C: 165.8 mA h g^{-1}	For cycles 5-100: 8 C: 152 mA h g^{-1}, 3.8% fading rate	27
Peony-like $Li_4Ti_5O_{12}$ (discharge range: 2.5-1.0 V)	Hydrothermal: 180℃ for 24 h with CTAB. Anneal: 400°C for 2 h	First discharge 1 C: 176.0 mA h g^{-1} 10 C: 119.7 mA h g^{-1}	For 10-100 cycles: 1 C: 137.1 mA h g^{-1}; 10 C: 100.1 mA h g^{-1}, 4.8% fading rate	28
Hierarchically porous $Li_4Ti_5O_{12}$ (discharge range: 2.0-1.0 V)	Sol-gel: 24 h + hydrothermal at 100°C for 24 h Anneal: 700°C for 2 h	3 cycles discharge: 10 C: 155 mA h g^{-1}; 30 C: 121 mA h g^{-1}	For 1-500 cycles: 5 C: 98% retention	19
Dandelion-like $Li_4Ti_5O_{12}$ (discharge range: 3.0-0.7 V)	Hydrothermal: 150°C for 6 h Anneal: 500°C for 4 h	First discharge 0.69 C: 138 mA h g^{-1}	For 1-100 cycles: 0.69 C: 117 mA h g^{-1}, 15.2% loss	29
Urchin-like hierarchical hollow $Li_4Ti_5O_{12}$ (discharge range: 3.0-1.0 V)	Hydrothermal: 150°C for 24 h Anneal: 600°C for 2 h	At cycles 80 and 90: 10 C: 134.6 mA h g^{-1}; 20 C: 120.8 mA h g^{-1}	For 1-100 cycles: 2 C: 1.9% capacity loss	25a

6.3. Conclusions

Nanostructured flower-like $Li_4Ti_5O_{12}$ structures have been successfully synthesized by a simplistic and rapid hydrothermal method involving short reaction times, relatively low reaction temperatures, and re-useable, recyclable Ti precursors. By taking advantage of the etching capability of the H_2O_2 solution under hydrothermal conditions, the resulting "flower-like" precursor to $Li_4Ti_5O_{12}$ possesses a high surface area as well as a uniform 3-D layered morphology. Upon calcination at a relatively low temperature of 500°C, a well-crystallized final product was generated.

The thin petal-like constituent nanosheets of individual $Li_4Ti_5O_{12}$ assemblies in addition to the 'sawtooth'-shaped roughened surface of the discrete petals greatly enhance the interfacial contact area with the surrounding electrolyte and shorten Li-ion diffusion distances, all of which are beneficial in terms of contributing to the excellent rate capability and stable cycling performance observed for as-prepared anodes. The resulting $Li_4Ti_5O_{12}$ electrodes exhibited remarkably high rate performances of 141, 137, 123, and 60 mAh g^{-1} under discharge rates of 10 C, 20 C, 50 C, and 100 C, respectively. When discharged at 0.2 C, the electrode evinced a capacity retention of ~97% from cycles 10 – 100, ~99% from cycles 20 – 100, and ~87% under a higher and more robust discharge rate of 20 C from cycles 101-300. As mentioned above, this facile, straightforward, and reasonably rapid synthesis protocol represents a promising technique to prepare 3D nanostructured $Li_4Ti_5O_{12}$ materials on a large scale for effective use in high-rate Li-ion batteries.

6.4. References

1. Wu, F. X.; Li, X. H.; Wang, Z. X.; Guo, H. J. Petal-like $Li_4Ti_5O_{12}$-TiO_2 nanosheets as high-performance anode materials for Li-ion batteries. *Nanoscale* **2013**, *5*, 6936-6943.
2. Zhang, Z. H.; Li, G. C.; Peng, H. R.; Chen, K. Z. Hierarchical hollow microspheres assembled from N-doped carbon coated $Li_4Ti_5O_{12}$ nanosheets with enhanced lithium storage properties. *J. Mater. Chem. A* **2013**, *1*, 15429-15434.
3. Tang, Y. F.; Yang, L.; Fang, S. H.; Qiu, Z. $Li_4Ti_5O_{12}$ hollow microspheres assembled by nanosheets as an anode material for high-rate lithium ion batteries. *Electrochim. Acta* **2009**, *54*, 6244-6249.
4. Kong, D.; Ren, W.; Luo, Y.; Yang, Y.; Cheng, C. Scalable synthesis of graphene-wrapped $Li_4Ti_5O_{12}$ dandelion-like microspheres for lithium-ion batteries with excellent rate capability and long-cycle life. *J. Mater. Chem. A* **2014**, *2*, 20221-20230.
5. Zhu, G. N.; Wang, Y. G.; Xia, Y. Y. Ti-based compounds as anode materials for Li-ion batteries. *Energy Environ. Sci.* **2012**, *5*, 6652-6667.
6. Liu, W. J.; Shao, D.; Luo, G. E.; Gao, Q. Z.; Yan, G. J.; He, J. R.; Chen, D. Y.; Yu, X. Y.; Fang, Y. P. Mesoporous Spinel $Li_4Ti_5O_{12}$ Nanoparticles for High Rate Lithium-ion Battery Anodes. *Electrochim. Acta* **2014**, *133*, 578-582.
7. Choi, J.-H.; Ryu, W.-H.; Park, K.; Jo, J.-D.; Jo, S.-M.; Lim, D.-S.; Kim, I.-D. Multi-layer electrode with nano- $Li_4Ti_5O_{12}$ aggregates sandwiched between carbon nanotube and graphene networks for high power Li-ion batteries. *Sci. Rep.* **2014**, *4*, 7334.
8. K. M. Colbow, J. R. D., R. R. Haering. Structure and electrochemistry of the spinel oxides LiTi2O4 and Li4/3Ti5/3O4. *J. Power Sources* **1989**, *26*, 397-402.
9. Norio Takami, K. H., Hiroki Inagaki. Lithium Diffusion in Li4/3Ti5/3O4 Particles during Insertion and Extraction. *J. Electrochem. Soc.* **2011**, *158*, A725-A730.
10. T. Brousse, P. F., R. Marchand, D. M. Schleich, O. Bohnke, K. West. All oxide solid-state lithium-ion cells. *J. Power Sources* **1997**, *1997*, 412-415.
11. C.Y. Ouyang, Z. Y. Z., M.S. Lei. Ab initio studies of structural and electronic properties of $Li_4Ti_5O_{12}$ spinel. *Electrochem. Commun.* **2007**, *2007*, 1107-1112.
12. Yi, T. F.; Jiang, L. J.; Shu, J.; Yue, C. B.; Zhu, R. S.; Qiao, H. B. Recent development and application of $Li_4Ti_5O_{12}$ as anode material of lithium ion battery. *J. Phys. Chem. Solids* **2010**, *71*, 1236-1242.
13. Yi, T.-F.; Yang, S.-Y.; Xie, Y. Recent advances of $Li_4Ti_5O_{12}$ as a promising next generation anode material for high power lithium-ion batteries. *J. Mater. Chem. A* **2015**, *3*, 5750-5777.
14. Lim, J.; Choi, E.; Mathew, V.; Kim, D.; Ahn, D.; Gim, J.; Kang, S. H.; Kim, J. Enhanced High-Rate Performance of $Li_4Ti_5O_{12}$ Nanoparticles for Rechargeable Li-Ion Batteries. *J. Electrochem. Soc.* **2011**, *158*, A275-A280.
15. Sun, L.; Wang, J. P.; Jiang, K. L.; Fan, S. S. Mesoporous $Li_4Ti_5O_{12}$ nanoclusters as high performance negative electrodes for lithium ion batteries. *J. Power Sources* **2014**, *248*, 265-272.
16. Shen, L. F.; Uchaker, E.; Zhang, X. G.; Cao, G. Z. Hydrogenated $Li_4Ti_5O_{12}$ Nanowire Arrays for High Rate Lithium Ion Batteries. *Adv. Mater.* **2012**, *24*, 6502-6506.
17. Liu, J.; Song, K. P.; van Aken, P. A.; Maier, J.; Yu, Y. Self-Supported $Li_4Ti_5O_{12}$ C Nanotube Arrays as High-Rate and Long-Life Anode Materials for Flexible Li-Ion Batteries. *Nano Lett.* **2014**, *14*, 2597-2603.

18. Chen, J. Z.; Yang, L.; Fang, S. H.; Tang, Y. F. Synthesis of sawtooth-like $Li_4Ti_5O_{12}$ nanosheets as anode materials for Li-ion batteries. *Electrochim. Acta* **2010**, *55*, 6596-6600.
19. Xia, H.; Luo, Z. T.; Xie, J. P. Nanostructured lithium titanate and lithium titanate/carbon nanocomposite as anode materials for advanced lithium-ion batteries. *Nanotechnology Reviews* **2014**, *3*, 161-175.
20. Kim, S.; Fang, S. H.; Zhang, Z. X.; Chen, J. Z.; Yang, L.; Penner-Hahn, J. E.; Deb, A. The electrochemical and local structural analysis of the mesoporous $Li_4Ti_5O_{12}$ anode. *J. Power Sources* **2014**, *268*, 294-300.
21. Tang, Y. F.; Yang, L.; Qiu, Z.; Huang, J. S. Preparation and electrochemical lithium storage of flower-like spinel $Li_4Ti_5O_{12}$ consisting of nanosheets. *Electrochem. Commun.* **2008**, *10*, 1513-1516.
22. Wu, F.; Li, X.; Wang, Z.; Guo, H. Petal-like $Li_4Ti_5O_{12}$-TiO_2 nanosheets as high-performance anode materials for Li-ion batteries. *Nanoscale* **2013**, *5*, 6936-6943.
23. Sha, Y. J.; Zhao, B. T.; Ran, R.; Cai, R.; Shao, Z. P. Synthesis of well-crystallized Li4Ti5O12 nanoplates for lithium-ion batteries with outstanding rate capability and cycling stability. *J. Mater. Chem. A* **2013**, *1*, 13233-13243.
24. Li, G. C.; Xia, J.; Jiao, J. Q.; Chen, L. P.; Shen, P. K. Low-temperature Synthesis of Peony-like Spinel $Li_4Ti_5O_{12}$ as a High-performance Anode Material for Lithium Ion Batteries. *Chin. J. Chem.* **2011**, *29*, 1824-1828.
25. Hasegawa, G.; Kanamori, K.; Kiyomura, T.; Kurata, H.; Nakanishi, K.; Abe, T. Hierarchically Porous $Li_4Ti_5O_{12}$ Anode Materials for Li- and Na-Ion Batteries: Effects of Nanoarchitectural Design and Temperature Dependence of the Rate Capability. *Adv. Energy Mater.* **2015**, *5*, 1400730.
26. Guo, J.; Zuo, W.; Cai, Y.; Chen, S.; Zhang, S.; Liu, J. A novel $Li_4Ti_5O_{12}$-based high-performance lithium-ion electrode at elevated temperature. *J. Mater. Chem. A* **2015**, *3*, 4938-4944.
27. Mao, Y. B.; Kanungo, M.; Hemraj-Benny, T.; Wong, S. S. Synthesis and growth mechanism of titanate and titania one-dimensional nanostructures self-assembled into hollow micrometer-scale spherical aggregates. *J. Phys. Chem. B* **2006**, *110*, 702-710.
28. Yang, R.; Gu, Y.; Li, Y.; Zheng, J.; Li, X. Self-assembled 3-D flower-shaped SnO_2 nanostructures with improved electrochemical performance for lithium storage. *Acta Mater.* **2010**, *58*, 866-874.
29. Wu, F.; Li, X.; Wang, Z.; Guo, H. Petal-like $Li_4Ti_5O_{12}$-TiO_2 nanosheets as high-performance anode materials for Li-ion batteries. *Nanoscale* **2013**, *5*, 6936-6943.
30. Tan, Y. F.; Yang, L.; Chen, J. Z.; Qiu, Z. Facile Fabrication of Hierarchical Hollow Microspheres Assembled by Titanate Nanotubes. *Langmuir* **2010**, *26*, 10111-10114.
31. Cheng, J.; Che, R. C.; Liang, C. Y.; Liu, J. W.; Wang, M.; Xu, J. J. Hierarchical hollow $Li_4Ti_5O_{12}$ urchin-like microspheres with ultra-high specific surface area for high rate lithium ion batteries. *Nano Research* **2014**, *7*, 1043-1053.
32. Cheng, Z. P.; Xu, J. M.; Zhong, H.; Chu, X. Z.; Song, J. Hydrogen peroxide-assisted hydrothermal synthesis of hierarchical CuO flower-like nanostructures. *Mater. Lett.* **2011**, *65*, 2047-2050.
33. Xiong, J. Y.; Cheng, G.; Lu, Z.; Tang, J. L.; Yu, X. L.; Chen, R. BiOCOOH hierarchical nanostructures: Shape-controlled solvothermal synthesis and photocatalytic degradation performances. *CrystEngComm* **2011**, *13*, 2381-2390.

34. Tang, Y. F.; Yang, L.; Qiu, Z.; Huang, J. S. Preparation and electrochemical lithium storage of flower-like spinel $Li_4Ti_5O_{12}$ consisting of nanosheets. *Electrochem. Commun.* **2008**, *10*, 1513-1516.
35. Li, G.; Xia, J.; Jiao, J.; Chen, L.; Shen, P. Low-temperature synthesis of peony-like spinel $Li_4Ti_5O_{12}$ as a high-performance anode material for lithium ion batteries. *Chin. J. Chem.* **2011**, *29*, 1824-1828.
36. Kong, D.; Ren, W.; Luo, Y.; Yang, Y.; Cheng, C. Scalable synthesis of graphene-wrapped $Li_4Ti_5O_{12}$ dandelion-like microspheres for lithium-ion batteries with excellent rate capability and long-cycle life. *J. Mater. Chem. A* **2014**, *2*, 20221-20230.

Chapter 7. Understanding the Effect of Preparative Approaches in the Formation of "Flower-like" $Li_4Ti_5O_{12}$ - Multiwalled Carbon Nanotube Composite Motifs with Performance as High-rate Anode Materials for Li-ion Battery Applications

7.1. Introduction

One of the key goals of sustainability is to create reliable, efficient, and cost-effective alternatives for fueling and powering conventional devices. In particular, the development of Li-ion batteries (LIBs) possessing high rate performance, superior durability, as well as desirable environmental sustainability is critical to advancing the practical applicability of batteries in applications ranging from smart electronics to electric vehicles.[1-3] Conventional LIBs associated with graphite anode materials suffer from lithium deposition on the anode surface, leading to poor cycling stability.[4-6] Hence, as a promising alternative anode material, the idea of using spinel $Li_4Ti_5O_{12}$ (LTO) has been extensively probed, because of the material's several intrinsic advantages. These include the fact that such anodes exhibit *(i)* a high and stable potential plateau value (*i.e.* 1.55 V *versus* Li/Li^+), thereby avoiding the deposition of lithium dendrites and suppressing the reduction of the electrolyte; *(ii)* an excellent durability over an extended cycle life due to a negligible volume change during electrochemical cycling; as well as *(iii)* a high thermal stability, potentially enabling their use at elevated temperatures.[4, 7] Hence, overcoming the inherently low conductivity ($<10^{-13}$ S cm^{-1}) coupled with the moderate lithium ion diffusion coefficient ($10^{-9}-10^{-13}$ cm^2 s^{-1}) of bulk LTO represent achievable objectives for further improvement of electrochemical performance.[4, 8, 9]

A significant amount of effort has been expended in terms of developing strategies to ameliorate the rate performance of LTO electrodes. The *first* approach has been to design unique nanostructure motifs of LTO in order to enhance their electronic and Li-ion conductivity, within the context of zero-dimensional (0D) nanoparticles,[10, 11] one-dimensional (1D) nanowires and

nanotubes,[12, 13] as well as three-dimensional (3D) structural architectures.[5, 14, 15] Recently, our group reported on being able to successfully generate novel hierarchical 'flower-like' LTO microspheres, consisting of thin saw-tooth shaped constituent nanosheets that had been synthesized by *(i)* a facile and large-scale hydrothermal process involving recyclable precursors followed by *(ii)* a short, relatively low-temperature calcination process in air. We noted that in our hierarchical assemblies, the thin nanosheets gave rise to shortened Li-ion diffusion distances and enhanced contact area with electrolyte, while the micron-scale spherical assemblies themselves possessed thermodynamic stability and high tap-density.[14, 16] The resulting electrodes exhibited both excellent rate capabilities and stable cycling performance, delivering, as an example, as much as 137 mAh g^{-1} with a capacity retention of ~87 % at a discharge rate of 20 C from cycles 101 to 300.[17]

The *second* generalized strategy has been to render LTO more conductive either through (a) the formation of a conductive coating onto an underlying LTO surface or (b) the doping of other ions within the underlying LTO lattices so as to enhance the electronic conductivity between the anode material and the current collector.[9, 18, 19] Carbon nanotubes (CNTs), which are unique and desirable as a result of their exceptional electrical conductivity and outstanding mechanical strength in part due to their anisotropic structure, may represent a particularly promising conductive additive for improving the rate capabilities of LTO composites.[7, 20, 21] Specifically, substantial research has successfully highlighted the plausibility of incorporating CNTs within the context of 0D, 1D, and 2D LTO-based anode materials, respectively, using either physical mixing or *in situ* deposition methods.[22-27]

Representative examples of these varied efforts are discussed. For example, Fang *et al.* prepared LTO/CNT-based composites by embedding submicron LTO particles within a network

of conductive multi-walled carbon nanotubes (MWNTs); the resulting composite exhibited excellent rate and cycling performance, i.e. a value of 163 mAh g^{-1} at 2 C after 1000 cycles.[28] In addition, Ni *et al.* reported on the use of CNTs to which LTO nanoparticles had been immobilized by means of liquid phase deposition as a composite anode material for high rate LIBs; these materials delivered 112 mAh g^{-1} at a 20 C discharge rate.[9] Moreover, Shen *et al.* were able to grow LTO sheathes with a measured thickness of ~25 nm on the exterior of a MWNT core, and noted that these structures exhibited significantly higher rate capabilities of 158.9, 147.8, 136.3, and 123.6 mAh g^{-1} at rates of 1, 5, 10 and 20 C, and an even better capacity retention potential, as compared with their uncoated analogues.[29] Finally, Zhang *et al.* recently fabricated LTO nanosheet/CNT composites, yielding 145 mAh g^{-1} and 118 mAh g^{-1} at discharge rates of 11C and 23 C, respectively.[27] However, to date, there have been few if any reports focused on the integration of CNTs with 3D hierarchical LTO motifs into a defined, discrete, and rationally designed architecture. Why hence is there an emphasis on this particular heterostructure motif?

The main reason is that a hybrid composite possesses a number of outstanding 'structural design' advantages that can assist in improving the measured anode performance. *First*, the thin constituent nanosheets within the flower-like LTO micron-scale spheres can provide for a reduced lithium ion diffusion distance.[30] *Second*, the numerous roughened surfaces of the thin petal-like nanosheets, associated with a high surface area, represent potentially favorable active sites for the interaction of the electrolyte with LTO, thereby ultimately providing for improved voltage profiles and charge/discharge dynamics. *Third*, the incorporation of the MWNT network not only efficiently provides for viable electrical pathways to the LTO flower-like structure from

the current collector but also increases the mechanical stability of the underlying electrode through the interweaving of the electrode components.[7]

As such, herein, we have constructed novel 3D hierarchical flower-like LTO-MWNT composites, for the first time, with the explicit aim of precisely tuning for and potentially optimizing the nature of the interaction of the LTO with the underlying MWNT framework. Furthermore, although prior work has been conducted in terms of generating MWNT-LTO nanocomposites to enhance electrode performance, to the best of our knowledge, there have been few if any efforts primarily focused on chemically controlling and improving upon the ion transport between the constituent LTO motifs and the adjoining CNTs in terms of systematically engineering the nature of the molecular junction between these two species through judiciously chosen attachment strategies.

Therefore, in separate experiments, our as-prepared 3D LTO microspheres have been subsequently embedded into the MWNT network through *(i)* physical sonication, *(ii)* direct *in situ* deposition, as well as *(iii)* simple and effective covalent attachment strategies, which had never, to the best of our knowledge, been previously reported with prior LTO-MWNT composite formation. In so doing, for the first time in these types of systems, we have sought to correlate the electrochemical performances of these individual distinctive LTO-MWNT composites with their specific attachment strategy, *i.e.* with the particular preparative treatment process used to generate each of these composite materials. Subsequent structural and electrochemical characterization has yielded valuable insights into the structural properties, the rate performance, as well as the relative impact of MWNTs loadings and the nature of the attachment modality upon the resulting ion transport of the composite material.

7.2. Results and Discussion

7.2.1 Morphology and structure of the materials

Typical XRD patterns of (i) MWNTs, (ii) pure 'flower-like' LTO micron-scale spheres, and (iii) LTO-MWNT composites, prepared using different synthetic strategies, respectively, are presented in Figure 7.1 (with the MWNT loading ratio in each composite as 5 wt%, as confirmed by the TGA profile, shown in Figure 7.2). The pure LTO can be indexed to the face-centered cubic (*fcc*) spinel structure of $Li_4Ti_5O_{12}$ (i.e. JCPDS card No. 49-0207). The broadened peaks in the XRD pattern suggest that as-synthesized LTO possesses a relatively small crystallite size, which has been calculated to be ~12.6 nm using the Debye-Scherrer equation.

Upon MWNT addition, it was observed that all of the diffraction peak positions of the LTO did not necessarily change, with the major diffraction peaks located at 2θ values of 18.4°, 35.7°, 43.3°, 47.4°, 57.3°, 62.8°, and 66.2°, which could be ascribed to the (111), (311), (400), (331), (333), (440), and (531) planes, respectively, of a face-centered cubic spinel structure, possessing a *Fd-3m* space group. A new and reasonably broadened peak centered at 26.2° could be assigned to the (002) lattice plane of the MWNTs, present in the XRD profile of the MWNTs alone, as highlighted in the top panel of Figure 7.1.[31]

When comparing these data with pure LTO, we found that the LTO-MWNT composite generated by the sonication method yielded little if any obvious change in the degree of overall crystallinity and that the LTO-MWNT sample, prepared by *in situ* methods, evinced sharper diffraction peaks, suggestive of the formation of a larger crystallite size, possibly due to the higher annealing temperature used. In effect, based on the Debye-Scherrer equation, the crystallite size derived from the composite prepared by the *in situ* method was calculated to be 30.0 nm as compared with a 12.6 nm value associated with both pure LTO as well as the composite generated by physical sonication. It has been reported that the presence of a larger

crystallite size may lead to a reduced rate performance of this composite material as compared with analogous composites possessing a smaller crystallite size. This assertion has been ascribed to the observation that a relatively small crystallite size often favors enhanced rate capabilities and long-term cyclability, because of a combination of not only low charge transfer impedance but also decreased Li^+ diffusion impedance.[32, 33]

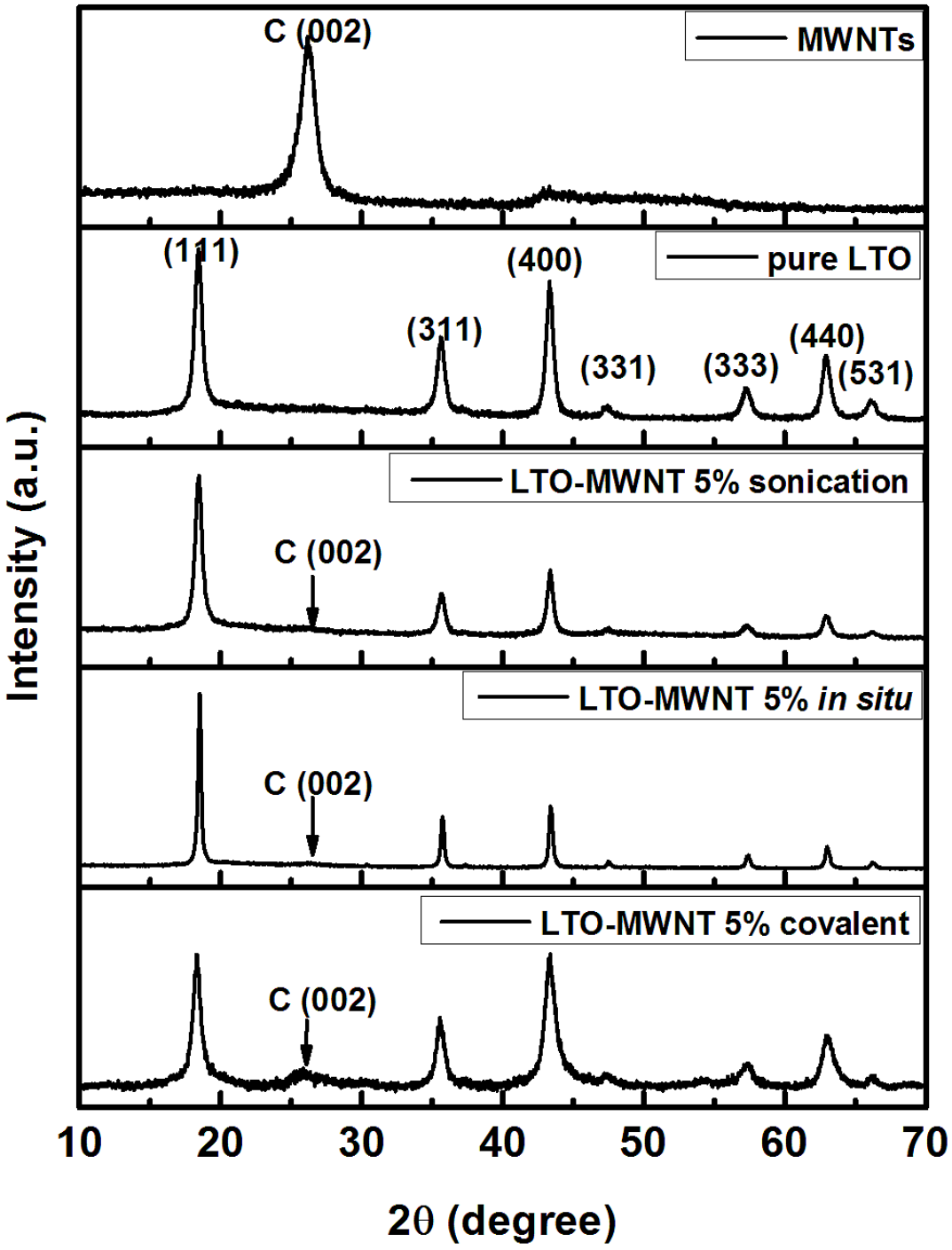

Figure 7.1. XRD patterns associated with (i) MWNTs, (ii) pure flower-shape LTO motifs, and (iii) the resulting LTO-MWNT composites, generated by sonication, direct *in situ*, and covalent attachment strategies, respectively.

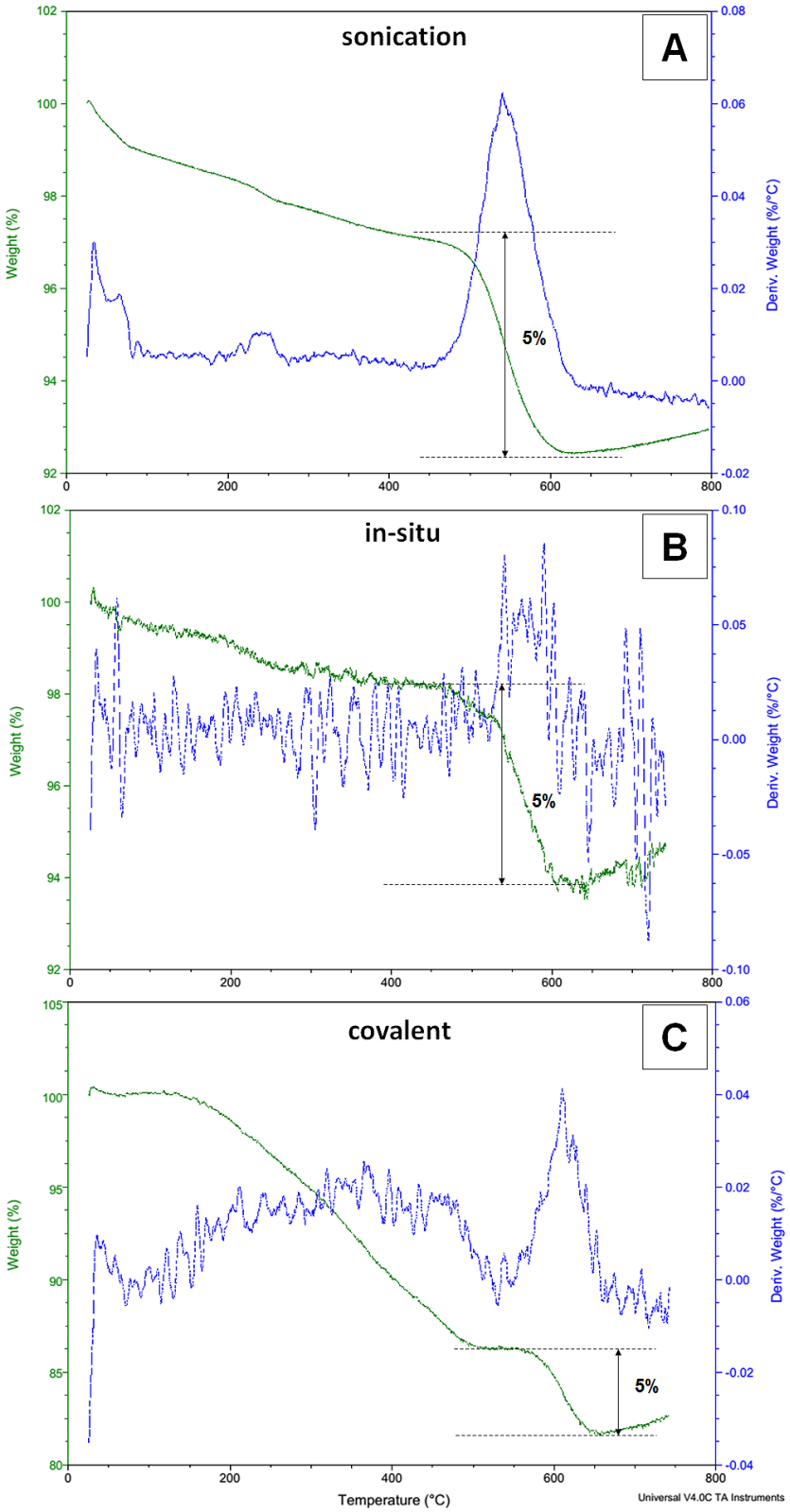

Figure 7.2. TGA curves of the LTO-MWNT (5 wt%) composite, generated by sonication (A), *in situ* deposition (B), and covalent attachment (C) strategies.

Additionally, the LTO-MWNT composite, prepared by means of covalent immobilization, gave rise to less well-defined XRD peaks and lower signal-to-noise ratios, thereby indicating the presence of material with a lower degree of crystallinity, a situation which could be possibly attributed to the existence of amorphous APTES linker molecules[34] on the LTO surface. The calculated crystallite size for this covalently formed composite was estimated to be 12.0 nm, similar to that of pure LTO alone, thereby indicating that the APTES functionalization process itself had not altered the apparent crystallinity of LTO itself.

Our pure LTO micron-scale spheres exhibited a hierarchical 'flower-shape' structure with an overall diameter of 1 μm, as indicated by the SEM image in Figure 7.3A. The thin constituent, petal-like component nanosheets measured 12.5 ± 2.6 nm in thickness from the TEM image, as shown in Figure 7.3B. The morphologies and micron-scale structures of the LTO-MWNT (5 wt%) composites were investigated by TEM and SEM, as presented in Figure 7.4. The MWNTs, indicated by arrows, measure 10-30 nm in diameter and are intermingled with the LTO spheres.

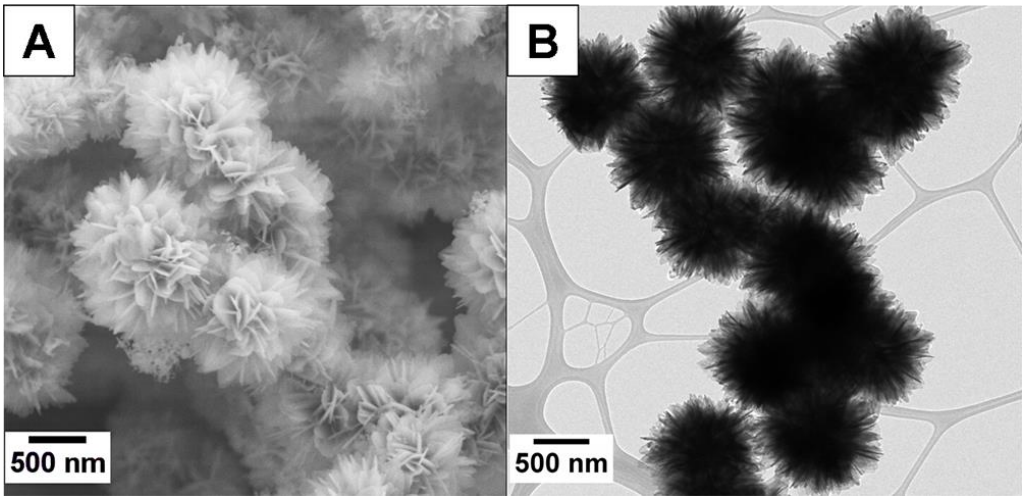

Figure 7.3. (A) SEM and (B) TEM images of pure LTO motifs, possessing hierarchical 'flower-shape' morphologies.

The composite generated through a physical sonication method (Figure 7.4A and D) evinced the presence of a relatively uniform coverage of evenly distributed MWNTs with no observable morphological change associated with the underlying LTO micron-scale spheres. As for the composite synthesized by the direct *in situ* deposition technique, the presence of the MWNTs might have potentially interfered with the growth of the LTO micron-scale spheres themselves during the process of the hydrothermal reaction, since we observed a certain degree of fragmentation, thereby resulting in the formation of 'broken up', particulate LTO structures, possessing an average diameter of 35.2 ± 5.3 nm, as well as individual, dissociated nanosheets,[1] as indicated by the white circles in Figures 7.4B and E. By contrast, we noted that the MWNTs appeared to be more uniformly dispersed and distributed throughout the network of LTO micron-scale spheres within the framework of composites generated through covalent attachment (Figures 7.4C and F). However, the occurrence of individual nanosheets themselves became less distinctive, possibly due to the presence of surface capping associated with APTES linker molecules, as indicated by the yellow circles in Figure 7.4F.

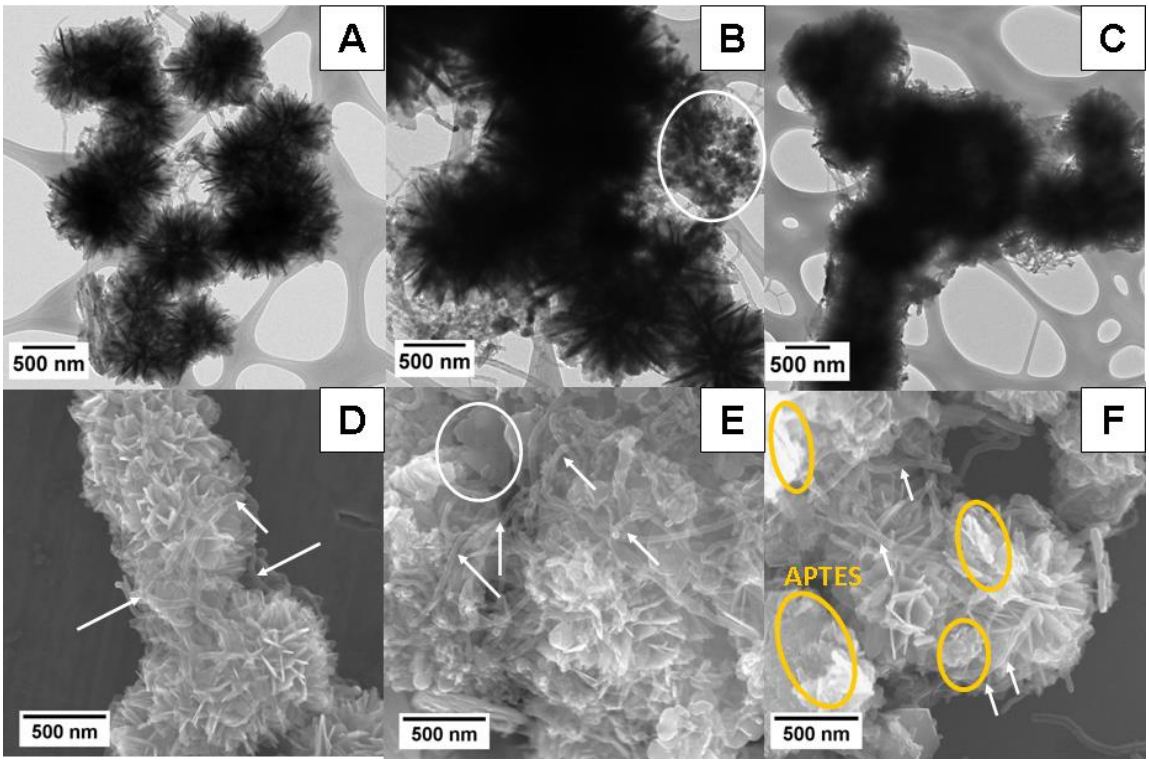

Figure 7.4. TEM (A-C) and SEM (D-F) images of LTO-MWNT (5 wt%) composites generated by sonication, direct *in situ*, and covalent attachment strategies, respectively. The MWNTs are indicated by the white arrows and the fragmented LTO structures are denoted by the white circles. The existence of APTES molecular linkers within the LTO-MWNT (5 wt%) sample generated by covalent attachment strategy is indicated by the yellow circles, shown in Figure F.

More detailed structural information was provided by HRTEM (Figure 7.5A-C) and selected area electron diffraction (SAED) (Figure 7.5D-F). In effect, within the HRTEM data, distinctive lattice fringes possessing distances of approximately 4.84 Å and 3.41 Å were observed, corresponding to the (111) planes of spinel LTO and the interlayer spacings of graphitic layers within the MWNTs themselves, respectively. The corresponding SAED patterns could be indexed to the (111), (311), and (400) lattice planes of spinel LTO as well as to the (002) lattice plane of MWNTs, respectively. These data provided further evidence for the presence of phase purity within our system. We found that the MWNTs are in close contact with the LTO nanosheets, thereby providing for the possibility of enhanced electron transport

pathways between adjacent LTO micron-scale spheres. It is also noteworthy that the covalently attached composite (Figure 7.5F) was less crystalline than the other two as-formed heterostructures (Figure 7.5D and E), an observation which again was consistent with the aforementioned XRD results.

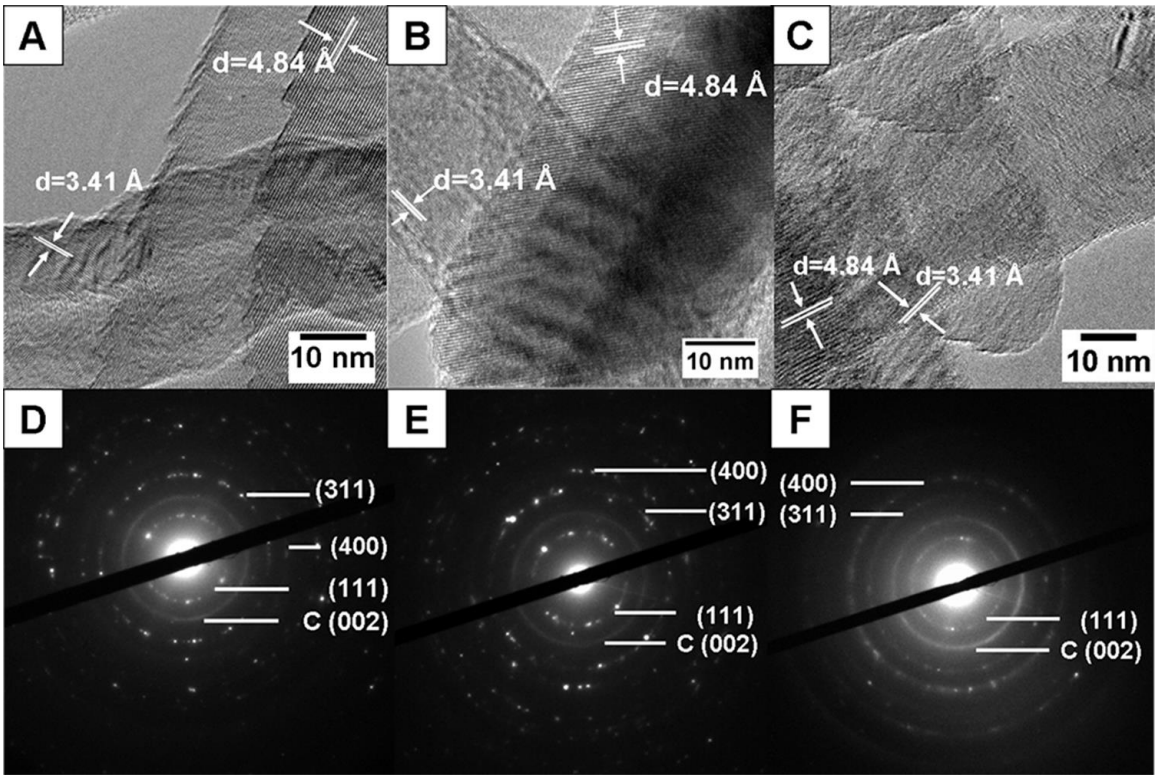

Figure 7.5. HRTEM images (A-C) and the corresponding insets to the SAED patterns (D-F) of LTO-MWNT (5 wt%) composites, generated by sonication, *in situ*, and covalent attachment strategies, respectively.

FT-IR spectroscopy was used to confirm the formation of amide bonds within the LTO-MWNT composite formed by means of covalent attachment. Specifically, spectra of oxidized MWNTs and of APTES-functionalized LTO, together with that of covalently-attached LTO - MWNT 5 wt% composites, are respectively shown in Figure 7.6. Upon treatment with nitric acid, the peaks located at 1694 cm^{-1} could be ascribed to the stretching bands of the C=O functionality derived from the carboxylic acid group,[35] while the broadened peak located

between 2400-3100 cm^{-1} corresponds to the –OH stretching modes associated with the carboxylic acid groups, thereby confirming the success of the acid functionalization protocol. In the APTES-LTO species, the characteristic peaks located at 1140 and 1030 cm^{-1} could be assigned to the Si-O-H and Si–O–Si groups connected with the APTES linker,[36] whereas the peaks localized at 3430 cm^{-1} and 1650 cm^{-1} were consistent with the N-H stretching and bending modes derived from the amine group, respectively. These data were indicative of the likely successful functionalization involving APTES. Peaks at 1650 cm^{-1}, 3406 cm^{-1}, and 1577 cm^{-1} associated within the LTO-MWNT composite likely corresponded to the C=O stretching bands in addition to the N-H stretching and bending modes from the amide group, respectively, all of which were suggestive of the probable formation of an amide bond between the MWNTs and the LTO micron-scale spheres.

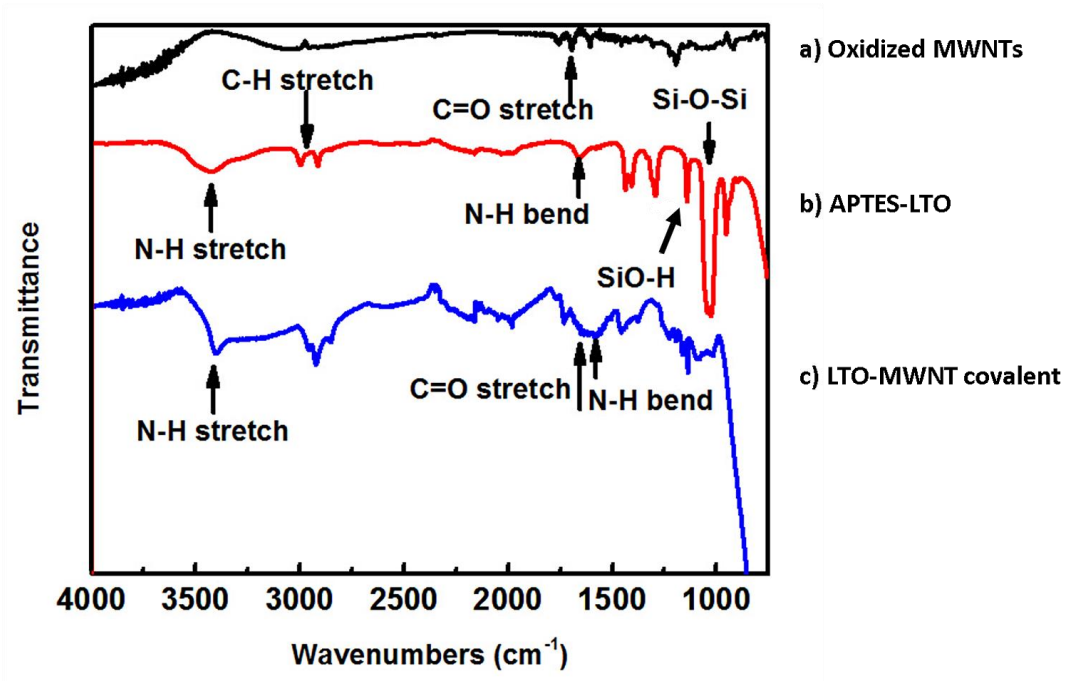

Figure 7.6. IR spectra of (a) oxidized MWNTs, (b) APTES-functionalized LTO motifs, as well as (c) LTO-MWNT (5 wt%) heterostructures, generated by a covalent attachment strategy.

In order to systematically investigate and correlate the optimal MWNT loading ratio with the electrochemical performance, composites of LTO-MWNT, possessing 1 wt% and 10 wt% of MWNTs as determined by the TGA profiles shown in Figure 7.7, were also generated by means of sonication.

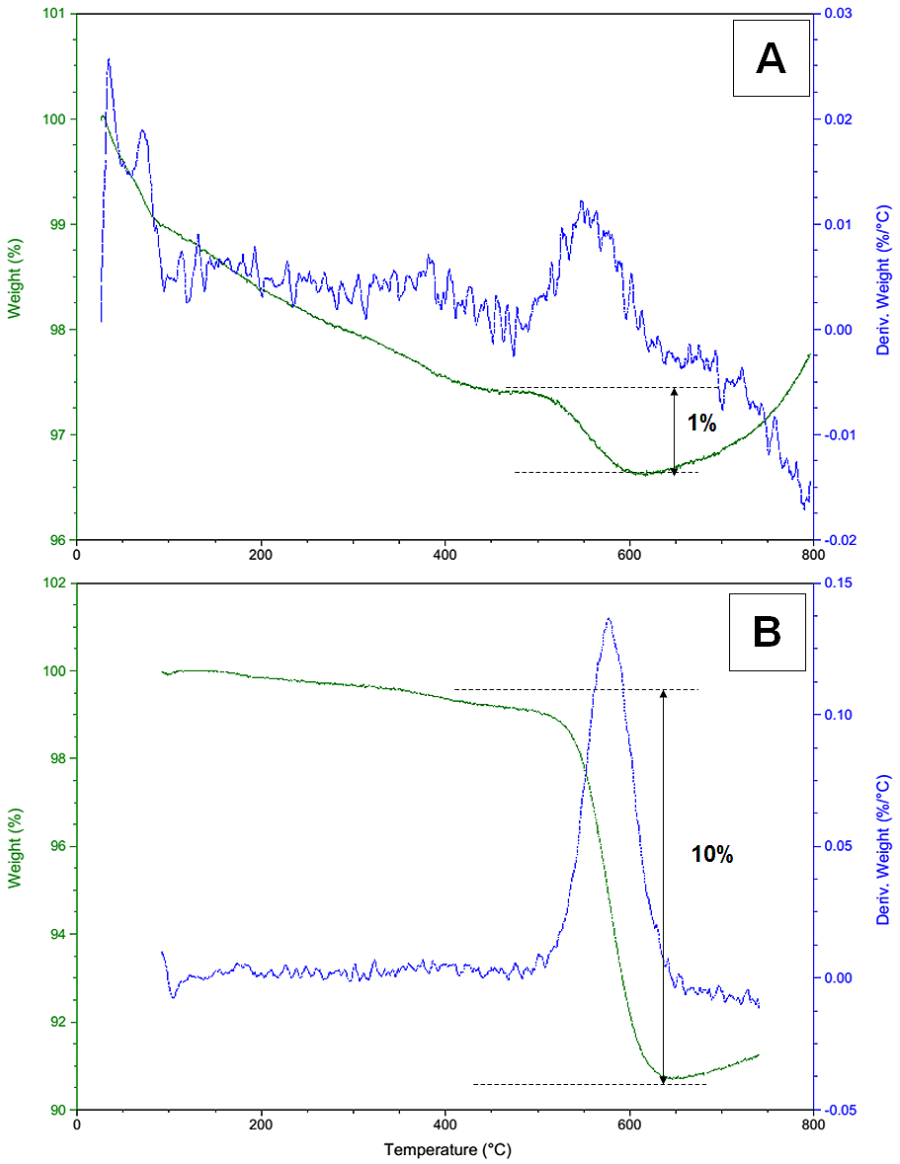

Figure 7.7. TGA profiles of the (A) LTO-MWNT (1 wt% loading) and the (B) LTO-MWNT (10 wt% loading) composite, respectively, generated by physical sonication.

The relevant structures and morphologies were characterized by TEM and SEM in Figure 7.8As compared with the aforementioned LTO-MWNT composites, possessing 5 wt% (Figure 7.4A and D) and 1 wt% of MWNTs (Figure 7.8A and C), we found that the coverage of the MWNTs was neither continuous nor evenly distributed; in effect, we noted domains rich with MWNTs adjacent to areas wherein there were very little if any MWNTs. When the weight addition ratios of MWNTs were increased to 10 wt% (Figure 7.8B and D), we determined that the MWNTs had essentially enveloped and completely covered the surfaces of the underlying LTO micron-scale spheres. This scenario favors an enhanced contact area and hence interaction between the 'flower-like' LTO structures and the surrounding conductive MWNT network.

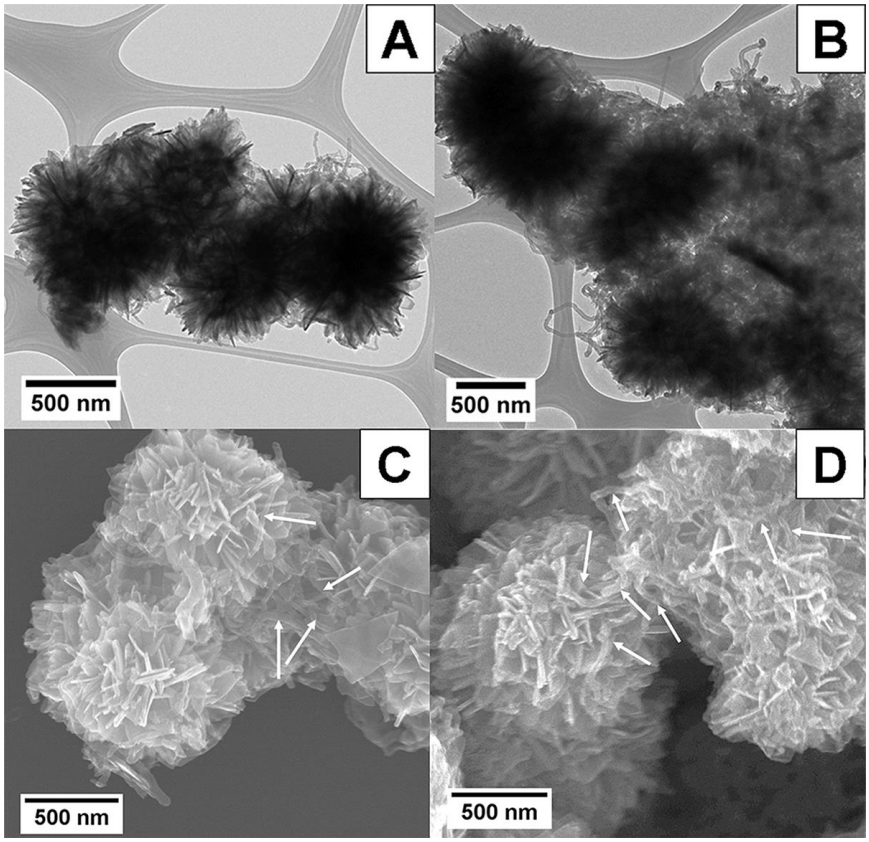

Figure 7.8. TEM (A and B) and SEM (C and D) images of a series of LTO-MWNT (1 wt%) and (10 wt %) composites, generated by the physical sonication method. The MWNTs are indicated by the presence of the white arrows.

7.2.2 Electrochemical properties of LTO-MWNT composite heterostructures

Figures associated with the following discussions will be presented in the thesis from Yiman Zhang (Takeuchi Group, Stony Brook University).

7.2.2.1. Cyclic voltammetry

Cyclic voltammetry of two electrode cells using the LTO-MWNT heterostructures was run at scan rates of 0.5, 1.0, 2.0, and 5.0 mV/s. The voltammograms of the 5% *in situ* sample revealed reversible electrochemistry at all scan rates wherein clear anodic and cathodic peaks were apparent. The ΔE_{peak} values were 0.36, 0.36, 0.48, and 0.60 V at the scan rates of 0.5, 1.0, 2.0, and 5.0 mV/s, respectively. Under the slower scan rates of 0.5 and 1.0 mV/sec, two features were present for the anodic wave. At the highest scan rate of 5.0 mV/s, the cathodic wave showed distortion, leading to a broadening of the appearance of the peak. The 5% physically sonicated LTO-MWNT sample demonstrated ΔE_{peak} values of 0.36, 0.44, 0.56, and 0.70 V at scan rates of 0.5, 1.0, 2.0, and 5.0 mV/s, respectively. The cathodic wave at the 5.0 mV/sec scan rate also gave rise to distortion, leading to a broadening of the appearance of the peak.

The CVs for the 5% covalent LTO-MWNT sample showed ΔE_{peak} values which were 0.32, 0.44, 0.62, and 0.93 V at scan rates of 0.5, 1.0, 2.0, and 5.0 mV/s, respectively. The ΔE_{peak} values for the covalently attached sample were comparable to the *in situ* and the sonicated samples measured at scan rates of 0.5 to 2.0 mV/s, yet these were higher at the scan rate of 5.0 mV/s. It is noteworthy that the CV peaks associated with the covalently attached composites are wider as compared with the other two preparative analogues, an observation which can be ascribed to the charge transfer resistance imparted by the presence of APTES linkers.

The anodic and cathodic peak current values were determined and plotted versus the square root of the scan rate in order to determine if the charge transfer kinetics were fast enough

to obey the Randles-Sevcik equation.[37] The sample prepared by the physical sonication method yielded correlation coefficients of 0.99 and 0.95 for the cathodic and anodic peak currents, respectively. The *in situ* sample resulted in correlation coefficients of 0.93 and 0.96 for the cathodic and anodic peak currents, while the covalent sample highlighted correlation coefficients of 0.062 and 0.95 for the cathodic and anodic peak currents, respectively. These results indicate that the fastest kinetics among the three attachment modalities were demonstrated by the sonication-prepared LTO-MWNT sample. Notably, the cathodic peak current for the covalently attached sample did not obey the Randles-Sevcik equation, thereby indicating slow kinetics.

The electrochemical cells were tested in galvanostatic mode for both discharge and charge processes. The LTO-MWNT composite samples were subjected to a total of 105 discharge-charge cycles, consisting of three rounds of 35 cycles at discharge rates of C/2 (20 cycles), 20 C (5 cycles), 50 C (5 cycles), and 100 C (5 cycles). This testing provided the opportunity to assess both rate capability and capacity retention. Different strategies of integration with and attachment of MWNTs onto LTO were investigated on samples possessing 5% MWNT loading amounts.

The capacity retention for the three as-generated LTO-MWNT composites was investigated. At cycles 20, 55, and 90, the capacities for the composite generated by the covalent method were measured to be 148, 145, and 143 mAh/g, respectively, under a rate of C/2. The capacities for the composite synthesized by the *in situ* protocol were found to be 150, 150, and 149 mAh/g, while the capacities for the composite derived from the physical sonication technique were computed to be 161, 160, and 159 mAh/g, respectively. Thus, the LTO-MWNT sample prepared using the chemical covalent method exhibited a slightly poorer capacity retention of ~97% from cycles 20 – 90 as compared with the samples prepared via either

physical sonication or *in situ* direct deposition methods, which yielded ~99% capacity retention from cycles 20 - 90.

At a rate of C/2, the LTO-MWNT 5 wt% fabricated by the sonication method out-performed all of the other analogues, delivering 161 mAh g^{-1}, which is close to the theoretical capacity of the LTO material. The differences among the measured capacities under the C/2 rate for the LTO-MWNT 5 wt% composites, synthesized by the *in situ* direct-deposition approach as well as by covalent attachment protocols were minimal.

The rate capability of the material samples was also assessed. Under C/2 conditions, both the *in situ* prepared LTO-MWNT sample and the sample prepared via physical sonication demonstrated an abrupt voltage drop upon initial discharge to ~20 mAh/g, followed by a broad voltage plateau at ~1.55 V. The sample prepared using covalent attachment gave rise to a more gradually sloping voltage profile with higher voltages from 2.2 - 1.6 V out to 60 mAh/g, and followed by a plateau at ~1.55 V for the remainder of the discharge process. Even though the realized capacities for the three electrode types were similar under low rate discharge conditions, dissimilarities in the shapes of the voltage profiles were even more apparent at higher rates.

Under high rates of discharge, more significant differences were observed, where the highest delivered capacity was achieved by the samples prepared via the sonication method. For example, under a 50 C discharge rate, the physical sonication-prepared samples delivered 90 mAh/g, while the *in situ*-derived samples produced 71 mAh/g and the covalently attached samples brought about 16 mAh/g. Under cycling, the samples prepared via the sonication method delivered 161, 145, 90, and 15 mAh/g, under discharge rates of C/2, 20 C, 50 C and 100 C, at cycles 20, 25, 30, and 35, respectively. By contrast, the 5% *in situ* LTO-MWNT material resulted in capacities of 150, 133, 71, and 8 mAh/g, while the sample prepared by the covalent

method gave rise to corresponding capacities of 148, 105, 16, and 0.15 mAh/g, respectively, through cycles 20, 25, 30, and 35. In all cases, the charge capacities reflected the discharge capacities measured under the same rate. These quantifiable differences are consistent with the prior observations from the CV experiments.

Electrochemical impedance spectroscopy was used to compare the inherent resistance of the Li/LTO-MWNT cells with 5% MWNT loading, prepared using different modes of attachment. The data were fit using an equivalent circuit, where R1 was attributed to ohmic resistance and R2 was ascribed to charge transfer resistance. The R1 values were consistent for all three cell types, with a range of 1.5 – 2.3 ohms. The R2 quantity, however, gave rise to more variation among the cells, with measured values of 52, 65, and 89 ohms noted for the cells prepared from LTO-MWNT samples associated with sonication, *in situ* deposition, and covalent attachment modalities, respectively. The higher charge transfer resistance ascribed to the covalent attachment modality was consistent with the poorer rate capability discussed above in the context of the voltammetry and galvanostatic testing results. Moreover, these results are consistent with a study, wherein covalent attachment of Fe_3O_4 onto a glassy carbon electrode surface using a 3-aminopropyltriethoxysilane (APTES) linker led to the observation of a higher charge transfer resistance as compared with a bare glassy carbon surface.[38] An increased charge transfer resistance associated with the covalent attachment process would also account for not only the lower delivered capacity but also, due to increased polarization effects, the poorer capacity retention observed.

Since the physical sonication method yielded the highest capacities at every C rate tested, the impact of the loading amount of MWNTs with sonication-prepared LTO-MWNT heterostructures was investigated further. Specifically, LTO-MWNT samples with 1%, 5%, and

10% MWNT loadings, respectively, were prepared and electrochemically evaluated. At cycles 20, 55, and 90, the capacities for the 1% loading samples were 167, 166, and 165 mAh/g, respectively. The corresponding capacities for the 5% loading amounts were 161, 160, and 159 mAh/g, while the associated capacities for 10% MWNT loading amount were 173, 171, and 170 mAh/g, respectively. All of the materials prepared by the physical sonication method exhibited similar capacity retention of ~99% from cycles 20 – 90.

The LTO material characterized by 10% MWNT loading showed the best rate capability at both 20 C and 50 C. The LTO samples with the 10% MWNT loading produced capacities of 148, 146, and 142 mAh/g under discharge rates of 20 C, at cycles 25, 60, and 95, respectively. At a discharge rate of 50 C, the values were determined to be 103, 95, and 81 mAh/g at cycles of 30, 65, and 100 respectively. The 5% MWNT loading materials yielded capacities of 141, 132, and 122 mAh/g under a discharge rate of 20 C at cycles of 25, 60, and 95, respectively. The corresponding data at a discharge rate of 50 C consisted of 85, 67, and 53 mAh/g at cycles of 30, 65, and 100 respectively. By comparison, the 1% MWNT loading materials gave rise to capacities of 149, 137, and 124 mAh/g, under a discharge rate of 20 C, at cycles of 25, 60, and 95, respectively. When the discharge rate was increased to 50 C for that specific heterostructure, the measured capacities were noted to be 79, 59, and 45 mAh/g at cycles of 30, 65, and 100, respectively.

The advantages for using 10% MWNT loading materials were more obvious at a higher discharge rate of 50 C. In effect, the observed capacities were not only 18 mAh/g higher than the 5% MWNT loading sample but also 24 mAh/g higher than the 1% MWNT loading sample at cycle 30. At 100 C, with respect to the samples which had been prepared by the physical sonication method, regardless of the loading amounts of MWNT tested, all samples delivered

approximately similar capacities of ~15, 13, and 10 mAh/g at cycles 35, 70, and 105, respectively. Indeed, the high reversible capacity and excellent cycling stability at C/2 and a high discharge rate of 20 C for as-prepared 'flower-like' LTO-MWNT 10 wt% composites are definitely superior to those of previously reported values associated with LTO-carbon nanotube composite materials. A detailed comparison of our results in the context of existing literature is presented in Table 7.1.

Table 7.1. Rate capability and cycling stability of the "flower-like" LTO-MWNT 10 wt% composite prepared in this work and those of analogous LTO-CNT composite materials, that had been reported in previous studies.

Material	**Method**	**Morphology**	**Rate Capability**	**Cycling Performance**	**Ref.**
"flower-like" LTO-MWNT 10 wt% (discharge range: 2.5-1.0 V)	Hydrother-mal+ sonication method	3D hierarchical "flower-like" LTO micron-scale spheres: ~1 μm	C/2: 173 mA h g^{-1}; 20 C: 148 mA h g^{-1}; 50 C: 103 mA h g^{-1} based on LTO mass	C/2: 99% from cycle 20 to cycle 90; 20 C: 96% from cycle 25 to cycle 95; 50 C: 79% from cycle 30 to cycle 100	This work
nanostruc-tured LTO/CNT 11 wt% (discharge range: 2.8-1.0 V)	aerosol spray drying + annealing	particles: ~400 nm	1 C: 163 mA h g^{-1}; 10 C: 143 mA h g^{-1}; 100C: 108 mA h g^{-1} based on LTO mass	100 C: 89% retention after 8000 cycles	[24]
LTO/CNT 15.2 wt% (discharge range: 2.0-1.0 V)	In situ growth of CNT by Ni–P-catalyzed thermal hydrolysis of acetylene on LTO	particles: ~500 nm	10 C: 103 mA h g^{-1}; 20 C: 73 mA h g^{-1}; 50 C: 48 mA h g^{-1} based on total mass	N/A	[26]
Cr doped-LTO / CNTs 10 wt%	ball-milling solid-state reaction	irregular particles	C/2: 140 mA h g^{-1}; 5 C: 128 mA h g^{-1}; 10 C: 120 mA h g^{-1}	10 C: 95.9% retention after 200 cycles	[39]

(discharge range: 2.5-1.0 V)					
nanosized LTO/ MWNT 5 wt% (discharge range: 2.5-1.0 V)	ball-milling solid-state reaction + anneal in Ar/H_2	particles: ~50-200 nm	1 C: 161 mA h g^{-1}; 5 C: 152 mA h g^{-1}; 10 C: 147 mA h g^{-1}	1 C: 99%, 10 C: 97% capacity retention after 100 cycles	[23]
nanoscale LTO/ MWNT 9.64 wt% (discharge range: 2.5-1.0 V)	liquid phase deposition + anneal in N_2	particles: ~50 nm	1 C: 171 mA h g^{-1}; 20 C: 112 mA h g^{-1} based on LTO mass	1 C: 0.5% and 5 C: 2%, capacity loss after 100 cycles	[9]
LTO/CNT 8.2 wt% (discharge range: 3.0-1.0 V)	sol-gel + annealing in N_2	particles: 100-180 nm	0.5 C: 163 mA h g^{-1}; 10 C: 147 mA h g^{-1}; 20 C: 115 mA h g-1 based on LTO mass	5 C: 97.9% retention after 500 cycles	[22]
LTO/CNT 17.5 wt% coaxial nanocable (discharge range: 2.5-1.0 V)	sol-gel + hydrother-mal+ anneal in N_2	LTO sheath thickness: 25 nm	C/50: 171 mA h g^{-1}; 10 C: 136 mA h g^{-1}; 20 C: 123 mA h g^{-1}; 40 C: 96 mA h g^{-1} based on LTO mass	1 C: 5.6% capacity loss after 100 cycles	[29]
nanoscale LTO/ MWNT 20 wt% (discharge range: 2.5-1.0 V)	solvother-mal + anneal in H_2/Ar	particles: 10-15 nm	1 C: 172 mA h g^{-1}; 20 C: 140 mA h g^{-1}; 50 C: 118 mA h g^{-1} based on LTO mass	1 C: 97% retention after 200 cycles; 10 C: 98% retention after 1000 cycles	[25]
LTO/AB/ MWNT 4.7 wt% (discharge range: 3.0-1.0 V)	ball-milling assisted solid-state reaction + anneal in Ar	particles: ~100-200 nm	1 C: 170.5 mA h g^{-1}; 20 C: 116 mA h g^{-1}; 30 C: 102 mA h g^{-1} based on LTO mass	2 C : 4% capacity loss after 1000 cycles	[28]

LTO/CNT/ CNF (LTO loading of 50%, 60%, and 70%) (discharge range: 2.5-1.0 V)	pressure-controlled aqueous extrusion process	particles: 100-200 nm	0.5 C: 157, 154, and 150 mA h g^{-1} for LTO-50, 60 and 70%, respectively; 10 C: 142, 129, and 115 mA h g^{-1} for LTO-50, 60 and 70%, respectively, based on LTO mass	10 C: 96.4% for LTO-50; 79.4% for LTO-60, and 68.8% LTO-70 after 500 cycles	[40]
LTO/CNT (CNT loading of 5%, 7.5% and 10%) (discharge range: 2.5-0.5 V)	In situ hydrother-mal + Ar anneal	nanosheets: 300 nm in diameter and 20 nm in thickness	157, 145, 132, 118, and 105 mA h g^{-1} at 1, 2, 3, 4, and 5 A g^{-1} (5.7, 11.4, 17.1, 22.9 and 28.6 C), respectively, for CNT-7.5% composite based on LTO mass	2 A g^{-1}(11.4 C): 6.9% capacity loss after 1000 cycles for CNT-7.5% composite	[27]

7.3. Conclusions

In the current Chapter, we have demonstrated the successful synthesis, for the first time, of "flower-like" LTO-MWNT composites systematically fabricated *via* different preparative approaches, including *(i)* physical sonication, *(ii)* an *in situ* direct deposition approach, as well as *(iii)* a covalent chemical attachment protocol. Data from our structural characterization analysis suggest that the composite generated by the physical sonication method retains not only the favorably small crystallite size (*i.e.* 12.6 nm) of the pure LTO but also the intrinsic "flower-like" morphology of the pure LTO both during and after the preparative process.

By contrast, the composite prepared through an *in situ* direct-deposition approach yielded not only fragmented LTO structures possibly due to curtailed crystal growth induced by the presence of interfering MWNTs but also larger overall crystallite sizes likely resulting from the higher annealing temperatures used, denoting factors which contributed to the lower electrochemical performance measured. Finally, the composite produced *via* covalent attachment

appeared to be enveloped with a coating of amorphous linker molecules, thereby leading to not only lower overall crystallinity but also a decreased contact area between LTO and MWNTs, giving rise to poorer performance.

Equally significant is that we have correlated the performance of these composite materials with their corresponding attachment chemistry. For example, in this study, the LTO sample with the 10% MWNT loading prepared via the physical sonication method evidenced the highest delivered discharge capacity at every C rate from C/2 to 100C with the most notable differences apparent under discharge rates ≥ 20 C. Notably, the LTO-MWNT samples prepared via the covalent attachment scheme delivered a lower capacity and displayed 97% capacity retention from cycle 20 to cycle 90 at C/2 rate as compared with the higher capacity and 99% capacity retention for both the physically sonicated and *in situ* samples. The voltammetric and galvanostatic data coupled with the impedance results indicate slower kinetics for the LTO-MWNT heterostructures, prepared using a novel covalent attachment method, denoting data consistent with a prior report on a totally different system of increased charge transfer resistance associated with a covalent coupling protocol involving the 3-aminopropyltriethoxysilane (APTES) linker.[38]

It is worth further mentioning that the LTO-MWNT 10 wt% composite, produced by sonication means, exhibited a reproducibly high rate capability and desirable cycling stability, delivering 173 mA h g^{-1} at C/2 with a 99% capacity retention from cycles 20-90 and 148 mA h g^{-1} at 20 C with a 96% capacity retention from cycles 25-95. These values denote, to the best of our knowledge, clearly superior performance to those of *any* previously reported LTO-carbon nanotube composite materials.

Hence, our work illustrates a clear example, wherein we have used deliberative processing protocols in order to tune and control fundamental material properties. Indeed, such a truly favorable cycling performance coupled with the high discharge capacity detected highlight distinctive advantages for our hierarchical architectures from a battery perspective. In addition, together with the rather simplistic attachment route used and the fairly economical production costs associated with fabricating our "flower-like" LTO-MWNT 10 wt% composites by the physical sonication method, these cumulative results suggest the practical viability of utilizing these novel hierarchical structures within the context of commercially relevant designs for energy storage.

7.4. References

1. Lin, C. F.; Fan, X. Y.; Xin, Y. L.; Cheng, F. Q.; Lai, M. O.; Zhou, H. H.; Lu, L. $Li_4Ti_5O_{12}$-based anode materials with low working potentials, high rate capabilities and high cyclability for high-power lithium-ion batteries: a synergistic effect of doping, incorporating a conductive phase and reducing the particle size. *J. Mater. Chem. A* **2014**, *2*, 9982-9993.
2. Guo, J.; Zuo, W.; Cai, Y.; Chen, S.; Zhang, S.; Liu, J. A novel $Li_4Ti_5O_{12}$-based high-performance lithium-ion electrode at elevated temperature. *J. Mater. Chem. A* **2015**, *3*, 4938-4944.
3. Sha, Y.; Zhao, B.; Ran, R.; Cai, R.; Shao, Z. Synthesis of well-crystallized $Li_4Ti_5O_{12}$ nanoplates for lithium-ion batteries with outstanding rate capability and cycling stability. *J. Mater. Chem. A* **2013**, *1*, 13233-13243.
4. Zhu, G. N.; Wang, Y. G.; Xia, Y. Y. Ti-based compounds as anode materials for Li-ion batteries. *Energy Environ. Sci.* **2012**, *5*, 6652-6667.
5. Tang, Y. F.; Yang, L.; Fang, S. H.; Qiu, Z. $Li_4Ti_5O_{12}$ hollow microspheres assembled by nanosheets as an anode material for high-rate lithium ion batteries. *Electrochim. Acta* **2009**, *54*, 6244-6249.
6. Qiao, J. L.; Liu, Y. Y.; Hong, F.; Zhang, J. J. A review of catalysts for the electroreduction of carbon dioxide to produce low-carbon fuels. *Chem. Soc. Rev.* **2014**, *43*, 631-675.
7. Choi, J.-H.; Ryu, W.-H.; Park, K.; Jo, J.-D.; Jo, S.-M.; Lim, D.-S.; Kim, I.-D. Multi-layer electrode with nano-$Li_4Ti_5O_{12}$ aggregates sandwiched between carbon nanotube and graphene networks for high power Li-ion batteries. *Sci. Rep.* **2014**, *4*, 7334.
8. Kim, S.; Fang, S. H.; Zhang, Z. X.; Chen, J. Z.; Yang, L.; Penner-Hahn, J. E.; Deb, A. The electrochemical and local structural analysis of the mesoporous $Li_4Ti_5O_{12}$ anode. *J. Power Sources* **2014**, *268*, 294-300.
9. Ni, H. F.; Fan, L. Z. Nano-$Li_4Ti_5O_{12}$ anchored on carbon nanotubes by liquid phase deposition as anode material for high rate lithium-ion batteries. *J. Power Sources* **2012**, *214*, 195-199.
10. Lim, J.; Choi, E.; Mathew, V.; Kim, D.; Ahn, D.; Gim, J.; Kang, S. H.; Kim, J. Enhanced High-Rate Performance of $Li_4Ti_5O_{12}$ Nanoparticles for Rechargeable Li-Ion Batteries. *J. Electrochem. Soc.* **2011**, *158*, A275-A280.
11. Sun, L.; Wang, J. P.; Jiang, K. L.; Fan, S. S. Mesoporous $Li_4Ti_5O_{12}$ nanoclusters as high performance negative electrodes for lithium ion batteries. *J. Power Sources* **2014**, *248*, 265-272.
12. Shen, L. F.; Uchaker, E.; Zhang, X. G.; Cao, G. Z. Hydrogenated $Li_4Ti_5O_{12}$ Nanowire Arrays for High Rate Lithium Ion Batteries. *Adv. Mater.* **2012**, *24*, 6502-6506.
13. Liu, J.; Song, K. P.; van Aken, P. A.; Maier, J.; Yu, Y. Self-Supported $Li_4Ti_5O_{12}$-C Nanotube Arrays as High-Rate and Long-Life Anode Materials for Flexible Li-Ion Batteries. *Nano Lett.* **2014**, *14*, 2597-2603.
14. Chen, J. Z.; Yang, L.; Fang, S. H.; Tang, Y. F. Synthesis of sawtooth-like $Li_4Ti_5O_{12}$ nanosheets as anode materials for Li-ion batteries. *Electrochim. Acta* **2010**, *55*, 6596-6600.
15. Kong, D.; Ren, W.; Luo, Y.; Yang, Y.; Cheng, C. Scalable synthesis of graphene-wrapped $Li_4Ti_5O_{12}$ dandelion-like microspheres for lithium-ion batteries with excellent rate capability and long-cycle life. *J. Mater. Chem. A* **2014**, *2*, 20221-20230.

16. Xia, H.; Luo, Z. T.; Xie, J. P. Nanostructured lithium titanate and lithium titanate/carbon nanocomposite as anode materials for advanced lithium-ion batteries. *Nanotechnol. Rev.* **2014**, *3*, 161-175.
17. Wang, L.; Zhang, Y. M.; Scofield, M. E.; Yue, S. Y.; McBean, C.; Marschilok, A. C.; Takeuchi, K. J.; Takeuchi, E. S.; Wong, S. S. Enhanced Performance of "Flower-like" $Li_4Ti_5O_{12}$ Motifs as Anode Materials for High-Rate Lithium-Ion Batteries. *ChemSusChem* **2015**, *8*, 3304-3313.
18. Shen, L.; Zhang, X.; Uchaker, E.; Yuan, C.; Cao, G. $Li_4Ti_5O_{12}$ Nanoparticles Embedded in a Mesoporous Carbon Matrix as a Superior Anode Material for High Rate Lithium Ion Batteries. *Adv. Energy Mater.* **2012**, *2*, 691-698.
19. Xu, G. B.; Li, W.; Yang, L. W.; Wei, X. L.; Ding, J. W.; Zhong, J. X.; Chu, P. K. Highly-crystalline ultrathin $Li_4Ti_5O_{12}$ nanosheets decorated with silver nanocrystals as a high-performance anode material for lithium ion batteries. *J. Power Sources* **2015**, *276*, 247-254.
20. Zhang, W. D.; Xu, B.; Jiang, L. C. Functional hybrid materials based on carbon nanotubes and metal oxides. *J. Mater. Chem.* **2010**, *20*, 6383-6391.
21. Marschilok, A.; Lee, C. Y.; Subramanian, A.; Takeuchi, K. J.; Takeuchi, E. S. Carbon nanotube substrate electrodes for lightweight, long-life rechargeable batteries. *Energy Environ. Sci.* **2011**, *4*, 2943-2951.
22. Huang, J. J.; Jiang, Z. Y. The preparation and characterization of $Li_4Ti_5O_{12}$/carbon nanotubes for lithium ion battery. *Electrochim. Acta* **2008**, *53*, 7756-7759.
23. Jhan, Y. R.; Duh, J. G. Synthesis of entanglement structure in nanosized $Li_4Ti_5O_{12}$/multi-walled carbon nanotubes composite anode material for Li-ion batteries by ball-milling-assisted solid-state reaction. *J. Power Sources* **2012**, *198*, 294-297.
24. Jia, X. L.; Kan, Y. F.; Zhu, X.; Ning, G. Q.; Lu, Y. F.; Wei, F. Building flexible $Li_4Ti_5O_{12}$/CNT lithium-ion battery anodes with superior rate performance and ultralong cycling stability. *Nano Energy* **2014**, *10*, 344-352.
25. Kim, H. K.; Roh, K. C.; Kang, K.; Kim, K. B. Synthesis of nano-$Li_4Ti_5O_{12}$ decorated on non-oxidized carbon nanotubes with enhanced rate capability for lithium-ion batteries. *RSC Adv.* **2013**, *3*, 14267-14272.
26. Shu, J.; Hou, L.; Ma, R.; Shui, M.; Shao, L. Y.; Wang, D. J.; Ren, Y. L.; Zheng, W. D. In situ fabrication of $Li_4Ti_5O_{12}$@CNT composites and their superior lithium storage properties. *RSC Adv.* **2012**, *2*, 10306-10309.
27. Zhang, P.; Chen, M.; Shen, X.; Wu, Q.; Zhang, X.; Huan, L.; Diao, G. Preparation of $Li_4Ti_5O_{12}$ nanosheets/carbon nanotubes composites and application of anode materials for lithium-ion batteries. *Electrochim. Acta* **2016**, *204*, 92-99.
28. Fang, W.; Zuo, P. J.; Ma, Y. L.; Cheng, X. Q.; Liao, L. X.; Yin, G. P. Facile preparation of $Li_4Ti_5O_{12}$/AB/MWCNTs composite with high-rate performance for lithium ion battery. *Electrochim. Acta* **2013**, *94*, 294-299.
29. Shen, L. F.; Yuan, C. Z.; Luo, H. J.; Zhang, X. G.; Xu, K.; Zhang, F. In situ growth of $Li_4Ti_5O_{12}$ on multi-walled carbon nanotubes: novel coaxial nanocables for high rate lithium ion batteries. *J. Mater. Chem.* **2011**, *21*, 761-767.
30. Li, N.; Mei, T.; Zhu, Y.; Wang, L.; Liang, J.; Zhang, X.; Qian, Y.; Tang, K. Hydrothermal synthesis of layered $Li_{1.81}H_{0.19}Ti_2O_5$-xH_2O nanosheets and their transformation to single-crystalline $Li_4Ti_5O_{12}$ nanosheets as the anode materials for Li-ion batteries. *CrystEngComm* **2012**, *14*, 6435-6440.

31. Kim, H.-K.; Roh, K. C.; Kang, K.; Kim, K.-B. Synthesis of nano-$Li_4Ti_5O_{12}$ decorated on non-oxidized carbon nanotubes with enhanced rate capability for lithium-ion batteries. *RSC Adv.* **2013**, *3*, 14267-14272.
32. Hasegawa, G.; Kanamori, K.; Kiyomura, T.; Kurata, H.; Nakanishi, K.; Abe, T. Hierarchically Porous $Li_4Ti_5O_{12}$ Anode Materials for Li- and Na-Ion Batteries: Effects of Nanoarchitectural Design and Temperature Dependence of the Rate Capability. *Adv. Energy Mater.* **2015**, *5*, 1400730.
33. Shen, Y. B.; Eltzholtz, J. R.; Iversen, B. B. Controlling Size, Crystallinity, and Electrochemical Performance of $Li_4Ti_5O_{12}$ Nanocrystals. *Chem. Mater.* **2013**, *25*, 5023-5030.
34. Cheng, H.-Y.; Lai, L.-J.; Ko, F.-H. Rapid and sensitive detection of rare cancer cells by the coupling of immunomagnetic nanoparticle separation with ELISA analysis. *Int. J. Nanomedicine* **2012**, *7*, 2967-2973.
35. Wang, L.; Han, J.; Hoy, J.; Hu, F.; Liu, H.; Gentleman, M. M.; Sfeir, M. Y.; Misewich, J. A.; Wong, S. S. Probing differential optical and coverage behavior in nanotube-nanocrystal heterostructures synthesized by covalent versus non-covalent approaches. *Dalton Trans.* **2014**, *43*, 7480-7490.
36. Villalonga, R.; Villalonga, M. L.; Diez, P.; Pingarron, J. M. Decorating carbon nanotubes with polyethylene glycol-coated magnetic nanoparticles for implementing highly sensitive enzyme biosensors. *J. Mater. Chem.* **2011**, *21*, 12858-12864.
37. Bard, A. J.; Faulkner, L. R. *Electrochemical Methods: Fundamentals and Applications*. Second Edition ed.; Wiley: New York, 2000.
38. Yin, H. S.; Zhou, Y. L.; Liu, T.; Tang, T. T.; Ai, S. Y.; Zhu, L. S. Determination aminopyrine in pharmaceutical formulations based on APTS-Fe_3O_4 nanoparticles modified glassy carbon electrode. *J. Solid State Electrochem.* **2012**, *16*, 731-738.
39. Lin, C. F.; Fan, X. Y.; Xin, Y. L.; Cheng, F. Q.; Lai, M. O.; Zhou, H. H.; Lu, L. $Li_4Ti_5O_{12}$-based anode materials with low working potentials, high rate capabilities and high cyclability for high-power lithium-ion batteries: a synergistic effect of doping, incorporating a conductive phase and reducing the particle size. *J. Mater. Chem. A* **2014**, *2*, 9982-9993.
40. Cao, S. M.; Feng, X.; Song, Y. Y.; Xue, X.; Liu, H. J.; Miao, M.; Fang, J. H.; Shi, L. Y. Integrated Fast Assembly of Free-Standing Lithium Titanate/Carbon Nanotube/Cellulose Nanofiber Hybrid Network Film as Flexible Paper-Electrode for Lithium-Ion Batteries. *ACS Appl. Mater. Interfaces* **2015**, *7*, 10695-10701.

Chapter 8. Conclusions and Future Directions

Carbon nanotube (CNT)-based hetero-nanostructures represent exciting and distinctive structural paradigms in the development of high-performance energy conversion and storage devices, particularly owing to their intriguing electronic, optical, magnetic and catalytic properties. Extensive research efforts have unambiguously shown that nanotechnology can potentially bring about revolutionary improvements in a wide variety of areas including catalysis, photovoltaics, and batteries. Despite the growing interest in synthesizing, chemically modifying, and utilizing rationally designed CNT-based heterostructures in practical energy conversion applications, there has been a surprising lack of effort placed on carefully scrutinizing and correlating the influence of various physicochemical properties of each individual component within the heterostructure (*e.g.* chemical composition, particle dimension, and attachment modality, all of which can be controlled experimentally) with their resulting optoelectronic and electrochemical performance.

Hence, in this thesis, we have sought to acquire fundamental insights into the unique structural properties of these CNT-based heterostructures, which may shed light upon the rational design and engineering of clean-energy driven devices with enhanced efficiency and durability with the objective of potentially revolutionalizing the field. Towards this goal, we have highlighted herein several tangible advances in synthesis, nanomaterial purification, as well as the characterization of structures and their properties, both experimentally and theoretically.

8.1. CNT-CdSe QD Heterostructures for photovoltaic applications

In the context of photovoltaics (Chapters 3-5), DWNT-CdSe QD heterostructures have been judiciously chosen as the model system with the focus of probing interfacial charge transfer behavior between the adjoining two components. Specifically, in Chapter 3, we have analyzed

the effects of using differential synthetic coupling approaches, *i.e.* covalent attachment and non-covalent π–π stacking with respect to the resulting CdSe quantum dot (QD) coverage on the underlying DWNT template. That notably differential impact upon coverage, for example, yielded correspondingly substantial and measurable discrepancies in the degree of charge transfer between the CdSe QDs and the underlying DWNT linked together by 4-aminothiophenol (4-ATP). Specifically, electron microscopy as well as PL and Raman spectroscopy data collectively suggested that heterostructures generated by noncovalent π–π stacking interactions evinced not only higher QD coverage density but also possibly more efficient charge transfer behavior as compared with their counterparts produced using covalent linker-mediated protocols (Figure 8.1).

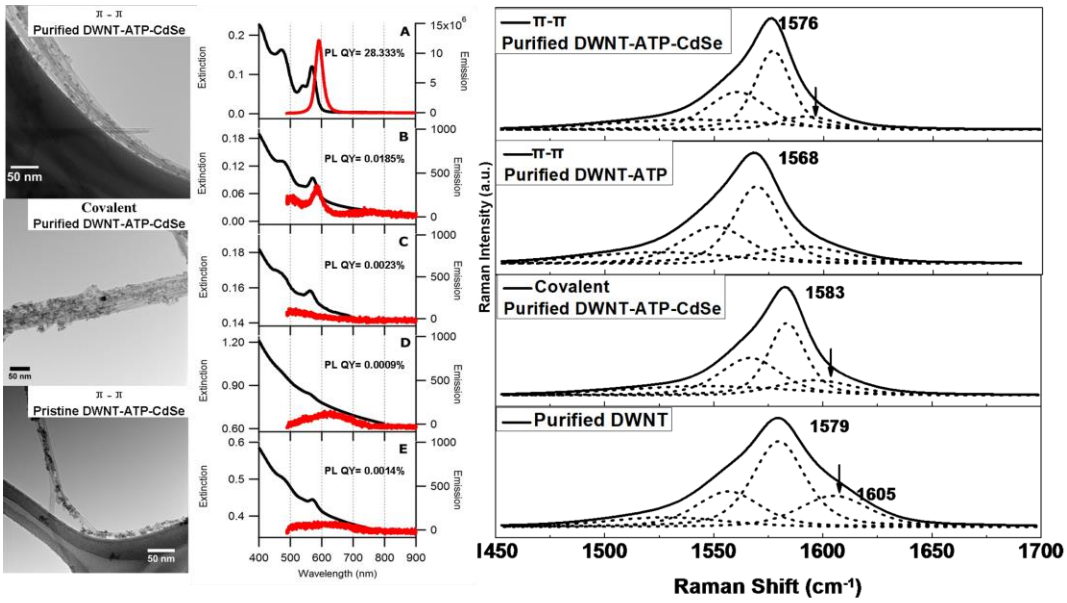

Figure 8.1. TEM, UV-Vis, PL and Raman data of DWNT-ATP-CdSe QD heterostructures prepared by covalent and non-covalent attachment strategies. (Reprinted TOC figure with permission from *Dalton Trans.*, **2014**, *43*, 7480 – 7490. Copyright 2014 Royal Society of Chemistry.)

As a culmination of our efforts, we have demonstrated a unique combination and compilation of experimental and theoretical studies that were collectively used to probe charge

transfer behavior in the DWNT-CdSe QD nanoscale heterostructures (Figure 8.2). Specifically, we correlated evidence of charge transfer as manifested by (i) changes in the NEXAFS intensities of π*resonance in the C *K*-edge and Cd M_3-edge spectra bolstered by complementary theoretical modeling results, (ii) a perceptible outer tube G-band downshift in frequency in Raman spectra, as well as (iii) alterations in the threshold characteristics present in transport data as a function of QD size (Chapter 4) and linker chemistry (Chapter 5).

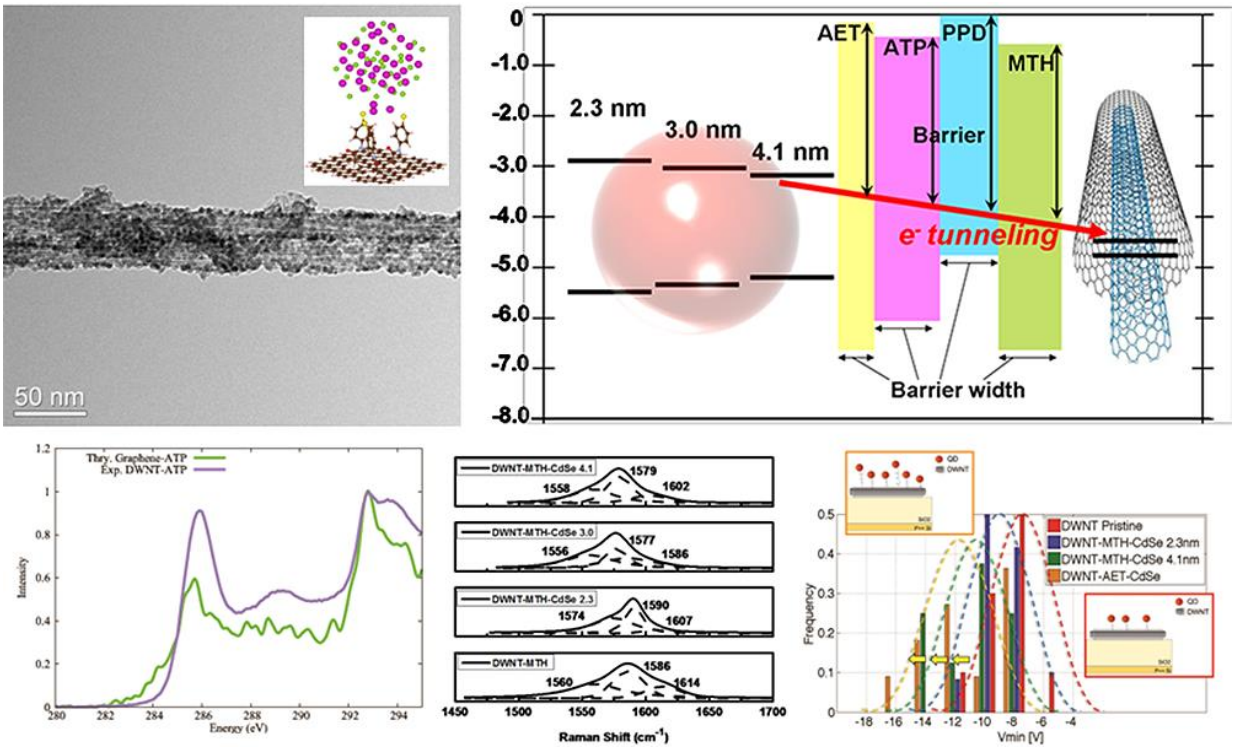

Figure 8.2. Compilation of experimental and theoretical characterization data on various DWNT-CdSe QD heterostructures.

In Chapter 4, our efforts are directed towards comparing charge transfer behavior, i.e. specifically electron transfer trends, at the interfaces of a number of different DWNT-CdSe heterostructures possessing various QD average diameters (i.e. 2.3 nm, 3.0 nm, and 4.1 nm), created through the mediation of 4-mercaptophenol (MTH) through a facile, noncovalent π–π stacking attachment strategy. Our results confirm that the interfacial electron transfer falls within

the “normal” Marcus theory region, wherein the heterostructure possessing the smallest QD size (i.e., 2.3 nm) gives rise to the largest driving force for charge transfer. The heterostructure possessing larger 4.1 nm diameter QDs yielded anomalously greater charge-transfer behavior with respect to that containing 3.0 nm diameter QDs, an observation which can be ascribed to differential coverage densities onto the underlying DWNT templates.

In Chapter 5, a combination of complementary data from experiment and theory has been used to investigate DWNT-CdSe QD heterostructures, within which the QD average diameter was measured to be ~4.1 nm and the ligands used to mediate the covalent attachment between the QDs and DWNTs were systematically varied to include p-phenylenediamine (PPD), 2-aminoethanethiol (AET), and 4-aminothiophenol (ATP). Our overall data suggest that (i) the QD coverage density on the DWNTs varies, based upon the different ligand pendant groups used, and that (ii) the presence of a π-conjugated carbon framework within the ligands themselves coupled with the electron affinity of their pendant groups collectively play important roles in the resulting charge transfer from QDs to the underlying CNTs.

Nonetheless, in order to test the photovoltaic power conversion efficiency of our heterostructure systems, future work will be necessarily focused upon building up a bulk heterojunction (BHJ) cell device. BHJs are similar to bilayer devices with respect to the donor-acceptor architecture concept. Instead of using a design incorporating two sub-layers which often requires a very thin film layer in order to ensure that the charges can diffuse, the BHJ cell utilizes a blend of electron donor and acceptor materials.

In this configuration, the active material is cast as a mixture, thereby resulting in a largely increased interfacial area wherein charge separation can be expected to occur. Regions of each material within the device are separated by only several nanometers, a distance suited for carrier

diffusion. In this case, a thicker active layer can be obtained, which can contribute to an enhanced sunlight absorption capability. The efficiency of exciton separation within a BHJ geometry is significant, because all excitons can be theoretically dissociated. Moreover, while charges are separated within the different phases, the recombination process is reduced to a large extent, and the resulting photocurrent trend often follows the light intensity either linearly[1, 2] or slightly sub-linearly.[3-5] For future studies, we propose to apply our DWNT-QD heterostructures within a photovoltaic regime and to vary the (a) cell architecture; (b) film thickness and homogeneity; (c) ratios of active materials as well as (d) the buffer layer in order to achieve the optimal cell performance.

(a) Cell architecture

Both the normal (Figure 8.3a) and inverted (Figure 8.3b) architectures of photovoltaics will be studied, wherein electrons and holes exit the device in opposite directions.[6] In the 'normal' photovoltaic configuration, the indium tin oxide (ITO) side will serve as the positive electrode, and hence, poly(3,4-ethylenedioxythiophene) (PEDOT) and poly(3-hexylthiophene) (P3HT) layers will be deposited on top to extract holes. In the 'inverted' design, the TiO_2 electron extraction layer will be deposited onto the ITO glass substrate and the MoO_3 layer will be subsequently immobilized on top of the active layers in order to extract holes.

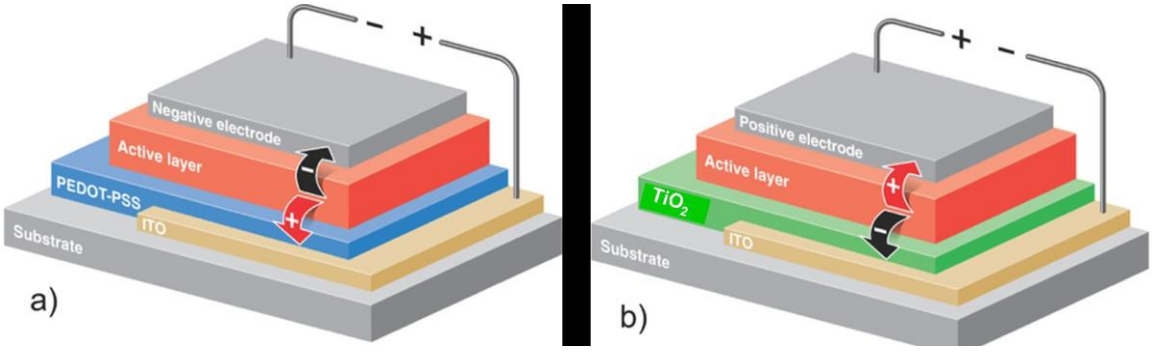

Figure 8.3. Schematic of (a) normal and (b) inverted solar cell devices (Reprinted from Ref. 6).

(b) Film thickness and homogeneity.

The thickness of each layer within the photovoltaic device is very important in terms of charge diffusion and transport. Indeed, the thickness of each layer, which will be measured by cross-section SEM, can be precisely controlled by varying the spin coating parameters and the physical vapor deposition (PVD) deposition time. Film homogeneity is another key contributing factor that determines the overall device performance. The film homogeneity is significantly affected by the dispersibility of the functionalized DWNTs in the selected solvent. Preliminary results on the DWNT-P3HT-based device (Figure 8.4A) generated by our group has suggested that the films deposited by using DWNT-P3HT in dichlorobenzene (DCB) (Figure 8.4C) are much more uniform than those fabricated by using dimethyl sulfoxide (DMSO) (Figure 8.4B). Since the film homogeneity is significantly affected by the solvent, by judiciously choosing solvent, a well-dispersed solution of the active materials can be obtained. Moreover, different spin coating parameters will be tested in order to obtain a film with a high homogeneity when transferring the active material from solution onto a solid substrate.

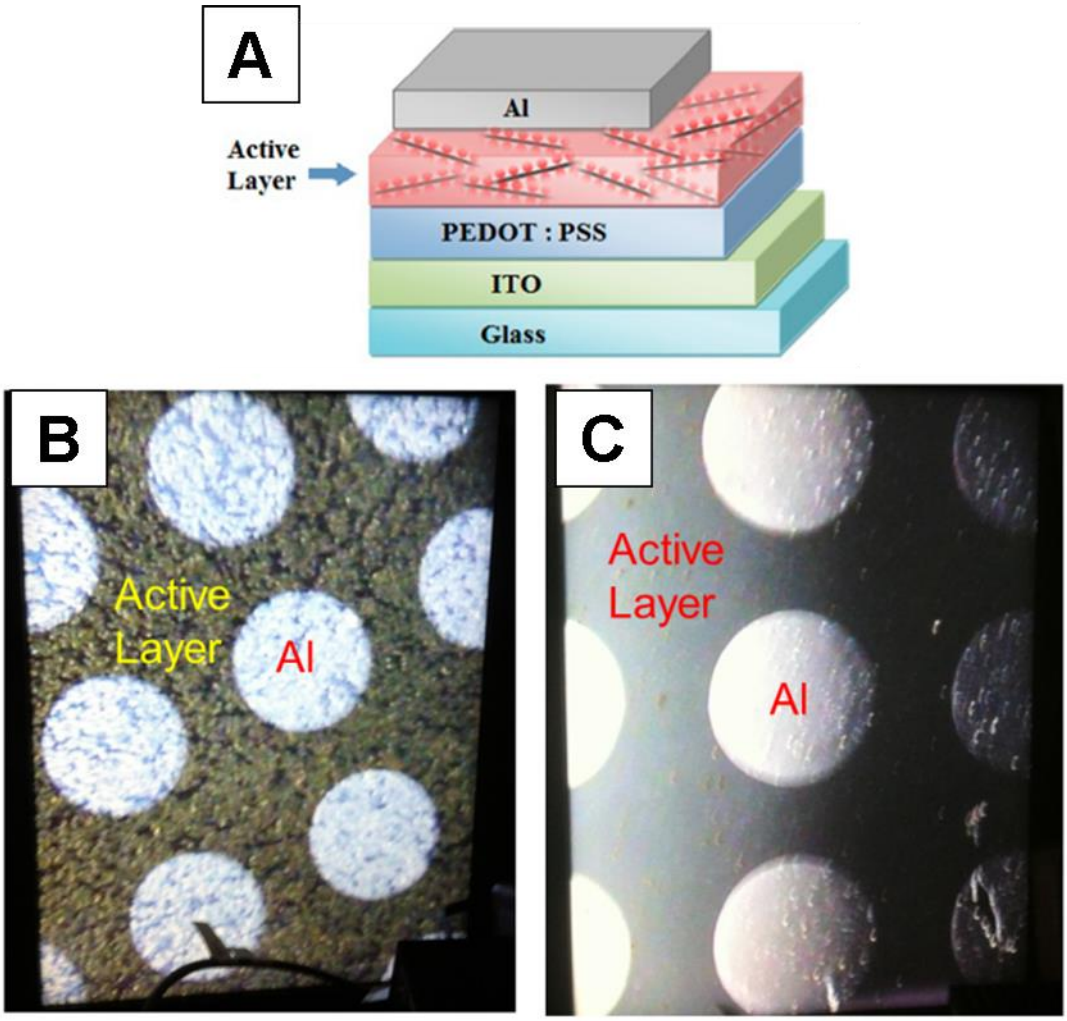

Figure 8.4. Schematic of a photoconducting DWNT-P3HT device (A) as well as the photograph of the device (top view), generated by using DMSO (B) and DCB (C), respectively, as dispersing solvents.

(c) Ratios between DWNTs and QDs

A careful tuning of the DWNT concentration is required within our DWNT-QD system, wherein a delicate balance must be achieved between maximizing contact with QDs while minimizing incident light absorption by the DWNTs.

(d) Buffer layer

I-V characteristics and corresponding efficiency of PV cell are significantly dependent upon active materials, layer thickness, and the thin film quality of the buffer layer between ITO

and the active layer. For example, the external quantum efficiency of PV is greatly improved when poly-ethylenedioxythiophene doped with poly-styrenesulfonate (PEDOT: PSS) is used as a buffer layer.[7] Figure 8.5 denotes an energy diagram of how such a device might function. PbS possesses a narrow intrinsic band gap (i.e. 0.41 eV for bulk PbS) and a large excitonic Bohr radius. It serves as a light harvesting system for absorbing radiation over a wide wavelength range of the entire solar spectrum. MWNT and P3HT have been used as acceptors of photoexcited electrons and holes to the cathode and anode, respectively. PEDOT: PSS was used as the buffer layer, due to the possibility of allowing for well-aligned energy levels, as shown in Figure 8.5. Overall, this device exhibits a largely enhanced conversion efficiency of 3.03% as compared with 2.57% for the standard bulk hetero-junction photovoltaic (PV) cell, constructed from P3HT and [6,6]-Phenyl-C_{60}-Butyric Acid Methyl Ester (PCBM) mixtures.[8]

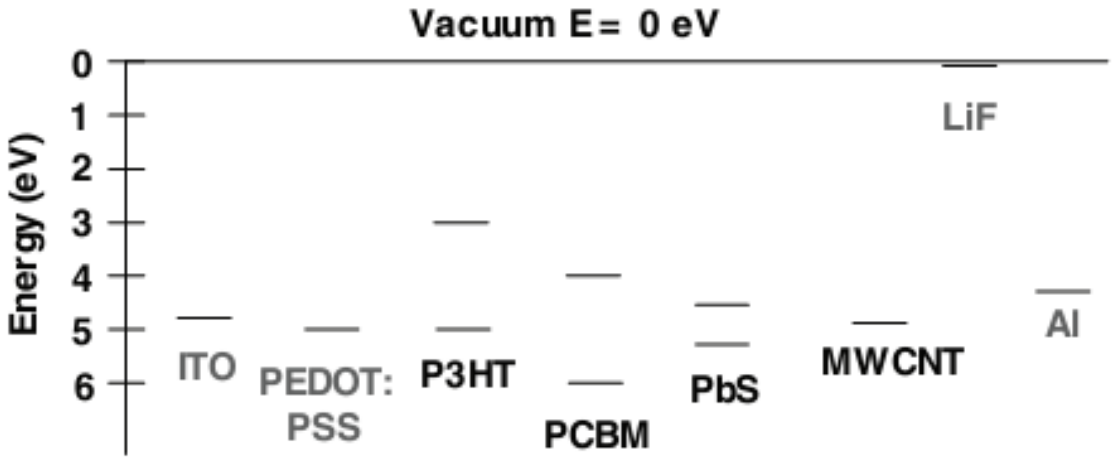

Figure 8.5. Energy-level diagram of various materials used for fabricating P3HT: PbS-QD / MWNT nanohybrid PV devices. (Adapted in part from Ref. 8.)

Although the incorporation of PEDOT:PSS as the buffer layer is often beneficial for facilitating the hole transport within the photovoltaic regime, the interface between ITO and PEDOT: PSS is not stable and a chemical reaction between ITO and PEDOT can result in a

degraded device performance.[9] Several metal oxides have been demonstrated as efficient hole injection materials for organic electroluminescent devices.[10] Molybdenum oxide (MoO_3) has been tested and proven to be able to successfully substitute for PEDOT: PSS as a buffer layer within the PV cell. Furthermore, the thickness of the buffer layer needs to be optimized and will be investigated in the future work.

It is worth noting that although extensive research efforts have been expended on the design and engineering of the CNT-QD based photovoltaic devices, there has been no report with respect to correlating either the ligand chemistry or attachment strategies between the CNT and QD components of the composite heterostructure with the resulting device performance. We believe that our studies on charge transfer behaviors within these various DWNT-CdSe QD systems joined together by different ligands and attachment modalities can shed light upon optimizing the device design as well as improving upon the resulting device efficiencies.

8.2. CNT-$Li_4Ti_5O_{12}$ Heterostructures for Li-ion battery applications

In Chapter 6, we demonstrated a novel flower-like nanostructured $Li_4Ti_5O_{12}$ (LTO) motif synthesized by a facile, low-cost, and large-scale hydrothermal process involving unique, re-useable, and recyclable precursors followed by a short, relatively low-temperature calcination in air (Figure 8.6). A brief and viable scheme has been proposed to clearly illustrate the structural evolution of the material. The resulting electrodes based on the as-synthesized material exhibited excellent high-rate capability and stable cycling performance.

In terms of synthetic attributes and advantages: (i) Ti foil was used instead of an organic titanium precursor to synthesize a three-dimensional hierarchical $Li_4Ti_5O_{12}$ material. Subsequent experiments showed that the Ti foil itself can be repeatedly re-used without either a noticeable alteration in sample morphology and quality or a drop-off in the yield of the resulting product.

(ii) No other solvents except for water were needed for the hydrothermal reaction. (iii) The hydrothermal reaction was carried out at 130°C for 4 h, which effectively shortened the reaction time and lowered the reaction temperature as compared with previous reported experiments. (iv) A subsequent calcination process was performed at a relatively low temperature of 500°C for only 3 h.

With respect to electrochemical performance, the LTO material (i) delivered a capacity of 141, 137, 123, and 60 mAh g^{-1} under high discharge rates of 10 C, 20 C, 50 C, and 100 C at cycles of 55, 60, 65, and 70, respectively; (ii) maintained a capacity retention of ~97% from cycle 10 – 100, ~99% from cycle 20 – 100 at discharge rate of 0.2 C, and an impressive capacity retention of ~87% using a more rigorous discharge rate of 20 C from cycles 101-300; and (iii) at highest discharge rate of 100 C, the flower-like material provided for ~3X the discharge capacity of the spherical commercial material.

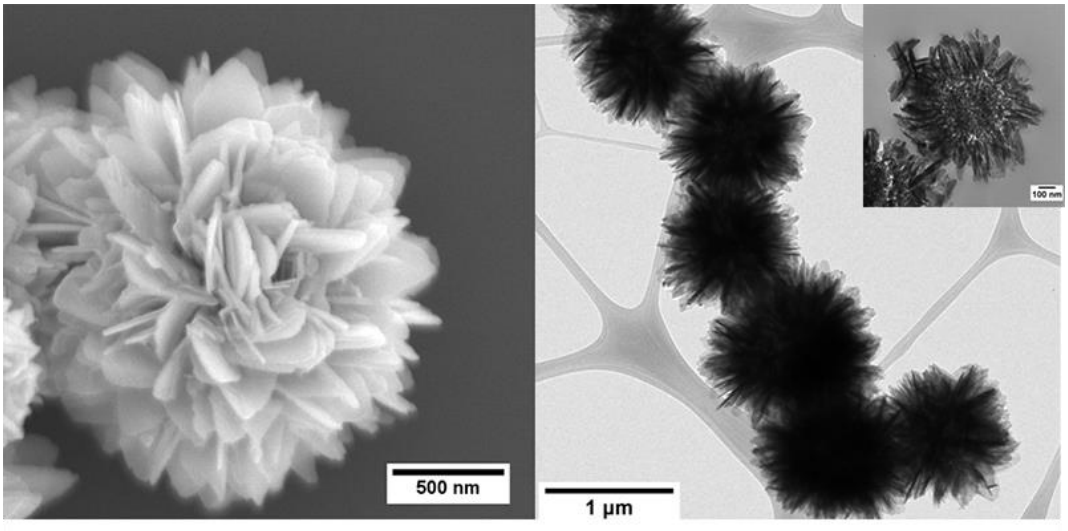

Figure 8.6. Structural and electrochemical characterization of the as-synthesized "flower-like" LTO microspheres. (Reprinted TOC figure from *ChemSusChem* **2015**, *8*, 3304 –3313. Copyright 2015 John Wiley & Sons, Inc..)

To further improve upon the electron conductivity of the as-prepared flower-like LTO, in Chapter 7, we demonstrated the first attempt in successfully correlating the effect of different attachment modalities with electrochemical performance in LTO- multiwalled carbon nanotube (MWNT) anode composites, with the goal of shedding light upon the judicious selection of preparative strategies for LTO-CNT composites with the possibility of enhanced electrode performance. Specifically, data from both structural and electrochemical characterization suggest that the composite generated by the physical sonication method outperforms the other two analogues.

The composite generated by sonication evinces the lowest electrochemical impedance and the "flower-like" morphology of the pure LTO remains intact during and after the preparative process. By contrast, the composite prepared through an in situ direct-deposition approach yielded fragmented LTO structures with overall larger crystallite sizes possibly due to truncated crystal growth induced not only by the presence of MWNTs but also by the higher annealing temperatures used. Finally, the composite fabricated via covalent attachment appeared to be enveloped with a coating of amorphous linker molecules, thereby leading to not only lower overall crystallinity and decreased contact area between LTO and MWNTs but also larger electrochemical impedance.

With different MWNT loading ratios of 1, 5, and 10%, the LTO sample with the 10% MWNT loading prepared via the physical sonication method appeared to yield the highest delivered discharge capacity at every C rate from C/2 to 100C, possibly due to the more uniform MWNT distribution. Such LTO-MWNT 10 wt% composites, produced by sonication means, exhibited an outstanding high rate capability and cycling stability, delivering 173 mA h g^{-1} at C/2 with a 99% capacity retention from cycles 20-90 and 148 mA h g^{-1} at 20 C with a 96% capacity

retention from cycles 25-95. These values denote, to the best of our knowledge, clearly superior performance to those of any previously reported LTO-carbon nanotube composite materials.

Generally, two strategies have been employed to improve the electrochemical performance of LTO, which maintains a low electronic conductivity (10^{-13}-10^{-9} S/cm)[11] and decreased diffusion coefficients of lithium ions (estimated 10^{-8}-10^{-13}cm^2/s).[12] One of them is to design a new nanoscale type of morphology in order to reduce the lithium diffusion distance. The other approach is to increase the conductivity and ionic diffusion in order to accelerate charge-transfer reaction via either surface modification or ion doping.[13]

In this dissertation, we have successfully synthesized a promising flower-like LTO anode material with enhanced high-rate performance and further attached MWNTs in order to further enhance the electron conductivity. With respect to future studies, we propose to further improve upon the electron conductivity and ionic diffusion rate through doping with ions. The advantages associated with ion doping of LTO are several fold. First, LTO is relatively insulating, due in part to the empty 3d orbital of Ti^{4+}.[14] Hence, doping ions with different charges might potentially drive the transformation of partial Ti^{4+} into Ti^{3+}, based upon charge compensation considerations. Hence, the goal would be to increase the concentration of electrons within the 3d orbitals and thereby enhance conductivity.[13] Second, doping ions with a larger radius could potentially induce a lattice expansion, which could enlarge the lithium ion diffusion pathway, and thereby enhance the conductivity of $Li_4Ti_5O_{12}$.[15] There has been extensive research focusing on doping of either the Li^{8a}, Li^{16d}, Ti^{16d} or O^{32e} sites, with ions such as Ni^{2+}, Mg^{2+}, Zn^{2+}, Al^{3+}, Cr^{3+}, Zr^{4+}, Nb^{5+}, V^{5+}, Ta^{5+}, and F^-.[15] Herein, for future directions, we aim to select a proper cation and anion to further improve the electrode performance of the as-prepared flower-like LTO.

In a cubic spinel LTO, the 32e sites are occupied by oxygen atoms, 5/6 of the 16d sites are taken by Ti atoms, and the rest of the 16d are filled by Li atoms. Moreover, the tetrahedral holes are filled by Li atoms at the 8a site, and the 16c octahedral holes are empty (Figure 8.7). The formulae could be expressed as $Li_{8a}[Li_{1/3}Ti_{5/3}]_{16d}O_{4,32e}$.[16] There are two possible diffusion pathways for lithium ion insertion and de-insertion: 8a-16c-8a, which is the predominant one, due to a shorter diffusion distance and its having more available reactive sites, and 8a-16c-48f-16d. Based on the structure, two principles need to be followed for selecting ion dopants.

First, the doped ions should be either larger than the replaced ion, which can enhance the lithium ion diffusion by lattice expansion, or these should possess more charge than the replaced ions, which can increase the electron density by driving the Ti^{4+} toTi^{3+} transformation. Among all ion dopants, we propose to choose three of them to further explore these issues. These include Ca^{2+} (replacing Li^{+} at the 16d site), Nb^{5+} (replacing Ti^{4+} at the 16d site), and F^{-} (replacing O^{2-} at the 32e site). Useful information can be gained, such as the optimal "key site" for dopants which can efficiently enhance the measured electron conductivity and Li-ion diffusion.

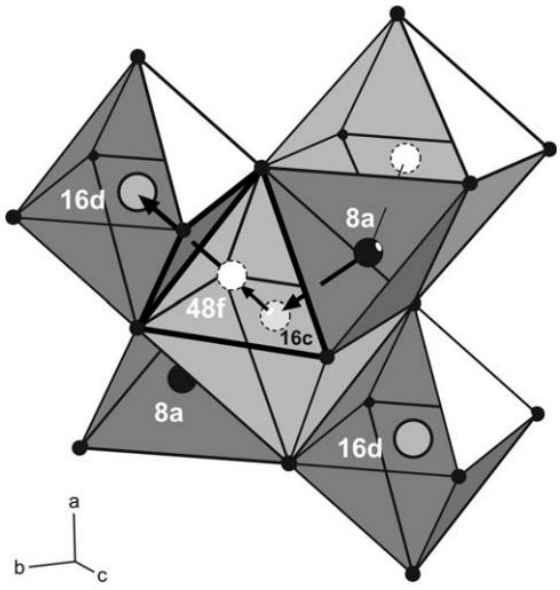

Figure 8.7. Crystal structure and lithium ion diffusion pathway. Black balls indicate Li ions, grey circles denote Ti ions, and circles with the dashed line highlight temporarily occupied sites. Arrows show possible diffusion pathways (reprinted from Ref. 15).

Ca^{2+} possesses a radius (Pauling's crystal radius) of 114 pm (6 coordination), which is larger than Li^{+} with 90 pm. Therefore, doping with Ca^{2+} could induce a transition of Ti^{4+} to Ti^{3+} and result in an optimal lattice expansion, thereby contributing to a better rate and cycle performance of this system.[17, 18] Previously, only one other group has reported data on Ca-doped LTO nanoparticles, in which $Li_{3.9}Ca_{0.1}Ti_5O_{12}$ material showed a discharge capacity of 138.7 mAh g^{-1} after 100 cycles with 10 C charge–discharge rates, denoting operational performance representing a dramatic improvement as compared with the 70 mAh g^{-1} capacity value expected for pure LTO.[17] With respect to our specific flower motif, $Li_{4-x}Ca_xTi_5O_{12}$ can be potentially generated by adding in as the Ca source, i.e. $Ca(Ac)_2{\cdot}H_2O$, at different ratios within the autoclave for a hydrothermal reaction.

The radius of Nb^{5+} is 78 pm (6 coordination), which is larger than the 74.5 pm for Ti^{4+}. The extra positive charge in Nb^{5+} should drive the transition of Ti^{4+} towards Ti^{3+}. Previously reported Nb-doped LTO work only focused on the motif of nanoparticles, which were generated

by solid-state reactions. The $Li_4Ti_{4.97}Nb_{0.03}O_{12}$ achieved a capacity of 130.2 mAh g^{-1} after 200 cycles at the charge–discharge rate of 20C, which was about 2.5 times higher than that of the pure LTO.[19] In the context of our 3D LTO motif, the precursor of Nb_2O_5 can also be added into the hydrothermal reaction in order to generate a family of desired $Li_4Ti_{5-x}Nb_xO_{12}$ materials.

Distinctive from and in addition to the principle of cation selection, the choice of an anionic dopant with less negative charge should drive Ti^{4+} to Ti^{3+} transformation due to charge compensation effects. Specifically, F^- replaces the O^{2-} at the 32e position, with a relative smaller radius of 133 pm (6 coordination) than O^{2-} measuring 140 pm. As compared with either Br^- (182 pm) or Cl^- (167 pm), F^- possesses a similar size to O^{2-}, thereby leading to a larger tendency to replace the original O atom, which ultimately yields a formula of $Li_4Ti_5O_{12-x}F_x$. Previously reported carbon-encapsulated F-doped LTO, generated by a solid state reaction, denoted a high charge capacity of ~158 mA h g^{-1} at the 1 C rate with negligible capacity fading for 200 cycles and an extremely high rate performance up to 140 C.[20]

Based upon the previous literature reports, we believe our Ca, Nb and F-doped LTO structures should demonstrate enhanced capacity as well as high rate capability. With the unique 3D flower-like morphology of our as-prepared LTO motif, we propose that our doped LTO samples will potentially evince better performance than those reported in literature, due to the enhanced ion and electron transport rate within the distinct 3D motif as compared with the 0D nanoparticles. The phase structure, morphologies, electrochemical properties and the doping ratio of all of these samples will be characterized using either X-ray diffraction, scanning electron microscopy (SEM), or transmission electron microscopy (TEM) as well as cyclic voltammetry (CV), EDS-mapping, and inductively coupled plasma optical emission spectrometry (ICP–OES), respectively. Electron Energy Loss Spectroscopy (EELS) will also be

applied in order to assist in tracking the transformation of Ti^{4+} to Ti^{3+}. The approximate doping ratio as well as the dopant ion distribution can be measured by means of EDS mapping and ICP measurements. We do expect some degree of non-uniformity in terms of the dopant distribution within the flower LTO motif. In order to track down the dopant locations more accurately, we plan to perform EDS mapping on one particular LTO flower from the petal through to the core area using microtoming, by which LTO flowers can be cut into multiple parallel slices individually possessing average thicknesses of 80 nm. Moreover, electrochemical performance will be assessed to confirm expected improvements after ion doping.

8.3. References

1. Dyakonov, V. The polymer–fullerene interpenetrating network: one route to a solar cell approach. *Physica E: Low-dimensional Systems and Nanostructures* **2002**, *14*, 53-60.
2. G. Yu, J. G., J. C. Hummelen, F. Wudl, A. J. Heeger. Polymer Photovoltaic Cells: Enhanced Efficiencies via a Network of Internal Donor-Acceptor Heterojunctions. *Science* **1995**, *270*, 1789-1791.
3. Sariciftci, N. S.; Braun, D.; Zhang, C.; Srdanov, V. I.; Heeger, A. J.; Stucky, G.; Wudl, F. Semiconducting polymer-buckminsterfullerene heterojunctions: Diodes, photodiodes, and photovoltaic cells. *Appl. Phys. Lett.* **1993**, *62*, 585-587.
4. Halls, J. J. M.; Pichler, K.; Friend, R. H.; Moratti, S. C.; Holmes, A. B. Exciton diffusion and dissociation in a poly(p-phenylenevinylene)/C_{60} heterojunction photovoltaic cell. *Appl. Phys. Lett.* **1996**, *68*, 3120-3122.
5. Hummelen, J. C.; Knight, B. W.; LePeq, F.; Wudl, F.; Yao, J.; Wilkins, C. L. Preparation and characterization of fulleroid and methanofullerene derivatives. *J. Organ. Chem.* **1995**, *60*, 532-538.
6. Kramer, I. J.; Sargent, E. H. The Architecture of Colloidal Quantum Dot Solar Cells: Materials to Devices. *Chem. Rev.* **2014**, *114*, 863-882.
7. Roman, L. S.; Mammo, W.; Pettersson, L. A. A.; Andersson, M. R.; Inganas, O. High quantum efficiency polythiophene/C_{60} photodiodes. *Adv. Mater.* **1998**, *10*, 774-777.
8. Wang, D. F.; Baral, J. K.; Zhao, H. G.; Gonfa, B. A.; Truong, V. V.; El Khakani, M. A.; Izquierdo, R.; Ma, D. L. Controlled Fabrication of PbS Quantum-Dot/Carbon-Nanotube Nanoarchitecture and its Significant Contribution to Near-Infrared Photon-to-Current Conversion. *Adv. Funct. Mater.* **2011**, *21*, 4010-4018.
9. Wong, K. W.; Yip, H. L.; Luo, Y.; Wong, K. Y.; Lau, W. M.; Low, K. H.; Chow, H. F.; Gao, Z. Q.; Yeung, W. L.; Chang, C. C. Blocking reactions between indium-tin oxide and poly

(3,4-ethylene dioxythiophene): poly(styrene sulphonate) with a self-assembly monolayer. *Appl. Phys. Lett.* **2002**, *80*, 2788-2790.
10. Frey, G. L.; Reynolds, K. J.; Friend, R. H. Novel electrodes from solution-processed layer-structure materials. *Adv. Mater.* **2002**, *14*, 265.
11. Ma, J.; Wang, C.; Wroblewski, S. Kinetic characteristics of mixed conductive electrodes for lithium ion batteries. *J. Power Sources* **2007**, *164*, 849-856.
12. Kavan, L.; Procházka, J.; Spitler, T. M.; Kalbáč, M.; Zukalová, M. t.; Drezen, T.; Grätzel, M. Li Insertion into $Li_4]Ti_5O_{12}$ (Spinel). *J. Electrochem. Soc.* **2003**, *150*, A1000.
13. Zhu, G.-N.; Wang, Y.-G.; Xia, Y.-Y. Ti-based compounds as anode materials for Li-ion batteries. *Energy Environ. Sci.* **2012**, *5*, 6652.
14. Ouyang, C. Y.; Zhong, Z. Y.; Lei, M. S. Ab initio studies of structural and electronic properties of $Li_4Ti_5O_{12}$ spinel. *Electrochem. Commun.* **2007**, *9*, 1107-1112.
15. Yi, T.-F.; Jiang, L.-J.; Shu, J.; Yue, C.-B.; Zhu, R.-S.; Qiao, H.-B. Recent development and application of $Li_4Ti_5O_{12}$ as anode material of lithium ion battery. *J. Phys. Chem. Solids* **2010**, *71*, 1236-1242.
16. Wilkening, M.; Amade, R.; Iwaniak, W.; Heitjans, P. Ultraslow Li diffusion in spinel-type structured $Li_4Ti_5O_{12}$ - a comparison of results from solid state NMR and impedance spectroscopy. *Phys. Chem. Chem. Phys.* **2007**, *9*, 1239-1246.
17. Zhang, Q.; Zhang, C.; Li, B.; Kang, S.; Li, X.; Wang, Y. Preparation and electrochemical properties of Ca-doped $Li_4Ti_5O_{12}$ as anode materials in lithium-ion battery. *Electrochim. Acta* **2013**, *98*, 146-152.
18. Zhang, Q.; Li, X. Improving the Energy Density of Ca-Doped $Li_4Ti_5O_{12}$ Through Discharging to 0 V Cut-off Voltage. *Int. J. Electrochem. Sci.* **2013**, *8*, 9734-9740.
19. Shi, L.; Hu, X.; Huang, Y. Fast microwave-assisted synthesis of Nb-doped $Li_4Ti_5O_{12}$ for high-rate lithium-ion batteries. *Journal of Nanoparticle Research* **2014**, *16*, 1-11.
20. Ma, Y.; Ding, B.; Ji, G.; Lee, J. Y. Carbon-Encapsulated F-Doped $Li_4Ti_5O_{12}$ as a High Rate Anode Material for Li+ Batteries. *ACS Nano* **2013**, *7*, 10870-10878.

Chapter 9. References

1. Kamat, P. V. Meeting the clean energy demand: Nanostructure architectures for solar energy conversion. *J. Phys. Chem. C* **2007**, *111*, 2834-2860.
2. Hou, Y.; Cheng, Y. W.; Hobson, T.; Liu, J. Design and Synthesis of Hierarchical MnO_2 Nanospheres/Carbon Nanotubes/Conducting Polymer Ternary Composite for High Performance Electrochemical Electrodes. *Nano Lett.* **2010**, *10*, 2727-2733.
3. Mann, M. E.; Bradley, R. S.; Hughes, M. K. Global-scale temperature patterns and climate forcing over the past six centuries. *Nature* **1998**, *392*, 779-787.
4. Dresselhaus, M. S.; Thomas, I. L. Alternative energy technologies. *Nature* **2001**, *414*, 332-337.
5. Nozik, A. J.; Miller, J. Introduction to Solar Photon Conversion. *Chem. Rev.* **2010**, *110*, 6443-6445.
6. Umeyama, T.; Imahori, H. Carbon nanotube-modified electrodes for solar energy conversion. *Energy Environ. Sci.* **2008**, *1*, 120-133.
7. Lunt, R. R.; Osedach, T. P.; Brown, P. R.; Rowehl, J. A.; Bulovic, V. Practical Roadmap and Limits to Nanostructured Photovoltaics. *Adv. Mater.* **2011**, *23*, 5712-5727.
8. Hanna, M. C.; Nozik, A. J. Solar conversion efficiency of photovoltaic and photoelectrolysis cells with carrier multiplication absorbers. *J. Appl. Phys.* **2006**, *100*.
9. Green, M. A.; Emery, K.; Hishikawa, Y.; Warta, W.; Dunlop, E. D. Solar cell efficiency tables. *Progress in Photovoltaics* **2011**, *19*, 565-572.
10. Wu, F. X.; Li, X. H.; Wang, Z. X.; Guo, H. J. Petal-like $Li_4Ti_5O_{12}$-TiO_2 nanosheets as high-performance anode materials for Li-ion batteries. *Nanoscale* **2013**, *5*, 6936-6943.
11. Zhang, Z. H.; Li, G. C.; Peng, H. R.; Chen, K. Z. Hierarchical hollow microspheres assembled from N-doped carbon coated $Li_4Ti_5O_{12}$ nanosheets with enhanced lithium storage properties.*J. Mater. Chem. A* **2013**, *1*, 15429-15434.
12. Tang, Y. F.; Yang, L.; Fang, S. H.; Qiu, Z. $Li_4Ti_5O_{12}$ hollow microspheres assembled by nanosheets as an anode material for high-rate lithium ion batteries. *Electrochim. Acta* **2009**, *54*, 6244-6249.
13. Chen, P. C.; Shen, G.; Shi, Y.; Chen, H.; Zhou, C. Preparation and characterization of flexible asymmetric supercapacitors based on transition-metal-oxide nanowire/single-walled carbon nanotube hybrid thin-film electrodes. *ACS Nano* **2010**, *4*, 4403-4411.
14. Landi, B. J.; Ganter, M. J.; Cress, C. D.; DiLeo, R. A.; Raffaelle, R. P. Carbon nanotubes for lithium ion batteries. *Energy Environ. Sci.* **2009**, *2*, 638-654.
15. Kong, D.; Ren, W.; Luo, Y.; Yang, Y.; Cheng, C. Scalable synthesis of graphene-wrapped $Li_4Ti_5O_{12}$ dandelion-like microspheres for lithium-ion batteries with excellent rate capability and long-cycle life. *J. Mater. Chem. A* **2014**, *2*, 20221-20230.
16. Zhu, G. N.; Wang, Y. G.; Xia, Y. Y. Ti-based compounds as anode materials for Li-ion batteries. *Energy Environ. Sci.* **2012**, *5*, 6652-6667.
17. Tiwari, J. N.; Tiwari, R. N.; Kim, K. S. Zero-dimensional, one-dimensional, two-dimensional and three-dimensional nanostructured materials for advanced electrochemical energy devices. *Progress in Materials Science* **2012**, *57*, 724-803.
18. Iijima, S. Helical Microtubules of Graphitic Carbon. *Nature* **1991**, *354*, 56-58.
19. Moore, K. E.; Tune, D. D.; Flavel, B. S. Double-Walled Carbon Nanotube Processing. *Adv. Mater.* **2015**, *27*, 3105-3137.

20. Lin, Y.; Taylor, S.; Li, H. P.; Fernando, K. A. S.; Qu, L. W.; Wang, W.; Gu, L. R.; Zhou, B.; Sun, Y. P. Advances toward bioapplications of carbon nanotubes. *J. Mater. Chem.* **2004**, *14*, 527-541.
21. Guo, T.; Nikolaev, P.; Thess, A.; Colbert, D. T.; Smalley, R. E. Catalytic Growth of Single-Walled Nanotubes by Laser Vaporization. *Chem. Phys. Lett.* **1995**, *243*, 49-54.
22. Journet, C.; Maser, W. K.; Bernier, P.; Loiseau, A.; delaChapelle, M. L.; Lefrant, S.; Deniard, P.; Lee, R.; Fischer, J. E. Large-scale production of single-walled carbon nanotubes by the electric-arc technique. *Nature* **1997**, *388*, 756-758.
23. Kumar, M.; Ando, Y. Chemical Vapor Deposition of Carbon Nanotubes: A Review on Growth Mechanism and Mass Production. *J. Nanosci. Nanotechnol.* **2010**, *10*, 3739-3758.
24. Inami, N.; Mohamed, M. A.; Shikoh, E.; Fujiwara, A. Synthesis-condition dependence of carbon nanotube growth by alcohol catalytic chemical vapor deposition method. *Science and Technology of Adv. Mater.* **2007**, *8*, 292-295.
25. Liu, J.; Rinzler, A. G.; Dai, H. J.; Hafner, J. H.; Bradley, R. K.; Boul, P. J.; Lu, A.; Iverson, T.; Shelimov, K.; Huffman, C. B.; Rodriguez-Macias, F.; Shon, Y. S.; Lee, T. R.; Colbert, D. T.; Smalley, R. E. Fullerene pipes. *Science* **1998**, *280*, 1253-1256.
26. Hiura, H.; Ebbesen, T. W.; Tanigaki, K. Opening and Purification of Carbon Nanotubes in High Yields. *Adv. Mater.* **1995**, *7*, 275-276.
27. Fu, K. F.; Huang, W. J.; Lin, Y.; Riddle, L. A.; Carroll, D. L.; Sun, Y. P. Defunctionalization of functionalized carbon nanotubes. *Nano Lett.* **2001**, *1*, 439-441.
28. Diao, P.; Liu, Z. F.; Wu, B.; Nan, X. L.; Zhang, J.; Wei, Z. Chemically assembled single-wall carbon nanotubes and their electrochemistry. *ChemPhysChem* **2002**, *3*, 898-901.
29. Khabashesku, V. N.; Billups, W. E.; Margrave, J. L. Fluorination of single-wall carbon nanotubes and subsequent derivatization reactions. *Acc. Chem. Res.* **2002**, *35*, 1087-1095.
30. Mickelson, E. T.; Huffman, C. B.; Rinzler, A. G.; Smalley, R. E.; Hauge, R. H.; Margrave, J. L. Fluorination of single-wall carbon nanotubes. *Chem. Phys. Lett.* **1998**, *296*, 188-194.
31. Rahman, G. M. A.; Guldi, D. M.; Campidelli, S.; Prato, M. Electronically interacting single wall carbon nanotube-porphyrin nanohybrids. *J. Mater. Chem.* **2006**, *16*, 62-65.
32. Ehli, C.; Rahman, G. M. A.; Jux, N.; Balbinot, D.; Guldi, D. M.; Paolucci, F.; Marcaccio, M.; Paolucci, D.; Melle-Franco, M.; Zerbetto, F.; Campidelli, S.; Prato, M. Interactions in single wall carbon nanotubes/pyrene/porphyrin nanohybrids. *J. Am. Chem. Soc.* **2006**, *128*, 11222-11231.
33. Olek, M.; Busgen, T.; Hilgendorff, M.; Giersig, M. Quantum dot modified multiwall carbon nanotubes. *J. Phys. Chem. B* **2006**, *110*, 12901-12904.
34. Hammel, E.; Tang, X.; Trampert, M.; Schmitt, T.; Mauthner, K.; Eder, A.; Potschke, P. Carbon nanofibers for composite applications. *Carbon* **2004**, *42*, 1153-1158.
35. Wang, J.; Deo, R. P.; Poulin, P.; Mangey, M. Carbon nanotube fiber microelectrodes. *J. Am. Chem. Soc.* **2003**, *125*, 14706-14707.
36. Rajesh, B.; Thampi, K. R.; Bonard, J. M.; Mathieu, H. J.; Xanthopoulos, N.; Viswanathan, B. Conducting polymeric nanotubules as high performance methanol oxidation catalyst support. *Chem. Commun.***2003**, 2022-2023.
37. Wang, F.; Dukovic, G.; Brus, L. E.; Heinz, T. F. The optical resonances in carbon nanotubes arise from excitons. *Science* **2005**, *308*, 838-841.
38. Berger, C.; Yi, Y.; Wang, Z. L.; de Heer, W. A. Multiwalled carbon nanotubes are ballistic conductors at room temperature. *Appl. Phys. A* **2002**, *A74*, 363-365.

39. Wind, S. J.; Appenzeller, J.; Avouris, P. Lateral scaling in carbon-nanotube field-effect transistors. *Phys. Rev. Lett.* **2003**, *91*, 058301/058301-058301/058304.
40. Javey, A.; Jing, G.; Qian, W.; Lundstrom, M.; Dai, H. Ballistic carbon nanotube field-effect transistors. *Nature* **2003**, *424*, 654-657.
41. Brennan, L. J.; Byrne, M. T.; Bari, M.; Gun'ko, Y. K. Carbon Nanomaterials for Dye-Sensitized Solar Cell Applications: A Bright Future. *Adv. Energy. Mater.* **2011**, *1*, 472-485.
42. Campidelli, S.; Klumpp, C.; Bianco, A.; Guldi, D. M.; Prato, M. Functionalization of CNT: Synthesis and applications in photovoltaics and biology. *J. Phys. Org. Chem.* **2006**, *19*, 531-539.
43. Tune, D. D.; Flavel, B. S.; Krupke, R.; Shapter, J. G. Carbon Nanotube-Silicon Solar Cells. *Adv. Energy. Mater.* **2012**, *2*, 1043-1055.
44. Zhang, W. D.; Xu, B.; Jiang, L. C. Functional hybrid materials based on carbon nanotubes and metal oxides. *J. Mater. Chem.* **2010**, *20*, 6383-6391.
45. Zhang, Z. H.; Peng, J. C.; Zhang, H. Low-temperature resistance of individual single-walled carbon nanotubes: A theoretical estimation. *Appl. Phys. Lett.* **2001**, *79*, 3515-3517.
46. Dai, H. J. Carbon nanotubes: opportunities and challenges. *Surf. Sci.* **2002**, *500*, 218-241.
47. Berber, S.; Kwon, Y. K.; Tomanek, D. Unusually high thermal conductivity of carbon nanotubes. *Phys. Rev. Lett.* **2000**, *84*, 4613-4616.
48. Zhang, X. F.; Sreekumar, T. V.; Liu, T.; Kumar, S. Properties and structure of nitric acid oxidized single wall carbon nanotube films. *J. Phys. Chem. B* **2004**, *108*, 16435-16440.
49. Zhao, M. W.; Xia, Y. Y.; Liu, X. D.; Tan, Z. Y.; Huang, B. D.; Li, F.; Ji, Y. J.; Song, C. Curvature-induced condensation of lithium confined inside single-walled carbon nanotubes: First-principles calculations. *Phys. Lett. A* **2005**, *340*, 434-439.
50. Zhao, M. W.; Xia, Y. Y.; Mei, L. M. Diffusion and condensation of lithium atoms in single-walled carbon nanotubes. *Phys. Rev. B* **2005**, *71*, 165413.
51. Zhao, J.; Buldum, A.; Han, J.; Lu, J. P. First-principles study of Li-intercalated carbon nanotube ropes. *Phys. Rev. Lett.* **2000**, *85*, 1706-1709.
52. Valizadeh, A.; Mikaeili, H.; Samiei, M.; Farkhani, S. M.; Zarghami, N.; Kouhi, M.; Akbarzadeh, A.; Davaran, S. Quantum dots: synthesis, bioapplications, and toxicity. *Nanoscale Research Letters* **2012**, *7*, 480.
53. Rossetti, R.; Nakahara, S.; Brus, L. E. Quantum Size Effects in the Redox Potentials, Resonance Raman-Spectra, and Electronic-Spectra of Cds Crystallites in Aqueous-Solution. *J. Chem. Phys.* **1983**, *79*, 1086-1088.
54. Boatman, E. M.; Lisensky, G. C.; Nordell, K. J. A safer, easier, faster synthesis for CdSe quantum dot nanocrystals. *J. Chem. Educ.* **2005**, *82*, 1697-1699.
55. Schaller, R. D.; Klimov, V. I. High efficiency carrier multiplication in PbSe nanocrystals: Implications for solar energy conversion. *Phys. Rev. Lett.* **2004**, *92*, 186601.
56. Ellingson, R. J.; Beard, M. C.; Johnson, J. C.; Yu, P. R.; Micic, O. I.; Nozik, A. J.; Shabaev, A.; Efros, A. L. Highly efficient multiple exciton generation in colloidal PbSe and PbS quantum dots. *Nano Lett.* **2005**, *5*, 865-871.
57. Beard, M. C.; Knutsen, K. P.; Yu, P. R.; Luther, J. M.; Song, Q.; Metzger, W. K.; Ellingson, R. J.; Nozik, A. J. Multiple exciton generation in colloidal silicon nanocrystals. *Nano Lett.* **2007**, *7*, 2506-2512.
58. Weller, H. Quantized Semiconductor Particles - a Novel State of Matter for Materials Science. *Adv. Mater.* **1993**, *5*, 88-95.

59. Alivisatos, A. P. Perspectives on the physical chemistry of semiconductor nanocrystals. *J. Phys. Chem.* **1996**, *100*, 13226-13239.
60. Hu, M. Z.; Zhu, T. Semiconductor Nanocrystal Quantum Dot Synthesis Approaches Towards Large-Scale Industrial Production for Energy Applications. *Nanoscale Research Letters* **2015**, *10*, 469.
61. Peng, Z. A.; Peng, X. G. Nearly monodisperse and shape-controlled CdSe nanocrystals via alternative routes: Nucleation and growth. *J. Am. Chem. Soc.* **2002**, *124*, 3343-3353.
62. Yin, Y.; Alivisatos, A. P. Colloidal nanocrystal synthesis and the organic-inorganic interface. *Nature* **2005**, *437*, 664-670.
63. Peng, Z. A.; Peng, X. G. Formation of high-quality CdTe, CdSe, and CdS nanocrystals using CdO as precursor. *J. Am. Chem. Soc.* **2001**, *123*, 183-184.
64. Yu, W. W.; Peng, X. Formation of high-quality CdS and other II-VI semiconductor nanocrystals in noncoordinating solvents: tunable reactivity of monomers. *Angew. Chem. Int. Ed.* **2002**, *41*, 2368-2371.
65. Owen, J. S.; Chan, E. M.; Liu, H. T.; Alivisatos, A. P. Precursor Conversion Kinetics and the Nucleation of Cadmium Selenide Nanocrystals. *J. Am. Chem. Soc.* **2010**, *132*, 18206-18213.
66. Reiss, P.; Bleuse, J.; Pron, A. Highly luminescent CdSe/ZnSe core/shell nanocrystals of low size dispersion. *Nano Lett.* **2002**, *2*, 781-784.
67. Kalasad, M. N.; Rabinal, A. K.; Mulimani, B. G. Ambient Synthesis and Characterization of High-Quality CdSe Quantum Dots by an Aqueous Route. *Langmuir* **2009**, *25*, 12729-12735.
68. Zhou, L.; Gao, C.; Hu, X. Z.; Xu, W. J. One-Pot Large-Scale Synthesis of Robust Ultrafine Silica-Hybridized CdTe Quantum Dots. *ACS Appl. Mater. Interfaces* **2010**, *2*, 1211-1219.
69. Zhang, H.; Wang, L. P.; Xiong, H. M.; Hu, L. H.; Yang, B.; Li, W. Hydrothermal synthesis for high-quality CdTe nanocrystals. *Adv. Mater.* **2003**, *15*, 1712-1715.
70. Virgili, T.; López, I. S.; Vercelli, B.; Angella, G.; Zotti, G.; Cabanillas-Gonzalez, J.; Granados, D.; Luer, L.; Wannemacher, R.; Tassone, F. Spectroscopic Signature of Trap States in Assembled CdSe Nanocrystal Hybrid Films. *J. Phys. Chem. C* **2012**, *116*, 16259-16263.
71. Querner, C.; Reiss, P.; Sadki, S.; Zagorska, M.; Pron, A. Size and ligand effects on the electrochemical and spectroelectrochemical responses of CdSe nanocrystals. *Phys. Chem. Chem. Phys.* **2005**, *7*, 3204-3209.
72. Newton, J. C.; Ramasamy, K.; Mandal, M.; Joshi, G. K.; Kumbhar, A.; Sardar, R. Low-Temperature Synthesis of Magic-Sized CdSe Nanoclusters: Influence of Ligands on Nanocluster Growth and Photophysical Properties. *J. Phys. Chem. C* **2012**, *116*, 4380-4389.
73. Klem, E. J. D.; MacNeil, D. D.; Cyr, P. W.; Levina, L.; Sargent, E. H. Efficient solution-processed infrared photovoltaic cells: Planarized all-inorganic bulk heterojunction devices via inter-quantum-dot bridging during growth from solution. *Appl. Phys. Lett.* **2007**, *90*, 183113.
74. Talapin, D. V.; Murray, C. B. PbSe nanocrystal solids for n- and p-channel thin film field-effect transistors. *Science* **2005**, *310*, 86-89.
75. Pattantyus-Abraham, A. G.; Kramer, I. J.; Barkhouse, A. R.; Wang, X.; Konstantatos, G.; Debnath, R.; Levina, L.; Raabe, I.; Nazeeruddin, M. K.; Gratzel, M.; Sargent, E. H. Depleted-heterojunction colloidal quantum dot solar cells. *ACS Nano* **2010**, *4*, 3374-3380.
76. Tang, J.; Kemp, K. W.; Hoogland, S.; Jeong, K. S.; Liu, H.; Levina, L.; Furukawa, M.; Wang, X.; Debnath, R.; Cha, D.; Chou, K. W.; Fischer, A.; Amassian, A.; Asbury, J. B.; Sargent, E. H. Colloidal-quantum-dot photovoltaics using atomic-ligand passivation. *Nat. Mater.* **2011**, *10*, 765-771.

77. Brown, P. R.; Kim, D.; Lunt, R. R.; Zhao, N.; Bawendi, M. G.; Grossman, J. C.; Bulovic, V. Energy level modification in lead sulfide quantum dot thin films through ligand exchange. *ACS Nano* **2014**, *8*, 5863-5872.
78. Liu, I. S.; Lo, H. H.; Chien, C. T.; Lin, Y. Y.; Chen, C. W.; Chen, Y. F.; Su, W. F.; Liou, S. C. Enhancing photoluminescence quenching and photoelectric properties of CdSe quantum dots with hole accepting ligands. *J. Mater. Chem.* **2008**, *18*, 675-682.
79. Mora-Sero, I.; Bertoluzzi, L.; Gonzalez-Pedro, V.; Gimenez, S.; Fabregat-Santiago, F.; Kemp, K. W.; Sargent, E. H.; Bisquert, J. Selective contacts drive charge extraction in quantum dot solids via asymmetry in carrier transfer kinetics *Nat. Commun.* **2013**, *4*, 3272.
80. Peng, X. H.; Wong, S. S. Controlling Nanocrystal Density and Location on Carbon Nanotube Templates. *Chem. Mater.* **2009**, *21*, 682-694.
81. Carey, G. H.; Abdelhady, A. L.; Ning, Z.; Thon, S. M.; Bakr, O. M.; Sargent, E. H. Colloidal Quantum Dot Solar Cells. *Chem. Rev.* **2015**, *115*, 12732–12763.
82. Shockley, W.; Queisser, H. J. Detailed Balance Limit of Efficiency of p-n junction Solar Cells. *J. Appl. Phys.* **1961**, *32*, 510.
83. Gerischer, H.; Lubke, M. A Particle-Size Effect in the Sensitization of TiO_2 Electrodes by a Cds Deposit. *J. Electroanal. Chem.* **1986**, *204*, 225-227.
84. Vogel, R.; Pohl, K.; Weller, H. Sensitization of Highly Porous, Polycrystalline TiO_2 Electrodes by Quantum Sized Cds. *Chem. Phys. Lett.* **1990**, *174*, 241-246.
85. Kohtani, S.; Kudo, A.; Sakata, T. Spectral Sensitization of a TiO_2 Semiconductor Electrode by Cds Microcrystals and Its Photoelectrochemical Properties. *Chem. Phys. Lett.* **1993**, *206*, 166-170.
86. Liu, D.; Kamat, P. V. Electrochemical Rectification in CdSe+TiO_2 Coupled Semiconductor-Films. *J. Electroanal. Chem.* **1993**, *347*, 451-456.
87. Azoz, S.; Jiang, J.; Keskar, G.; McEnally, C.; Alkas, A.; Ren, F.; Marinkovic, N.; Haller, G. L.; Ismail-Beigi, S.; Pfefferle, L. D. Mechanism for strong binding of CdSe quantum dots to multiwall carbon nanotubes for solar energy harvesting. *Nanoscale* **2013**, *5*, 6893-6900.
88. Kao, L. C.; Liou, S. Y. H.; Dong, C. L.; Yeh, P. H.; Chen, C. L. Tandem Structure of QD Cosensitized TiO_2 Nanorod Arrays for Solar Light Driven Hydrogen Generation. *ACS. Sustain. Chem. Eng.* **2016**, *4*, 210-218.
89. Wang, L. D.; Zhao, D. X.; Su, Z. S.; Shen, D. Z. Hybrid polymer/ZnO solar cells sensitized by PbS quantum dots. *Nanoscale Research Letters* **2012**, *7*, 1-6.
90. Robel, I.; Bunker, B. A.; Kamat, P. V. Single-walled carbon nanotube-CdS nanocomposites as light-harvesting assemblies: Photoinduced charge-transfer interactions. *Adv. Mater.* **2005**, *17*, 2458.
91. Banerjee, S.; Wong, S. S. Formation of CdSe nanocrystals onto oxidized, ozonized single-walled carbon nanotube surfaces. *Chem. Commun.***2004**, 1866-1867.
92. Haremza, J. M.; Hahn, M. A.; Krauss, T. D.; Chen, S.; Calcines, J. Attachment of Single CdSe Nanocrystals to Individual Single-Walled Carbon Nanotubes. *Nano Lett.* **2002**, *2*, 1253-1258.
93. Kamat, P. V. Quantum Dot Solar Cells. Semiconductor Nanocrystals as Light Harvesters. *J. Phys. Chem. C* **2008**, *112*, 18737-18753.
94. Vietmeyer, F.; Seger, B.; Kamat, P. V. Anchoring ZnO Particles on Functionalized Single Wall Carbon Nanotubes. Excited State Interactions and Charge Collection. *Adv. Mater.* **2007**, *19*, 2935-2940.

95. Tian, J. J.; Shen, T.; Liu, X. G.; Fei, C. B.; Lv, L. L.; Cao, G. Z. Enhanced Performance of PbS-quantum-dot-sensitized Solar Cells via Optimizing Precursor Solution and Electrolytes. *Sci. Rep.* **2016**, *6*, 23094.
96. Olek, M.; Büsgen, T.; Hilgendorff, M.; Giersig, M. Quantum Dot Modified Multiwall Carbon Nanotubes. *J. Phys. Chem. B* **2006**, *110*, 12901-12904.
97. Wang, D.; Baral, J. K.; Zhao, H.; Gonfa, B. A.; Truong, V.-V.; El Khakani, M. A.; Izquierdo, R.; Ma, D. Controlled Fabrication of PbS Quantum-Dot/Carbon-Nanotube Nanoarchitecture and its Significant Contribution to Near-Infrared Photon-to-Current Conversion. *Adv. Funct. Mater.* **2011**, *21*, 4010-4018.
98. Schulz-Drost, C.; Sgobba, V.; Gerhards, C.; Leubner, S.; Calderon, R. M. K.; Ruland, A.; Guldi, D. M. Innovative Inorganic-Organic Nanohybrid Materials: Coupling Quantum Dots to Carbon Nanotubes. *Angew. Chem. Int. Ed.* **2010**, *49*, 6425-6429.
99. Ji, L. W.; Lin, Z.; Alcoutlabi, M.; Zhang, X. W. Recent developments in nanostructured anode materials for rechargeable lithium-ion batteries. *Energy Environ. Sci.* **2011**, *4*, 2682-2699.
100. Wang, B.; Chen, J. S.; Wu, H. B.; Wang, Z.; Lou, X. W. Quasiemulsion-templated formation of alpha-Fe_2O_3 hollow spheres with enhanced lithium storage properties. *J. Am. Chem. Soc.* **2011**, *133*, 17146-17148.
101. Liu, H.; Du, X. W.; Xing, X. R.; Wang, G. X.; Qiao, S. Z. Highly ordered mesoporous Cr_2O_3 materials with enhanced performance for gas sensors and lithium ion batteries. *Chem. Commun.***2012**, *48*, 865-867.
102. Li, H.; Wang, Z. X.; Chen, L. Q.; Huang, X. J. Research on advanced materials for Li-ion Batteries. *Adv. Mater.* **2009**, *21*, 4593-4607.
103. Ellis, B. L.; Knauth, P.; Djenizian, T. Three-Dimensional Self-Supported Metal Oxides for Advanced Energy Storage. *Adv. Mater.* **2014**, *26*, 3368-3397.
104. Yi, T.-F.; Liu, H.; Zhu, Y.-R.; Jiang, L.-J.; Xie, Y.; Zhu, R.-S. Improving the high rate performance of $Li_4Ti_5O_{12}$ through divalent zinc substitution. *J. Power Sources* **2012**, *215*, 258-265.
105. Chen, Z.; Belharouak, I.; Sun, Y. K.; Amine, K. Titanium-Based Anode Materials for Safe Lithium-Ion Batteries. *Adv. Funct. Mater.* **2013**, *23*, 959-969.
106. Choi, J.-H.; Ryu, W.-H.; Park, K.; Jo, J.-D.; Jo, S.-M.; Lim, D.-S.; Kim, I.-D. Multi-layer electrode with nano- $Li_4Ti_5O_{12}$ aggregates sandwiched between carbon nanotube and graphene networks for high power Li-ion batteries. *Sci. Rep.* **2014**, *4*, 7334.
107. K. M. Colbow, J. R. D., R. R. Haering. Structure and electrochemistry of the spinel oxides $LiTi_2O_4$ and $Li_{4/3}Ti_{5/3}O_4$. *J. Power Sources* **1989**, *26*, 397-402.
108. Norio Takami, K. H., Hiroki Inagaki. Lithium Diffusion in $Li_{4/3}Ti_{5/3}O_4$ Particles during Insertion and Extraction. *J. Electrochem. Soc.* **2011**, *158*, A725-A730.
109. T. Brousse, P. F., R. Marchand, D. M. Schleich, O. Bohnke, K. West. All oxide solid-state lithium-ion cells. *J. Power Sources* **1997**, *1997*, 412-415.
110. C.Y. Ouyang, Z. Y. Z., M.S. Lei. Ab initio studies of structural and electronic properties of $Li_4Ti_5O_{12}$ spinel. *Electrochem. Commun.* **2007**, *2007*, 1107-1112.
111. Jiang, J.; Li, Y.; Liu, J.; Huang, X.; Yuan, C.; Lou, X. W. Recent advances in metal oxide-based electrode architecture design for electrochemical energy storage. *Adv. Mater.* **2012**, *24*, 5166-5180.
112. Huang, J. J.; Jiang, Z. Y. The preparation and characterization of $Li_4Ti_5O_{12}$/carbon nano-tubes for lithium ion battery. *Electrochim. Acta* **2008**, *53*, 7756-7759.

113. Jhan, Y. R.; Duh, J. G. Synthesis of entanglement structure in nanosized $Li_4Ti_5O_{12}$/multi-walled carbon nanotubes composite anode material for Li-ion batteries by ball-milling-assisted solid-state reaction. *J. Power Sources* **2012**, *198*, 294-297.
114. Jia, X. L.; Kan, Y. F.; Zhu, X.; Ning, G. Q.; Lu, Y. F.; Wei, F. Building flexible $Li_4Ti_5O_{12}$/CNT lithium-ion battery anodes with superior rate performance and ultralong cycling stability. *Nano Energy* **2014**, *10*, 344-352.
115. Kim, H. K.; Roh, K. C.; Kang, K.; Kim, K. B. Synthesis of nano-$Li_4Ti_5O_{12}$ decorated on non-oxidized carbon nanotubes with enhanced rate capability for lithium-ion batteries. *RSC Adv.* **2013**, *3*, 14267-14272.
116. Shu, J.; Hou, L.; Ma, R.; Shui, M.; Shao, L. Y.; Wang, D. J.; Ren, Y. L.; Zheng, W. D. In situ fabrication of $Li_4Ti_5O_{12}$@CNT composites and their superior lithium storage properties. *RSC Adv.* **2012**, *2*, 10306-10309.
117. Zhang, P.; Chen, M.; Shen, X.; Wu, Q.; Zhang, X.; Huan, L.; Diao, G. Preparation of $Li_4Ti_5O_{12}$ nanosheets/carbon nanotubes composites and application of anode materials for lithium-ion batteries. *Electrochim. Acta* **2016**, *204*, 92-99.
118. Fang, W.; Zuo, P. J.; Ma, Y. L.; Cheng, X. Q.; Liao, L. X.; Yin, G. P. Facile preparation of $Li_4Ti_5O_{12}$/AB/MWCNTs composite with high-rate performance for lithium ion battery. *Electrochim. Acta* **2013**, *94*, 294-299.
119. Ni, H. F.; Fan, L. Z. Nano-$Li_4Ti_5O_{12}$ anchored on carbon nanotubes by liquid phase deposition as anode material for high rate lithium-ion batteries. *J. Power Sources* **2012**, *214*, 195-199.
120. Shen, L. F.; Yuan, C. Z.; Luo, H. J.; Zhang, X. G.; Xu, K.; Zhang, F. In situ growth of $Li_4Ti_5O_{12}$ on multi-walled carbon nanotubes: novel coaxial nanocables for high rate lithium ion batteries. *J. Mater. Chem.* **2011**, *21*, 761-767.
121. Ernzerhof, M.; Scuseria, G. E. Assessment of the Perdew-Burke-Ernzerhof exchange-correlation functional. *J. Chem. Phys.* **1999**, *110*, 5029-5036.
122. Adamo, C.; Barone, V. Toward reliable density functional methods without adjustable parameters: The PBE0 model. *J. Chem. Phys.* **1999**, *110*, 6158-6170.
123. Rassolov, V. A.; Pople, J. A.; Ratner, M. A.; Windus, T. L. 6-31G* basis set for atoms K through Zn. *J. Chem. Phys.* **1998**, *109*, 1223-1229.
124. Qu, L. H.; Peng, X. G. Control of photoluminescence properties of CdSe nanocrystals in growth. *J. Am. Chem. Soc.* **2002**, *124*, 2049-2055.
125. Wang, L.; Han, J. K.; Zhu, Y. Q.; Zhou, R. P.; Jaye, C.; Liu, H. Q.; Li, Z. Q.; Taylor, G. T.; Fischer, D. A.; Appenzeller, J.; Wong, S. S. Probing the Dependence of Electron Transfer on Size and Coverage in Carbon Nanotube-Quantum Dot Heterostructures. *J. Phys. Chem. C* **2015**, *119*, 26327-26338.
126. Wang, L.; Han, J.; Sundahl, B.; Thornton, S.; Zhu, Y.; Zhou, R.; Jaye, C.; Liu, H.; Li, Z. Q.; Taylor, G. T.; Fischer, D. A.; Appenzeller, J.; Harrison, R. J.; Wong, S. S. Ligand-induced dependence of charge transfer in nanotube-quantum dot heterostructures. *Nanoscale* **2016,** *in press*.
127. Byrappa, K.; Adschiri, T. Hydrothermal technology for nanotechnology. *Prog. Cryst. Growth Charact. Mater.* **2007**, *53*, 117-166.
128. Sankaraiah, S.; Lee, J. M.; Kim, J. H.; Choi, S. W. Preparation and characterization of surface-functionalized polysilsesquioxane hard spheres in aqueous medium. *Macromolecules* **2008**, *41*, 6195-6204.

129. Noda, I.; Kamoto, T.; Yamada, M. Size-controlling synthesis of narrowly distributed particles of methylsilsesquioxane derivatives. *Chem. Mater.* **2000**, *12*, 1708-1714.
130. Asenath-Smith, E.; Chen, W. How To Prevent the Loss of Surface Functionality Derived from Aminosilanes. *Langmuir* **2008**, *24*, 12405-12409.
131. Stanjek, H.; Hausler, W. Basics of X-ray diffraction. *Hyperfine Interact.* **2004**, *154*, 107-119.
132. Nellist, P. Seeing with electrons. *Physics World* **2005**, *18*, 24-29.
133. An Introduction to Electron Microscopy booklet *FEI company*.
134. A Beginners Guide Thermogravimetric Analysis (TGA). *PerkinElmer*, 1-19.
135. Brunauer, S.; Emmett, P. H.; Teller, E. Adsorption of gases in multimolecular layers. *J. Am. Chem. Soc.* **1938**, *60*, 309-319.
136. Langmuir, I. The Adsorption of Gases on Plane Surfaces of Glass, Mica and Platimum. *J. Am. Chem. Soc.* **1918**, *40*, 1361-1403.
137. Brunauer, S.; Deming, L. S.; Deming, W. E.; Teller, E. On a theory of the van der Waals adsorption of gases. *J. Am. Chem. Soc.* **1940**, *62*, 1723-1732.
138. Giessibl, F. J. Advances in atomic force microscopy. *Rev. Mod. Phys.* **2003**, *75*, 949-983.
139. Dufrene, Y. F. AFM for nanoscale microbe analysis. *Analyst* **2008**, *133*, 297-301.
140. Zhong, Q.; Inniss, D.; Kjoller, K.; Elings, V. B. Fractured Polymer Silica Fiber Surface Studied by Tapping Mode Atomic-Force Microscopy. *Surf. Sci.* **1993**, *290*, L688-L692.
141. Schultz, C. P. Precision infrared spectroscopic imaging: The future of FT-IR spectroscopy. *Spectroscopy* **2001**, *16*, 24.
142. Brault, J. W. New approach to high-precision Fourier transform spectrometer design. *Appl. Opt.* **1996**, *35*, 2891-2896.
143. Kloprogge, J. T. Short introduction to infrared and Raman spectroscopy. *Application of Vibrational Spectroscopy to Clay Minerals and Layered Double Hydroxides* **2005**, *13*, 1-7.
144. Dresselhaus, M. S.; Dresselhaus, G.; Saito, R.; Jorio, A. Raman spectroscopy of carbon nanotubes. *Physics Reports-Review Section of Physics Letters* **2005**, *409*, 47-99.
145. Souza, A. G.; Jorio, A.; Samsonidze, G. G.; Dresselhaus, G.; Saito, R.; Dresselhaus, M. S. Raman spectroscopy for probing chemically/physically induced phenomena in carbon nanotubes. *Nanotechnology* **2003**, *14*, 1130-1139.
146. Rauf, H.; Pichler, T.; Pfeiffer, R.; Simon, F.; Kuzmany, H.; Popov, V. N. Detailed analysis of the Raman response of n-doped double-wall carbon nanotubes. *Phys. Rev. B* **2006**, *74*, 235419.
147. Mayerhöfer, T. G.; Mutschke, H.; Popp, J. Employing Theories Far beyond Their Limits—The Case of the (Boguer-) Beer–Lambert Law. *ChemPhysChem* **2016**, *17*, 1948-1955.
148. Gilliland, G. D. Photoluminescence spectroscopy of crystalline semiconductors. *Materials Science & Engineering R-Reports* **1997**, *18*, 99-399.
149. Hahner, G. Near edge X-ray absorption fine structure spectroscopy as a tool to probe electronic and structural properties of thin organic films and liquids. *Chem. Soc. Rev.* **2006**, *35*, 1244-1255.
150. De Jesus, L. R.; Dennis, R. V.; Depner, S. W.; Jaye, C.; Fischer, D. A.; Banerjee, S. Inside and Outside: X-ray Absorption Spectroscopy Mapping of Chemical Domains in Graphene Oxide. *J. Phys. Chem. Lett.* **2013**, *4*, 3144-3151.
151. Kuznetsova, A.; Popova, I.; Yates, J. T.; Bronikowski, M. J.; Huffman, C. B.; Liu, J.; Smalley, R. E.; Hwu, H. H.; Chen, J. G. G. Oxygen-containing functional groups on single-wall

carbon nanotubes: NEXAFS and vibrational spectroscopic studies. *J. Am. Chem. Soc.* **2001**, *123*, 10699-10704.
152. Wang, Z.; Wu, L.; Zhou, J.; Cai, W.; Shen, B.; Jiang, Z. Magnetite Nanocrystals on Multiwalled Carbon Nanotubes as a Synergistic Microwave Absorber. *J. Phys. Chem. C* **2013**, *117*, 5446-5452.
153. Perez-Dieste, V.; Castellini, O. M.; Crain, J. N.; Eriksson, M. A.; Kirakosian, A.; Lin, J. L.; McChesney, J. L.; Himpsel, F. J.; Black, C. T.; Murray, C. B. Thermal decomposition of surfactant coatings on Co and Ni nanocrystals. *Appl. Phys. Lett.* **2003**, *83*, 5053-5055.
154. Hemraj-Benny, T.; Banerjee, S.; Sambasivan, S.; Balasubramanian, M.; Fischer, D. A.; Eres, G.; Puretzky, A. A.; Geohegan, D. B.; Lowndes, D. H.; Han, W. Q.; Misewich, J. A.; Wong, S. S. Near-edge X-ray absorption fine structure spectroscopy as a tool for investigating nanomaterials. *Small* **2006**, *2*, 26-35.
155. Winter, A. D.; Larios, E.; Alamgir, F. M.; Jaye, C.; Fischer, D. A.; Omastova, M.; Campo, E. M. Thermo-Active Behavior of Ethylene-Vinyl Acetate I Multiwall Carbon Nanotube Composites Examined by in Situ near-Edge X-ray Absorption Fine-Structure Spectroscopy. *J. Phys. Chem. C* **2014**, *118*, 3733-3741.
156. Zaumseil, J.; Sirringhaus, H. Electron and ambipolar transport in organic field-effect transistors. *Chem. Rev.* **2007**, *107*, 1296-1323.
157. Cai, X. Y.; Burand, M. W.; Newman, C. R.; da Silva, D. A.; Pappenfus, T. M.; Bader, M. M.; Bredas, J. L.; Mann, K. R.; Frisbie, C. D. N- and P-channel transport behavior in thin film transistors based on tricyanovinyl-capped oligothiophenes. *J. Phys. Chem. B* **2006**, *110*, 14590-14597.
158. Warszawski, E.; Adler, J.; Hoffman, A.; Silverman, A. Experiment (NEXAFS) versus simulation (DOS) for carbon allotropes. *Proceedings of the 22th Workshop on Computer Simulation Studies in Condensed Matter Physics* **2010**, *3*, 1381-1385.
159. Qian, X.; Sambe, H.; Ramaker, D. E. Theoretical study on Cl L_{23} NEXAFS and UV absorption data for metal chlorides. *Phys. Rev. B* **1995**, *52*, 15115-15121.
160. Voloshina, E.; Ovcharenko, R.; Shulakov, A.; Dedkov, Y. Theoretical description of X-ray absorption spectroscopy of the graphene-metal interfaces. *J. Chem. Phys.* **2013**, *138*, 154706.
161. Schultz, B. J.; Jaye, C.; Lysaght, P. S.; Fischer, D. A.; Prendergast, D.; Banerjee, S. On chemical bonding and electronic structure of graphene-metal contacts. *Chem. Sci.* **2013**, *4*, 494-502.
162. Harrison, N. A. An introduction to density functional theory. *Comput. Mater. Sci.* **2003**, *187*, 45-70.
163. Valiev, M.; Bylaska, E. J.; Govind, N.; Kowalski, K.; Straatsma, T. P.; Van Dam, H. J. J.; Wang, D.; Nieplocha, J.; Apra, E.; Windus, T. L.; de Jong, W. A. NWChem: A comprehensive and scalable open-source solution for large scale molecular simulations. *Comput. Phys. Commun.* **2010**, *181*, 1477-1489.
164. Brouwer, A. M. Standards for photoluminescence quantum yield measurements in solution (IUPAC Technical Report). *Pure Appl. Chem.* **2011**, *83*, 2213-2228.
165. Ravel, B.; Newville, M. ATHENA, ARTEMIS, HEPHAESTUS: data analysis for X-ray absorption spectroscopy using IFEFFIT. *J. Synchrotron Rad.* **2005**, *12*, 537-541.
166. Prendergast, D.; Galli, G. X-ray absorption spectra of water from first principles calculations. *Phys. Rev. Lett.* **2006**, *96*, 215502.
167. Momma, K. I., F. VESTA 3 for three-dimensional visualization ofcrystal, volumetric and morphology data. *J. Appl. Cryst.* **2011**, *44*, 1272-1276.

168. Humphrey, W.; Dalke, A.; Schulten, K. VMD: Visual molecular dynamics. *J. Mol. Graphics* **1996**, *14*, 33-38.
169. Hanwell, M. D.; Curtis, D. E.; Lonie, D. C.; Vandermeersch, T.; Zurek, E.; Hutchison, G. R. Avogadro: an advanced semantic chemical editor, visualization, and analysis platform. *J. Cheminformatics* **2012**, *4*, 17-33.
170. Xu, Y. N.; Ching, W. Y. Electronic, Optical, and Structural-Properties of Some Wurtzite Crystals. *Phys. Rev. B* **1993**, *48*, 4335-4351.
171. Kasuya, A.; Sivamohan, R.; Barnakov, Y. A.; Dmitruk, I. M.; Nirasawa, T.; Romanyuk, V. R.; Kumar, V.; Mamykin, S. V.; Tohji, K.; Jeyadevan, B.; Shinoda, K.; Kudo, T.; Terasaki, O.; Liu, Z.; Belosludov, R. V.; Sundararajan, V.; Kawazoe, Y. Ultra-stable nanoparticles of CdSe revealed from mass spectrometry. *Nat. Mater.* **2004**, *3*, 99-102.
172. Banerjee, S.; Wong, S. S. Synthesis and Characterization of Carbon Nanotube-Nanocrystal Heterostructures. *Nano Lett.* **2002**, *2*, 195-200.
173. Banerjee, S.; Wong, S. S. In Situ Quantum Dot Growth on Multiwalled Carbon Nanotubes. *J. Am. Chem. Soc* **2003**, *125*, 10342-10350.
174. Banerjee, S.; Wong, S. S. In Situ Growth of 'Fused', Ozonized Single-Walled Carbon Nanotube - Quantum Dot Junctions. *Adv. Mater.* **2004**, *16*, 34-37.
175. Banerjee, S.; Wong, S. S. Formation of CdSe nanocrystals onto oxidized, ozonized single-walled carbon nanotube surfaces. *Chem. Commun.* **2004**, *(16)*, 1866-1867.
176. Peng, X.; Wong, S. S. Controlling Nanocrystal Density and Location on Carbon Nanotube Templates. *Chem. Mater.* **2009**, *21*, 682-694.
177. Robel, I.; Bunker, B. A.; Kamat, P. V. Single-walled carbon nanotube-CdS nanocomposites as light-harvesting assemblies: Photoinduced charge-transfer interactions. *Adv. Mater.* **2005**, *17*, 2458-2463.
178. Cho, N.; Choudhury, K. R.; Thapa, R. B.; Sahoo, Y.; Ohulchanskyy, T.; Cartwright, A. N.; Lee, K. S.; Prasad, P. N. Efficient photodetection at IR wavelengths by incorporation of PbSe-carbon-nanotube conjugates in a polymeric nanocomposite. *Adv. Mater.* **2007**, *19*, 232-236.
179. Kongkanand, A.; Dominguez, R. M.; Kamat, P. V. Single wall carbon nanotube scaffolds for photoelectrochemical solar cells. Capture and transport of photogenerated electrons. *Nano Lett* **2007**, *7*, 676-680.
180. Vietmeyer, F.; Seger, B.; Kamat, P. V. Anchoring ZnO particles on functionalized single wall carbon nanotubes. Excited state interactions and charge collection. *Adv. Mater.* **2007**, *19*, 2935-2940.
181. Banerjee, S.; Wong, S. S. In situ growth of "fused", ozonized single-walled carbon nanotube - CdTe quantum dot junctions". *Adv. Mater.* **2004**, *16*, 34-37.
182. Biju, V.; Itoh, T.; Baba, Y.; Ishikawa, M. Quenching of photoluminescence in conjugates of quantum dots and single-walled carbon nanotube. *J. Phys. Chem. B* **2006**, *110*, 26068-26074.
183. Tison, Y.; Giusca, C. E.; Stolojan, V.; Hayashi, Y.; Silva, S. R. P. The inner shell influence on the electronic structure of double-walled carbon nanotubes. *Adv. Mater.* **2008**, *20*, 189-194.
184. Hashimoto, A.; Suenaga, K.; Urita, K.; Shimada, T.; Sugai, T.; Bandow, S.; Shinohara, H.; Iijima, S. Atomic correlation between adjacent graphene layers in double-wall carbon nanotubes. *Phys. Rev. Lett.* **2005**, *94*, 45504.

185. Bouilly, D.; Cabana, J.; Meunier, F.; Desjardins-Carriere, M.; Lapointe, F.; Gagnon, P.; Larouche, F. L.; Adam, E.; Paillet, M.; Martel, R. Wall-selective probing of double-walled carbon nanotubes using covalent functionalization. *ACS Nano* **2011**, *5*, 4927-4934.
186. Peng, X.; Sfeir, M. Y.; Zhang, F.; Misewich, J. A.; Wong, S. S. Covalent Synthesis and Optical Characterization of Double-walled Carbon Nanotube-Nanocrystal Heterostructures. *J. Phys. Chem. C* **2010**, *114*, 8766-8733.
187. Jeong, S.; Shim, H. C.; Kim, S.; Han, C. S. Efficient electron transfer in functional assemblies of pyridine-modified NQDs on SWNTs. *ACS Nano* **2010**, *4*, 324-330.
188. Li, Q.; Sun, B.; Kinloch, I. A.; Zhi, D.; Sirringhaus, H.; Windle, A. H. Enhanced Self-Assembly of Pyridine-Capped CdSe Nanocrystals on Individual Single-Walled Carbon Nanotubes. *Chem. Mater.* **2005**, *18*, 164-168.
189. Schulz-Drost, C.; Sgobba, V.; Gerhards, C.; Leubner, S.; Krick Calderon, R. M.; Ruland, A.; Guldi, D. M. Innovative inorganic-organic nanohybrid materials: coupling quantum dots to carbon nanotubes. *Angew. Chem. Int. Ed.* **2010**, *49*, 6425-6429.
190. Williams, R. J.; Lipowska, M.; Patonay, G.; Strekowski, L. Comparison of covalent and noncovalent labeling with near-infrared dyes for the high-performance liquid chromatographic determination of human serum albumin. *Anal. Chem.* **1993**, *65*, 601-605.
191. Debgupta, J.; Pillai, V. K. Thiolated graphene - a new platform for anchoring CdSe quantum dots for hybrid heterostructures. *Nanoscale* **2013**, *5*, 3615-3619.
192. Chen, G. G.; Bandow, S.; Margine, E. R.; Nisoli, C.; Kolmogorov, A. N.; Crespi, V. H.; Gupta, R.; Sumanasekera, G. U.; Iijima, S.; Eklund, P. C. Chemically doped double-walled carbon nanotubes: Cylindrical molecular capacitors. *Phys. Rev. Lett.* **2003**, *90*, 257403.
193. do Nascimento, G. M.; Hou, T.; Kim, Y. A.; Muramatsu, H.; Hayashi, T.; Endo, M.; Akuzawa, N.; Dresselhaus, M. S. Double-wall carbon nanotubes doped with different Br_2 doping levels: a resonance Raman study. *Nano Lett* **2008**, *8*, 4168-4172.
194. do Nascimento, G. M.; Hou, T.; Kim, Y. A.; Muramatsu, H.; Hayashi, T.; Endo, M.; Akuzawa, N.; Dresselhaus, M. S. Comparison of the Resonance Raman Behavior of Double-Walled Carbon Nanotubes Doped with Bromine or Iodine Vapors. *J. Phys. Chem. C* **2009**, *113*, 3934-3938.
195. Cambedouzou, J.; Sauvajol, J. L.; Rahmani, A.; Flahaut, E.; Peigney, A.; Laurent, C. Raman spectroscopy of iodine-doped double-walled carbon nanotubes. *Phys. Rev. B* **2004**, *69*, 235422.
196. do Nascimento, G. M.; Hou, T.; Kim, Y. A.; Muramatsu, H.; Hayashi, T.; Endo, M.; Akuzawa, N.; Dresselhaus, M. S. Behavior of the high frequency Raman modes of double-wall carbon nanotubes after doping with bromine or iodine vapors. *Carbon* **2011**, *49*, 3585-3596.
197. Souza, A. G.; Endo, M.; Muramatsu, H.; Hayashi, T.; Kim, Y. A.; Barros, E. B.; Akuzawa, N.; Samsonidze, G. G.; Saito, R.; Dresselhaus, M. S. Resonance Raman scattering studies in Br_2-adsorbed double-wall carbon nanotubes. *Phys. Rev. B* **2006**, *73*, 235413.
198. Akey, A. J.; Lu, C. G.; Wu, L. J.; Zhu, Y. M.; Herman, I. P. Anomalous photoluminescence Stokes shift in CdSe nanoparticle and carbon nanotube hybrids. *Phys. Rev. B* **2012**, *85*, 045404.
199. Guyot-Sionnest, P.; Wehrenberg, B.; Yu, D. Intraband relaxation in CdSe nanocrystals and the strong influence of the surface ligands. *J. Chem. Phys.* **2005**, *123*, 074709.
200. Wang, X. Y.; Qu, L. H.; Zhang, J. Y.; Peng, X. G.; Xiao, M. Surface-related emission in highly luminescent CdSe quantum dots. *Nano Lett* **2003**, *3*, 1103-1106.

201. Peng, X. H.; Misewich, J. A.; Wong, S. S.; Sfeir, M. Y. Efficient Charge Separation in Multidimensional Nanohybrids. *Nano Lett.* **2011**, *11*, 4562-4568.
202. Osswald, S.; Flauhaut, E.; Ye, H.; Gogotsi, Y. Elimination of D-band in Raman spectra of double-wall carbon nanotubes by oxidation. *Chem. Phys. Lett.* **2005**, *402*, 422-427.
203. Gyeong Bok, J.; Yoon, M.; Park, J.; Inhee, M.; Joo-Hiuk, S. In *Terahertz spectroscopy of platinum, copper sulfide, and tin oxide nanocrystals-carbon nanotube hybrid nanostructures*, Infrared, Millimeter, and Terahertz Waves, 2009. IRMMW-THz 2009. 34th International Conference on, 21-25 Sept. 2009; 2009; pp 1-2.
204. Campidelli, S.; Sooambar, C.; Lozano Diz, E.; Ehli, C.; Guldi, D. M.; Prato, M. Dendrimer-Functionalized Single-Wall Carbon Nanotubes: Synthesis, Characterization, and Photoinduced Electron Transfer. *J Am Chem Soc* **2006**, *128*, 12544-12552.
205. Rahmani, A.; Sauvajol, J. L.; Rols, S.; Benoit, C. Nonresonant Raman spectrum in infinite and finite single-wall carbon nanotubes. *Phys. Rev. B* **2002**, *66*, 125404.
206. Panchakarla, L. S.; Govindaraj, A.; Rao, C. N. R. Nitrogen- and Boron-doped double-walled carbon nanotubes. *ACS Nano* **2007**, *1*, 494-500.
207. Panchakarla, L. S.; Govindaraj, A.; Rao, C. N. R. Boron- and nitrogen-doped carbon nanotubes and graphene. *Inorg. Chim. Acta.* **2010**, *363*, 4163-4174.
208. Martinez, M. T.; Callejas, M. A.; Benito, A. M.; Cochet, M.; Seeger, T.; Anson, A.; Schreiber, J.; Gordon, C.; Marhic, C.; Chauvet, O.; Fierro, J. L. G.; Maser, W. Sensitivity of single-walled carbon nanotubes to oxidative processing: structural modification, intercalation, and functionalisation. *Carbon* **2003**, *41*, 2247-2256.
209. Ellis, A. V.; Bubendorfer, A. Raman scattering analysis of changes induced by chemical treatment of double-walled carbon nanotubes. *Chem. Phys. Lett.* **2005**, *412*, 449-453.
210. Kong, J.; Dai, H. Full and Modulated Chemical Gating of Individual Carbon Nanotubes by Organic Amine Compounds. *J. Phys. Chem. B* **2001**, *105*, 2890-2893.
211. do Nascimento, G. M.; Hou, T.; Kim, Y. A.; Muramatsu, H.; Hayashi, T.; Endo, M.; Akuzawa, N.; Dresselhaus, M. S. Double-Wall Carbon Nanotubes Doped with Different Br_2 Doping Levels: A Resonance Raman Study. *Nano Lett* **2008**, *8*, 4168-4172.
212. Chen, G. G.; Bandow, S.; Margine, E. R.; Nisoli, C.; Kolmogorov, A. N.; Crespi, V. H.; Gupta, R.; Sumanasekera, G. U.; Iijima, S.; Eklund, P. C. Chemically doped double-walled carbon nanotubes: Cylindrical molecular capacitors. *Phys. Rev. Lett.* **2003**, *90*, 257403.
213. Li, X.; Jia, Y.; Cao, A. Tailored Single-Walled Carbon Nanotube−CdS Nanoparticle Hybrids for Tunable Optoelectronic Devices. *ACS Nano* **2009**, *4*, 506-512.
214. Baranov, A. V.; Rakovich, Y. P.; Donegan, J. F.; Perova, T. S.; Moore, R. A.; Talapin, D. V.; Rogach, A. L.; Masumoto, Y.; Nabiev, I. Effect of ZnS shell thickness on the phonon spectra in CdSe quantum dots. *Phys. Rev. B* **2003**, *68*, 165306.
215. Souza, A. G.; Endo, M.; Muramatsu, H.; Hayashi, T.; Kim, Y. A.; Barros, E. B.; Akuzawa, N.; Samsonidze, G. G.; Saito, R.; Dresselhaus, M. S. Resonance Raman scattering studies in Br-2-adsorbed double-wall carbon nanotubes. *Phys. Rev. B* **2006**, *73*, 235413.
216. Wang, D. F.; Baral, J. K.; Zhao, H. G.; Gonfa, B. A.; Truong, V. V.; El Khakani, M. A.; Izquierdo, R.; Ma, D. L. Controlled Fabrication of PbS Quantum-Dot/Carbon-Nanotube Nanoarchitecture and its Significant Contribution to Near-Infrared Photon-to-Current Conversion. *Adv. Funct. Mater.* **2011**, *21*, 4010-4018.
217. Reiss, P.; Protiere, M.; Li, L. Core/Shell Semiconductor Nanocrystals. *Small* **2009**, *5*, 154-168.

218. Zhang, L. H.; Shi, E. Z.; Li, Z.; Li, P. X.; Jia, Y.; Ji, C. Y.; Wei, J. Q.; Wang, K. L.; Zhu, H. W.; Wu, D. H.; Cao, A. Y. Wire-supported CdSe nanowire array photoelectrochemical solar cells. *Phys. Chem. Chem. Phys.* **2012**, *14*, 3583-3588.
219. Peng, X. H.; Sfeir, M. Y.; Zhang, F.; Misewich, J. A.; Wong, S. S. Covalent Synthesis and Optical Characterization of Double-Walled Carbon Nanotube-Nanocrystal Heterostructures. *J. Phys. Chem. C* **2010**, *114*, 8766-8773.
220. Banerjee, S.; Wong, S. S. Formation of CdSe nanocrystals onto oxidized, ozonized single-walled carbon nanotube surfaces. *Chem. Commun.***2004**, 1866-1867.
221. Ning, Z.; Voznyy, O.; Pan, J.; Hoogland, S.; Adinolfi, V.; Xu, J.; Li, M.; Kirmani, A. R.; Sun, J.-P.; Minor, J.; Kemp, K. W.; Dong, H.; Rollny, L.; Labelle, A.; Carey, G.; Sutherland, B.; Hill, I.; Amassian, A.; Liu, H.; Tang, J.; Bakr, O. M.; Sargent, E. H. Air-stable n-type colloidal quantum dot solids. *Nat. Mater.* **2014**, *13*, 822-828.
222. Fischer, A.; Rollny, L.; Pan, J.; Carey, G. H.; Thon, S. M.; Hoogland, S.; Voznyy, O.; Zhitomirsky, D.; Kim, J. Y.; Bakr, O. M.; Sargent, E. H. Directly Deposited Quantum Dot Solids Using a Colloidally Stable Nanoparticle Ink. *Adv. Mater.* **2013**, *25*, 5742.
223. Anderson, N. C.; Hendricks, M. P.; Choi, J. J.; Owen, J. S. Ligand Exchange and the Stoichiometry of Metal Chalcogenide Nanocrystals: Spectroscopic Observation of Facile Metal-Carboxylate Displacement and Binding. *J. Am. Chem. Soc.* **2013**, *135*, 18536-18548.
224. Mora-Sero, I.; Bertoluzzi, L.; Gonzalez-Pedro, V.; Gimenez, S.; Fabregat-Santiago, F.; Kemp, K. W.; Sargent, E. H.; Bisquert, J. Selective contacts drive charge extraction in quantum dot solids via asymmetry in carrier transfer kinetics *Nat. Commun.* **2013**, *4*, 2272.
225. Tang, J.; Kemp, K. W.; Hoogland, S.; Jeong, K. S.; Liu, H.; Levina, L.; Furukawa, M.; Wang, X. H.; Debnath, R.; Cha, D. K.; Chou, K. W.; Fischer, A.; Amassian, A.; Asbury, J. B.; Sargent, E. H. Colloidal-quantum-dot photovoltaics using atomic-ligand passivation. *Nat. Mater.* **2011**, *10*, 765-771.
226. Wang, L.; Han, J.; Hoy, J.; Hu, F.; Liu, H. Q.; Gentleman, M. M.; Sfeir, M. Y.; Misewich, J. A.; Wong, S. S. Probing differential optical and coverage behavior in nanotube-nanocrystal heterostructures synthesized by covalent versus non-covalent approaches. *Dalton Trans.* **2014**, *43*, 7480-7490.
227. Liu, I. S.; Lo, H.-H.; Chien, C.-T.; Lin, Y.-Y.; Chen, C.-W.; Chen, Y.-F.; Su, W.-F.; Liou, S.-C. Enhancing photoluminescence quenching and photoelectric properties of CdSe quantum dots with hole accepting ligands. *J. Mater. Chem.* **2008**, *18*, 675-682.
228. Wuister, S. F.; de Mello Donegá, C.; Meijerink, A. Influence of Thiol Capping on the Exciton Luminescence and Decay Kinetics of CdTe and CdSe Quantum Dots. *J. Phys. Chem. B* **2004**, *108*, 17393-17397.
229. Yu, K.; Lu, G.; Chen, K.; Mao, S.; Kim, H.; Chen, J. Controllable photoelectron transfer in CdSe nanocrystal-carbon nanotube hybrid structures. *Nanoscale* **2012**, *4*, 742-746.
230. Hines, D. A.; Forrest, R. P.; Corcelli, S. A.; Kamat, P. V. Predicting the Rate Constant of Electron Tunneling Reactions at the CdSe-TiO_2 Interface. *J. Phys. Chem. B* **2015,** *119*, 7439–7446.
231. Weaver, J. E.; Dasari, M. R.; Datar, A.; Talapatra, S.; Kohli, P. Investigating Photoinduced Charge Transfer in Carbon Nanotube-Perylene-Quantum Dot Hybrid Nanocomposites. *ACS Nano* **2010**, *4*, 6883-6893.
232. Zhu, N.; Zheng, K.; Karki, K. J.; Abdellah, M.; Zhu, Q.; Carlson, S.; Haase, D.; Žídek, K.; Ulstrup, J.; Canton, S. E.; Pullerits, T.; Chi, Q. Sandwiched confinement of quantum dots in

graphene matrix for efficient electron transfer and photocurrent production. *Sci. Rep.* **2015**, *5*, 9860.
233. Zhou, J. G.; Fang, H. T.; Maley, J. M.; Ko, J. Y. P.; Murphy, M.; Chu, Y.; Sammynaiken, R.; Sham, T. K. An X-ray Absorption, Photoemission, and Raman Study of the Interaction between SnO_2 Nanoparticle and Carbon Nanotube. *J. Phys. Chem. C* **2009**, *113*, 6114-6117.
234. Koroteev, V. O.; Bulusheva, L. G.; Asanov, I. P.; Shlyakhova, E. V.; Vyalikh, D. V.; Okotrub, A. V. Charge Transfer in the MoS_2/Carbon Nanotube Composite. *J. Phys. Chem. C* **2011**, *115*, 21199-21204.
235. Yueh, C. L.; Jan, J. C.; Chiou, J. W.; Pong, W. F.; Tsai, M. H.; Chang, Y. K.; Chen, Y. Y.; Lee, Y. F.; Tseng, P. K.; Wei, S. L.; Wen, C. Y.; Chen, L. C.; Chen, K. H. Electronic structure of the Fe-layer-catalyzed carbon nanotubes studied by x-ray-absorption spectroscopy. *Appl. Phys. Lett.* **2001**, *79*, 3179-3181.
236. Li, Y. F.; Hatakeyama, R.; Kaneko, T.; Izumida, T.; Okada, T.; Kato, T. Synthesis and electronic properties of ferrocene-filled double-walled carbon nanotubes. *Nanotechnology* **2006**, *17*, 4143-4147.
237. Zhang, L. H.; Jia, Y.; Wang, S. S.; Li, Z.; Ji, C. Y.; Wei, J. Q.; Zhu, H. W.; Wang, K. L.; Wu, D. H.; Shi, E. Z.; Fang, Y.; Cao, A. Y. Carbon Nanotube and CdSe Nanobelt Schottky Junction Solar Cells. *Nano Lett.* **2010**, *10*, 3583-3589.
238. Bang, J. H.; Kamat, P. V. Quantum Dot Sensitized Solar Cells. A Tale of Two Semiconductor Nanocrystals: CdSe and CdTe. *ACS Nano* **2009**, *3*, 1467-1476.
239. Bolotin, K. I.; Sikes, K. J.; Jiang, Z.; Klima, M.; Fudenberg, G.; Hone, J.; Kim, P.; Stormer, H. L. Ultrahigh electron mobility in suspended graphene. *Solid State Commun.* **2008**, *146*, 351-355.
240. Zhao, J.; Cao, M.; Cheng, B.; Wu, G.; Guo, H.; Ai, Y.; Su, X.; Xiao, Y.; Lei, S. Carbon-encapsulated CdSe quantum dot inorganic hybrid nanobelts for high performance photoelectronic devices based on the efficient separation and transfer of photoinduced holes. *J. Mater. Chem. C* **2015**, *3*, 2471-2478.
241. Liu, C.; Lee, S.; Su, D.; Zhang, Z.; Pfefferle, L.; Haller, G. L. Synthesis and Characterization of Nanocomposites with Strong Interfacial Interaction: Sulfated ZrO_2 Nanoparticles Supported on Multiwalled Carbon Nanotubes. *J. Phys. Chem. C* **2012**, *116*, 21742-21752.
242. Banerjee, S.; Hemraj-Benny, T.; Balasubramanian, M.; Fischer, D. A.; Misewich, J. A.; Wong, S. S. Surface chemistry and structure of purified, ozonized, multiwalled carbon nanotubes probed by NEXAFS and vibrational spectroscopies. *ChemPhysChem* **2004**, *5*, 1416-1422.
243. Leon, V.; Parret, R.; Almairac, R.; Alvarez, L.; Babaa, M. R.; Doyle, B. P.; Ienny, P.; Parent, P.; Zahab, A.; Bantignies, J. L. Spectroscopic study of double-walled carbon nanotube functionalization for preparation of carbon nanotube/epoxy composites. *Carbon* **2012**, *50*, 4987-4994.
244. Lee, J. R. I.; Meulenberg, R. W.; Hanif, K. M.; Mattoussi, H.; Klepeis, J. E.; Terminello, L. J.; van Buuren, T. Experimental observation of quantum confinement in the conduction band of CdSe quantum dots. *Phys. Rev. Lett.* **2007**, *98*.
245. Wright, J. T.; Meulenberg, R. W. Modification of the conduction band edge energy via hybridization in quantum dots. *Appl. Phys. Lett.* **2012**, *101*, 193104.
246. Leon, V.; Parret, R.; Almairac, R.; Alvarez, L.; Babaa, M. R.; Doyle, B. P.; Ienny, P.; Parent, P.; Zahab, A.; Bantignies, J. L. Spectroscopic study of double-walled carbon nanotube

functionalization for preparation of carbon nanotube / epoxy composites. *Carbon* **2012**, *50*, 4987-4994.
247. Liang, Y.; Wang, H.; Zhou, J.; Li, Y.; Wang, J.; Regier, T.; Dai, H. Covalent Hybrid of Spinel Manganese–Cobalt Oxide and Graphene as Advanced Oxygen Reduction Electrocatalysts. *J. Am. Chem. Soc.* **2012**, *134*, 3517-3523.
248. Marcus, R. A. On the Theory of Oxidation-Reduction Reactions Involving Electron Transfer .1. *J. Chem. Phys.* **1956**, *24*, 966-978.
249. Marcus, R. A. Chemical and Electrochemical Electron-Transfer Theory. *Annu. Rev. Phys. Chem.* **1964**, *15*, 155.
250. Tarafder, K.; Surendranath, Y.; Olshansky, J. H.; Alivisatos, A. P.; Wang, L. W. Hole Transfer Dynamics from a CdSe/CdS Quantum Rod to a Tethered Ferrocene Derivative. *J. Am. Chem. Soc.* **2014**, *136*, 5121-5131.
251. Tafen, D.; Prezhdo, O. V. Size and Temperature Dependence of Electron Transfer between CdSe Quantum Dots and a TiO_2 Nanobelt. *J. Phys. Chem. C* **2015**, *119*, 5639-5647.
252. Tvrdy, K.; Frantsuzov, P. A.; Kamat, P. V. Photoinduced electron transfer from semiconductor quantum dots to metal oxide nanoparticles. *Proc. Natl. Acad. Sci. U. S. A.* **2011**, *108*, 29-34.
253. Robel, I.; Kuno, M.; Kamat, P. V. Size-dependent electron injection from excited CdSe quantum dots into TiO_2 nanoparticles. *J. Am. Chem. Soc.* **2007**, *129*, 4136.
254. Meulenberg, R. W.; Lee, J. R.; Wolcott, A.; Zhang, J. Z.; Terminello, L. J.; van Buuren, T. Determination of the exciton binding energy in CdSe quantum dots. *ACS Nano* **2009**, *3*, 325-330.
255. Mintmire, J. W.; White, C. T. Electronic and structural properties of carbon nanotubes. *Carbon* **1995**, *33*, 893-902.
256. Shan, B.; Cho, K. First-principles study of work functions of double-wall carbon nanotubes. *Phys. Rev. B* **2006**, *73*, 081401.
257. Jasieniak, J.; Califano, M.; Watkins, S. E. Size-Dependent Valence and Conduction Band-Edge Energies of Semiconductor Nanocrystals. *ACS Nano* **2011**, *5*, 5888-5902.
258. Li, J.; Zhang, M. Atomic insights into adsorption of thiophenol derivatives as corrosion inhibitors for mild steel in hydrochloric acid solution. *Mater. Res. Innovations* **2014**, *18*, 38-42.
259. Kalimuthu, P.; Sivanesan, A.; John, S. A. Charge-transfer interaction of aromatic thiols with 2,3-dichloro-5,6-dicyano-p-benzoquinone: Spectral and quantum mechanical studies. *J. Phys. Chem. A* **2007**, *111*, 12086-12092.
260. Liu, Y.; Gibbs, M.; Puthussery, J.; Gaik, S.; Ihly, R.; Hillhouse, H. W.; Law, M. Dependence of Carrier Mobility on Nanocrystal Size and Ligand Length in PbSe Nanocrystal Solids. *Nano Lett.* **2010**, *10*, 1960-1969.
261. Wang, H.; McNellis, E. R.; Kinge, S.; Bonn, M.; Canovas, E. Tuning Electron Transfer Rates through Molecular Bridges in Quantum Dot Sensitized Oxides. *Nano Lett.* **2013**, *13*, 5311-5315.
262. Kongkanand, A.; Tvrdy, K.; Takechi, K.; Kuno, M.; Kamat, P. V. Quantum dot solar cells. Tuning photoresponse through size and shape control of CdSe-TiO_2 architecture. *J. Am. Chem. Soc.* **2008**, *130*, 4007-4015.
263. Osswald, S.; Flauhaut, E.; Ye, H.; Gogotsi, Y. Elimination of D-band in Raman spectra of double-wall carbon nanotubes by oxidation. *Chem. Phys. Lett.* **2005**, *402*, 422-427.
264. Kataura, H.; Kumazawa, Y.; Maniwa, Y.; Umezu, I.; Suzuki, S.; Ohtsuka, Y.; Achiba, Y. Optical properties of single-wall carbon nanotubes. *Synth. Met.* **1999**, *103*, 2555-2558.

265. Bandow, S.; Chen, G.; Sumanasekera, G. U.; Gupta, R.; Yudasaka, M.; Iijima, S.; Eklund, P. C. Diameter-selective resonant Raman scattering in double-wall carbon nanotubes. *Phys. Rev. B* **2002**, *66*, 075416.
266. Villalpando-Paez, F.; Son, H.; Nezich, D.; Hsieh, Y. P.; Kong, J.; Kim, Y. A.; Shimamoto, D.; Muramatsu, H.; Hayashi, T.; Endo, M.; Terrones, M.; Dresselhaus, M. S. Raman Spectroscopy Study of Isolated Double-Walled Carbon Nanotubes with Different Metallic and Semiconducting Configurations. *Nano Lett.* **2008**, *8*, 3879-3886.
267. Huynh, W. U.; Dittmer, J. J.; Teclemariam, N.; Milliron, D. J.; Alivisatos, A. P.; Barnham, K. W. J. Charge transport in hybrid nanorod-polymer composite photovoltaic cells. *Phys. Rev. B* **2003**, *67*.
268. Green, A. A.; Hersam, M. C. Properties and application of double-walled carbon nanotubes sorted by outer-wall electronic type. *ACS Nano* **2011**, *5*, 1459-1467.
269. Liu, K.; Wang, W.; Xu, Z.; Bai, X.; Wang, E.; Yao, Y.; Zhang, J.; Liu, Z. Chirality-dependent transport properties of double-walled nanotubes measured in situ on their field-effect transistors. *J. Am. Chem. Soc.* **2009**, *131*, 62-63.
270. Tison, Y.; Giusca, C. E.; Stolojan, V.; Hayashi, Y.; Silva, S. R. P. The inner shell influence on the electronic structure of double-walled carbon nanotubes. *Adv. Mater.* **2008**, *20*, 189-194.
271. Hashimoto, A.; Suenaga, K.; Urita, K.; Shimada, T.; Sugai, T.; Bandow, S.; Shinohara, H.; Iijima, S. Atomic correlation between adjacent graphene layers in double-wall carbon nanotubes. *Phys. Rev. Lett.* **2005**, *94*, 045504/045501-045504/045504.
272. Saito, R.; Matsuo, R.; Kimura, T.; Dresselhaus, G.; Dresselhaus, M. S. Anomalous potential barrier of double-wall carbon nanotube. *Chem. Phys. Lett.* **2001**, *348*, 187-193.
273. Wang, L.; Han, J.; Hoy, J.; Hu, F.; Liu, H.; Gentleman, M. M.; Sfeir, M. Y.; Misewich, J. A.; Wong, S. S. Probing differential optical and coverage behavior in nanotube-nanocrystal heterostructures synthesized by covalent versus non-covalent approaches. *Dalton Trans.* **2014**, *43*, 7480-7490.
274. Guo, S. R.; Bao, D. D.; Upadhyayula, S.; Wang, W.; Guvenc, A. B.; Kyle, J. R.; Hosseinibay, H.; Bozhilov, K. N.; Vullev, V. I.; Ozkan, C. S.; Ozkan, M. Photoinduced Electron Transfer Between Pyridine Coated Cadmium Selenide Quantum Dots and Single Sheet Graphene. *Adv. Funct. Mater.* **2013**, *23*, 5199-5211.
275. Munro, A. M.; Jen-La Plante, I.; Ng, M. S.; Ginger, D. S. Quantitative Study of the Effects of Surface Ligand Concentration on CdSe Nanocrystal Photoluminescence. *J. Phys. Chem. C* **2007**, *111*, 6220-6227.
276. Park, C.; Yoon, T. L-cysteine adsorption on thiol-coated quantum dot (QD) in aqueous solution: An implication on the QD speciation in biological media. *Toxicology and Environmental Health Sciences* **2009**, *1*, 151-158.
277. Qu, L.; Peng, X. Control of photoluminescence properties of CdSe nanocrystals in growth. *J. Am. Chem. Soc.* **2002**, *124*, 2049-2055.
278. Liu, I. S.; Lo, H.-H.; Chien, C.-T.; Lin, Y.-Y.; Chen, C.-W.; Chen, Y.-F.; Su, W.-F.; Liou, S.-C. Enhancing photoluminescence quenching and photoelectric properties of CdSe quantum dots with hole accepting ligands. *J. Mater. Chem.* **2008**, *18*, 675-682.
279. Katari, J. E. B.; Colvin, V. L.; Alivisatos, A. P. X-ray Photoelectron Spectroscopy of CdSe Nanocrystals with Applications to Studies of the Nanocrystal Surface. *J. Phys. Chem.* **1994**, *98*, 4109-4117.

280. Young, A. G.; McQuillan, A. J.; Green, D. P. In Situ IR Spectroscopic Studies of the Avidin−Biotin Bioconjugation Reaction on CdS Particle Films. *Langmuir* **2009**, *25*, 7416-7423.
281. Liu, C.; Lee, S.; Su, D.; Zhang, Z.; Pfefferle, L.; Haller, G. L. Synthesis and Characterization of Nanocomposites with Strong Interfacial Interaction: Sulfated ZrO_2 Nanoparticles Supported on Multiwalled Carbon Nanotubes. *J. Phys. Chem. C* **2012**, *116*, 21742-21752.
282. Wang, Z.; Wu, L.; Zhou, J.; Cai, W.; Shen, B.; Jiang, Z. Magnetite Nanocrystals on Multiwalled Carbon Nanotubes as a Synergistic Microwave Absorber. *J. Phys. Chem. C* **2013**, *117*, 5446-5452.
283. Lee, J. R. I.; Meulenberg, R. W.; Hanif, K. M.; Mattoussi, H.; Klepeis, J. E.; Terminello, L. J.; van Buuren, T. Experimental observation of quantum confinement in the conduction band of CdSe quantum dots. *Phys. Rev. Lett.* **2007**, *98*, 146803.
284. Wright, J. T.; Meulenberg, R. W. Modification of the conduction band edge energy via hybridization in quantum dots. *Appl. Phys. Lett.* **2012**, *101*, 193104.
285. Si, H. Y.; Liu, C. H.; Xu, H.; Wang, T. M.; Zhang, H. L. Shell-Controlled Photoluminescence in CdSe/CNT Nanohybrids. *Nanoscale Research Letters* **2009**, *4*, 1146-1152.
286. Ortiz, J. V. Electron-Affinity Calculations on NH_2-, PH_2-, CN-, SH-, OH-, Cl-, and F- - Basis-Sets and Direct Vs Indirect Methods. *J. Chem. Phys.* **1987**, *86*, 308-312.
287. Metzger, R. M. Unimolecular electrical rectifiers. *Chem. Rev.* **2003**, *103*, 3803-3834.
288. Bandow, S.; Chen, G.; Sumanasekera, G. U.; Gupta, R.; Yudasaka, M.; Iijima, S.; Eklund, P. C. Diameter-selective resonant Raman scattering in double-wall carbon nanotubes. *Phys. Rev. B* **2002**, *66*, 075416.
289. Rahmani, A.; Sauvajol, J. L.; Rols, S.; Benoit, C. Nonresonant Raman spectrum in infinite and finite single-wall carbon nanotubes. *Phys. Rev. B* **2002**, *66*, 125404.
290. Rauf, H.; Pichler, T.; Pfeiffer, R.; Simon, F.; Kuzmany, H.; Popov, V. N. Detailed analysis of the Raman response of n-doped double-wall carbon nanotubes. *Phys. Rev. B* **2006**, *74*, 235419.
291. Wang, L.; Han, J.; Zhu, Y.; Zhou, R.; Jaye, C.; Liu, H.; Li, Z.-Q.; Taylor, G. T.; Fischer, D. A.; Appenzeller, J.; Wong, S. S. Probing the Dependence of Electron Transfer on Size and Coverage in Carbon Nanotube–Quantum Dot Heterostructures. *J. Phys. Chem. C* **2015**, *119*, 26327-26338.
292. Liu, W. J.; Shao, D.; Luo, G. E.; Gao, Q. Z.; Yan, G. J.; He, J. R.; Chen, D. Y.; Yu, X. Y.; Fang, Y. P. Mesoporous Spinel $Li_4Ti_5O_{12}$ Nanoparticles for High Rate Lithium-ion Battery Anodes. *Electrochim. Acta* **2014**, *133*, 578-582.
293. Yi, T. F.; Jiang, L. J.; Shu, J.; Yue, C. B.; Zhu, R. S.; Qiao, H. B. Recent development and application of $Li_4Ti_5O_{12}$ as anode material of lithium ion battery. *J. Phys. Chem. Solids* **2010**, *71*, 1236-1242.
294. Yi, T.-F.; Yang, S.-Y.; Xie, Y. Recent advances of $Li_4Ti_5O_{12}$ as a promising next generation anode material for high power lithium-ion batteries. *J. Mater. Chem. A* **2015**, *3*, 5750-5777.
295. Lim, J.; Choi, E.; Mathew, V.; Kim, D.; Ahn, D.; Gim, J.; Kang, S. H.; Kim, J. Enhanced High-Rate Performance of $Li_4Ti_5O_{12}$ Nanoparticles for Rechargeable Li-Ion Batteries. *J. Electrochem. Soc.* **2011**, *158*, A275-A280.
296. Sun, L.; Wang, J. P.; Jiang, K. L.; Fan, S. S. Mesoporous $Li_4Ti_5O_{12}$ nanoclusters as high performance negative electrodes for lithium ion batteries. *J. Power Sources* **2014**, *248*, 265-272.

297. Shen, L. F.; Uchaker, E.; Zhang, X. G.; Cao, G. Z. Hydrogenated $Li_4Ti_5O_{12}$ Nanowire Arrays for High Rate Lithium Ion Batteries. *Adv. Mater.* **2012**, *24*, 6502-6506.
298. Liu, J.; Song, K. P.; van Aken, P. A.; Maier, J.; Yu, Y. Self-Supported $Li_4Ti_5O_{12}$-C Nanotube Arrays as High-Rate and Long-Life Anode Materials for Flexible Li-Ion Batteries. *Nano Lett.* **2014**, *14*, 2597-2603.
299. Chen, J. Z.; Yang, L.; Fang, S. H.; Tang, Y. F. Synthesis of sawtooth-like $Li_4Ti_5O_{12}$ nanosheets as anode materials for Li-ion batteries. *Electrochim. Acta* **2010**, *55*, 6596-6600.
300. Xia, H.; Luo, Z. T.; Xie, J. P. Nanostructured lithium titanate and lithium titanate/carbon nanocomposite as anode materials for advanced lithium-ion batteries. *Nanotechnology Reviews* **2014**, *3*, 161-175.
301. Kim, S.; Fang, S. H.; Zhang, Z. X.; Chen, J. Z.; Yang, L.; Penner-Hahn, J. E.; Deb, A. The electrochemical and local structural analysis of the mesoporous $Li_4Ti_5O_{12}$ anode. *J. Power Sources* **2014**, *268*, 294-300.
302. Tang, Y. F.; Yang, L.; Qiu, Z.; Huang, J. S. Preparation and electrochemical lithium storage of flower-like spinel $Li_4Ti_5O_{12}$ consisting of nanosheets. *Electrochem. Commun.* **2008**, *10*, 1513-1516.
303. Wu, F.; Li, X.; Wang, Z.; Guo, H. Petal-like $Li_4Ti_5O_{12}$-TiO_2 nanosheets as high-performance anode materials for Li-ion batteries. *Nanoscale* **2013**, *5*, 6936-6943.
304. Sha, Y. J.; Zhao, B. T.; Ran, R.; Cai, R.; Shao, Z. P. Synthesis of well-crystallized $Li_4Ti_5O_{12}$ nanoplates for lithium-ion batteries with outstanding rate capability and cycling stability. *J. Mater. Chem. A* **2013**, *1*, 13233-13243.
305. Li, G. C.; Xia, J.; Jiao, J. Q.; Chen, L. P.; Shen, P. K. Low-temperature Synthesis of Peony-like Spinel $Li_4Ti_5O_{12}$ as a High-performance Anode Material for Lithium Ion Batteries. *Chin. J. Chem.* **2011**, *29*, 1824-1828.
306. Hasegawa, G.; Kanamori, K.; Kiyomura, T.; Kurata, H.; Nakanishi, K.; Abe, T. Hierarchically Porous $Li_4Ti_5O_{12}$ Anode Materials for Li- and Na-Ion Batteries: Effects of Nanoarchitectural Design and Temperature Dependence of the Rate Capability. *Adv. Energy Mater.* **2015**, *5*, 1400730.
307. Guo, J.; Zuo, W.; Cai, Y.; Chen, S.; Zhang, S.; Liu, J. A novel $Li_4Ti_5O_{12}$-based high-performance lithium-ion electrode at elevated temperature. *J. Mater. Chem. A* **2015**, *3*, 4938-4944.
308. Mao, Y. B.; Kanungo, M.; Hemraj-Benny, T.; Wong, S. S. Synthesis and growth mechanism of titanate and titania one-dimensional nanostructures self-assembled into hollow micrometer-scale spherical aggregates. *J. Phys. Chem. B* **2006**, *110*, 702-710.
309. Yang, R.; Gu, Y.; Li, Y.; Zheng, J.; Li, X. Self-assembled 3-D flower-shaped SnO_2 nanostructures with improved electrochemical performance for lithium storage. *Acta Mater.* **2010**, *58*, 866-874.
310. Wu, F.; Li, X.; Wang, Z.; Guo, H. Petal-like $Li_4Ti_5O_{12}$-TiO_2 nanosheets as high-performance anode materials for Li-ion batteries. *Nanoscale* **2013**, *5*, 6936-6943.
311. Tan, Y. F.; Yang, L.; Chen, J. Z.; Qiu, Z. Facile Fabrication of Hierarchical Hollow Microspheres Assembled by Titanate Nanotubes. *Langmuir* **2010**, *26*, 10111-10114.
312. Cheng, J.; Che, R. C.; Liang, C. Y.; Liu, J. W.; Wang, M.; Xu, J. J. Hierarchical hollow $Li_4Ti_5O_{12}$ urchin-like microspheres with ultra-high specific surface area for high rate lithium ion batteries. *Nano Research* **2014**, *7*, 1043-1053.

313. Cheng, Z. P.; Xu, J. M.; Zhong, H.; Chu, X. Z.; Song, J. Hydrogen peroxide-assisted hydrothermal synthesis of hierarchical CuO flower-like nanostructures. *Mater. Lett.* **2011**, *65*, 2047-2050.
314. Xiong, J. Y.; Cheng, G.; Lu, Z.; Tang, J. L.; Yu, X. L.; Chen, R. BiOCOOH hierarchical nanostructures: Shape-controlled solvothermal synthesis and photocatalytic degradation performances. *CrystEngComm* **2011**, *13*, 2381-2390.
315. Tang, Y. F.; Yang, L.; Qiu, Z.; Huang, J. S. Preparation and electrochemical lithium storage of flower-like spinel $Li_4Ti_5O_{12}$ consisting of nanosheets. *Electrochem. Commun.* **2008**, *10*, 1513-1516.
316. Li, G.; Xia, J.; Jiao, J.; Chen, L.; Shen, P. Low-temperature synthesis of peony-like spinel $Li_4Ti_5O_{12}$ as a high-performance anode material for lithium ion batteries. *Chin. J. Chem.* **2011**, *29*, 1824-1828.
317. Kong, D.; Ren, W.; Luo, Y.; Yang, Y.; Cheng, C. Scalable synthesis of graphene-wrapped $Li_4Ti_5O_{12}$ dandelion-like microspheres for lithium-ion batteries with excellent rate capability and long-cycle life. *J. Mater. Chem. A* **2014**, *2*, 20221-20230.
318. Lin, C. F.; Fan, X. Y.; Xin, Y. L.; Cheng, F. Q.; Lai, M. O.; Zhou, H. H.; Lu, L. $Li_4Ti_5O_{12}$-based anode materials with low working potentials, high rate capabilities and high cyclability for high-power lithium-ion batteries: a synergistic effect of doping, incorporating a conductive phase and reducing the particle size. *J. Mater. Chem. A* **2014**, *2*, 9982-9993.
319. Sha, Y.; Zhao, B.; Ran, R.; Cai, R.; Shao, Z. Synthesis of well-crystallized $Li_4Ti_5O_{12}$ nanoplates for lithium-ion batteries with outstanding rate capability and cycling stability. *J. Mater. Chem. A* **2013**, *1*, 13233-13243.
320. Zhu, G. N.; Wang, Y. G.; Xia, Y. Y. Ti-based compounds as anode materials for Li-ion batteries. *Energy Environ. Sci.* **2012**, *5*, 6652-6667.
321. Qiao, J. L.; Liu, Y. Y.; Hong, F.; Zhang, J. J. A review of catalysts for the electroreduction of carbon dioxide to produce low-carbon fuels. *Chem. Soc. Rev.* **2014**, *43*, 631-675.
322. Choi, J.-H.; Ryu, W.-H.; Park, K.; Jo, J.-D.; Jo, S.-M.; Lim, D.-S.; Kim, I.-D. Multi-layer electrode with nano-$Li_4Ti_5O_{12}$ aggregates sandwiched between carbon nanotube and graphene networks for high power Li-ion batteries. *Sci. Rep.* **2014**, *4*, 7334.
323. Shen, L. F.; Uchaker, E.; Zhang, X. G.; Cao, G. Z. Hydrogenated $Li_4Ti_5O_{12}$ Nanowire Arrays for High Rate Lithium Ion Batteries. *Adv. Mater.* **2012**, *24*, 6502-6506.
324. Xia, H.; Luo, Z. T.; Xie, J. P. Nanostructured lithium titanate and lithium titanate/carbon nanocomposite as anode materials for advanced lithium-ion batteries. *Nanotechnol. Rev.* **2014**, *3*, 161-175.
325. Wang, L.; Zhang, Y. M.; Scofield, M. E.; Yue, S. Y.; McBean, C.; Marschilok, A. C.; Takeuchi, K. J.; Takeuchi, E. S.; Wong, S. S. Enhanced Performance of "Flower-like" $Li_4Ti_5O_{12}$ Motifs as Anode Materials for High-Rate Lithium-Ion Batteries. *ChemSusChem* **2015**, *8*, 3304-3313.
326. Shen, L.; Zhang, X.; Uchaker, E.; Yuan, C.; Cao, G. $Li_4Ti_5O_{12}$ Nanoparticles Embedded in a Mesoporous Carbon Matrix as a Superior Anode Material for High Rate Lithium Ion Batteries. *Adv. Energy Mater.* **2012**, *2*, 691-698.
327. Xu, G. B.; Li, W.; Yang, L. W.; Wei, X. L.; Ding, J. W.; Zhong, J. X.; Chu, P. K. Highly-crystalline ultrathin $Li_4Ti_5O_{12}$ nanosheets decorated with silver nanocrystals as a high-performance anode material for lithium ion batteries. *J. Power Sources* **2015**, *276*, 247-254.

328. Marschilok, A.; Lee, C. Y.; Subramanian, A.; Takeuchi, K. J.; Takeuchi, E. S. Carbon nanotube substrate electrodes for lightweight, long-life rechargeable batteries. *Energy Environ. Sci.* **2011**, *4*, 2943-2951.
329. Li, N.; Mei, T.; Zhu, Y.; Wang, L.; Liang, J.; Zhang, X.; Qian, Y.; Tang, K. Hydrothermal synthesis of layered $Li_{1.81}H_{0.19}Ti_2O_5$-xH_2O nanosheets and their transformation to single-crystalline $Li_4Ti_5O_{12}$ nanosheets as the anode materials for Li-ion batteries. *CrystEngComm* **2012**, *14*, 6435-6440.
330. Kim, H.-K.; Roh, K. C.; Kang, K.; Kim, K.-B. Synthesis of nano-$Li_4Ti_5O_{12}$ decorated on non-oxidized carbon nanotubes with enhanced rate capability for lithium-ion batteries. *RSC Adv.* **2013**, *3*, 14267-14272.
331. Hasegawa, G.; Kanamori, K.; Kiyomura, T.; Kurata, H.; Nakanishi, K.; Abe, T. Hierarchically Porous $Li_4Ti_5O_{12}$ Anode Materials for Li- and Na-Ion Batteries: Effects of Nanoarchitectural Design and Temperature Dependence of the Rate Capability. *Adv. Energy Mater.* **2015**, *5*, 1400730.
332. Shen, Y. B.; Eltzholtz, J. R.; Iversen, B. B. Controlling Size, Crystallinity, and Electrochemical Performance of $Li_4Ti_5O_{12}$ Nanocrystals. *Chem. Mater.* **2013**, *25*, 5023-5030.
333. Cheng, H.-Y.; Lai, L.-J.; Ko, F.-H. Rapid and sensitive detection of rare cancer cells by the coupling of immunomagnetic nanoparticle separation with ELISA analysis. *Int. J. Nanomedicine* **2012**, *7*, 2967-2973.
334. Wang, L.; Han, J.; Hoy, J.; Hu, F.; Liu, H.; Gentleman, M. M.; Sfeir, M. Y.; Misewich, J. A.; Wong, S. S. Probing differential optical and coverage behavior in nanotube-nanocrystal heterostructures synthesized by covalent versus non-covalent approaches. *Dalton Trans.* **2014**, *43*, 7480-7490.
335. Villalonga, R.; Villalonga, M. L.; Diez, P.; Pingarron, J. M. Decorating carbon nanotubes with polyethylene glycol-coated magnetic nanoparticles for implementing highly sensitive enzyme biosensors. *J. Mater. Chem.* **2011**, *21*, 12858-12864.
336. Bard, A. J.; Faulkner, L. R. *Electrochemical Methods: Fundamentals and Applications*. Second Edition ed.; Wiley: New York, 2000.
337. Yin, H. S.; Zhou, Y. L.; Liu, T.; Tang, T. T.; Ai, S. Y.; Zhu, L. S. Determination aminopyrine in pharmaceutical formulations based on APTS-Fe_3O_4 nanoparticles modified glassy carbon electrode. *J. Solid State Electrochem.* **2012**, *16*, 731-738.
338. Lin, C. F.; Fan, X. Y.; Xin, Y. L.; Cheng, F. Q.; Lai, M. O.; Zhou, H. H.; Lu, L. $Li_4Ti_5O_{12}$-based anode materials with low working potentials, high rate capabilities and high cyclability for high-power lithium-ion batteries: a synergistic effect of doping, incorporating a conductive phase and reducing the particle size. *J. Mater. Chem. A* **2014**, *2*, 9982-9993.
339. Cao, S. M.; Feng, X.; Song, Y. Y.; Xue, X.; Liu, H. J.; Miao, M.; Fang, J. H.; Shi, L. Y. Integrated Fast Assembly of Free-Standing Lithium Titanate/Carbon Nanotube/Cellulose Nanofiber Hybrid Network Film as Flexible Paper-Electrode for Lithium-Ion Batteries. *ACS Appl. Mater. Interfaces* **2015**, *7*, 10695-10701.
340. Dyakonov, V. The polymer–fullerene interpenetrating network: one route to a solar cell approach. *Physica E: Low-dimensional Systems and Nanostructures* **2002**, *14*, 53-60.
341. G. Yu, J. G., J. C. Hummelen, F. Wudl, A. J. Heeger. Polymer Photovoltaic Cells: Enhanced Efficiencies via a Network of Internal Donor-Acceptor Heterojunctions. *Science* **1995**, *270*, 1789-1791.

342. Sariciftci, N. S.; Braun, D.; Zhang, C.; Srdanov, V. I.; Heeger, A. J.; Stucky, G.; Wudl, F. Semiconducting polymer-buckminsterfullerene heterojunctions: Diodes, photodiodes, and photovoltaic cells. *Appl. Phys. Lett.* **1993**, *62*, 585-587.
343. Halls, J. J. M.; Pichler, K.; Friend, R. H.; Moratti, S. C.; Holmes, A. B. Exciton diffusion and dissociation in a poly(p-phenylenevinylene)/C_{60} heterojunction photovoltaic cell. *Appl. Phys. Lett.* **1996**, *68*, 3120-3122.
344. Hummelen, J. C.; Knight, B. W.; LePeq, F.; Wudl, F.; Yao, J.; Wilkins, C. L. Preparation and characterization of fulleroid and methanofullerene derivatives. *J. Organ. Chem.* **1995**, *60*, 532-538.
345. Kramer, I. J.; Sargent, E. H. The Architecture of Colloidal Quantum Dot Solar Cells: Materials to Devices. *Chem. Rev.* **2014**, *114*, 863-882.
346. Roman, L. S.; Mammo, W.; Pettersson, L. A. A.; Andersson, M. R.; Inganas, O. High quantum efficiency polythiophene/C_0 photodiodes. *Adv. Mater.* **1998**, *10*, 774-777.
347. Wong, K. W.; Yip, H. L.; Luo, Y.; Wong, K. Y.; Lau, W. M.; Low, K. H.; Chow, H. F.; Gao, Z. Q.; Yeung, W. L.; Chang, C. C. Blocking reactions between indium-tin oxide and poly (3,4-ethylene dioxythiophene): poly(styrene sulphonate) with a self-assembly monolayer. *Appl. Phys. Lett.* **2002**, *80*, 2788-2790.
348. Frey, G. L.; Reynolds, K. J.; Friend, R. H. Novel electrodes from solution-processed layer-structure materials. *Adv. Mater.* **2002**, *14*, 265.
349. Ma, J.; Wang, C.; Wroblewski, S. Kinetic characteristics of mixed conductive electrodes for lithium ion batteries. *J. Power Sources* **2007**, *164*, 849-856.
350. Kavan, L.; Procházka, J.; Spitler, T. M.; Kalbáč, M.; Zukalová, M. t.; Drezen, T.; Grätzel, M. Li Insertion into $Li_4Ti_5O_{12}$. *J. Electrochem. Soc.* **2003**, *150*, A1000.
351. Zhu, G.-N.; Wang, Y.-G.; Xia, Y.-Y. Ti-based compounds as anode materials for Li-ion batteries. *Energy Environ. Sci.* **2012**, *5*, 6652.
352. Ouyang, C. Y.; Zhong, Z. Y.; Lei, M. S. Ab initio studies of structural and electronic properties of $Li_4Ti_5O_{12}$ spinel. *Electrochem. Commun.* **2007**, *9*, 1107-1112.
353. Yi, T.-F.; Jiang, L.-J.; Shu, J.; Yue, C.-B.; Zhu, R.-S.; Qiao, H.-B. Recent development and application of $Li_4Ti_5O_{12}$ as anode material of lithium ion battery. *J. Phys. Chem. Solids* **2010**, *71*, 1236-1242.
354. Wilkening, M.; Amade, R.; Iwaniak, W.; Heitjans, P. Ultraslow Li diffusion in spinel-type structured $Li_4Ti_5O_{12}$ - a comparison of results from solid state NMR and impedance spectroscopy. *Phys. Chem. Chem. Phys.* **2007**, *9*, 1239-1246.
355. Zhang, Q.; Zhang, C.; Li, B.; Kang, S.; Li, X.; Wang, Y. Preparation and electrochemical properties of Ca-doped $Li_4Ti_5O_{12}$ as anode materials in lithium-ion battery. *Electrochim. Acta* **2013**, *98*, 146-152.
356. Zhang, Q.; Li, X. Improving the Energy Density of Ca-Doped $Li_4Ti_5O_{12}$ Through Discharging to 0 V Cut-off Voltage. *Int. J. Electrochem. Sci.* **2013**, *8*, 9734-9740.
357. Shi, L.; Hu, X.; Huang, Y. Fast microwave-assisted synthesis of Nb-doped $Li_4Ti_5O_{12}$ for high-rate lithium-ion batteries. *Journal of Nanoparticle Research* **2014**, *16*, 1-11.
358. Ma, Y.; Ding, B.; Ji, G.; Lee, J. Y. Carbon-Encapsulated F-Doped $Li_4Ti_5O_{12}$ as a High Rate Anode Material for Li+ Batteries. *ACS Nano* **2013**, *7*, 10870-10878.